Design and performance analysis of a picosecond-pulsed laser raman spectrometer for fluorescence rejection in raman spectroscopy

Everall, Neil John

DESIGN AND PERFORMANCE ANALYSIS OF A PICOSECOND-PULSED LASER RAMAN SPECTROMETER FOR FLUORESCENCE REJECTION IN RAMAN SPECTROSCOPY

by

Neil John Everall, B.Sc.(Hons.)

York

A thesis submitted

for the Degree of Doctor of Philosophy

to the University of Durham

1986

To

Mum and Dad

In physics too, instead of saying "I have explained such and such a phenomenon", one might say "I have determined causes for it, the absurdity of which cannot be conclusively proved."

G.C. Lichtenberg.

MEMORANDUM

The work reported in this thesis was carried out in the Chemistry Laboratories of the University of Durham between September 1983 and August 1986. This work has not been submitted for any other degree and is the original work of the author except where acknowledged by references.

Parts of this work have been the subject of the following publications:

(i) N. Everall, J. Howard, R.W. Jackson and K. Hutchinson, "Proceedings of the Second International Conference on Time-Resolved Vibrational Spectroscopy", A. Lauberau and M. Stockburger (Eds.), Springer-Verlag, Berlin (1985).

(ii) N. Everall, J. Howard, K. Hutchinson and R.W.Jackson, Rev.Sci.Instrum., 56 (12), 2335 (1985).

(iii) N. Everall, R.W. Jackson, J. Howard and K. Hutchinson, J. Raman Spectrosc., 17, 415 (1986).

(iv) J. Howard, N. Everall, R.W. Jackson and K. Hutchinson, J.Phys.E: Sci.Instrum., in press.

DECLARATION

ACKNOWLEDGEMENTS

The work which is described in this thesis was greatly facilitated by the assistance and advice which I received from many associates during the course of my research at Durham. In particular, I am indebted to my supervisor, Dr. Joe Howard, for his advice, encouragement and support during this work.

I would particularly like to thank Dr. Robert Jackson for providing invaluable training in the use and maintenance of the pulsed laser system, and for advice upon various aspects of computing associated with this work. Several practical aspects of this project would have been made much more difficult without his experience to draw upon.

Thanks are also due to Dr. Tony Royston, and the staff of the Chemistry department electrical/electronics workshop, for their expertise in the construction and maintenance of several items of ancillary equipment used during this work, and to the technical staff of Durham University in general.

Much of the development and fault-finding work associated with this project was greatly simplified by the advice and assistance of equipment manufacturers, and their willingness to loan equipment to this laboratory. In particular, the advice and cooperation of Spectra-Physics and EG&G Ortec Ltd. is gratefully acknowledged.

I would also like to thank the Science and Engineering Research Council for the provision of a CASE award, and the Ministry of Defence for a grant to purchase the diode array detector and the loan of the Spex Ramalog spectrometer. The CASE award was in conjunction with British Petroleum Co.

Finally, I am grateful to Mrs. Marion Wilson for her secretarial skill (and speed!) in typing this manuscript.

DESIGN AND PERFORMANCE ANALYSIS OF A PICOSECOND-PULSED LASER RAMAN SPECTROMETER FOR FLUORESCENCE REJECTION IN RAMAN SPECTROSCOPY

by

NEIL EVERALL

ABSTRACT

Many attempts have been made to reduce fluorescence backgrounds in Raman spectra. A critical appraisal of fluoresence rejection techniques reveals that while many techniques are available which improve the Raman/fluorescence ratio (R/F), very few actually increase the spectral signal/noise (R/N), which is the most important parameter.

Temporal-resolution of Raman and fluorescence photons was investigated in this laboratory, using a picosecond-laser system and gated photon detection. Two detection methods were evaluated. The first, an intensified diode array detector (DAD), could be gated "on" for periods of *ca.* 5 ns, at rates of up to 5kHz. This gave a 5-fold increase in R/F, but a slight reduction in R/N, for a fluorescor with $\tau_f \simeq 10.5$ ns. The R/N degradation arose as a result of the low laser output intensity at kHz pulse rates, rather than inefficiency in fluorescence rejection.

The second method used a continuously-operated photomultiplier tube (PMT), and time-correlated photon counting with *ca.* 1 ns timing-resolution. This yielded R/F and R/N improvements of *ca.* 15 and 3 respectively ($\tau_f \simeq 12$ ns).

Although efficient fluorescence rejection was obtained with each system, the corresponding R/N enhancements were not practically significant. However, the development of theoretical models describing the performance of each system has identified modifications which should give valuable improvements. These include the use of a laser with MW peak powers at kHz pulse rates (DAD system), and use of a microchannel-plate PMT with 50 ps timing resolution. When these (and other) modifications are made, significant R/N enhancements (*ca.* 7 and 13 (DAD and PMT systems respectively)) are expected, thus enabling the study of the majority of "real world" samples. In addition, the limiting theoretical and practical performance of time-resolved rejection is considered, and several hitherto unreported aspects of the behaviour of the laser and detection systems are discussed.

Other techniques were also evaluated, in particular utilising the differing Raman and fluorescence response to variations in laser intensity. While the non-linear fluorescence response to intensity variations of cw lasers has been previously exploited, simple calculations indicate that the use of high-powered pulsed sources could allow discrimination at *ca.* 100-fold lower average powers. However, a satisfactory test of the calculations requires the construction of apparatus not presently available in this laboratory.

CONTENTS

Page No.

CHAPTER ONE

THE ORIGIN AND NATURE OF THE FLUORESCENCE PROBLEM IN RAMAN SPECTROSCOPY

1.1 Introduction - general aspects of vibrational Raman spectroscopy and the fluorescence problem

Raman spectroscopy is an extremely versatile technique which can supply information upon the rotational, vibrational and electronic energy levels of materials in the gas, liquid or solid state. By far the commonest chemical application of the Raman effect is its use to obtain vibrational spectra of materials. Analysis of the vibrational spectrum yields information upon molecular structure and geometry;[1] vibrational frequencies enable computation of force-fields *via* normal coordinate analyses,[1] while bandshapes can be analysed to provide information upon the dynamics of molecular motion.[2] Furthermore, time-resolved measurements of spectra are valuable in elucidating reaction kinetics.[3]

Raman spectroscopy is not merely an alternative to infrared spectroscopy as a means of obtaining vibrational data. The techniques are complementary, since the intensities of Raman and infrared bands are determined by different selection rules and hence different molecular parameters, namely the change in polarizability and dipole moment respectively during vibrations.[1] Therefore, bands which are strong in the infrared are often weak or absent in the Raman spectrum, and so if a complete set of vibrational frequencies are required (for example, in a normal coordinates analysis) it is essential to record both IR and Raman spectra. Furthermore, Raman has several advantages over IR as a spectroscopic technique in its own right, including:

(a) The Raman experiment accesses the entire vibrational range ($0 \rightarrow 4000$ cm^{-1}) in a single experiment, whereas good far IR data ($0 \rightarrow 400$ cm^{-1}) is difficult to obtain.

(b) In general, Raman scattering is sensitive to deformations of non-polar bonds (C=C, C-C, *etc.*) and is insensitive to polar bond vibrations. The converse is true for IR absorption, which illustrates the complementarity of the methods.

(c) Sample preparation is usually very simple in Raman spectroscopy. Solids or gases may be illuminated directly, whereas liquids may be conveniently handled in glass sample cells, or capillaries, which give rise to weak Raman scatter (but strong IR absorption).

(d) The scattered radiation usually lies in the visible/uv region, which allows the use of efficient photoelectric detectors (*e.g.* photomultiplier tubes) compared to the relatively inefficient detectors used for IR radiation.

(e) Time-resolution is higher in Raman spectroscopy, since laser pulses of picosecond duration are now readily attainable at optical wavelengths.

(f) Spatially-resolved vibrational data are often of interest in the study of heterogeneous samples. The spatial resolution of the IR and Raman techniques is governed by the wavelength of the radiation involved, and is typically 1-5μm for Raman compared to 15-20μm for IR.

(g) The Raman spectrum often contains additional information to an equivalent IR spectrum, in that an analysis of the polarisation properties of the scattered radiation allows unambiguous assignment of the symmetry of the vibrations responsible for certain bands in the spectrum (Chapter Three). This is invaluable for a normal-coordinate analysis or in determining molecular geometries.

The applications and relative advantages of IR and Raman spectroscopy are too numerous to be discussed in detail here, and the subject is well covered in the literature.[1-6] Here it suffices to note that it is usually highly desirable to record both IR and Raman spectra in order to obtain the maximum amount of information about a sample, although certain types of problem are studied almost exclusively by one technique or the other due to experimental difficulties. For example, Raman scattering from water is weak, and so the technique is ideal for studying molecules in aqueous solution, whereas surface-adsorbed species have been primarily investigated by IR spectroscopy, due to the sensitivity limitations of Raman at low sample concentrations, and the problem of sample fluorescence.

Since the advent of the laser as a source of high intensity, monochromatic radiation, Raman spectroscopy has undergone a transformation in terms of applicability and versatility. The high power illumination increases the intensity of the (weak) scattered radiation, and tunable lasers allow resonance enhanced spectra to be obtained (Chapter Two), overcoming the problem of lack of sensitivity when studying low concentrations of scattering species.

In addition, the development of high-power pulsed lasers (kW-GW) has allowed access to a whole range of nonlinear Raman techniques, (hyper-Raman, stimulated Raman, CARS, inverse-Raman), which are more difficult (or impossible) to observe with medium power (*ca.* 1W) cw lasers, and which have extended the sensitivy and versatility of Raman spectroscopy as a family of techniques.[7]

Multichannel detectors (Chapter Six) have made possible rapid spectral accumulation, opening new fields of kinetic

studies on millisecond timescales which were impossible with scanning spectrometers and single channel detection. Also, the very efficient stray-light rejection provided by double and triple monochromators allows highly reflective samples to be studied, without swamping the weak Raman signal with that of the elastically scattered light.

The main problem with Raman spectroscopy is the weakness of the effect, in that less than *ca.* 10^{-8} of the incident intensity is scattered as a Raman signal.[8] This is not a problem in itself, since modern photoelectric detectors operate at virtually single photon sensitivity,[9] but the presence of other, non-Raman photons at the detector can completely swamp the Raman signal. If the photons are of a different wavelength to the Raman photons (*eg.* stray elastically-scattered light), then a suitably efficient monochromator can solve the problem. However, if the wavelengths are identical (as in the case of fluorescence emission over the wavelength region of interest), discrimination is much more difficult. In our work we are primarily concerned with obtaining Raman spectra where the noise levels are determined solely by intense fluorescence backgrounds.

Unfortunately, fluorescence emission from optically-excited materials is a very common phenomena; Hirschfeld[10] estimated that Raman spectroscopy does not approach to within an order of magnitude the widespread usage of IR techniques, as a direct result of fluorescence preventing the observation of spectra for over 50% of "real-world" samples, *i.e.* compounds that either cannot be purified to eliminate fluorescing species, or which are intrinsically fluorescent themselves. Thus many samples (*eg.* many oils, paints, catalysts, polymers and materials of biological interest) cannot be studied by this technique,

particularly as the source of the fluorescence is often unknown.[11] For this reason, techniques for suppressing fluorescence levels while recording Raman spectra are of great practical interest, and the evaluation and developments of such methods are the main subjects with which this thesis is concerned. It is worthwhile noting that, at present, no entirely satisfactory method is available, with the results attained being very much sample dependent.

No detailed exposition of the theory of the Raman effect, or of optical absorption and fluorescence emission, will be given in this thesis, since the relevant treatments have been presented in a large number of texts.[1,4,12-17] Only those aspects which directly relate to discrimination between the two processes are included.

1.2 Origin of the fluorescence problem

When a sample is illuminated by a pulse of monochromatic radiation of frequency ν, a variety of competing processes occur, which are essentially either scattering or absorption phenomena (Figure 1.1). For the purposes of our work, we are concerned solely with the scattering which occurs as a result of the vibrational Raman effect, whereby the incident radiation is scattered with a frequency shift of $\pm\nu_{vib}$, where ν_{vib} is the frequency of a Raman-active vibrational mode of the sample.

If the frequency ν is in resonance with an electronic transition, absorption of the radiation can occur (Figure 1.2), resulting in an electronically excited state. The population of this excited state may decay by radiative or non-radiative

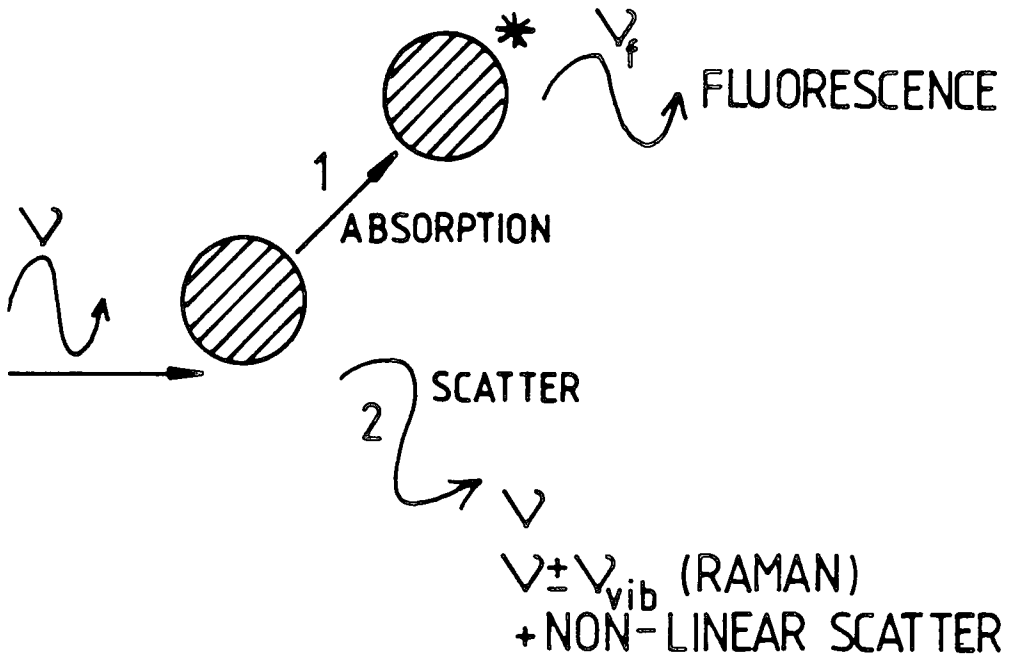

FIGURE 1.1 Competing processes which occur upon the incidence of photons on a sample.

1. Absorption to an excited state, followed by emission of photons with frequency ν_f (where $\nu_f < \nu$).

2. Scattering of photons, which may occur elastically (Rayleigh), inelastically (Raman) or by a non-linear process (Chapter Two). In the vibrational Raman effect, the scattered photons are shifted in frequency by $\pm\nu_{vib}$, the vibrational frequency of a normal mode.

   If $\nu_f = (\nu - \nu_{vib})$, the Raman feature will be obscured by fluorescence emission.

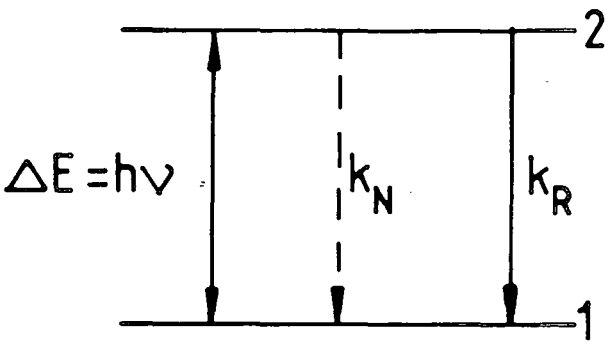

FIGURE 1.2 Deactivation of excited 2 level system after the incidence of an optical pulse of frequency ν. Decay may be radiative or non-radiative (rate constants k_R and k_N. Population of upper state (N_2) decays according to rate equation

$\frac{dN_2}{dt} = -(k_N+k_R)N_2(t)$. In the presence of an optical pulse, absorption and stimulated emission will also be important (Chapter Three).

Three level systems are discussed in Chapters Two and Three.

transitions, the rate of which are governed by rate constants k_R and k_N (with corresponding lifetimes τ_R $(1/k_R)$ and $\tau_N(1/k_N)$). If we assume that once the optical pulse has ended the excited state decays by a simple first order process, the rate equation for the deactivation of the upper state is then:

$$\frac{dN_2(t)}{dt} = -kN_2(t) \qquad (1.1)$$

where $k=(k_R + k_N)$. If $k_N >> k_R$, the upper state decays essentially without the emission of radiation. The fluorescence lifetime of the upper state, τ_f, is given by:

$$\tau_f = 1/k_R + k_N) \qquad (1.2)$$

and represents the average lifetime of a molecule in the excited state.[17] Measurement of fluorescence decay kinetics essentially involves recording the temporal variation of the quantity $k_R N_2(t)$, and so yields a measure of τ_f rather than τ_R. It should be noted that a short fluorescence lifetime does not necessarily imply that the molecule decays by rapid radiative emission, since a large value of k_N also leads to a short τ_f, and results in <u>weak</u> fluorescence. In this work we are interested in materials which primarily suffer radiative deactivation and so fluoresce strongly.

Since τ_f gives no indication of the probability of radiative emission occurring, the fluorescence efficiency is actually better described by the fluorescence quantum yield, which is defined as:

$$Q_F = k_R/k_R + k_N) \qquad (1.3)$$

Q_F gives the fraction of excited molecules which suffer radiative decay.

1.3 The relative efficiencies of the fluorescence and Raman processes

1.3.1 Definition of absorption, fluorescence and scattering cross sections

In order to quantify the magnitude of the fluorescence problem in Raman spectroscopy, it is convenient to compare the relative efficiency of Raman and fluorescence processes in terms of the scattering and fluorescence cross sections, σ_s and σ_F. In general, the cross section represents an area which is associated with each molecule, such that if a photon enters that area it will either be absorbed by the molecule (σ_a) or scattered (σ_s). Since Q_F gives the fraction of molecules which, having absorbed photons, suffer radiative decay, we may assign a fluorescence cross section σ_F, given by equation (1.4)

$$\sigma_F = \sigma_a Q_F \qquad (1.4)$$

Thus, if N molecules are subjected to a photon flux I, we expect, on average, $\sigma_F I$ molecules to yield fluorescence photons. The corresponding Raman scattered intensity is $\sigma_s I$. Clearly, the ratio σ_s/σ_F gives a measure of the relative probability of the Raman and fluorescence events.

1.3.2 Efficiency of Raman scatter

It is shown in numerous texts[4,6,12-15] that in the Placzec polarizability approximation, σ_s is determined effectively by the change in molecular polarizability which occurs as the molecule vibrates along a normal coordinate. In fact, it is found that σ_s is small, a typical value being *ca.* 10^{-28} cm^2 per molecule.[6] Measurement of absolute values of σ_s is difficult and has only been attempted in rare cases, for example the

992 cm^{-1} mode of benzene.[18] Measurement of fluorescence cross sections is somewhat simpler and is considered below.

1.3.3 Efficiency of fluorescence

A knowledge of the values of k_R and k_N allows us to calculate Q_F, and so to estimate the value of σ_F. Hirschfeld[19] gave an interesting calculation of the lower limit of Q_F as a function of the absorption cross section σ_a, which was based upon estimating the upper and lower bounds of k_N and k_R respectively. The radiative decay constant k_R is given by the Einstein coefficient for spontaneous emission,[20] which can be written (for a Lorentzian band) as[19]:

$$k_R = \frac{4\pi^2 c \Delta\lambda \sigma_a(\max) n^2 g_1}{\lambda_{max}^4 g_2} \qquad (1.5)$$

where c is the velocity of light, λ_{max} the wavelength at the peak of the absorption band, $\sigma_a(\max)$ the absorption cross section at λ_{max}, $\Delta\lambda$ the halfwidth of the band, g_2 and g_1 the excited and ground state multiplicities, and n is the refractive index of the medium. Thus k_R may be obtained from the intensity of the absorption band.

The theoretical treatment of nonradiative transitions is not as well developed as that for radiative transitions,[16] but Hirschfeld[19] showed how a lower limit could be calculated for k_N. The maximum uncertainty in the energy dissipated by nonradiative decay is given by the energy separation of levels 1 and 2:

$$\Delta E = hc/\lambda_{max} \qquad (1.6)$$

From Heisenberg's uncertainty principle[15] we know that $\Delta E \Delta t \geq \hbar$, and so the minimum uncertainty in the lifetime of the excited

state, Δt, is:

$$\Delta t \geq \lambda_{max}/2\pi c \tag{1.7}$$

Therefore, the maximum value of k_N is given by

$$k_N \leq 2\pi c/\lambda_{max} \tag{1.8}$$

Weak fluorescence is obtained when $k_N \gg k_R$, in which case $Q_F \approx k_R/k_N$. Since k_R is given by equation (1.5), and k_N has an upper limit, the lower bound for Q_F may be calculated as:

$$Q_F \geq \frac{2\pi\Delta\lambda\sigma_a(max)n^2g_1}{\lambda_{max}^3 g_2} \tag{1.9}$$

The fluorescence cross section for excitation at a wavelength λ is given by equation (1.10)

$$\sigma_F = \sigma_a Q_F$$

$$\geq \frac{2\pi\Delta\lambda\sigma_a(\lambda)\sigma_a(max)n^2g_1}{\lambda_{max}^3 g_2} \tag{1.10}$$

where $\sigma_a(\lambda)$ is the absorption cross section at a wavelength λ. Typical values of the parameters in equation (1.10) would be n=1.5, λ=600 nm, $\Delta\lambda$ = 50 nm, $g_1 = g_2$ and $\sigma_a(max) = 10^{-16}$ cm^2. This yields a total fluorescence cross section of

$$\sigma_F = 3\times10^{-8}\sigma_a(\lambda) \tag{1.11}$$

Therefore, unless $\sigma_a(\lambda) << 10^{-20}$ cm^2, the fluorescence cross section will be comparable to or greater than the Raman cross section. Such a low $\sigma_a(\lambda)$ would be extremely rare for condensed phase samples, and so it is apparent that almost all materials studied by Raman spectroscopy will fluoresce, irrespective of whether impurities are present or not, provided that the laser photon has sufficient energy to be absorbed by the sample.

Fortunately, as Hirschfeld pointed out,[19] a similar cross section does not necessarily result in a similar spectral intensity, since fluorescence emission usually occurs over a much wider spectral bandwidth than the Raman scatter, and may occur in a wavelength range not overlapping the Raman bands. However, for samples which are intrinsically fluorescent over the wavelength range spanned by the Raman scatter, no amount of pretreatment or purification will improve the spectral quality. The aim of the work presented in this thesis was to investigate methods of reducing the fluorescence background which is detected with samples such as these.

1.4 Effect of fluorescence upon a Raman spectrum, and the importance of background noise

Figure 1.3 illustrates schematically the problem encountered when recording the Raman spectrum of a sample which fluoresces strongly over the wavelength region of interest. Since the fluorescence cross section is usually orders of magnitude higher than the Raman cross section, the Raman bands (intensity R) are superimposed upon an intense, broad background (intensity F). This would not be a problem if the background were noise-free, since the Raman bands would be visible on a smooth background irrespective of its intensity. However, the noise associated with the background (N) is often sufficient to totally mask the Raman feature, in which case the vibrational information is lost.

It is very important to realise that it is the noise on the background which causes the problems in Raman spectroscopy, rather than the intensity *per se*. Unless the background is so intense that the detection system is saturated, its magnitude is irrelevant, and so any technique which merely reduces the

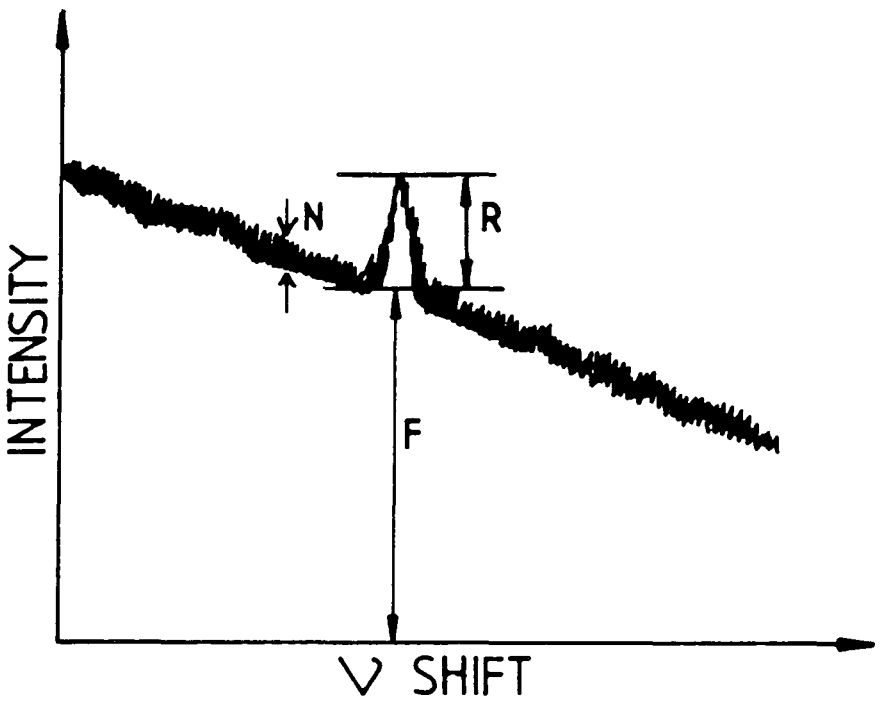

FIGURE 1.3 Effect of fluorescence upon a Raman spectrum. Quality of spectrum is determined by R/N, not R/F. For many samples, N is determined solely by random fluctuations in F, such that $N = \sqrt{F}$. We must therefore increase the ratio R/N by decreasing $\sqrt{F}$ relative to R.

background level without improving the signal/noise (S/N) of the spectrum is virtually useless. This may seem to be a rather obvious point, but it will become apparent that many of the fluorescence rejection techniques which have been reported successfully decrease the background level, and improve the R/F ratio, while degrading the S/N of the Raman band. This arises as a result of the Raman signal being simultaneously reduced in intensity along with the fluorescence.

1.4.1 The object of the fluorescence rejection technique

The object of the fluorescence rejection technique can be stated quite simply as being to reduce the intensity of the fluorescence background F, relative to the Raman signal R, such as to bring about an improvement in the S/N ratio of the Raman band compared to that which would be obtained by using a conventional Raman spectrometer. Unfortunately, it is possible to improve the R/F without improving, sometimes even degrading, the S/N ratio. Such a result is clearly undesirable, and has proved to be the major handicap of many of the techniques which are discussed in the following chapters.

1.4.2 Definition of the S/N and R/N parameters

It is necessary at this point to clarify the definition of the S/N ratio. Strictly speaking, the S/N of the observed Raman band is given by the ratio of the Raman signal to the noise measured at the peak of the Raman band. It is worth noting at this point that the R/F and S/N ratios depend upon the relative magnitudes of the spectral bandwidth of the Raman and fluorescence signals, and upon the instrument resolution (bandpass) of the spectrometer.[21] Therefore, we assume that these factors are kept constant throughout any given re-

jection experiment. In many cases, we can assume that the fluctuations in the light intensity reaching the detector may be described by Poisson statistics (Chapter Two), in which case the S/N is given[21] by equation (1.12)

$$S/N = R/(R+F)^{\frac{1}{2}} \qquad (1.12)$$

Here it is assumed that all other sources of noise (*eg.* dark current, stray light) are negligible compared to the noise on the fluorescence background. For the samples which are of interest in our work, unless fluorescence rejection techniques are employed, F>>R, and so the S/N may be approximated by $R/\sqrt{F}$. This is illustrated in Table 1.1 for a typical Raman signal of 1000 counts on a background of varying intensity, and is seen to be a good approximation when F>10R.

TABLE 1.1 Comparison of R/N and S/N ratios

Raman signal (R)	Fluorescence signal (F)	R/N	R/F
1000	1000	31.6	22.4
1000	5000	14.1	12.9
1000	10000	10.0	9.5
1000	100000	3.2	3.2

For this reason many authors have assumed that the S/N is negligibly different to the $R/\sqrt{F}$ ratio. While this is usually true for the conventionally accumulated spectra, the majority of rejection techniques reduce the fluorescence such that $F \leqslant R$, in which case the S/N is significantly different from the $R/\sqrt{F}$ ratio, by a factor of $\sqrt{2}$ or more.

It is actually highly desirable to specify the efficiency of the fluorescence rejection system in terms of the improvements in the $R/\sqrt{F}$ ratio rather than the $R/(R+F)^{\frac{1}{2}}$ ratio, since it is experimentally much easier to measure the noise on the broad fluorescence background rather than that at the peak of the Raman signal. For this reason, rather than for computational ease, we calculate the improvements in the R/N ratio, where N is defined as the noise on the fluorescence background immediately adjacent to the Raman band ($N=\sqrt{F}$), on the understanding that this may be appreciably different to the S/N ratio, as measured at the peak of the Raman band, when $R \gtrsim F$.

1.4.3 Significance of the R/N improvements

Throughout our work, emphasis is laid upon the relative improvements in R/N obtained by fluorescence rejection, as opposed to the absolute R/N levels. The significance of any given R/N enhancement is obviously dependent upon the R/N level of the original spectrum. For example, the PMT based system described in Chapter Eight yields improvements in R/N of *ca.* 2 when τ_f=*ca.* 4 ns. If an R/N level of *ca.* 4 is acceptable in the fluorescence-suppressed spectrum, the original spectrum must satisfy $R/\sqrt{F}=2$, or $F<R^2/4$, in order for a satisfactory result to be obtained. In general, a system with an R/N enhancement of A, can produce a final spectrum with an R/N level of B, provided that:

$$F \lesssim (AR/B)^2 \qquad (1.13)$$

1.5 Relative timescales of scattering and emission processes

The majority of the work described in this thesis is based upon discriminating between Raman and fluorescence photons on the basis of the differing timescales over which scattering and emission takes place. Therefore, quantification of the rates at which scattering and emission processes occur is important and is considered briefly below.

1.5.1 Raman

Raman scattering of photons is considered to occur "instantaneously".[22,23] However, a lower time limit on the process can be estimated through the uncertainty principle. A typical vibrational transition will involve *ca.*1000 cm^{-1} change in energy, which corresponds to a photon of frequency $3x10^{13}$ Hz. This is the maximum uncertainty in the energy of the process, which implies that we must assign a minimum timescale of *ca.*$5x10^{-15}$ s for the transition. This time is *ca.*1/1000 of the duration of the laser pulses which were used in our work (Chapter Five), and so the temporal distribution of the Raman photons which are scattered from a laser pulse will be essentially identical to that of the laser pulse itself.

1.5.2 Fluorescence

Equation (1.5) enables calculation of the rate of radiative deactivation. Again, using the previous estimates of the parameters in this equation, it is calculated that k_R=*ca.*$10^8 s^{-1}$. Therefore, the lifetime for spontaneous emission would be expected to be of the order of 10 ns. In the absence of nonradiative decay, (k_N=0), the fluorescence lifetime would

equal τ_R, *i.e.* τ_f=10 ns. If k_N>0, the fluorescence lifetime will be reduced accordingly. It is important to remember that the lifetime of the excited state, τ_f, is determined by the rate of both radiative and nonradiative decay. Although either a high k_R or a high k_N can result in a short τ_f, only large values of k_R can give rise to efficient fluorescence.

Finally, we note that there are other differences between the Raman and fluorescence processes besides the temporal behaviour. These are discussed in the following chapters.

1.6 Conclusions

The above sections have given a brief introduction to some of the more important properties of the Raman and fluorescence processes which relate to the work which is described in this thesis, particularly in terms of the relative intensities of the two effects, and the timescale associated with each event. The following chapters expand upon the differences between the scattering and emission processes, and show how they can be exploited to selectively generate or detect Raman photons in preference to fluorescence photons.

REFERENCES - CHAPTER ONE

1. L.A. Woodward, "Introduction to the theory of molecular vibrations and vibrational spectroscopy", Oxford University press, London (1972).

2. R.S. Gordon, J.Chem.Phys. 43(4), 1307 (1965).

3. G.H. Atkinson in "Advances in Infrared and Raman Spectroscopy 9", R.E. Hester and R.J.H. Clark (Eds.), Heyden London, Philadelphia, Rheine (1982).

4. D. Steele, "Theory of Vibrational Spectroscopy", W.B. Saunders Company, Philadelphia, London, Toronto (1971).

5. B.P. Straughan and S. Walker, "Spectroscopy 2", Chapman and Hall, London (1976).

6. M.C. Tobin, "Laser Raman Spectroscopy", Wiley-Interscience, New York, London, Sydney, Toronto (1971).

7. "Chemical Applications of Nonlinear Raman Spectroscopy", A.B. Harvey (Ed.), Academic Press, New York, London, Toronto, Sydney, San Francisco (1981).

8. P.J. Hendra, P.M. Stratton, Chem.Rev., 69, 325 (1969).

9. R.W. Engstrom, "Photomultiplier Handbook", RCACorporation (1980).

10. T. Hirschfeld and B. Chase, Appl.Spectrosc., 40(2),133(1986).

11. C.L. Angell, J.Phys.Chem., 77(2), 222 (1973).

12. G. Placzek, "Rayleigh and Raman Scattering", U.S. Atomic Energy Commission, UCRL TRANS 526 (L), 1962.

13. T.R. Gilson and P.J. Hendra, "Laser Raman Spectroscopy", John Wiley, New York (1970).

14. J. Koningstein, "Introduction to the Theory of the Raman Effect", D. Reidel Publishing Company, Dordrecht-Holland,(1972)

15. W.J. Eyring, J. Walter and G.E. Kimball, "Quantum Chemistry" John Wiley, New York (1944).

16. N. Mataga and T. Kubota, "Molecular interactions and Electronic Spectra", Marcel Dekker, New York (1970).

17. J.R. Lakowicz, "Principles of Fluorescence Spectroscopy". Plenum Press, New York (1983).

18. J.G. Skinner, and W.G. Nilsen, J.Opt.Soc.Am., 58(1), 113 (1968).

19. T. Hirschfeld, Appl.Spectrosc., 31(4), 328 (1977).

20. O. Svelto, "Principles of Lasers", Plenum Press, New York, London (1982).

21. M.C. Tobin, J.Opt.Soc.Am., 58 (8), 1057 (1968).

22. P.F. Williams, D.L. Rousseau and S.H. Dworetsky, Phys. Rev.Lett. 32(5), 196 (1974).

23. D.L. Rousseau, J.M. Friedman and P.F. Williams in "Raman Spectroscopy of Gases and Liquids", A. Weber (Ed.), Springer-Verlag, Berlin, Heidelberg, New York (1979).

CHAPTER TWO

A CRITICAL COMPARISON OF METHODS FOR THE REDUCTION OF FLUORESCENCE NOISE LEVELS IN RAMAN SPECTRA

2.1 Introduction

There are several techniques which may be employed in an attempt to improve the signal/noise ratio (S/N) in Raman spectra which exhibit high fluorescence backgrounds. A high background is here defined as one where the noise associated with the Raman signal is negligible compared to that of the fluorescence background (Chapter One). We are chiefly concerned with cases where the S/N ratio is limited by shot-noise, *i.e.* where the dominant contribution to the noise is made by random fluctuations in the photon flux reaching the detector. This is usually the case in uv-visible spectroscopy, where detectors are relatively efficient.

For our work it is obviously important to be able to describe the noise quantitatively, and in practice it is found[1] that the photon intensity variations may be described by the Poisson distribution (equation 2.1).

$$P(r) = \frac{N_o^{\,r}}{r!} e^{-N_o} \qquad (2.1)$$

where P(r) represents the probability of r pulses being counted in a given time period, and N_o is the average count rate.

It is interesting to ask why the photon flux should follow these particular statistics. This is most easily seen by recalling some simple statistical ideas. It is shown in elementary texts on statistics[2] that, if the probability of an event happening is "p", and the probability that it will not happen is "q", (such that p+q=1), then the probability that it will happen "r" times in "n" different trials is given by the rth term in the binomial expansion of $(p+q)^n$, equation (2.2).

$$(p+q)^n = q^n + nq^{(n-1)}p + \frac{n(n-1)}{2!}p^2q^{(n-2)} \ldots + p^n \qquad (2.2)$$

The shape of the curve of probability *versus* frequency, specified by equation (2.2), varies according to the values of "p" and "n". One particularly important form arises when the probability "p" is very small, but the number of trials "n" is sufficiently large that the product n.p (the average number of occurrences) is significant. Under these conditions, the rth term in the binomial expansion can be shown[2] to approximate to equation (2.1), namely the Poisson distribution.

When a macroscopic sample is irradiated by a moderately intense light source, the probability of an individual photon giving rise to fluorescence emission or scattering is very small, but the number of "trials" is clearly very large, so we expect that the scattered or emitted photons should be well described by Poisson statistics.

The important properties of this distribution for the purposes of this work are that the mean count (N_o) is equal to the most probable count, and the standard deviation is given by $\sqrt{N_o}$. The standard deviation is a suitable measure of the noise level of a signal, so we should expect that a photon flux (of average intensity I), which is adequately described by Poisson statistics, should have a noise level of approximately $\sqrt{I}$. This particularly simple result allows development of mathematical models which are used to interpret experimental results.

Clearly, the S/N ratio for such a signal is given by $I/\sqrt{I} = \sqrt{I}$. This means that the S/N will improve as the square root of any relative increase in the number of photons counted by the detector. This could be achieved by either increasing the laser intensity, or by counting photons for longer periods of time. It might be supposed, therefore, that reasonable

quality Raman data should always be obtainable if one is prepared to record the spectrum over a suitably long time period, or if the incident laser beam is of sufficiently high intensity. This is rarely a feasible method when high backgrounds are present, for several reasons:

(a) with very noisy backgrounds, the period of time required to yield reasonable spectra may be impractical,

(b) problems of laser power drift over long time periods may occur, and this could become the dominant noise source,

(c) very high laser intensities can cause sample decomposition, particularly during prolonged exposure,

(d) very long scan times greatly increase the risk of low frequency noise being recorded, and this often causes far worse degradation of S/N levels than the shot-noise contribution.

Typical sources of low frequency noise are laser power instabilities, mechanical vibration, sample movement/decomposition, bubbles/particles in solution and drifts in the photomultiplier tube (PMT) voltage supply.

The factors noted above indicate that intense fluorescence backgrounds may give rise to noise problems in Raman spectroscopy which are not amenable to treatment by the methods which are successful in other shot-noise limited spectroscopies. Other techniques must therefore be employed, and some of the more successful of these are discussed in detail in Section 2.3 below.

The object of all the techniques described below is to better discern a Raman signal which is obscured by the noise levels of an intense fluorescence background. Naturally, in

order to do this the S/N ratio must be improved, and it is immediately obvious that this may be achieved in three distinct ways:

(a) by data processing (*e.g.* analogue or digital smoothing),

(b) by reducing the fluorescence background relative to the Raman signal,

(c) by enhancing the scattered (Raman) intensity relative to the fluorescence signal.

2.2 Data processing techniques

Signal smoothing is effected by passing the signal through a filter, (either by analogue or digital), such that the high frequency a.c. noise components are attenuated while the d.c. component of interest is passed to the output, thereby improving the S/N ratio.

2.2.1 Analogue smoothing

Analogue smoothing serves to remove noise from a signal prior to recording the data. In its simplest form, it involves passing the signal from a detector through an RC low pass filter, or integrating circuit, such that the high frequency noise components are severely attenuated.[3] The efficiency of such a filter depends upon it having a narrow bandpass relative to the noise bandwidth. Unfortunately, narrowing the bandpass necessitates lengthening the time constant of the smoothing circuit, which in turn increases the scan time of the spectrum. This may be undesirable for the reasons noted in Section 2.1.

2.2.2 Digital smoothing

Signal smoothing may also be effected after the spectrum has been recorded in digital form. The operation of a digital filter is conceptually quite simple.[4] We may convert the output signal of a detector, (essentially a representation in the time domain), into a frequency representation, by Fourier-transforming the data. Multiplication of the frequency representation of the signal with the frequency transfer function[4] of the digital filter will yield a representation of the signal in the frequency domain, but with certain harmonics being suppressed, in an exactly analogous fashion to the analogue smoothing technique. Reverse transforming the data then provides the smoothed data in the time domain.

Certain problems are common to both analogue and digital smoothing, the major one being that the signal of interest may be distorted by the smoothing process. This is most easily seen by remembering that the (ideal, noiseless) signal may equally well be regarded in terms of its Fourier components in the frequency domain. Unless these frequencies lie within the bandpass of the filter, the signal will inevitably be distorted. This is why, in analogue smoothing, the signal must be scanned slowly with respect to the time-constant of the RC circuit in order to avoid distortion. In either case, real bands may be damped by the smoothing process, and hence data lost, unless care is taken in filter design and application.

Finally, it is worthwhile mentioning at this point that it is possible to construct filters with a very narrow bandpass ($<< 1$Hz) of variable central frequency position. These are known as lock-in amplifiers, and their use in noise sup-

2.2.3 Baseline subtraction

One common approach to improving the signal/background ratio in Raman spectra has been to model the baseline by a polynomial fit,[5] and then to subtract the calculated background from the digitised data to yield a flat baseline of zero amplitude. This method sometimes allows easier estimation of the intensities of bands which lie on sloping backgrounds, but it is extremely important to realise that such an approach is purely cosmetic in terms of improvement in spectral quality, since no increase in the S/N ratio is obtained.

2.3 Reduction of the fluorescence background

2.3.1 Elimination of fluorescing impurities

The method applied here primarily depends upon the source of the fluorescence. As was discussed in Chapter One, all materials are intrinsically fluorescent, but for many samples the intensity of emission is not great enough to cause problems. Therefore, when the fluorescence arises from a contaminant in the sample, we can try physically to remove the fluorescor or to chemically alter it so that it no longer fluoresces in the region of interest. Thus typical routes include physical separation such as chromotography, or solution "clean-up" *via* mixing with activated charcoal and subsequent filtration.[6,7]

When suitably-stable materials are being investigated, they are sometimes pre-treated by heating to high temperatures, often in the presence of oxygen,[8,9,10] although it should be noted that with some samples this procedure can, in fact, worsen the background, for reasons that are not understood.[9,10]

The success of purification procedures is highly sample dependant and it is difficult to generalise.

One very common method is that of "drench-quenching", where the sample (usually a solid) is irradiated with copious quantities of laser-light in the hope of photolytically converting the contaminant into a non-fluorescing species, or of volatalising it. This technique is rather unreliable, and depends upon the sample of interest being stable under intense irradiation. Nevertheless, it has been successfully employed on a number of occasions, for example in the study of catalyst surfaces.[10]

2.3.2 Quenching of fluorescence with a chemical agent

The extent to which fluorescence is a problem depends very much upon the relative rates of the non-radiative energy transfer processes, compared to those of radiative transitions between the electronic singlet states (Figure 2.1). It is sometimes possible to increase the non-radiative transition probabilities to such an extent that the fluorescence emission becomes relatively ineffective as an energy transfer mechanism. Referring to Figure 2.1, if the transition $T_o \leftarrow S_1$ becomes much more favourable than fluorescent decay ($S_o \leftarrow S_1$), then the fluorescence is effectively quenched.

The theoretical treatment of non-radiative processes is poorly developed compared to that of radiative pathways, and several competing mechanisms are believed to play an important role.[11] However, one widely accepted mechanism[12] for the quenching process is that denoted "the heavy atom effect". It has long been realised that the fluorescence quantum yield of

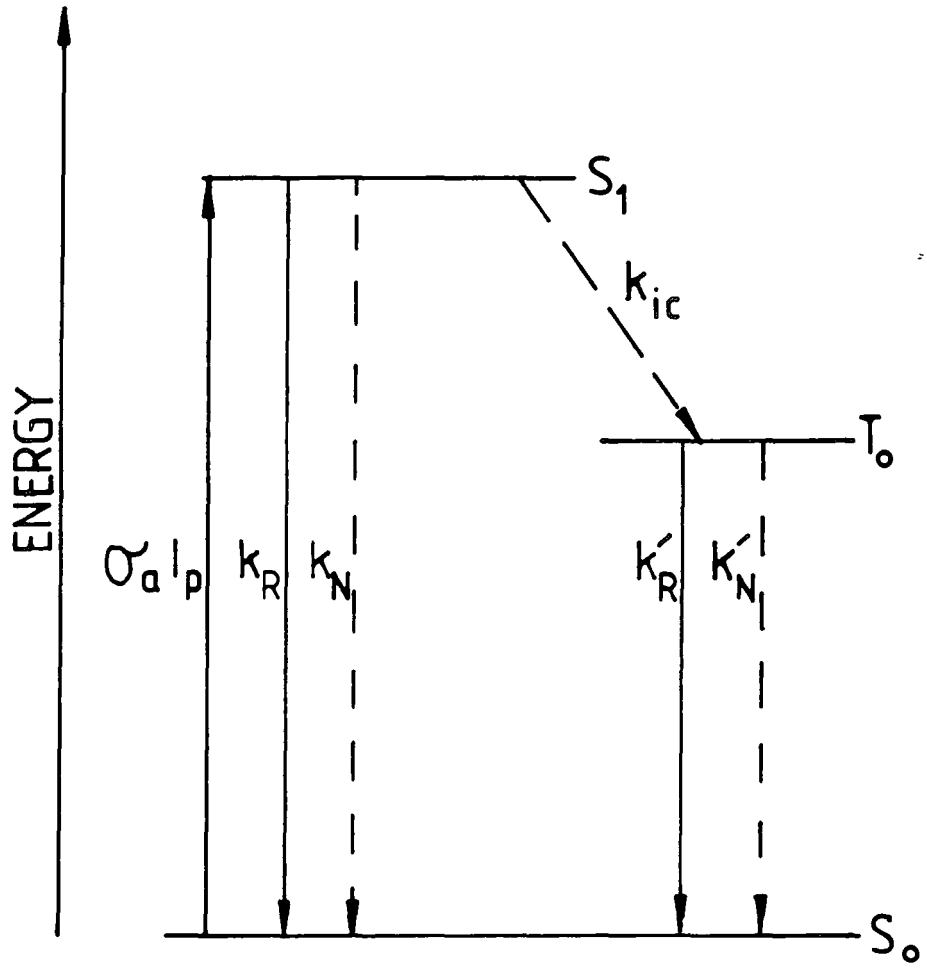

FIGURE 2.1 Chemical quenching of fluorescence. If the rate constant for intersystem crossing $T_o \leftarrow S_1$ can be enhanced over k_R, the fluorescence is quenched. Phosphorescence does not usually occur in solution since $k'_N >> k'_R$. (N.B. the effect of stimulated emission ($\sigma_e I_p$) is neglected in this diagram).

certain fluorophores in solution may be drastically reduced by the addition of certain particular heavy atoms or ions, most notably the halides. For example, the relative quenching efficiency of the halide ions varies as $F^- < Cl^- < Br^- << I^-$. This is believed to arise as a result of spin-orbital perturbation to the outer electrons of the fluorophore, (induced by the electric field near the nucleus of the heavy ion/atom), thereby resulting in an increased transition probability between singlet and triplet states. These transitions are normally spin-forbidden due to the orthogonality of the spin eigenfunctions, but the spin-orbit interaction is presumed to perturb the molecular wavefunctions sufficiently that non-zero transition moments result.

The spin orbit interaction may be thought of (at an elementary level) as the interaction of the magnetic dipole of the spin of the electron with the magnetic field generated by its motion around the nucleus. The magnitude of the interaction can be shown[13] to be approximately proportional to Z^4 (where Z is the atomic number of the nucleus), in the presence of coulombic fields. Therefore, we would predict (qualitatively) that heavy ions would cause the greatest perturbation and so effect the most efficient quenching. This <u>is</u> observed in practice.

Furthermore, Kasha[12] observed that the intensity of the $T_o \leftarrow S_o$ absorption band was greatly increased for certain aromatic fluorescers in solutions containing iodide ions, which again points to an enhancement in the "spin forbidden" intersystem crossings. Further details and references on the mechanisms of energy transfer between electronically excited states may be found in reference 11.

On a more practical level, Friedman and Hochstrasser[14] successfully employed iodide-ion quenching in order to obtain the resonance-Raman spectrum of a solution of the dye fluorescein, thus demonstrating that although the success of quenching is very much sample dependent, it can be very effective under suitable conditions.

2.3.3 Shifting the Wavelength of the exciting radiation

One very important difference between Raman and fluorescence processes is that for fluorescence to occur, the frequency of the incident radiation must be in resonance with an electronic transition, whereas Raman scatter can occur, in principle, irrespective of the excitation wavelength. Therefore it should be possible to avoid fluorescence by choosing an excitation frequency which lies outside the absorption bands of the fluorophore, while still observing Raman scatter.

This method suffers from several fundamental physical and technical limitations. The positions of electronic absorption bands vary widely from sample to sample, which means that if one decides to use a laser which operates in the visible region, a wide range of sources of exciting radiation must be available in order to cover every situation. This limitation may be overcome, in principle, by always employing a laser which operates in the near IR region, thereby missing all of the electronic absorption bands.

2.3.3.1 Use of near-I.R. Lasers as exciting sources

There are two major disadvantages to this approach. Firstly, it is a physical property of the Raman

process that the intensity of the scatter is proportional (in the non-resonant Raman effect) to the fourth power of the frequency of the scattered radiation,[15] so shifting the excitation wavelength from the visible to the near IR greatly attenuates the Raman signal. The problem is exacerbated by the fact that most PMT detectors are extremely inefficient in this wavelength region,[16] and this has led to the use of solid state detectors, which, although inherently noisy compared to PMTs, can have substantially higher quantum efficiencies at these wavelengths.[16,17]

Fujiwara *et al*[18] recently reported the use of a pulsed Nd:YAG laser, (operating at 1.06μ), with a germanium detector, in order to obtain reasonable quality Raman data from a variety of liquid samples. Use of a boxcar averager improved the S/N ratio of the spectrum over that which would have been obtained by a continuous detection technique. A conventional dispersive monochromator was used in this work. Unfortunately, no spectra were presented of samples which fluoresce strongly under visible excitation, so it is impossible to assess the usefulness of this approach for fluorescence rejection. There is no doubt that the spectra which were included were of significantly poorer quality than those obtained under visible excitation. However, it was shown that Raman data <u>can</u> be obtained with a conventional dispersive instrument using near-IR excitation. Considerably better results can be achieved if one employs a <u>interferometric</u> spectrometer in conjunction with the solid state detector; this is discussed in Section 2.3.4 below.

2.3.3.2 Tunable-wavelength radiation in the visible region

If it is decided to work with visible excitation, but to use a frequency which is not in resonance with an electronic transition, a different set of problems are encountered, primarily in terms of obtaining a suitable source of exciting radiation at the desired frequency. Although the common ion lasers (argon and krypton) do oscillate over a number of wavelengths, (*ca.* 334-799nm), it may still prove impossible (for a particular sample) to choose a wavelength which does not coincide with an electronic absorption. Also, the lasing efficiency varies considerably across the wavelength range, which limits power available for excitation.

The development of powerful, tunable dye lasers[19] provides (in principle) an ideal excitation source, but in practice the tuning range of any particular dye is fairly limited (*e.g.* 570-650nm for rhodamine 6G in methanol/glycerol). Since the absorption bands of organic fluorescors may extend over many tens of nanometers, this tuning range may be insufficient to move the excitation frequency outside the limits of an absorption band.

This point may be better appreciated by considering the uv-vis absorption spectrum of a 1×10^{-5}M solution of R6G in a 10:1 mixture of benzene/ethanol (Figure 2.2). The absorption cross section at the wavelength of maximum absorption (536nm) is *ca.* 4.2×10^{-16} cm^2. It appears from the spectrum that excitation at 595nm should <u>not</u> result in fluorescence, but in fact even the very small absorption cross section at this point ($\simeq 10^{-19}$ cm^2) is sufficient to result in fluorescence emission at many times the Raman intensity. This is

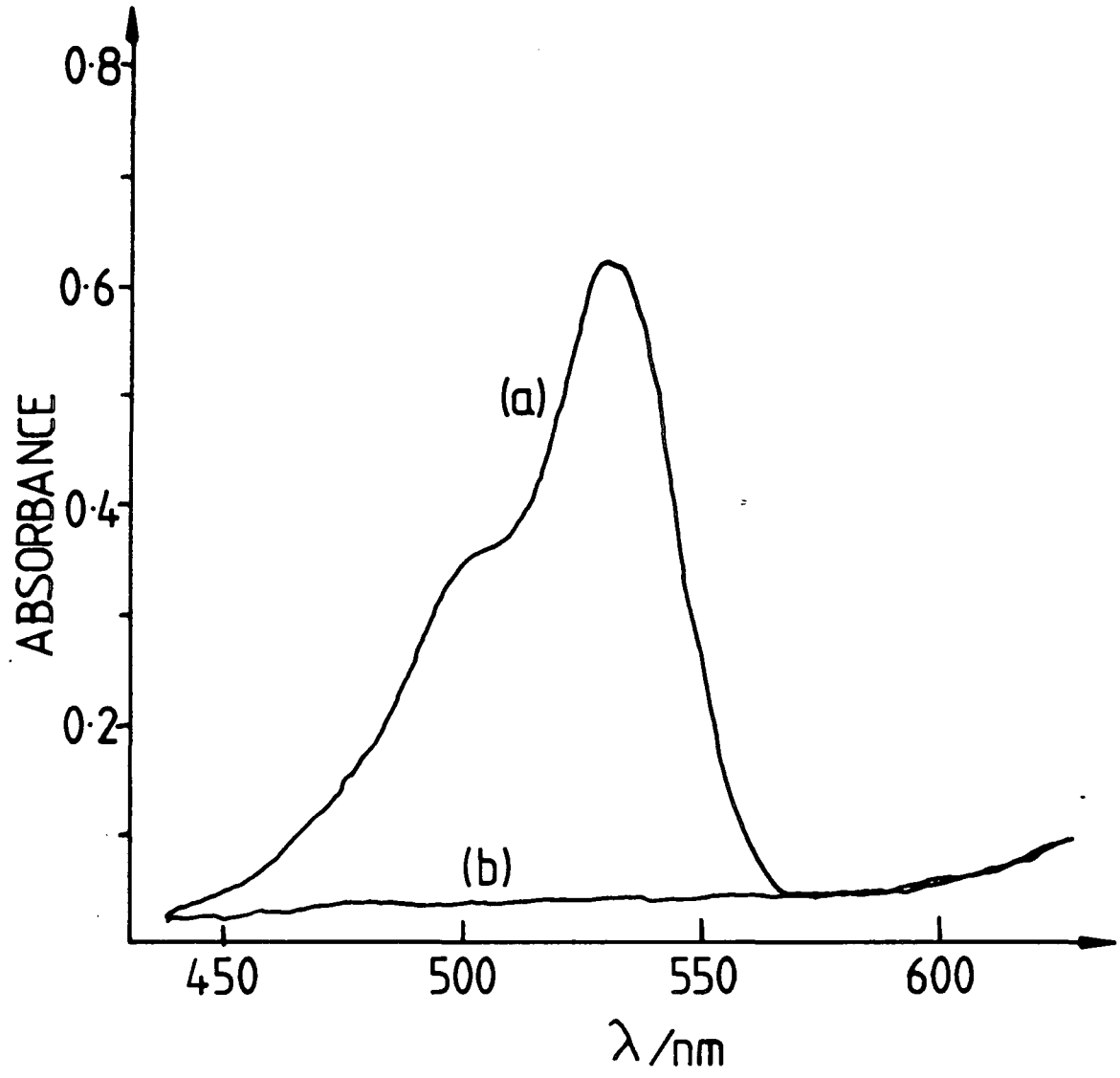

FIGURE 2.2 UV-visible absorption spectrum of R6G.

(a) 10^{-5}M solution of R6G in benzene/ethanol mixture.

(b) Benzene/ethanol blank.

demonstrated in Chapter Seven. Therefore, in order to avoid using wavelengths which stimulate electronic transitions, a number of different dyes would need to be available, and it would be impractical to change dyes as a routine matter from sample to sample.

2.3.4 Fourier transform Raman spectroscopy

Hirschfeld and Chase[20] recently reported the use of a Fourier transform (FT) Raman spectrometer to obtain high quality Raman data from samples which are normally highly fluorescent under visible excitation. The high degree of fluorescence rejection was due solely to the fact that a high power red laser line (647.1nm at 800mW) was employed, thereby avoiding electronic excitation of the molecules (see Section 2.3.3). One would anticipate that the use of a conventional dispersive instrument with a PMT detector would also have been effective under these conditions.

The authors also presented data obtained using a Nd:YAG laser (650mW at 1.06μ) and a cooled PbS detector, thereby eliminating fluorescence entirely. Conventional Raman detectors would be ineffective under these circumstances, since the quantum efficiency of photomultiplier tubes is very low at these wavelengths. Although solid state detectors do have the quantum efficiency[16,17] required to operate in this region, (60-80%), they are much noisier than PMTs. The use of an interferometer largely overcomes this problem because of the multiplex advantage of FT spectroscopy, namely the simultaneous acquisition of data over every spectral element of interest. Therefore, the time required to accumulate a spectrum of a given S/N ratio is reduced compared to a conventional dispersive instrument.

Interestingly, it is effectively the multiplexing process which has hindered the use of FT techniques in Raman spectroscopy. This is because unless the overwhelmingly intense Rayleigh line can be filtered out and prevented from reaching the detector, its shot noise is spread over every spectral element, causing problems at least as severe as the fluorescence background which has been eliminated! Hirschfeld and Chase[20] demonstrated that the extremely efficient stray light rejection required could be achieved by a variety of filtering techniques, and so produced a viable instrument.

Their results suggest that the usefulness of this method is limited only by the availability of suitable filters, but it remains to be seen whether the technique becomes widely adopted.

One might assume that similar benefits could be accrued by using multichannel detectors in order to collect data over all spectral elements simultaneously. The main problem with this approach is that the typical silicon photodiode arrays have very high quantum efficiencies over the visible region (60-70% over the range 400-800nm),[17] but this efficiency falls drastically for wavelengths above 900nm. This would limit the extent to which the laser radiation could be profitably shifted to the red. The advantage of this method compared to FT spectroscopy is that the noise associated with strong features is not spread over every spectral channel, and so the stray light rejection characteristics of conventional spectrographs is sufficient to produce good quality spectra, without the introduction of more "exotic" filtering systems.

2.3.5 Time resolution of Raman and fluorescence processes

Perhaps the most obvious distinguishing feature between the two processes lies in the timescale over which each event occurs. The Raman scattering is effectively instantaneous, while fluorescence lifetimes can range from a few picoseconds to hundreds of nanoseconds (Chapter One). It would appear that provided sufficiently good pulsed excitation sources and timing electronics are available, it should be possible to time-resolve the two processes. The physical basis and quantitative efficiency of temporal discrimination is discussed in detail in Chapter Four.

This has, in fact, been one of the most commonly applied methods. Various techniques may be used to achieve the time-resolution, and these will be discussed in Chapters Four and Six. The time-resolution method was chosen as the basis of the pulsed laser Raman spectrometer which will be described in this thesis.

2.3.6 Polarisation discrimination

When a laser beam is used as an excitation source, the incident radiation is linearly polarised (unless deliberate modifications are made) and it is found that the polarisation of the resulting Raman scatter (for the case of single crystals and liquids) bears a definite relationship to that of the incident beam.[21] (When powders are illumin-

ated this is not the case since the polarisation is "scrambled" by multiple reflections). The corresponding polarisation characteristics of the fluorescent emission are often sufficiently different to allow a certain amount of discrimination to be made between the two processes. This method will be discussed (along with experimental results) in Chapter Three.

2.3.7 Fluorescence rejection using modulation techniques

The methods described in this section all have the distinguishing feature that a property of the laser beam (wavelength, amplitude or polarisation) is modulated prior to irradiating the sample.

2.3.7.1 Frequency modulation (FM)

This technique involves modulation of the wavelength of a cw dye laser, and has been described in detail by Funfscilling and Williams.[22] The method relies on the fact that the absolute position of the Raman lines will be modulated in phase with the exciting frequency, but the broad, featureless fluorescence background will remain essentially unaltered, provided that the modulation limits are fairly close (typically 0.5nm). Use of phase-sensitive detection then allows selection of those signals which are modulated in phase with the laser, thereby accepting the Raman signal in preference to the luminescence. Unfortunately,

the authors calculated a six-fold decrease in S/N when the spectra are shot noise limited, assuming that the modulated and unmodulated spectra are accumulated for equal times. The technique appears to be of greater use when low frequency noise is dominant (Section 2.1), since this is more easily rejected by the lock-in amplifier (Section 2.3.7.4). Galeener[23] has also discussed the use of this method, but it does not appear to have been widely adopted.

2.3.7.2 Amplitude modulation (AM)

The use of amplitude modulated cw lasers for fluorescence rejection has recently been reported by van Hoek *et al*[24] and Genack.[25] The rationale behind this approach is that the Raman scatter will be modulated with exactly the same phase and frequency as the laser output, but the fluorescence emission lags the excitation in phase by an amount determined by the excitation frequency and the fluorescence lifetime τ_f. (This behaviour has been utilised extensively to determine fluorescence lifetimes, and has been discussed in detail in a recent review on fluorescence spectroscopy).[26] This implies that phase-sensitive detection can separate the Raman and fluorescence contributions to the overall modulated signal.

Signal/noise enhancements of *ca.* x 2 were reported when a dilute (20μM) solution of 3-methyl lumiflavin ($\tau_f \simeq 5$ns) was examined using a PMT/lock-in amplifier technique.[24] Genack[25] employed two electro-optic (EO) modulators, one to modulate the laser intensity, and the other to modulate the emitted/scattered light prior to detection with an optical multichannel analyser. Operating the modulators in and out of phase allowed subtraction of the fluorescence signal from the (fluorescence + Raman) signal. The very important point was made that although the fluorescence background can be removed by this method, the subtraction of one noisy signal from another results in a low, but noisy background, *i.e.* no improvement in S/N is obtained in shot-noise limited spectra. This necessitates considerable signal averaging to obtain reasonable spectra, and reinforces the point that merely suppressing the background level is not sufficient; the noise levels must be reduced also. The only reliable way to achieve this is to suppress the background signal before it is registered by the counting electronics.

Demas and Keller[27] have also discussed the use of phase-resolved spectroscopy in order to selectively isolate fluorescence and Raman signals. They stated that phase sensitive detection does not reduce statistical (shot) noise. Although this statement is technically correct, it is a fact that the correct use of a lock-in amplifier does result in suppression of statistical noise. This is discussed further in Section 2.3.7.4 below.

2.3.7.3 Polarisation modulation

Arguelo *et al*[28] utilised a polarisation

modulation technique, whereby the angle of a polarisation analyser was varied periodically prior to detection of the radiation scattered from the sample. The polarised Raman lines were modulated in phase with the analyser, but the non-polarised fluorescence was effectively unaltered. Again, phase sensitive detection allowed resolution of the two components. This method will be discussed in more detail in Chapter Three, but here it suffices to note that the success of the method depends critically upon the state of polarisation of the Raman lines, and so some Raman bands may actually be lost in this approach as a result of their depolarised nature.

2.3.7.4 Use of lock-in amplifiers in signal recovery

It is worthwhile at this stage to review briefly the operation of a lock-in amplifier (LIA), since it is apparent that these devices are used widely in extracting weak signals from noisy backgrounds. This is important in view of the remark by Demas and Keller[27] that phase sensitive detection (PSD) is ineffective in suppressing statistical noise. While this statement is strictly correct, it is also misleading, since a correctly set up LIA does significantly reduce random noise.

Figure 2.3 is a schematic representation of a LIA. The device can be considered simply as a signal multiplier followed by a low-pass filter.[29] The signals which are input into the multiplier consist of a reference waveform of frequency ω_r and a signal of frequency ω_s, shifted in phase relative to the reference through an angle ϕ. The output of the multiplier is then given by:

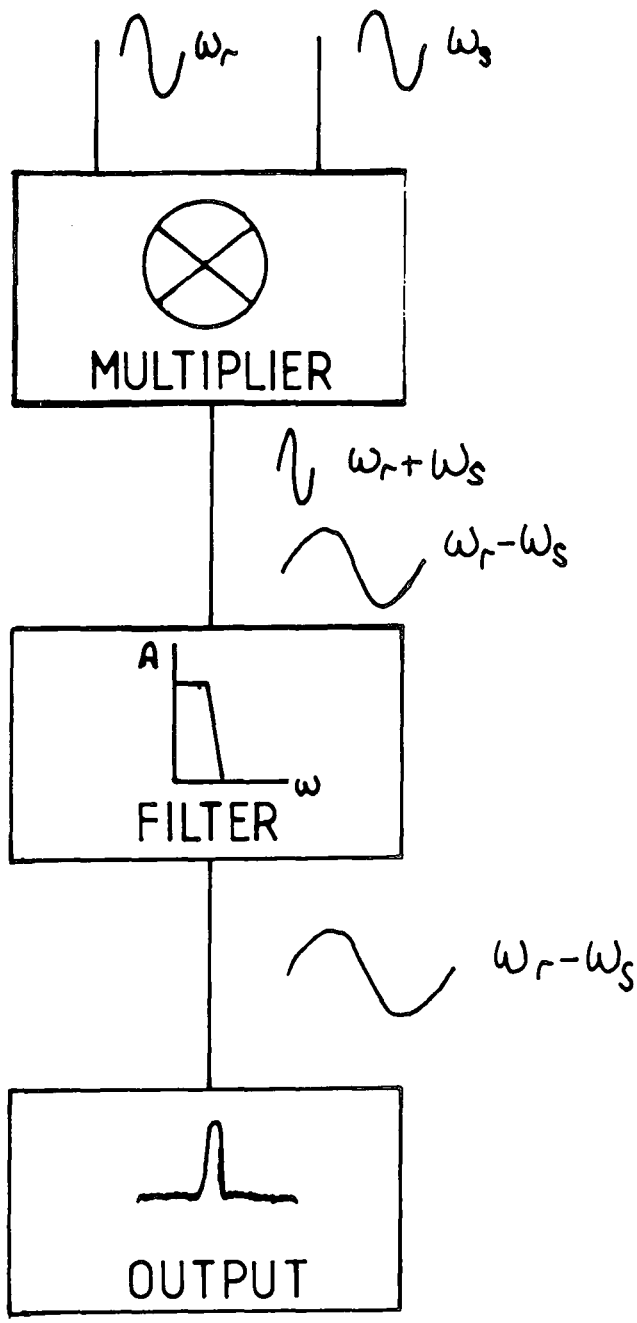

FIGURE 2.3 Schematic diagram of a lock-in amplifier. ω_r and ω_s are the reference and input signals respectively, which are multiplied together to give the beat frequencies $\omega_r \pm \omega_s$. The filter transmission amplitude (A) is such that only the heterodyne $(\omega_r-\omega_s)$ signal is passed freely. See text for details.

$$V_o = V_r\cos(\omega_r t).\ V_s\cos(\omega_s t-\phi) \qquad (2.3)$$

or

$$V_o = \frac{V_r V_s}{2}\{\cos[(\omega_r+\omega_s)t-\phi] + \cos[(\omega_r-\omega_s)t + \phi]\} \qquad (2.4)$$

where $V_r\cos(\omega_r t)$ and $V_s\cos(\omega_s t-\phi)$ are the reference and signal waveforms respectively. The output consists of beat frequencies $(\omega_r \pm \omega_s)$, shifted in phase by $\pm\phi$ relative to the reference. The low pass filter will reject the sum frequency $(\omega_r+\omega_s)$, but the heterodyne signal $(\omega_r-\omega_s)$ will be passed provided that $(\omega_r-\omega_s)$ falls within the bandpass of the filter.[29] The output of the low pass filter will therefore be given by equation (2.5).

$$V_o = \frac{V_r V_s}{2}\{\cos[(\omega_r-\omega_s)t + \phi]\} \qquad (2.5)$$

The LIA therefore acts as a filter, the position of which may be altered from $0\rightarrow\omega_r$, and of width determined by the low-pass filter on the output. The output bandpass may be very small (*i.e.* 0.001 Hz).[29]

In the amplitude modulation experiments described above, the frequency of both the modulated Raman and fluorescence signals is identical to the reference frequency of the LIA, *i.e.* $\omega_r=\omega_s$. However, the Raman signal is not shifted in phase ($\phi_R=0$), but the modulation is arranged so that the fluorescence phase shift is $\pi/2$, *i.e.* $\phi_F=\pi/2$. Equation (2.5) then gives the response of the detector to each signal, namely, a constant voltage for the Raman ($V_r V_s/2$) and a <u>zero</u> output for the fluoresence ($[V_r V_s/2].\cos(\pi/2)=0$). Therefore, the fluorescence signal is totally suppressed. An identical analysis may be made when non-sinusoidal waveforms are under investigation, by first expanding the periodic waveform as a

Fourier series of sinusoidal waves, and then carrying out the procedure outlined above.[29]

The random noise associated with the fluorescence is not phase-correlated with the reference waveform, and so cannot be suppressed merely by phase analysis. The bandwidth of random noise is wide, and so many of the frequency components of the noise, (ω_N), will be rejected since the heterodyne signal ($\omega_r - \omega_N$) will not pass through the output filter unless $\omega_r \simeq \omega_N$. Therefore, assuming the noise is white (*i.e.* constant amplitude over the entire bandwidth), it will be rejected by a factor BP/BW, where BP is the bandpass of the filter and BW is the noise bandwidth.

It should be clear that although statistical noise is not discriminated against by phase analysis, it is suppressed by the action of the low pass filter of the LIA. Unfortunately, narrowing the bandpass of this filter raises the time constant of the circuit, and so necessitates longer accumulation times. Therefore, the modulation techniques discussed above should result in an increase in S/N provided that the time constant is suitably chosen, although this may result in impractically long data accumulation periods.

This very brief discussion has barely outlined the operation and application of lock-in amplifiers. For a more detailed review of these important devices, the reader is referred to the literature.[29,30]

2.3.8 Saturation of fluorescence response

It is perhaps ironic that fluorescence spectroscopists are often faced with the problem of interfering Raman signals, and so considerable effort has been expended in developing Raman

rejection techniques! Of course, this only becomes a problem when very dilute solutions of fluorophores are being studied, (approaching single-molecule detection in state-of-the-art experiments[31]), and Raman scatter from the vast excess of solvent molecules masks the fluoresence signals. One popular approach has been to utilise the fact that the fluorescence can be saturated (owing to the effect of stimulated emission), and so the fluorescence intensity does not increase linearly with laser intensity, but reaches a limiting value[31-33] (Figure 2.4). The Raman scatter, on the other hand, increases in direct proportion to the incident intensity (except at very high irradiances, when non-linear effects predominate). High laser intensities may be required in order to cause substantial deviations from linearity in the fluorescence response, depending upon the relative magnitudes of the rate constants for excitation and de-excitation.[34]

The major experimental requirement is that a powerful laser beam is focussed to a diffraction limited spot, in order to ensure that the power density is sufficient to saturate the fluorescence response. Modulating the laser intensity at a frequency ω causes the Raman signal to be modulated (in phase) at ω, but the non-linear fluorescence response gives a distorted signal which is enriched in harmonics at 2ω, 3ω, *etc*. Phase sensitive detection at one of the higher harmonics, *e.g*. 2ω, will then eliminate the interfering scattered background at ω and allow detection of the isolated fluoresence component at 2ω.

This fundamental difference has been employed to effectively eliminate the Raman background in fluorescence

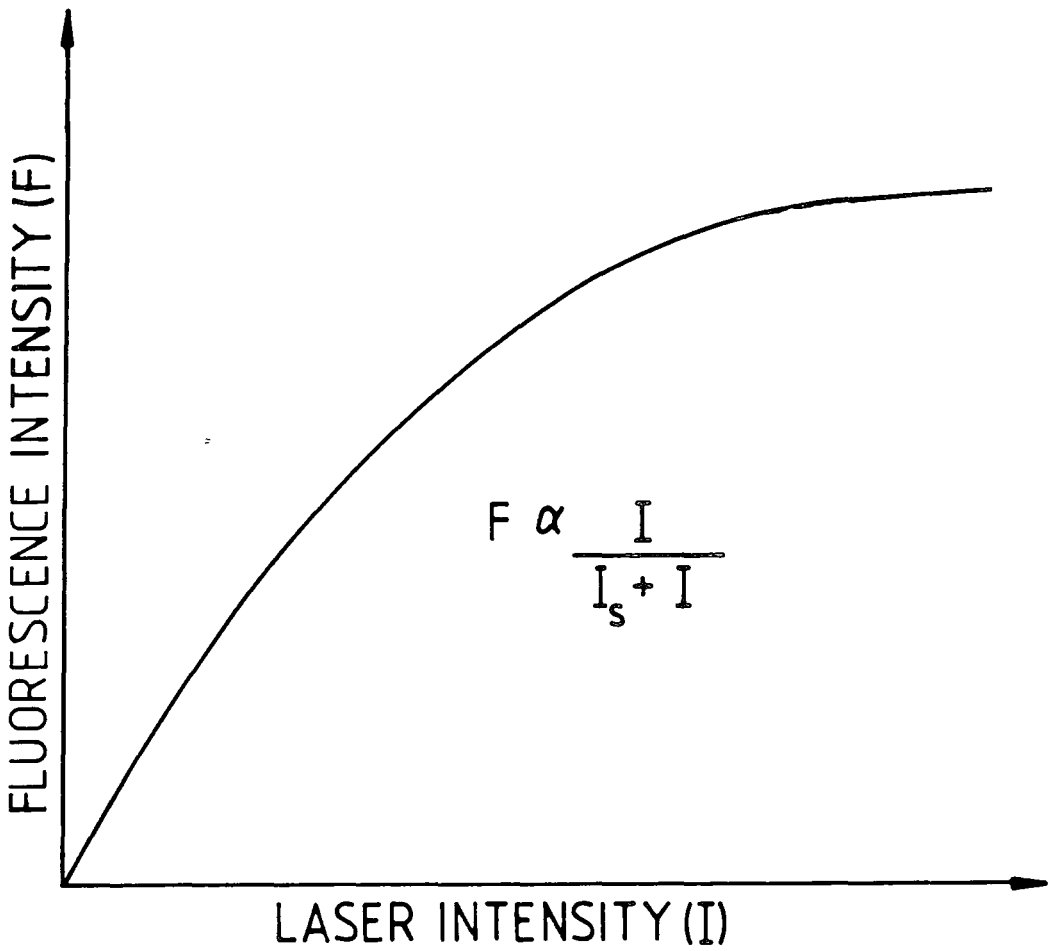

FIGURE 2.4 Curve showing the response of a fluorophore as a function of laser intensity. The response is effectively linear at low intensity, with a gradient of $1/I_S$, where I_S is a constant known as the "saturation intensity".

spectra,[31-33] but it should be noted that although the amplitude of the scattered background was reduced, there was no reduction in the statistical noise level associated with the background.[33] Trkula and Keller pointed that the 2nd harmonic detection method actually degrades the S/N ratio when the spectra are shot-noise limited. It will become apparent that this problem exists with many of the fluorescence suppression techniques which have been applied in the past.

However, it seems possible that a combination of this method, and the AM modulation discussed by Genack[25] (Section 2.3.7.2) might prove useful in eliminating fluorescence signals rather than the Raman features. That is, the AM experiment could be performed with a laser intensity that is sufficient to saturate the fluorescence response (Figure 2.4). Then, phase sensitive detection at ω, both in and out of phase, with the modulation (as in the AM case), would allow the usual subtraction of the fluorescence signal at ω, but with the added advantage that a substantial proportion of the fluorescence signal is now carried in the higher harmonics, thereby reducing the noise levels in the subtracted spectra.

This method does not appear to have been reported in the literature, but should be relatively easy to evaluate by any group which has access to the modulation/phase sensitive detection equipment necessary.

The fact that the fluorescence eventually reaches a limiting intensity suggests that simply monotonically raising the laser intensity at the sample should eventually yield a proportionate Raman response while the fluorescence noise level stays constant. The possibility of achieving this with a pulsed laser beam is considered quantitatively in Chapter Three.

2.4 Methods involving the enhancement of the Raman signal

We will now consider the possibility of improving the R/N ratio, (Raman signal/fluorescence noise), by increasing R rather than decreasing N. Only a brief discussion will be presented here since a full consideration of these techniques is outside the scope of this thesis. The enhancement effects can be divided into two classes, namely, the nonlinear Raman processes which arise as a result of high laser intensities, and enhancements which occur as a result of special sample conditions.

2.4.1 Nonlinear Raman spectroscopy

A host of nonlinear Raman effects are now known to exist, and are utilised in a range of techniques, including Coherent Antistokes Raman Spectroscopy (CARS[35]), Inverse Raman Spectrometry,[36] Stimulated Raman spectroscopy,[37] and Hyper Raman scattering.[37] The usefulness of these approaches lies in the fact that the Raman signal is enhanced by several orders of magnitude, and in the case of antistokes transitions the scattered radiation is far removed in energy from the fluorescence emission. Furthermore, the Raman signal is carried in a collimated beam which may be easily spatially isolated from the more isotropically distributed fluorescence, further reducing the background.

However, some drawbacks do exist, particularly in terms of the expensive, complex equipment which is required, and the non-trivial practical problems in setting up a working system. Fundamental physical limitations exist, such as the fact that stimulated Raman spectra are only obtained for the transition which has the highest spontaneous Raman cross section.[37]

Also, the forward scattering nature of these processes constrains the sample type to fluids or optically transparent solids, which is a serious limitation to the applicability of these techniques as general analytical tools.

There is no doubt that nonlinear Raman spectroscopies can be very useful techniques in certain areas of study, but at the present time it seems fair to say that their application has been somewhat limited in terms of general chemical analysis. The techniques have been successfully applied to chemical problems,[35] but not as general spectroscopic tools for routine study of materials. Since the aim of this work was to design a fluorescence rejection system which can be applied to a wide range of sample types (most notably materials which are optically opaque), these techniques were rejected. It is important that the efficiency of the fluorescence rejection system should be determined solely by the fluorescence properties of the sample, and that the spectrometer should not in itself impose further unnecessary constraints upon the nature of the materials which may be studied.

The range and application of nonlinear Raman spectroscopies is now too large for a thorough discussion here, and the reader is referred to the literature for further details.[35]

2.4.2 Raman enhancement as a result of special sample conditions

The two techniques which are of major importance in this area are Surface Enhanced Raman Spectroscopy (SERS)[38] and Resonance Raman Spectroscopy (RRS)[37,39]. Both of these approaches are dependent upon a suitable choice of sample, but under favourable conditions can result in enhancements of many

orders of magnitude over spontaneous Raman signals.

The condition for RR scattering is that the exciting frequency should be in resonance with the separation of the ground level and an excited state. However even when this condition is met, large enhancements are not always observed, for reasons such as strong absorption, fluorescence and non-radiative processes dissipating the laser intensity and the scattered radiation.[39]

SERS, on the other hand, can prove useful in the study of adsorbed species at metal surfaces, and has (under suitable conditions) provided enhancements sufficient to record Raman spectra of strongly fluorescing species.[40] Unfortunately, the effect is limited to very few metals (*e.g.* silver and copper) and so is by no means generally applicable. The two effects (SERS and RR) are often employed in tandem.[40] Both methods suffer from the fact that not all vibrational modes give equally enhanced signals, and that they are by no means generally applicable to all sample types, which is an important consideration when designing a general purpose spectrometer.

2.5 Conclusions

The above discussion summarises the major techniques which have been employed in the reduction of fluorescence levels in Raman spectra. It is clear that no single ideal method seems to exist at present, and that each approach has significant drawbacks. If it is assumed that the technique employed must be generally applicable regardless of sample state, then the nonlinear spectroscopies can be immediately disregarded.

Modulation techniques have been used with some success in

reducing the fluorescence background, but it should be noted that the authors often report no improvement (or even a degradation!) in signal/noise levels. Since the object of the work is to improve R/N levels, the value of such techniques is not immediately apparent when the spectra are shot-noise limited.

Wavelength shifts, quenching, purification treatments and data smoothing will obviously remain applicable regardless of special spectrometer design, as do the RR and SERS effects, and so will not be considered further. Interferometer based systems, employing near IR excitation, are an exciting recent development which could well make a significant impact on the fluorescence problem. These spectrometers are currently being evaluated by other workers in this field, and it remains to be seen whether this becomes a widely adopted technique. The use of fluorescence saturation does not appear to have been explored in the literature, and will be discussed in detail in Chapter Three, along with an appraisal of polarisation discrimination techniques.

Time-resolved detection seems to present a generally applicable approach (limited only by the lifetime of the fluorescence and the timing resolution of the detection/counting electronics), and has certainly been one of the most widely studied. The major advantage of this method is that the undesired signal is eliminated prior to recording by the counting electronics, which means that noise levels are reduced. Techniques which involve background subtraction cannot achieve this and the shot-noise of the background is retained.

The time-resolved system should be applicable regardless of sample state, and has the additional advantage that the

necessary apparatus can be used for a variety of applications, *e.g.* fluorescence lifetime determination and time-resolved optical spectroscopy in general. Therefore it was decided to base the fluorescence rejection spectrometer upon time-resolved detection. The theory, application and performance analysis of this system will be given in subsequent chapters.

REFERENCES - CHAPTER TWO

1. R.R. Alfano and N. Ockman, J.Opt.Soc.Amer., 58, 90(1968).

2. R. Loveday, "Statistics", Cambridge University Press, (1971).

3. A.J. Diefenderfer, "Principles of electronic instrumentation", Holt-Saunders, Tokyo (1981).

4. A.R. Owens, J.Phys.E.Sci.Instrum., 15, 789 (1982).

5. J.T. Bulmer, D.E. Irish, F.W. Grassman, G. Herriot, M. Tseng and A.J. Weerheim, Appl.Spectrosc., 29(6), 506(1975).

6. M.C. Tobin, "Laser Raman Spectroscopy", Wiley-Interscience, New York, London, Sydney, Toronto (1971).

7. H.S. Haber, Amer.Lab. (November), 67 (1973).

8. T.A. Egerton, A.H. Hardin, Y. Kozinovski and N. Sheppard, Chem.Comm., 887 (1981).

9. C.L. Angell, J.Phys.Chem., 77 (2), 222 (1973).

10. T. A. Egerton and A.H. Hardin, Catal.Rev.Sci.Eng., 11 (1) 71 (1975).

11. N. Matoga and T. Kubota, "Molecular Interactions and Electronic Spectra", Marcel Dekker, New York (1970).

12. M. Kasha, J.Chem.Phys., 20 (1), 71 (1952).

13. Eyring, Walter and Kimball, "Quantum Chemistry", Wiley, New York (1944).

14. J.M. Friedmans and R.M. Hochstrasser, Chem.Phys.Lett., 33(2), 225 (1975).

15. G. Placzec in "Marx Handbuch der Radiologie", English Translation: "Rayleigh and Raman Scattering", U.S.Atomic Energy Commission, UCRL Trans 526(L) (1962).

16. "R.C.A. Photomultiplier Handbook", RCA Corporation (1980).

17. J.G. Timothy, Pub.ASP, 95, 810 (1983).

18. M. Fujiwara, H. Hamaguchi and M. Tasumi, Appl.Spectrosc. 40 (2), 137 (1986).

19. F.P. Schafer (Ed.), "Dye Lasers, Topics in Applied Physics volume 1", Springer-Verlag, Berlin, Heidelberg, New York(1973)

20. T. Hirschfeld and B. Chase, Appl.Spectrosc., 40(2), 133 (1986)

21. L. Woodward, "Introduction to the Theory of Molecular Vibrations and Vibrational Spectroscopy", Oxford University Press, (1972).

22. J. Funfschilling and D.F. Williams, Appl.Spectrosc., 30(4), 443 (1976).

23. F.L. Galeener, Chem.Phys.Lett., 48 (1), 7 (1977).

24. A. van Hoek and A.J.W.G. Visser, "Anal.Instrum.", 14 (2), 143 (1985).

25. A.Z. Genack, Anal.Chem., 56, 2457 (1984).

26. J.R. Lakowicz, "Principles of Fluorescence Spectroscopy", Plenum Press, New York (1983).

27. J.N. Demas and R. Keller, Anal.Chem., 57, 538 (1985).

28. C.A. Arguelo, G.F. Mendes and R.C.C. Leite, Appl.Opt., 13 (8), 1731 (1974).

29. D.P. Blair and P.H. Sydenham, J.Phys.E : Sci.Instrum., 8, 621 (1975).

30. M.L. Meade, J.Phys.E.:Sci.Instrum., 15, 395 (1982).

31. N.J. Dovichi, J.C. Martin, J.H. Jett, M. Trkula and R.A. Keller, Anal.Chem., 56 (3), 348 (1984).

32. R.P. Frueholz and J.A. Gelbuachs, Appl.Opt., 19 (16), 2735 (1980).

33. M. Trkula and R.A. Keller, Anal.Chem., 57, 1663 (1985).

34. C.V. Shank, Rev. Mod. Phys., 47 (3), 649 (1975).

35. "Chemical Applications of Nonlinear Raman Spectroscopy", A.B. Harvey (Ed.), Academic Press, New York (1981).

36. J. Baran, D. Elliott, A. Grofcsik, W.J. Jones, M. Kubinyi, A.J. Langley and V.U. Nayer, J.Chem.Soc., Faraday Trans.2, 79, 865 (1983).

37. J.A. Koningstein, "Introduction to the Theory of the Raman Effect", D. Reidel Publishing Company, Dordrecht-Holland,(1972).

38. R.P. Cooney, M.R. Mahoney and A.J. McQuillan in "Advances in Infrared and Raman Spectroscopy", 9, R.J.H. Clark and R.E. Hester (Eds.), Heyden, London, Philadelphia, Rheine,(1982)

39. D. Steele, "Theory of Vibrational Spectroscopy", W.B.Saunders Company, Philadelphia, London, Toronto (1971).

40. P. Hildebrandt and M. Stockburger, J.Phys.Chem., 88 (24), 5935 (1984).

CHAPTER THREE

UTILISATION OF POLARIZATION DISCRIMINATION AND FLUORESCENCE SATURATION FOR THE SUPPRESSION OF FLUORESCENCE BACKGROUNDS IN RAMAN SPECTRA

3.1 Introduction

In this chapter the possibility of discriminating between Raman and fluorescence signals by using two quite simple experimental techniques is assessed. The first method depends upon the fact that the polarisation of Raman scattered photons is in general quite different to that of fluorescence emission. The second approach utilises the differing response of the scattered and emitted intensities as a function of the incident laser power, namely the linear Raman and nonlinear fluorescence behaviour.

3.2 Discrimination of fluorescence and Raman photons *via* polarisation analysis

3.2.1 Introduction to polarization properties

3.2.1.1 Polarisation properties of Raman scattered radiation

When a laser beam is used as an excitation source, the incident radiation is linearly polarised and it is found that the polarisation of the resulting Raman scatter (for the case of single crystals and liquids) bears a definite relationship to that of the incident beam. (When powders are illuminated this is not the case, since the polarisation is "scrambled" by multiple reflections). Only a brief description of the polarisation properties of Raman scattering will be given here, and the reader is referred to the literature[1,2] for further details.

Consider a vibrating molecule which is fixed at the centre of the coordinate system illustrated in Figure 3.1. Suppose initially that the molecule can neither

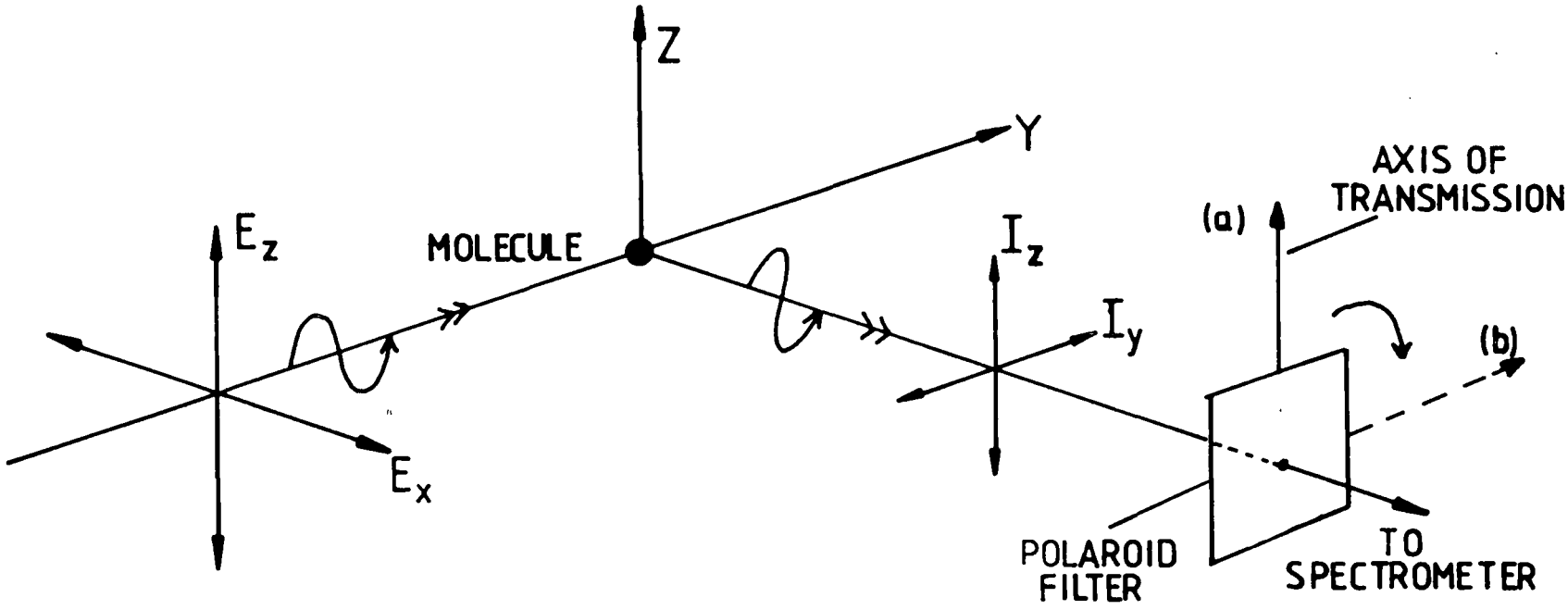

FIGURE 3.1. Analysis of polarisation properties. Radiation is incident along the y axis (electric field components E_x and E_z). Scattered/emitted radiation is observed along x axis. Intensity components I_z and I_y may be measured using a polaroid filter (positions (a) and (b) respectively).

rotate nor translate, and that unpolarised radiation is incident along the y axis. Observation of scattered radiation is made along the x axis. An elementary classical treatment of the vibrational Raman effect yields the result that the observed scattered intensity in the xy and xz planes is given by:

$$I_{xy} = K[E_x^2(\alpha'_{yx})^2 + E_z^2(\alpha'_{yz})^2] \tag{3.1}$$

$$I_{xz} = K[E_x^2(\alpha'_{zx})^2 + E_z^2(\alpha'_{zz})^2] \tag{3.2}$$

where α'_{ij} represents the derivative of the ij^{th} component of the polarizability tensor $\underset{\sim}{\alpha}$ with respect to the normal coordinate $\vec{Q}$, E_x and E_z are the maximum x and y components of the electric field vector $\vec{E}$, and K is a proportionality constant. In a fluid, the molecules will actually be oriented randomly with respect to the incident laser beam. Therefore equations (3.1) and (3.2) must be modified such that the $(\alpha'_{ij})^2$ are averaged over all orientations. The average values of the $(\alpha'_{ij})^2$ are denoted $\overline{(\alpha'_{ij})^2}$, and may be expressed in terms of the invariants of the tensor $\underset{\sim}{\alpha}'$.

$$\overline{(\alpha'_{ii})^2} = \frac{1}{45}\,[45(\bar{\alpha}'_o)^2 + 4(\gamma'_o)^2 \tag{3.3}$$

$$(\alpha'_{ij})^2 = \frac{1}{15}\,(\gamma'_o)^2 \tag{3.4}$$

The tensor invariants $\bar{\alpha}'_o$, γ'_o are defined by equations (3.5) and (3.6).

$$\bar{\alpha}'_o = \frac{1}{3}\,(\alpha'_{xx} + \alpha'_{yy} + \alpha'_{zz}) \tag{3.5}$$

$$(\gamma'_o)^2 = \frac{1}{2}\{(\alpha'_{xx}-\alpha'_{yy})^2 + (\alpha'_{yy}-\alpha'_{zz})^2 + (\alpha'_{zz}-\alpha'_{xx})^2 + 6[(\alpha'_{xy})^2 + (\alpha'_{yz})^2 + (\alpha'_{zx})^2]\} \tag{3.6}$$

When a laser is used to excite scattering, the beam may be polarised in the yx or yz plane. If the former is chosen, (E_z=0), the depolarisation ratio ρ (*i.e.* the observed ratio of the intensities in the xy and xz planes, $\rho = I_{xy}/I_{xz}$) is given by equation (3.7), while (3.8) holds if the beam is yz polarised, (E_x=0)

$$\rho_{11} = 1 \qquad (3.7)$$

$$\rho_{\underline{1r}} = 3(\gamma'_o)^2/[45(\bar{\alpha}'_o)^2 + 4(\gamma'_o)^2] \qquad (3.8)$$

The subscripts $_{11}$, $_{\underline{1r}}$ denote whether the electric vector of the laser is parallel (11) or perpendicular (1r) to the direction of observation (x). Clearly, if the beam is zy polarised, the resultant Raman scatter will be totally depolarised(*i.e.* $I_y=I_z$), for all active invariants $\bar{\alpha}'_o$, γ'_o. Since both invariants may be either equal to or greater than zero, the depolarisation ratio $\rho_{\underline{1r}}$ will range from 0 to 3/4.

It is well known[1,2] that the value of $\rho_{\underline{1r}}$ depends upon the symmetry of the vibration which gives rise to the scatter:- in particular, totally symmetric vibrations result in $\rho_{\underline{1r}}<3/4$. Symmetry considerations actually tell us nothing about how much less than 3/4 the ratio will be, except in one special case:- totally symmetric vibrations of isotropic molecules (*e.g.* CCl_4) give rise to totally polarised Raman lines, *i.e.* $\rho_{\underline{1r}}=0$. Fundamentals of any other symmetry always give the result $\rho_{\underline{1r}}=3/4$. The important conclusions are therefore that all Raman lines are polarised to a certain extent when excitation is made perpendicular to the plant of observation, and that symmetric vibrations often give

rise to strongly polarised scattering. This contrasts strongly with the situation found for fluorescence emission, which is discussed below.

3.2.1.2 Polarisation effects in fluorescence spectroscopy

In this section a simplified discussion of the factors affecting fluorescence polarisation is given. Measurement of polarisation anisotropies provides useful information concerning the rotational diffusion of fluorophores, and hence upon their size, shape and environment. A more detailed theoretical and practical account of this subject has been given by Lakowicz.[3]

Figure 3.2 illustrates the processes occurring when a rapidly tumbling molecule absorbs a photon and subsequently re-emits radiation some time later. Absorption of the photon can only occur if the transition moment (equation (3.9)) is non zero.

$$M = \langle \psi_f | \vec{\mu} | \psi_i \rangle \qquad (3.9)$$

where ψ_f and ψ_i represent the wavefunctions of the initial and final states respectively, and $\vec{\mu}$ is the electric dipole operator.[4] Group theory[5] indicates that the integral above can only be non-zero if the direct product of the irreducible representations to which ψ_i, ψ_f and $\vec{\mu}$ belong generates the totally symmetric species of the group. The symmetry of the direct product depends upon the orientation of the molecule with respect to the incident electric field vector, and in general not all molecular orientations can therefore allow absorption of photons when polarised light is used. In particular, if the polarisation of the laser beam is perpendicular to the dipole

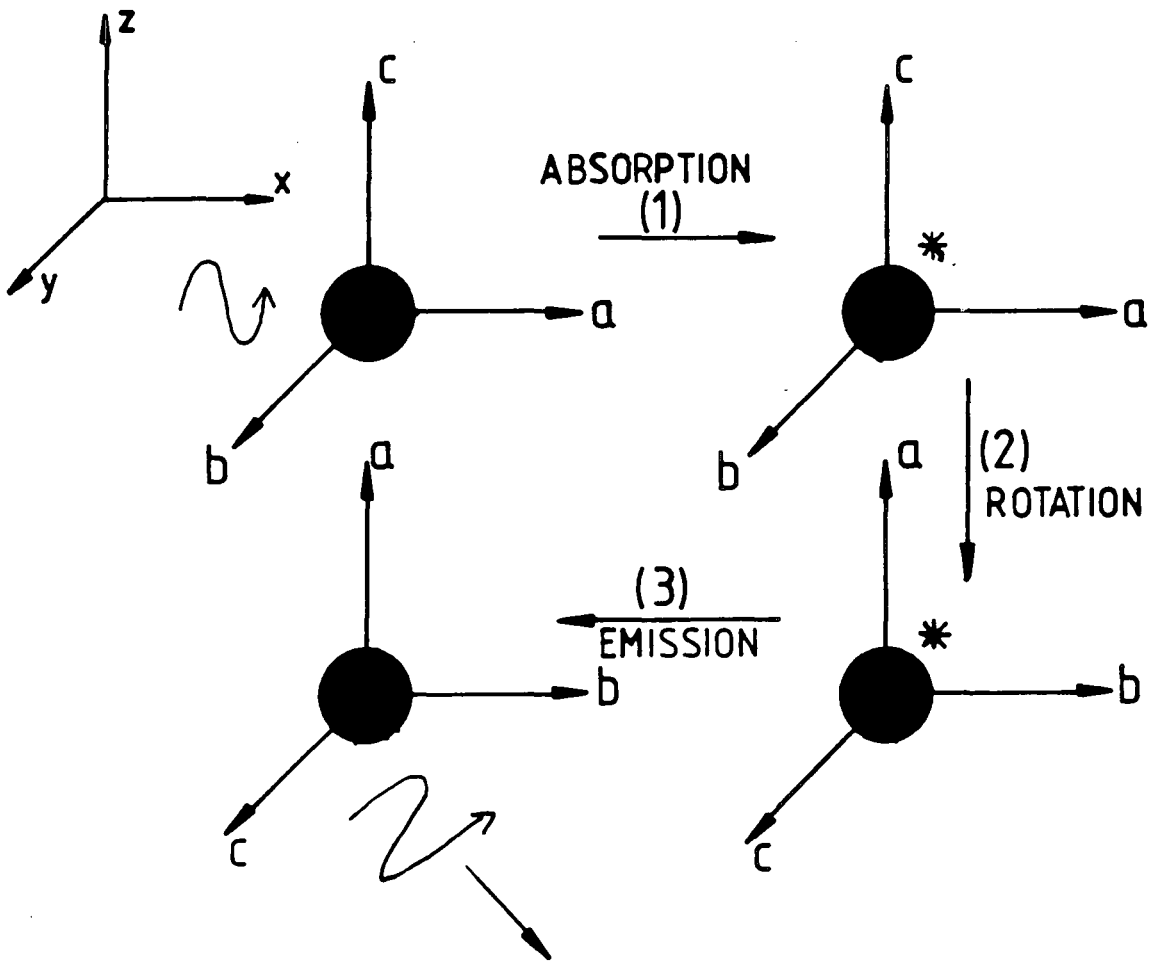

FIGURE 3.2 Fluoresence depolarisation.

(1) A z polarised photon is absorbed such that the dipole change responsible for the absorption is oriented along axis c of the molecule's internal coordinate system.

(2) The excited molecule undergoes rotation.

(3) The excited molecule re-emits a photon, again polarised parallel to the c axis. The polarisation of the emitted photon is therefore different to that of the incident one and the radiation is depolarised.

moment responsible for absorption, no absorption can occur.

A molecule which is suitably orientated may then absorb a photon, undergo rotation and collisional deactivation, and re-emit light. The polarisation of the fluorescence produced will be largely determined by the alignment of the molecule upon emission, although other factors such as light scattering may cause significant depolarisation in practice.

The degree to which the polarisation of the fluorescence differs from that of the incident radiation will depend upon the relative magnitudes of the fluorescence lifetime τ_f and the rate of rotation. If τ_f is short compared to rotational timescales, depolarisation will be negligible. Clearly, when a large number of molecules are illuminated, the polarisation of emitted photons will cover a range of values; and if rotation is fast compared to τ_f, the resultant macroscopic fluorescence will be totally depolarised and will be isotropically radiated.

3.2.2 Fluorescence rejection by polarisation analysis: practical aspects, methods and results

The different polarisation properties of Raman and fluorescence radiation may be employed to discriminate between the two effects. If Raman scatter in the x direction (Figure 3.1) is observed which has been excited by light polarised in the yz plane (*i.e.* perpendicular excitation), then we expect symmetric vibrations to give rise to radiation polarised to some extent in the xz plane, while the fluorescence emission will be depolarised (partially or totally). This means that a polarisation analyser positioned to pass radiation in the xz plane should pass the polarised Raman radiation but block the depolar-

ised fluorescence, thereby improving the R/F ratio (Chapter One).

3.2.2.1 Instrumentation and results

In order to test the polarisation-rejection method, the Raman spectrum of benzene contaminated by 1-cyanonaphthalene (as a fluorescing impurity) was recorded using a Cary 82 Raman spectrometer. The perpendicular exciation geometry was chosen (*i.e.* E_x=0 in Figure 3.1), and the 514.5 nm line of an argon-ion laser (Spectra Physics model 164) was used to excite the transition. The fluorescor was chosen because of its stability in the laser beam and its relatively long fluorescence lifetime (τ_f = *ca.* 19 ns in non-polar solvents[6]).

The 992 cm^{-1} band of the benzene was recorded under conditions of (a) no polarisation analyser and (b) with a polaroid filter positioned to pass radiation polarised in the z direction (Figure 3.1). The 992 cm^{-1} fundamental has a depolarisation ratio of 0 under these conditions (*i.e.* the scatter is z polarised), while the fluorescence would be expected to be totally depolarised (*i.e.* $I_{xz} = I_{xy}$). Figure 3.3 shows the relevant Raman spectra. Clearly, both the Raman and fluorescence intensities are decreased (the fluorescence more so) such that the R/F ratio is increased by *ca.* 1.9±0.1. The change in R/N (Chapter One) is more difficult to judge from the traces, but was estimated to be *ca.* 1.0±0.3 (in both cases taking the peak to peak background fluctuation as an estimate of the noise). Clearly there was no significant improvement in the R/N ratio under these conditions, even though the R/F ratio was doubled. These results are in good agreement with the calculations outlined below.

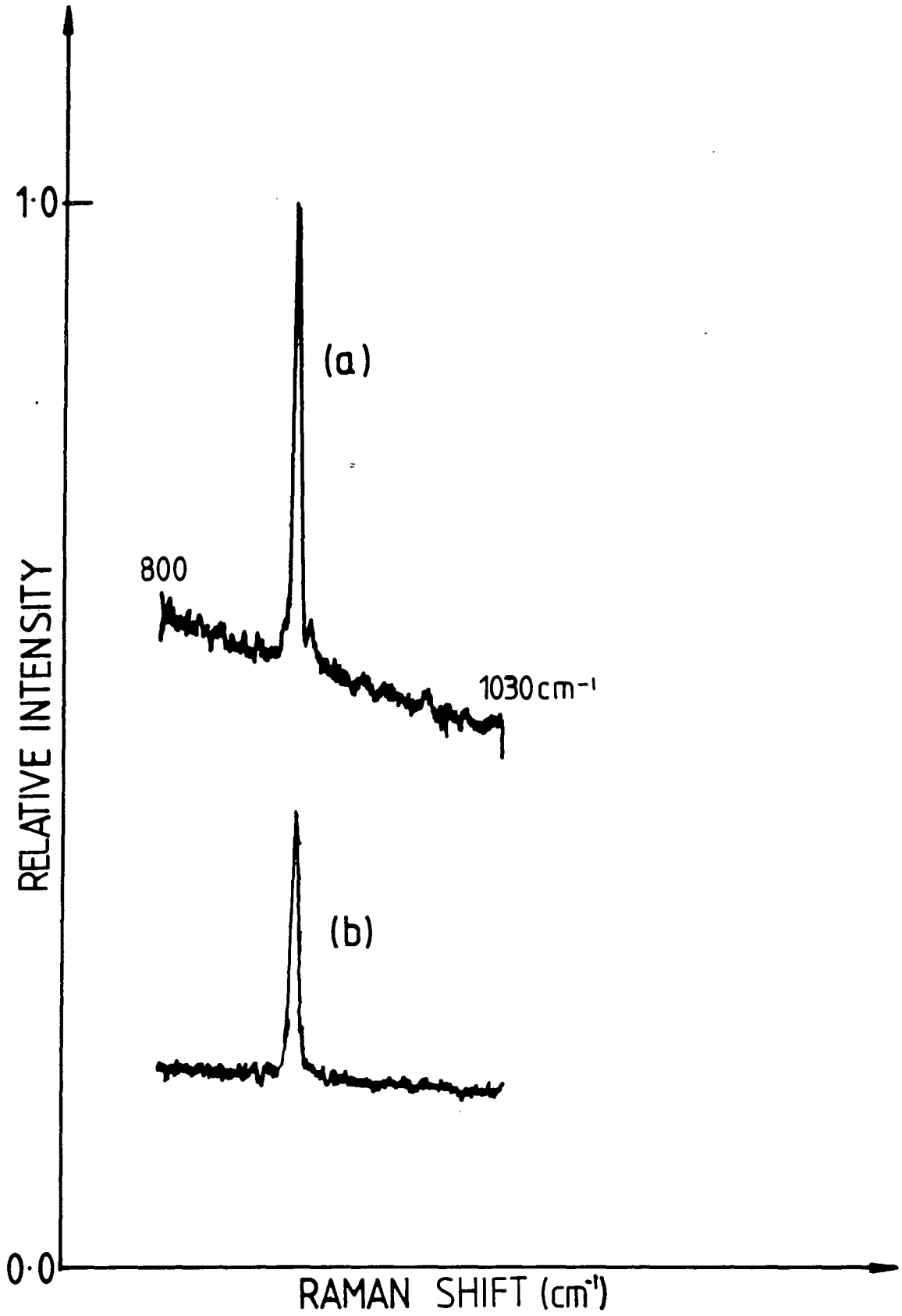

FIGURE 3.3 Polarisation analysis of Raman and fluorescence photons.

(a) No polaroid filter inserted.

(b) Polaroid filter inserted.

3.2.3 Calculation of expected improvements in R/F and R/N

Here it is assumed that the Raman scatter is totally polarised, and so passes through the filter with an attenuation governed solely by the optical density of the material. The fluorescence, on the other hand, is assumed to be totally depolarised, and so only the z component of the electric field vector is transmitted by the filter (Figure 3.4). This component will be given by $E\cos\theta$, (where $E=|\vec{E}|$), and the transmitted intensity is therefore $I=E^2\cos^2\theta$. When this component is averaged over all orientations of $\vec{E}$ (*i.e.* $0<\theta<\pi$), the average transmitted intensity is given by $E^2/2$, or 1/2 the total intensity of the depolarised light. This will be further attenuated by the optical density of the filter, denoted κ, such that the total transmitted intensity is $\kappa E^2/2$.

When no polaroid filter is present, the signal/background and signal/noise are given by R/F and $R/\sqrt{F}$. When the filter is in place these ratios become:

$$\text{signal/background} = \frac{\kappa R}{\kappa(F/2)} = 2R/F \qquad (3.10)$$

$$\text{signal/noise} = \frac{\kappa R}{[\kappa/F/2)]^{\frac{1}{2}}} = \left(\frac{2\kappa}{F}\right)^{\frac{1}{2}}.R \qquad (3.11)$$

$$E[R/F] = 2 \qquad (3.12)$$

$$E[R/N] = \sqrt{2\kappa}. \qquad (3.13)$$

It is clear that even with a perfect filter ($\kappa=1$) the maximum improvement in R/N (E[R/N]) would be a factor of 2. Furthermore, unless $\kappa>0.5$, degradation in R/N will occur.

The transmission factor κ was obtained by measuring the reduction in intensity of the 992 cm^{-1} band on inserting the polaroid filter so as to transmit the E_z component (Figure 3.1), and was found to be *ca.* 0.58. Using this value in

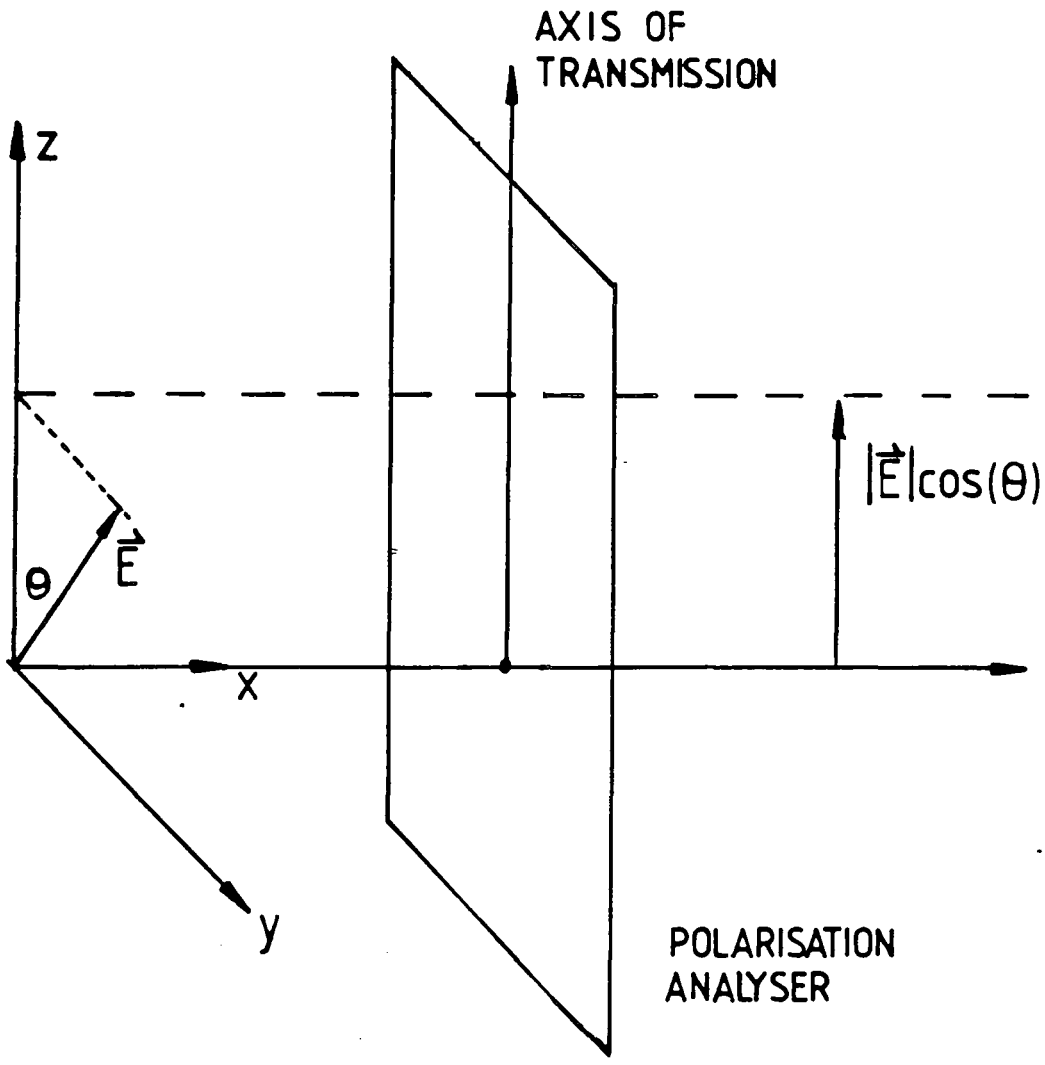

FIGURE 3.4 Transmission of a plane-polarised wave through a polarisation analyser. Transmitted field component is $|\vec{E}|\cos\theta$, with an average intensity of $|\vec{E}|^2\cos^2\theta$. For depolarised light, θ is a random angle, and the transmitted intensity is proportional to $\overline{\cos^2\theta}$.

equations (3.12) and (3.13), the calculated improvements are E[R/F]=2 and E[R/N]=1.1, which are in good agreement with the observed results.

The calculations above indicate that polarisation analysis does discriminate between Raman and fluorescence signals, but that even under ideal conditions the improvement in R/N levels will be small (*i.e.* $\sqrt{2}$). Also, since many Raman lines are only weakly polarised, the technique would result in a degradation in signal/noise levels in these cases.

3.2.4 Polarisation modulation techniques

Although it was concluded that the simple static polarisation discrimination was ineffective in improving the R/F and R/N ratios, considerable improvements on these results can be made if the radiation falling on the detector is modulated in intensity,by passing it through a polarisation analyser which is being rotated at a constant rate (Figure 3.5). Under these circumstances, the polarised Raman lines are modulated in intensity in phase with the rotation of the analyser, while the intensity of the depolarised fluorescence emission remains constant. Therefore, a phase-sensitive detector, tuned to accept signals oscillating at the modulation frequency, should reject the constant fluorescence background.

Arguelo *et al*[7] first demonstrated the feasibility of this method by completely rejecting the fluorescence background from a Raman spectrum of a sample of ethanol which had been doped with rhodamine 6G. This method also removes background fluctuations caused by laser power drift and sample decomposition, which can often degrade spectral quality (Chapter Two). However, as Demas and Keller[8] pointed out, phase sensitive detection has no effect on statistical (shot) noise.

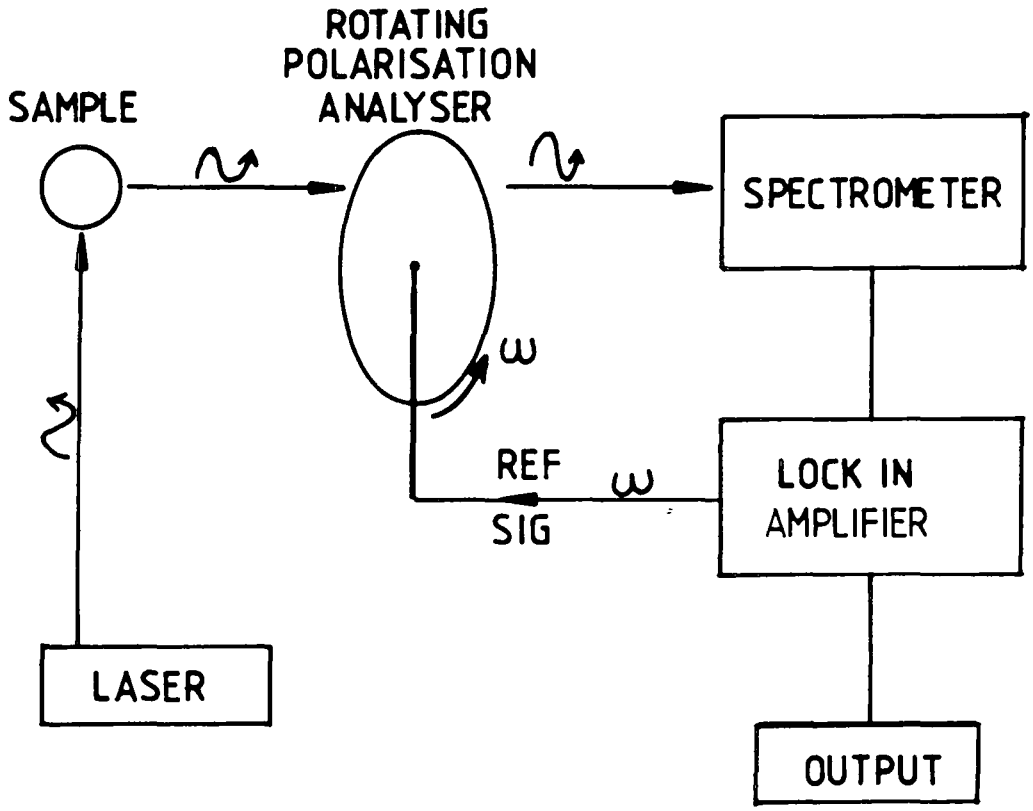

FIGURE 3.5 Polarisation Modulation Apparatus

The lock-in amplifier provides a reference signal to control the rotation of the polaroid filter. Polarized Raman lines are modulated in phase with the rotation of the filter, while the fluorescence signal is unchanged and so is rejected by the LIA.

Statistical noise is only rejected to the extent that it falls outside the bandpass of the output filter of the lock-in amplifier.[9] Reducing the bandwidth will reject more statistical noise, but at the expense of an increased time constant on the output circuit, *i.e.* the scan time must be increased. This is akin to increasing the counting time in a photon counting experiment. Lock-in amplifiers and phase-sensitive detection are discussed in more detail in Chapter Two.

Unfortunately, Arguelo *et al*[7] did not present quantitative results for the enhancements in R/F and R/N, and it is difficult to estimate these values from their spectra. Furthermore, no details of the time-constant of the amplifier output circuit, or of the nature of the noise in the spectra (*i.e.* high frequency shot noise or low frequency fluctuations), were reported, so it is difficult to assess the true performance of their system. No theoretical values for the expected improvements relative to conventional detection were given. If the background noise levels were dominated by statistical considerations, then it seems likely that merely photon-counting, or simple dc-filtering (Chapter Two) of the PMT output, would produce equally good improvements in R/N. Once again, we restate the point that merely reducing the background level is insufficient unless the noise levels are reduced also.

There are two further drawbacks to this method. Firstly, depolarised Raman lines will also be rejected (to a certain extent) along with the fluorescence, and so not all Raman features will be generally observable. This is evident in the spectra of Arguelo *et al*, where the ethanol bands at 1274 cm^{-1} and 1454 cm^{-1} were totally lost. (Also, the relative

intensities of the lines will be distorted in comparison to a normal spectrum, but this is not a severe problem in many applications).

Secondly, the technique is constrained to the study of fluid samples, where the polarisation properties of the Raman scatter is well defined. For solid samples such as powders, multiple scattering from the sample surface occurs, and so the Raman scatter is usually depolarised to a certain extent irrespective of the symmetry of the active vibration. Clearly, this results in the fluorescence and Raman scatter being less distinguishable by polarisation analysis. It does seem surprising, however, that the technique has not been applied more widely in the study of fluorescing liquids.

3.2.5 Conclusions

It may appear from the above discussion that the use of polarisation modulation might be a sensible route for the construction of a fluorescence rejection system. This would probably be the case if the background noise levels were essentially non-statistical in nature, such as background fluctuations due to sample movement or decomposition. Statistical noise (*i.e.* shot noise) can only be removed by selecting a suitably narrow output bandpass on the lock-in amplifier, which increases the scan time of the spectrum.

A further disadvantage of this technique is that in order to obtain optimum results it is constrained to liquid samples or optically transparent single crystals. However, the aim of our work was to construct a spectrometer which could be used primarily in the study of heterogeneous catalysis, particularly in terms of looking at adsorbed species on high

surface area powders. Finally, the very nature of the technique means that depolarised Raman lines are suppressed in the spectra, and so valuable information can be lost.

For the above reasons, it was decided to reject polarisation discrimination as the primary tool for fluorescence rejection.

3.3 Discrimination on the basis of the saturation of fluorescence response

3.3.1 Introduction

It was pointed out in Chapter Two that upon increasing the incident laser intensity on a sample, the intensity of spontaneous Raman scattering increases linearly, but the fluorescence response is nonlinear at high intensity, and reaches a limiting value. This differing behaviour has been utilised by fluorescence spectroscopists in rejecting the Raman background, (from solvent scatter), which interferes with the observation of fluorescence from dilute solutions of fluorophores.[10-12]

It is of interest to consider whether it is possible to obtain Raman spectra using laser intensities high enough to saturate the fluorescence response, but without causing sample degradation or the onset of nonlinear scattering processes (Chapter Two). Under these conditions, any increase in laser power will increase the Raman signal but should leave the fluorescence intensity unchanged. This would mean that merely focussing the laser beam to the smallest possible spot could result in significant improvement in R/N ratios.

In the following sections we consider the feasibility of using pulsed lasers to saturate the fluorescence res-

ponse, as opposed to the usual approach[10-12] of using cw laser excitation. This allows the application of higher peak powers, but for shorter time periods, compared to cw illumination. Calculations are presented (based upon an idealised model of the laser output) which indicate that fluorescence saturation should be achievable with the present system. The calculated results are compared with those expected with cw excitation at the same average power. Unfortunately, the experimental results which were obtained to test these calculations were inconclusive, owing to depletion of fluorophore concentration during irradiation causing a decrease in fluorescence intensity. Further investigations will require the construction of a flowing-sample system, to continually replenish the fluorophores during illumination.

3.3.2 Origin of fluorescence saturation:— response of a 2 level system

In order to understand the process of fluorescence saturation in multilevel systems, it is helpful to first consider the response of a 2 level system. In this way the physical vasis of saturation behaviour is made apparent without introducing undue mathematical complication. Extension of the model to a more realistic 3 level system is straightforward. In all of the analyses which follow, two simplifying approximations are made.

(a) The attenuation of the laser intensity on traversing the sample is negligible (optically thin layer approximation). The fluorescence intensity is therefore a function of time, but not of position within the sample.

(b) The laser pulse shape is approximated to a rectangle (*i.e.* constant intensity throughout the pulse).

Zunger and Bar-Eli[13] reported a treatment which took into account the precise laser pulse shape and allowed for the optical density of the sample. Unfortunately, when this is done the resulting differential equations are not analytically soluble, and a numerical solution must be obtained for each case of interest. Since the authors[13] considered pulse durations of 20 ns, and a specific four-level system, their results are not transferrable to our present studies. Furthermore, since the purpose of the present study is merely to evaluate the feasibility of the technique, our approximate solutions are sufficient for this purpose, at least in these initial stages, and so no attempt was made to obtain more accurate solutions.

3.3.2.1 Steady state response

First consider an idealised 2 level system, where two discrete singlet electronic states are subjected to monochromatic, continuous excitation of intensity I_p (photons s^{-1} cm^{-2}) and frequency ν_p (Figure 3.6). The cross sections[14] for absorption and stimulated emission are denoted σ_a and σ_e respectively, and the fluorescence lifetime $\tau_f=1/k_1$). The rate constant for spontaneous deactivation, k_1, is actually the sum of the rate constants for nonradiative (k_N) and radiative (k_R) decays respectively (Chapter One). The rate equation for the population of the upper state N_2 is given by equation (3.14):

$$\frac{dN_2}{dt} = \dot{N}_2 = \sigma_a I_p N_1 - (\sigma_e I_p + k_1) N_2 \qquad (3.14)$$

Assuming that the total number of molecules under irradiation (N_o) is constant ($N_o=N_1+N_2$), and using the fact that the cross

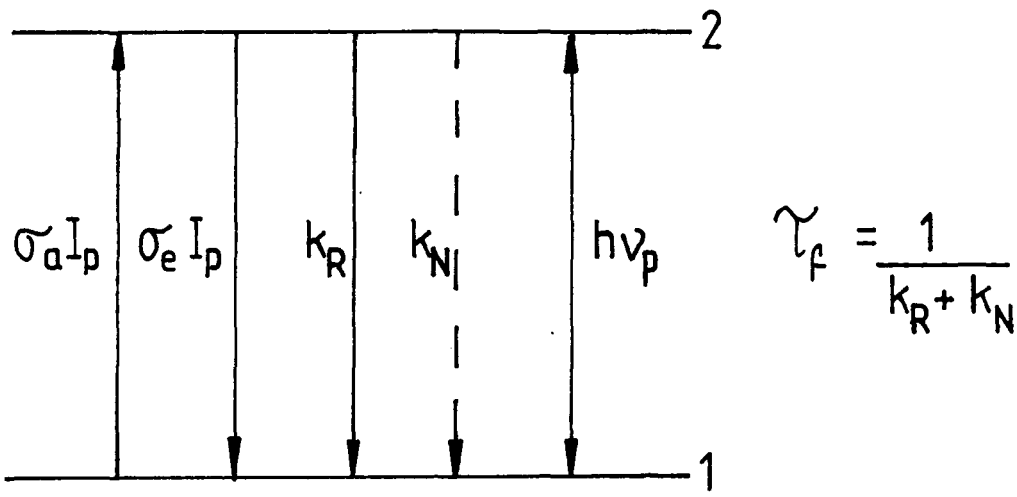

FIGURE 3.6 Population dynamics of two-level system. The level separation is $h\nu_p$, where h is Planck's constant and ν_p is the frequency of the resonant laser radiation of intensity I_p. σ_a and σ_e are the cross sections for absorption and stimulated emission, and τ_f is the fluorescence lifetime. k_R and k_N are the rate constants for radiative and nonradiative transitions.

sections for absorption and stimulated emission are equal for transitions between discrete levels,[14] equation (3.14) may be rewritten as:

$$\dot{N}_2 = \sigma_a I_p N_o - (2\sigma_a I_p + k_1) N_2 \qquad (3.15)$$

Under cw excitation, the system will eventually reach equilibrium, and so $\dot{N}_2 = 0$. In this case, equation (3.15) can be solved to yield the equilibrium population of the second level:

$$N_2 = \sigma_a N_o I_p / (2\sigma_a I_p + k_1) \qquad (3.16)$$

Equation (3.16) describes the saturation behaviour of the system. When $I_p << k_1/2\sigma_a$, N_2 responds linearly with increasing intensity. The limiting population for N_2, at infinite pump power, is clearly $N_o/2$. The resulting spontaneous fluorescence intensity is given by $k_R N_2$, and so reaches a limiting value of $k_R N_o/2$ at infinite pump power.

3.3.2.2 Transient excitation of 2 level system

We now consider the response of the two level system to a laser pulse as opposed to continuous irradiation. An idealised rectangular laser pulse of width τ, and peak intensity I_p is assumed. When the width τ is comparable to, or less than, the lifetime of the fluorophore, we can no longer invoke equilibrium considerations, but instead must solve (3.15) explicitly as a function of time.

Equation (3.15) is a linear first order differential equation in N_2, and is solved by the "integrating factor" technique.[15] The solution is:

$$N_2(t) = \frac{\sigma_a I_p N_o}{(2\sigma_a I_p + k_1)} \left[1 - e^{-(2\sigma_a I_p + k_1)t}\right] \qquad (3.17)$$

The intensity of fluorescence from level 2 at time t is $k_R N_2(t)$. The upper time limit for which equation (3.17) holds is $t=\tau$, the laser pulse width. If τ is large, equation (3.17) reduces to the steady state approximation (equation (3.16)).

The linearity/nonlinearity of equation (3.17) is not immediately obvious. However, if the exponential factor is expanded as a power series in $(2\sigma_a I_p+K_1)t$, equation (3.18), we may terminate the series after 2 terms provided that the factor $(2\sigma_a I_p+K_1)t$ is small, which leads to equation (3.19).

$$N_2(t) = \frac{\sigma_a I_p N_o}{(2\sigma_a I_p+k_1)} [1-1+(2\sigma_a I_p+k_1)t +....] \qquad (3.18)$$

$$N_2(t) = \sigma_a I_p N_o t \qquad (3.19) .$$

Equation (3.19) implies that $N_2(t)$ increases linearly with laser intensity provided that $(2\sigma_a I_p+k_1)t$ is small.

It is of interest to compare the fluorescence response of a sample subjected to transient and cw excitation with the same average power. Figure 3.7 illustrates the form of equations (3.17) and (3.18), under the conditions $\sigma_a=10^{-16}cm^2$, $k_1=10^8 s^{-1}$ and τ=40 ps. The response is plotted as a function of the average photon intensity. (Assuming that the laser is operated at 4MHz, with a pulsewidth of *ca.* 40 ps, the peak pulse power is *ca.* 6250 times the average power). Clearly, pulsed excitation should result in fluorescence at *ca.* 2 orders of magnitude lower average power than a cw source under these conditions

Figure 3.7 indicates that a linear response is expected up to *ca.* 10^{22} photons s^{-1} cm^{-2}. For our laser,

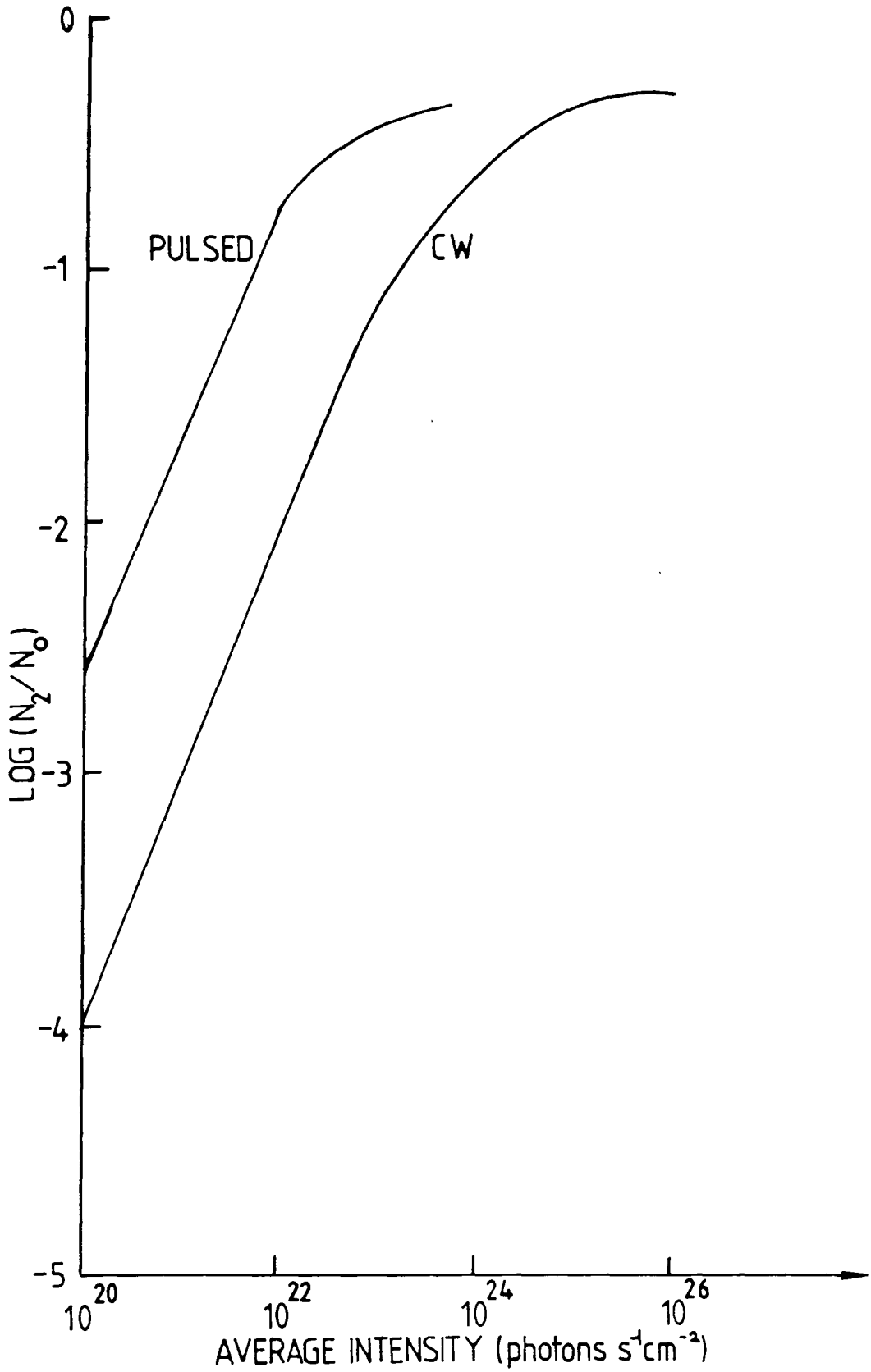

FIGURE 3.7 Saturation of fluorescence response using pulsed/cw excitation of the same average power. A pulse rate of 4MHz (40 ps pulse duration) is assumed. Note the onset of saturation at *ca.* 2 orders of magnitude lower average power using pulsed excitation.

operating at 595 nm and focussed to a 30μ diameter spot, this is equivalent to an output intensity of *ca.* 23mW (average) which is easily within reach of the system capabilities.

3.3.3 A more realistic model: the 3 level system

The model discussed above is not realistic in terms of the usual samples encountered in Raman spectroscopy, *i.e.* multilevel systems with broadened levels, and can only account for the phenomenon of resonance fluorescence (*i.e.* fluorescence at the exciting wavelength). The complexity of the model must be extended in order to account for multilevel systems which have broad rather than discrete bands.

3.3.3.1 Transient excitation of a discrete three level system

The population dynamics of a system of three discrete electronic levels subject to transient excitation have been discussed by Di Bartalo,[16] and the following analysis is based upon this work. Figure 3.8 illustrates the processes occurring in such a system during optical excitation. We assume that levels 1 and 2 are the ground and excited singlet states and level 3 is a triplet state. The constants k_1 and k_3 account for spontaneous transitions from levels 2 and 3 respectively. The intersystem crossing governed by k_2 is assumed to be a radiationless process. The rate equations which govern the populations N_2 and N_3 are (3.20) and (3.21) respectively

$$\dot{N}_2 = wN_o - (k_1+k_2+2w)N_2 - wN_3 \qquad (3.20)$$

$$\dot{N}_3 = k_2N_2 - k_3N_3 \qquad (3.21)$$

where we have used the conservation of number of particles condition $N_o=N_1+N_2+N_3$, and have written $\sigma_a I_p$ as "w". These

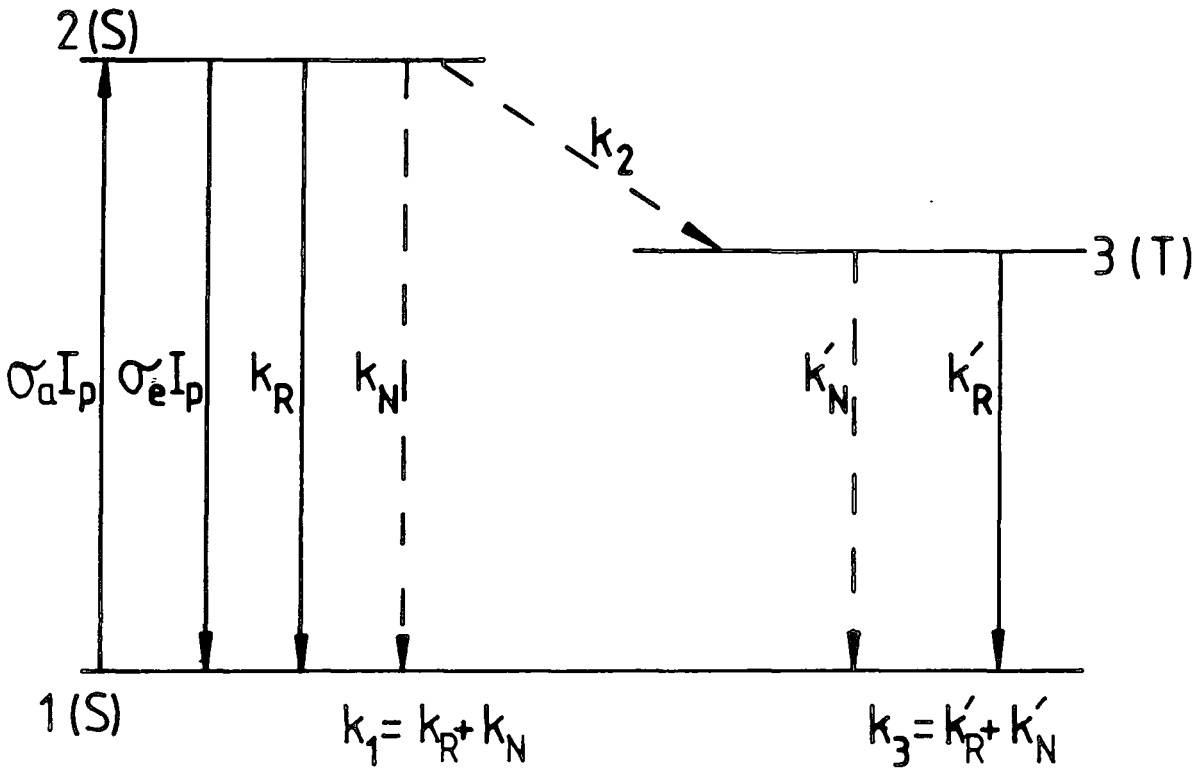

FIGURE 3.8 Population dynamics of a 3 level system. Levels 1 and 2 are singlet states, level 3 is a triplet state. K_2 is the rate constant for radiationless intersystem crossing, k_1 and k_3 govern spontaneous deactivation (both radiative and nonradiative) from the singlet and triplet states respectively. Fluorescence lifetime $\tau_f = 1/k_1$ phosphorescence lifetime $\tau_p = 1/k_3$

rate equations can be solved through the use of Laplace transforms.[17] The general solutions are:

$$N_2(t) = \frac{wN_o k_3}{2a}\{C_1 e^{(b+a)t} - C_2 e^{(b-a)t} + \frac{2a}{(b^2-a^2)}\} \quad (3.22)$$

$$N_3(t) = \frac{wN_o k_2}{2a}\{\frac{e^{(b+a)t}}{(b+a)} - \frac{e^{(b-a)t}}{(b-a)} + \frac{2a}{(b^2-a^2)}\} \quad (3.23)$$

$$a^2 = [\frac{(k_3+A)^2}{4} - k_1 w - k_3 w] \quad (3.24)$$

$$b = -(k_3 + A)/2 \quad (3.25)$$

$$A = k_1 + k_2 + 2w \quad (3.26)$$

$$C1 = \frac{(a+b+k_3)}{k_3(b+a)} \quad (3.27)$$

$$C2 = \frac{(b-a+k_3)}{k_3(b-a)} \quad (3.28)$$

Equations (3.22) - (3.28) describe the variation of N_2 and N_3 over the duration of the laser pulse. The variation of the fluorescence intensity from the second level is given by $k_R N_2(t)$.

3.3.3.2 Total fluorescence intensity observed for the three level system

While Di Bartalo[16] considered only the time response of the fluorescence emission, in our work we are interested in the total intensity emitted during the decay of the second level. The total fluorescence intensity from the second level is given by $\int_0^\infty k_R N_2(t)dt$. The population dynamics of N_2 and N_3 will obviously alter when the laser pulse has finished, and so the rate equations to be solved over the period $\tau<t<\infty$ will differ from equations (3.20) and (3.21).

Figure 3.9 illustrates the situation once the laser pulse has ended. Clearly, the pump intensity is zero, and so the second level decays *via* transitions to levels

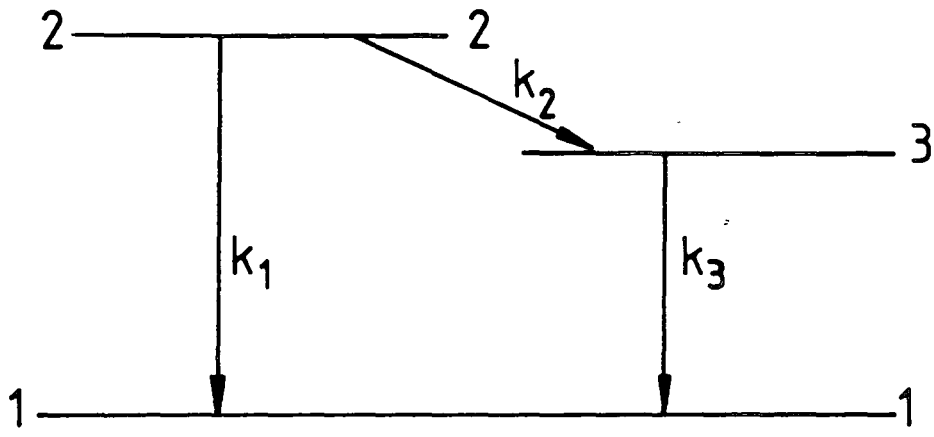

FIGURE 3.9 Transitions occurring when laser pulse is terminated. Absorption and stimulated emission no longer occur, and system decays to ground state (1).

1 and 3, while the third level is "pumped" by transitions from level 2 and itself decays into level 3. The dynamics of N_2 are governed by equation (3.29)

$$N_2(t) = N_2(\tau)e^{[-(k_1+k_2)(t-\tau)]} \tag{3.29}$$

where $N_2(\tau)$ is the population of N_2 at the end of the excitation pulse. The total fluorescence intensity from level 2 during the period $\tau<t<\infty$ is then given by $I_1(F)$ (equation 3.30).

$$I_1(F) = \int_{\tau}^{\infty} k_R N_2(t)\,dt = \frac{k_R N_2(\tau)}{(k_1+k_2)} \tag{3.30}$$

The intensity emitted over the period $0<t<\tau$ is given by equation (3.31)

$$I_2(F) = \int_{0}^{\tau} k_R N_2(t)\,dt \tag{3.31}$$

When the integral (3.31) is evaluated, we find that

$$I_2(F) = \frac{wN_o k_3}{2a}\left\{\frac{C_1}{(b+a)}\left[e^{(b+a)\tau}-1\right] + \frac{C_2}{(b-a)}\left[1-e^{(b-a)\tau}\right] + \frac{2a\tau}{(b^2-a^2)}\right\} \tag{3.32}$$

The <u>total</u> fluorescence intensity from the second level due to each laser pulse is given by the <u>sum</u> of equations (3.30) and (3.32), *i.e.* $I_1(F) + I_2(F)$. Since we are only concerned with emission from level 2, the dynamics of the third level are not considered further.

3.3.4 <u>Effect of level broadening</u>

Although it may appear that the results obtained so far are quite detailed, and should give a reasonable representation of the response of a 3 level system, there is one more complication to consider. The equations above are adequate to

describe systems where the levels are discrete, *i.e.* gases or metal ions in crystals. Indeed, Yaney made use of this type of approach (albeit with some approximations about the relative rates of energy transfer) in order to describe the behaviour of Mn-doped ZnSe.[18]

The discrete level approximation breaks down for molecules in solution, since the electronic levels are perturbed by vibrational, rotational and collisional interactions. The net effect is that for samples such as dye molecules in solution, the electronic levels are broadened into a set of closely spaced rovibrational levels, which merge into continuum extending over several tens of nanometers.[3,19] This broadening has a large effect upon the properties of the levels.

The optical properties of broadened electronic energy levels have been reviewed by Shank,[20] with particular emphasis on the operating characteristics of cw dye lasers. A more detailed discussion can be found in the report of Stepanov.[21] Here we are only concerned with the effect of level broadening upon the cross sections σ_a and σ_e.

Following the treatment of Stepanov,[21] it is assumed that the individual electronic levels are broadened into a continuum, and that the distribution of molecules within each level is given by the function $\eta(\varepsilon_i)$, where ε_i is the energy of a particular state within the i^{th} level (Figure 3.10). The crucial assumption is made that thermalisation within the electronic levels is rapid (of the order of 1 ps) compared to the rate of transitions between the levels ($\gtrsim$100 ps). This is discussed further in Section 3.3.5. Under these conditions. the molecules within each broad level are distributed according to a Boltzmann distribution (Figure 3.10). This is expressed

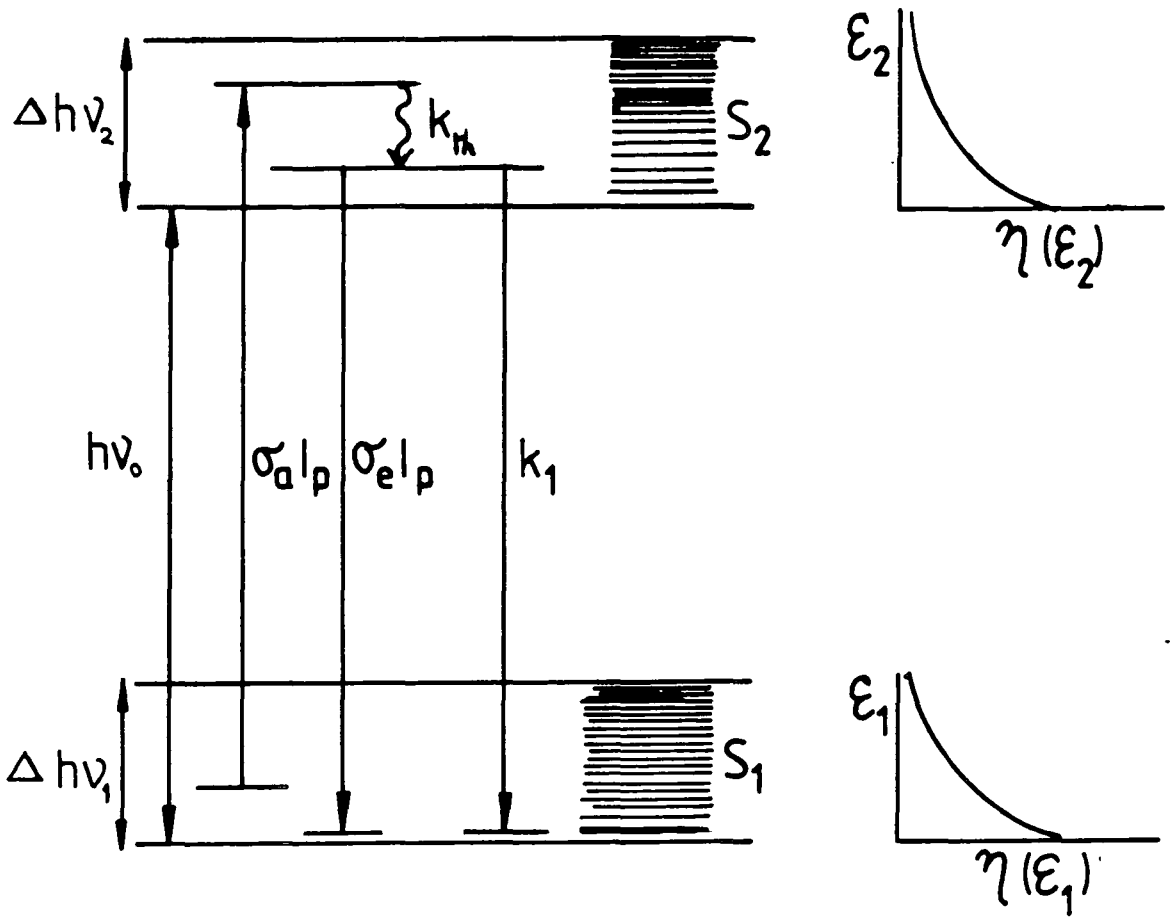

FIGURE 3.10 Population dynamics in a broad-level system. Each broad level is composed of very many closely spaced rovibrational states, the separation of the ground states of each level being $h\nu_o$. ε_i is the energy of a state within level i, relative to the ground state of the i^{th} level, and $\eta(\varepsilon_i)$ specifies the distribution of particles within each level as a function of energy. k_{th} is the rate constant for thermalisation within levels.

quantitatively in equation (3.33), where g_i is the state degeneracy and C_i is a normalising factor.

$$\eta(\varepsilon_i) = C_i g_i e^{-\varepsilon_i/kT} \qquad (3.33)$$

Here k is the Boltzmann constant and T is the temperature of the system. Pump radiation of frequency I_p can stimulate transitions between any states which are separated by energy ν_p, where h is Planck's constant. Since the absorption/emission cross section for an individual rovibrational state depends upon both its position within the broadened energy level, and upon the radiation frequency ν_p, the <u>total</u> cross section is obtained by summing the individual cross sections of all of the states within the level (equations 3.34-3.35).

$$\sigma_a(\nu_p) = \int \sigma_a(\varepsilon_1,\nu_p)\eta(\varepsilon_1)d\varepsilon_1 \qquad (3.34)$$

$$\sigma_e(\nu_p) = \int \sigma_e(\varepsilon_2,\nu_p)\eta(\varepsilon_2)d\varepsilon_2 \qquad (3.35)$$

Stepanov[20] showed that under these conditions, the ratio of the total cross sections is given by (3.36)

$$\sigma_e(\nu_p) = \sigma_a(\nu_p)e^{[h(\nu_o-\nu_p)/kT]} \qquad (3.36)$$

where ν_o is the frequency of the transition between the ground states of each electronic level (Figure 3.10). <u>This is an important result</u>, since it shows that $\sigma_e(\nu_p) > \sigma_a(\nu_p)$ when $\nu_p < \nu_o$. (For a discrete level system, $\nu_o = \nu_p$ and so $\sigma_e = \sigma_a$ under all circumstances). This result provides the mechanism by which a 2 level dye laser can function. In <u>optically pumped</u> discrete level systems, at least <u>3</u> levels are required to achieve lasing, since the equality of the cross sections σ_a and σ_e prevents the formation of a population inversion in a two level system, if

$\sigma_e(\nu_p) > \sigma_a(\nu_p)$, no population inversion is required to achieve lasing action in the broadened level sample.

To allow for the effect of level broadening in our treatment, we simply substitute equation (3.36) for $\tilde{\sigma}_e$ in our rate equations and solutions. This results in the factor A (equation 3.26) being changed according to equation (3.37).

$$A = (k_1 + k_2 + \sigma_a(\nu_p)\{1+e^{[h(\nu_o-\nu_p)/kT]}\}) \qquad (3.37)$$

3.3.5 Practical calculation of the expected fluorescence response

3.3.5.1 Measurement of the parameters in the rate equations

In order to calculate the fluorescence response to changes in pump intensity, we need to know the values of I_p, $\sigma_a(\nu_p)$, ν_o, the laser pulsewidth τ and the relevant rate constants. The absorption cross section at the pump frequency may be calculated from the absorption spectrum of the sample using the relation $\sigma_a(\nu_p) = 3.82 \times 10^{-21}\, \varepsilon(\nu_p)\,cm^2$, where $\varepsilon(\nu_p)$ is the decadic molar extinction coefficient[3] at the pump frequency ν_p. Then $\sigma_e(\nu_p)$ is obtained from equation (3.36) above. The frequency ν_o is obtained by a comparison of the absorption and emission spectra of the molecule, and is given (in the ideal case) by the frequency about which the two spectra are symmetric.[19] This is illustrated in Figure 3.11.

The fluorescence lifetime of the sample may be measured with the time-correlated photon counting apparatus described in Chapter Six. The constants for intersystem crossing (k_2) and triplet deactivation (k_3) may be estimated from typical values given in the literature,[22] since

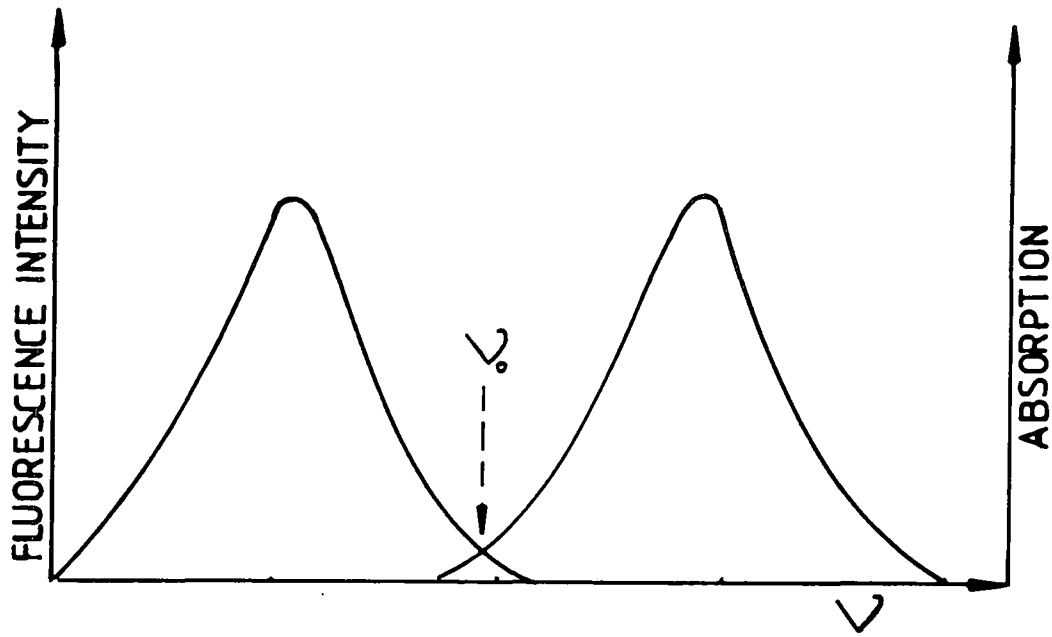

FIGURE 3.11.

Measurement of ν_0. A correct comparison of absorption and emission spectra requires that each be presented in the correct units. This correction is discussed in detail in reference 17.

generally speaking the values of these constants are much less than those for the spin allowed transitions, and so are not crucial in determining the fluorescence response.

3.3.5.2 Photon rate I_p

The calculation of I_p, the photon rate per cm^2 over the duration of the laser pulse, presents more of a problem. Since we have assumed that the laser output consists of a series of equally spaced rectangular pulses, the photon count rate per pulse may be estimated from a knowledge of the average power of the beam, its wavelength, the pulse repetition rate and the width of the individual pulses. However in order to obtain the count rate per unit area, we require the diameter of the focussed laser spot at the sample. Measurement of this quantity is not trivial, but an approximation can be obtained from a standard formula[23] (equation 3.38), which yields the diameter (D) of the diffraction-limited spot formed on focussing a laser beam of diameter d and wavelength λ, with a lens of focal length f.

$$D = 2.44\ f\lambda/d \qquad (3.38)$$

Under typical experimental conditions (*i.e.* d=2mm, f=4cm, λ=595nm), this results in a spot of *ca.* 30μ diameter, although much smaller spots may be achieved by expanding the beam diameter, and using a lens of smaller focal length. Focussed diameters of the order of a few microns can be obtained in practice, but this was not necessary for the purposes of our work.

It should be remembered that this formula (3.38) only holds in the ideal case of a perfect lens, and any defects will result in larger, distorted spots.[23] However, this estimate of the spot size is sufficient for the purposes

of the feasibility study.

The pulsewidth τ is also required in the calculation of the response. Ideally this would be measured by second harmonic autocorrelation (Chapter Five), but suitable equipment was not available during this work. Instead, we obtained an estimate of the pulsewidth from certain system diagnostics which are described in Chapter Five. These diagnostics lead us to believe that the pulsewidth is certainly less than 40 ps during the course of these experiments. The uncertainty in the pulsewidth is not actually too important for this work, since although this affects the time-evolution of the fluorescence response, the total integrated fluorescence intensity depends upon the product of pulsewidth and intensity (equations (3.22) and 3.23)), and these two quantities are inversely related for a given pulse power. Furthermore, since the treatment above is based upon an idealised, rectangular laser pulse, an exact measurement of the true (often Gaussian) pulse is not essential.

3.3.5.3 Response as a function of spot size

It is of interest to calculate the fluorescence response under various conditions. The maximum absorption cross section for a typical dye is of the order of 10^{-16} cm^2. We assume that excitation occurs at the wavelength of maximum absorption. Reasonable estimates of the relevant rate constants would be $k_1=10^8 s^{-1}$, $k_2=10^5 s^{-1}$ and $k_3=10^4 s^{-1}$, although it should be noted that the rate constants for spin forbidden processes (k_2 and k_3) will be affected by the presence of quenching agents (Chapter Two). Figure 3.12 describes the variation of fluorescence intensity with the average laser power,

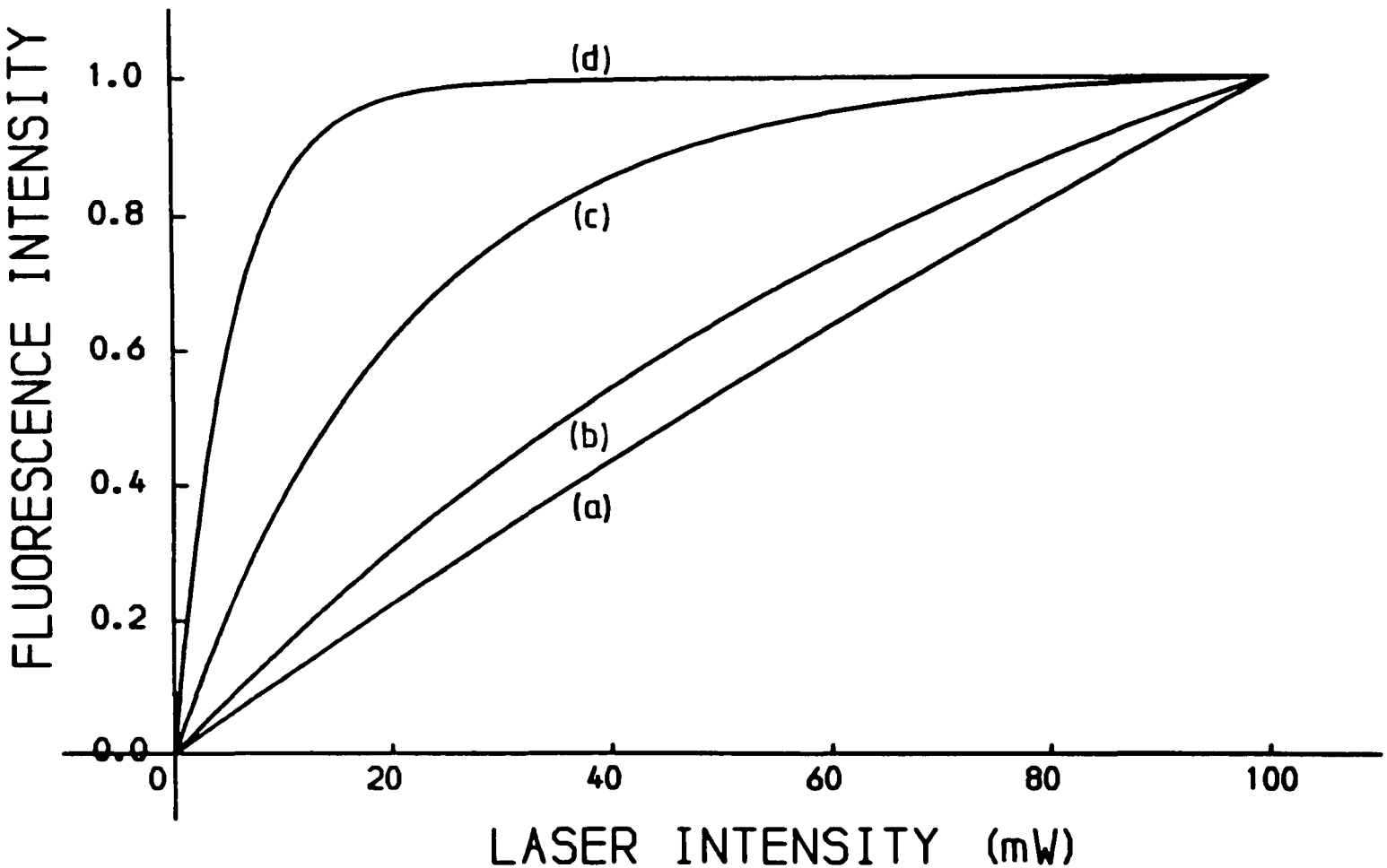

FIGURE 3.12 Effect of spot size upon fluorescence response.
(a) 40μm radius, (b) 20μm, (c) 10μm and (d) 5μm.
$\sigma_a = 10^{-16} cm^{-2}$, $k_1 = 10^8 s^{-1}$, $k_2 = 10^5 s^{-1}$ and $k_3 = 10^4 s^{-1}$. λ = 595nm, pulsewidth = 40 ps.

assuming λ = 595 nm, for a variety of focussed spot sizes. It is immediately apparent that merely focussing the spot to small dimensions is expected to substantially enhance fluorescence saturation on the basis of our rather crude model.

Some care is required here, since monotonically decreasing the spot size may eventually result in a situation where the laser intensity is so high that the rate of optically induced transitions becomes comparable to the rate of thermalisation within the electronic levels. The relation between the absorption and emission cross section (equation (3.36)), would then no longer hold and under these conditions equations (3.22-3.23) are not valid. The onset of such behaviour will be governed chiefly by the cross sections $\sigma_a(\nu_p)$ and $\sigma_e(\nu_p)$, since the products $\sigma_a(\nu_p)I_p$ and $\sigma_e(\nu_p)I_p$ determine the stimulated optical transition rates. These factors must be considered for each sample individually.

Table 3.1 contains a comparison of the optical transition rates compared to thermalisation rates, under a typical set of conditions.

TABLE 3.1 Effect of decreasing size of focussed laser spot. Evaluated assuming $\sigma_a = 10^{16}$ cm^3 average power = 50mW, pulse rate=4MHz, pulse width=40 ps. k_{th} represents the rate of thermalisation of states within a level, $\sigma_a(\nu_p)I_p$ is the rate of optical absorption and k_1 is the rate constant for spontaneous decay from the upper singlet level to the ground state

Lens focal length (cm)	Spot radius (μ)	$\sigma_a(\nu_p)I_p$ (s^{-1})	k_1 (s^{-1})	k_{th} (s^{-1})
6	22	6.1×10^9	10^8-10^{11}	10^{12}
4	14.5	1.4×10^{10}	"	"
2	7.3	5.6×10^{10}	"	"
1	3.6	2.3×10^{11}	"	"

According to the calculations summarised in Table 3.1, the thermalisation rate within levels remains considerably faster than the transition rate between levels until very small (*i.e.* a few microns) spots are used. It must be remembered that this will be sample dependent, and no general conclusions can be made as to what spot size should be used.

3.3.6 Comparison of observed and calculated fluorescence response

3.3.6.1 Experimental

It is not trivial to design an accurate experimental test of the theoretical treatment given above. Several difficulties arise:

(a) Choice of the sample itself is a major problem - we require a fluorophore which has a suitable absorption spectrum, and which is not degraded under intense irradiation.

(b) The fluorescence lifetime τ_f must be reasonably long compared to thermalisation times, and intersystem crossing to the triplet state should be unfavourable compared to singlet-singlet transitions.

(c) It is necessary to study very thin layers of the dye solution - in this way, attenuation of the laser intensity across the sample layer will be reduced such that all of the molecules in the sample are subjected to the same irradiation intensity (thin layer approximation, Section 3.3.2), and the width of the beam will remain roughly constant across the entire sample.

To a large extent, the problem of sample instability may be overcome by studying flowing systems, such that slow depletion of fluorophores in the path of the laser

beam is avoided. This has been a common approach in fluorescence spectroscopy, where jets of solution are squirted through a narrow aperture at high speeds.[10,11] However, in the brief study which was undertaken in this laboratory, it was not considered worthwhile to set up a complex system. Indeed, any saturation effect which will be of real value in Raman spectroscopy will be observable under normal experimental conditions, and an effect such as decomposition of a fluorophore under laser irradiation would be wholeheartedly welcomed under normal circumstances! (Of course, when the molecule of interest is itself fluorescent, as opposed to contamination by a fluorophore, decomposition must be avoided at all costs and a flow system is a common solution to the problem).

The experimental configuration which was chosen to investigate the fluorescence response is illustrated in Figure 3.13. The solution under investigation was contained between two cover slips (separated by 200μ spacers), and was irradiated by the pulsed laser beam, the intensity of which could be controlled with two calibrated neutral density filters (Ealing Optics 26-5975 and 26-5991). The laser was operated at a pulse rate of 4MHz(≤40 ps pulses) at a wavelength of 595 nm, with an unattenuated power of *ca.* 50 mW. The laser system is described in detail in Chapter Five).

The radiation emerging from the sample was collected and measured with the photon counting Raman spectrometer described in Chapters Six and Eight. In order to calibrate the neutral density filters, a sample of benzene was substituted in place of the dye solution, and the spectrometer was tuned to accept radiation scattered by the 992 cm^{-1} vibrational mode. The variation of intensity of the Raman signal was re-

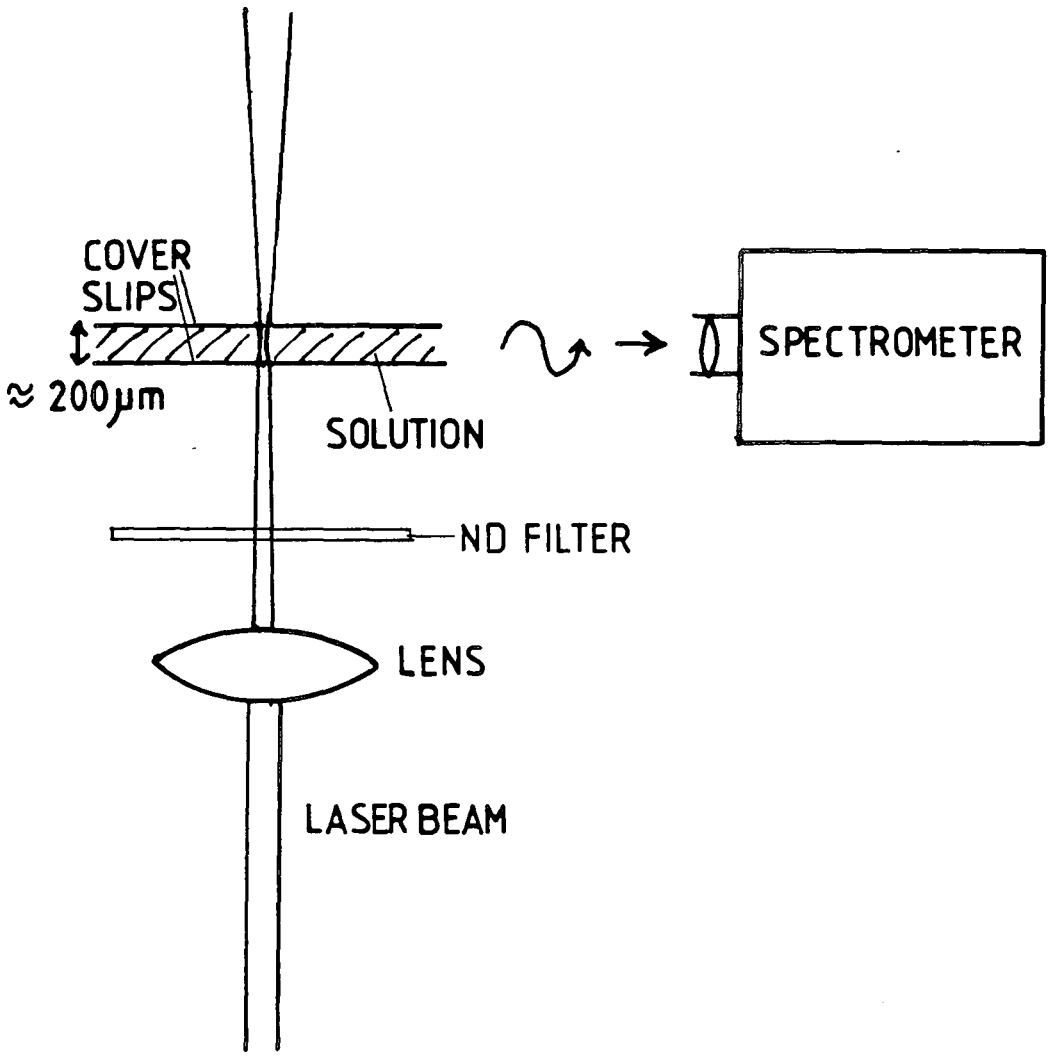

FIGURE 3.13 Experimental configuration used for measuring fluorescence saturation. The laser intensity at the sample is controlled by calibrated neutral-density (ND) filters.

corded as the filters were inserted in the path of the laser beam. Since the Raman signal is proportional to the laser intensity, (neglecting nonlinear effects), this yields a measure of the attenuation caused by each filter. One filter had a transmission of *ca.* 0.76 while the other transmitted 0.51 of the incident laser radiation, and so by utilising different filter combinations, the laser transmission could be selected as 1.0, 0.76, 0.51 or 0.38 of the unattenuated power.

This method of calibrating the filters, rather than directly measuring the attenuation with a power meter, has the advantage that any nonlinearity in the detection system is automatically compensated for.

The fluorescence response to variation in laser intensity was measured in an identical manner to the Raman signal. The laser was focussed at the sample by a lens of suitable focal length, in order to obtain the maximum fluorescence signal. This signal was then recorded for a suitable length of time with each filter in place. Any systematic variation of this signal with time indicates that the fluorescor is not stable under the irradiation, and this clearly invalidates the theoretical treatment outlined above.

Two dyes were examined for fluorescence saturation, namely rhodamine 6G (R6G) and "Brilliant Green" (BG). The structures are illustrated in Figure 3.14.

These dyes were chosen chiefly because of their differing absorption characteristics. BG[24] absorbs strongly over the range 570-670nm, with a maximum at around 630nm, whereas R6G[19,25] absorbs strongly in the region 460-560nm, with a maximum at *ca.* 530-540 nm. (These values are solvent dependent). It is apparent, therefore, that 595 nm laser

radiation will be absorbed strongly by BG, but weakly by R6G, and so it was hoped to study saturation behaviour under two extreme conditions.

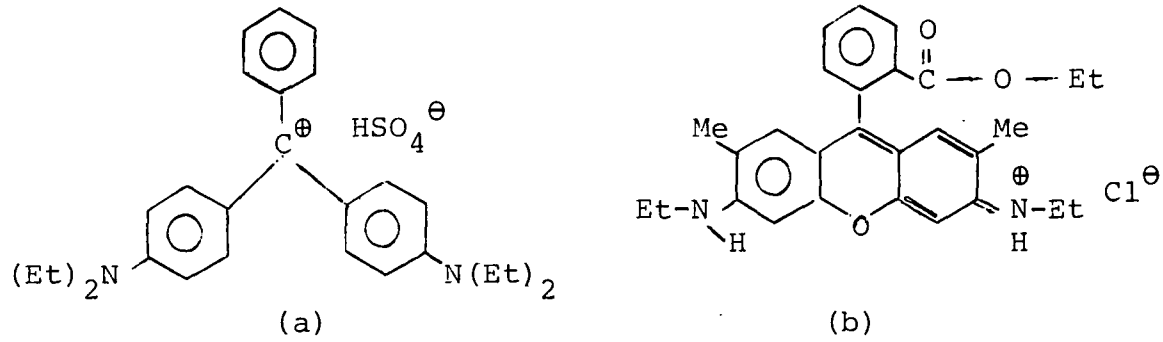

FIGURE 3.14 Molecular structure of (a) Brilliant Green and (b) Rhodamine 6G

3.3.6.2 Fluorescence response of BG: fluorophore depletion during irradiation

A $1x10^{-5}$M solution of BG in glycerol was examined for saturation behaviour. The laser beam was focussed with a 4 cm focal length lens upon the sample, which should yield a 29μ diameter diffraction-limited spot. The laser wavelength was 595 nm, (pulse rate 4MHz), and the intensity was decreased stepwise by the insertion of the neutral density filters, with the resultant fluorescence signal being recorded for 8-10 minutes at each laser intensity.

Figure 3.15 illustrates the variation in fluorescence signal as the laser intensity was decreased. Clearly, the fluorescence intensity recorded immediately after a filter was changed was unstable, which indicates that the fluorophores were in a non-equilibrium condition. It appears that the concentration of fluorophores within the path of the laser beam are gradually depleted. When a filter was inserted into the beam, the laser intensity was reduced and so the con-

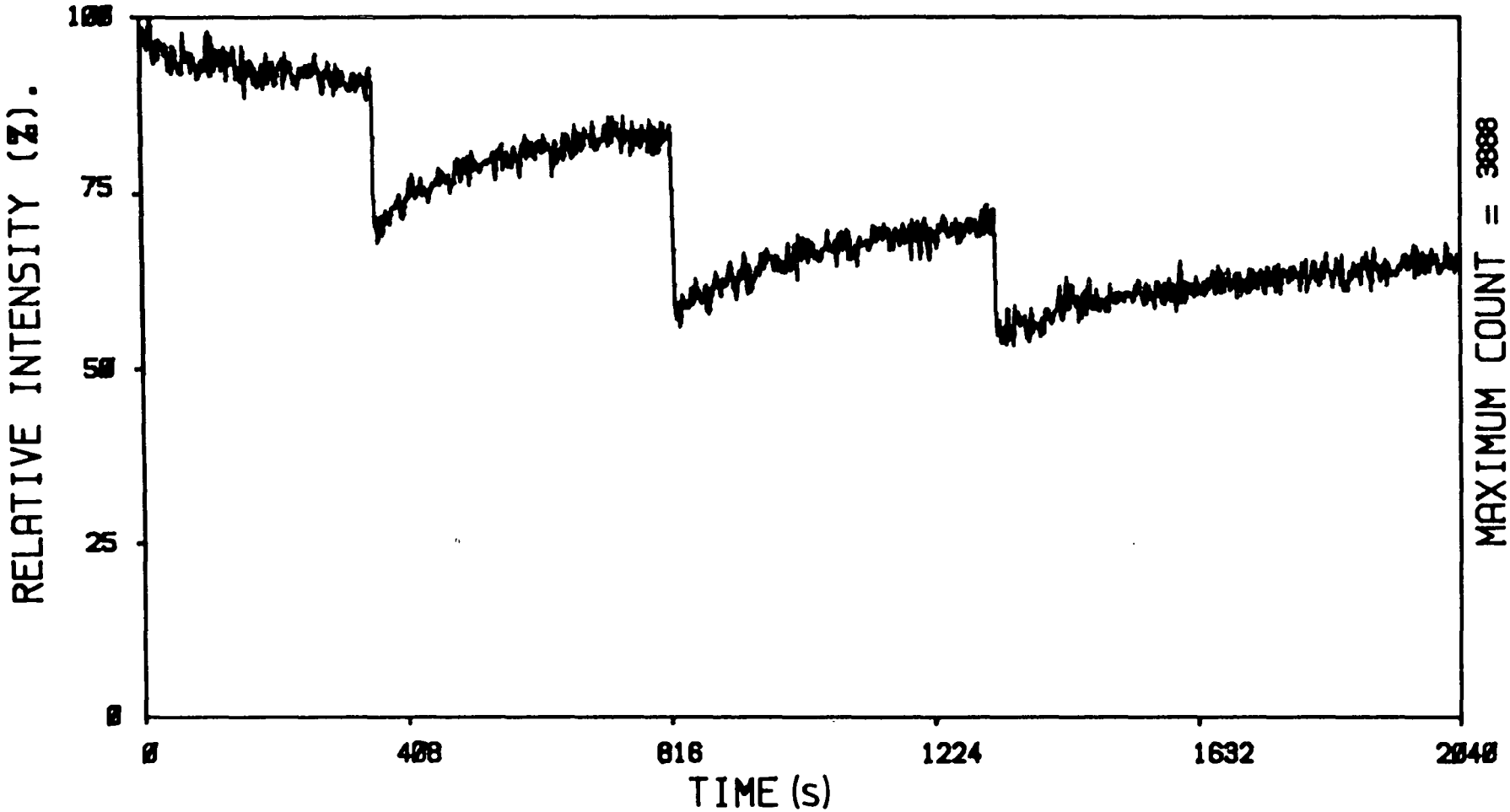

FIGURE 3.15 Variation in fluorescence intensity as a function of laser power. Each vertical line corresponds to the insertion of a neutral density filter. (a) No filter - gradual depletion of fluoropphores (50mW intensity), (b) 0.76 transmission filter - gradual increase in fluorophore concentration to level determined by new (lower) laser intensity, (c), (d) - same effect as (b) (0.56 and 0.38 transmission of laser power respectively).

centration of fluorophores began to increase again: hence the behaviour exhibited in Figure 3.15. This was repeated each time the laser beam was further attenuated.

The experimental procedure was then reversed immediately, in that filters were removed in order to increase the laser intensity. The sudden increase in irradiance resulted in a decrease in the fluorophore concentration, as would be expected. This behaviour is depicted in Figure 3.16. The fluorophores appear to approach an equilibrium concentration, but may take more than 10 minutes to do so after the laser intensity is increased.

It is obvious that this behaviour was not due to fluorescence saturation, since this should occur over much shorter timescales. The observed response is more akin to a drench-quenching effect (Chapter Two). It is interesting to compare this behaviour with that which would be expected purely from saturation considerations.

In order to calculate the expected saturation behaviour, we need to know the value of the fluorescence lifetime of the excited singlet state. This lifetime was actually too short to measure with the apparatus described in Chapter Six, and so it was estimated from literature values. Sundstrom *et al*[26] observed the decay kinetics of several triphenylmethane dyes, including BG, in various solvents. Unfortunately, the work on BG was rather incomplete in that only solutions in low viscosity solvents were examined. They did, however, report lifetime data for several other TPM dyes in high viscosity glycerol/water mixtures. Generally speaking, in high viscosity solutions (*e.g.* 1000 centipoise), the decay kinetics

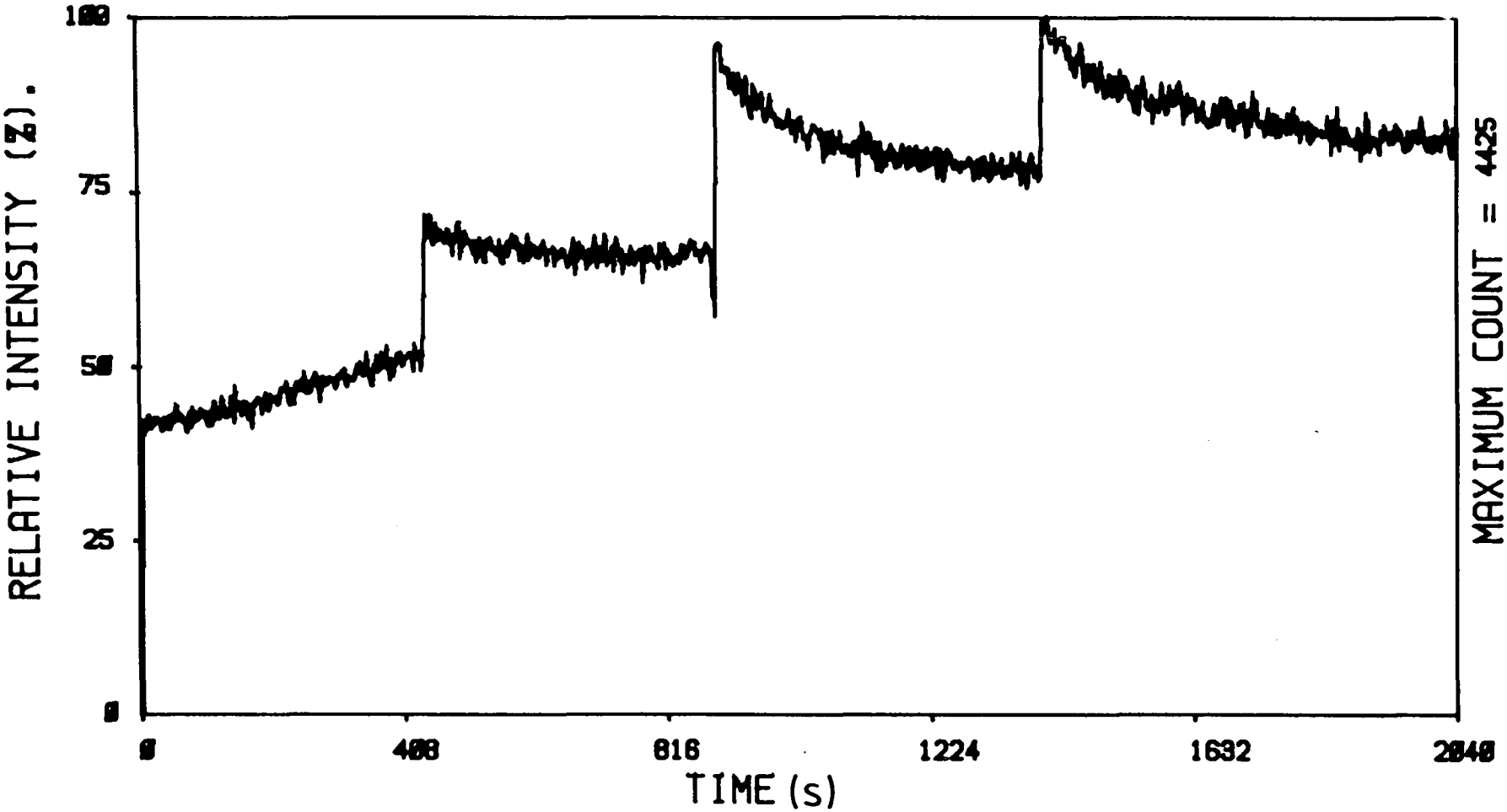

FIGURE 3.16. Fluorescence response upon increasing laser intensity.

(a) Increase in intensity due to insertion of filters, allowing build up of fluorophore concentration, (b), (c) and (d) - depletion of fluorophores upon increasing laser intensity. Other conditions as for Figure 3.15.

were described by a single exponential decay of lifetime *ca.* 100 ps.

Since BG exhibited similar behaviour to these other dyes (in low viscosity solvents), it seems reasonable to assume that its fluorescence lifetime in high viscosity solvents will also be similar. The nonradiative decay constants k_2 and k_3 were given values of 10^4-10^5 s^{-1}. This choice of value is not critical, since in the absence of quenching agents, the singlet-singlet transitions occur much more quickly than these spin-forbidden processes, and should dominate the observed kinetics.

The other factors which are required are the absorption cross section at 595 nm, and the frequency ν_o. The latter was obtained from published data,[24] and corresponds to a wavelength of 650 nm. The absorption spectrum was measured with a uv-vis spectrometer, and $\sigma_a(\nu_p)$ was calculated from this spectrum in the manner outlined in Section 3.3.5, to yield the value $\sigma_a(595nm) = 2.25x10^{-16}$ cm^2.

Figure 3.17 depicts the calculated fluorescence response compared to that which was actually observed. It is clear that the effect of drench quenching is considerably greater than that expected from our simple model of saturation. Although this means that the effects (if any) of saturation are obscured, it does demonstrate that quenching by irradiation can be very effective (more so than saturation in this case!), and that samples containing fluorophores with similar behaviour to BG would produce better Raman spectra by increasing the laser intensity on the sample. Figure 3.17 shows that any increase in laser power over 50 mW should increase the Raman intensity

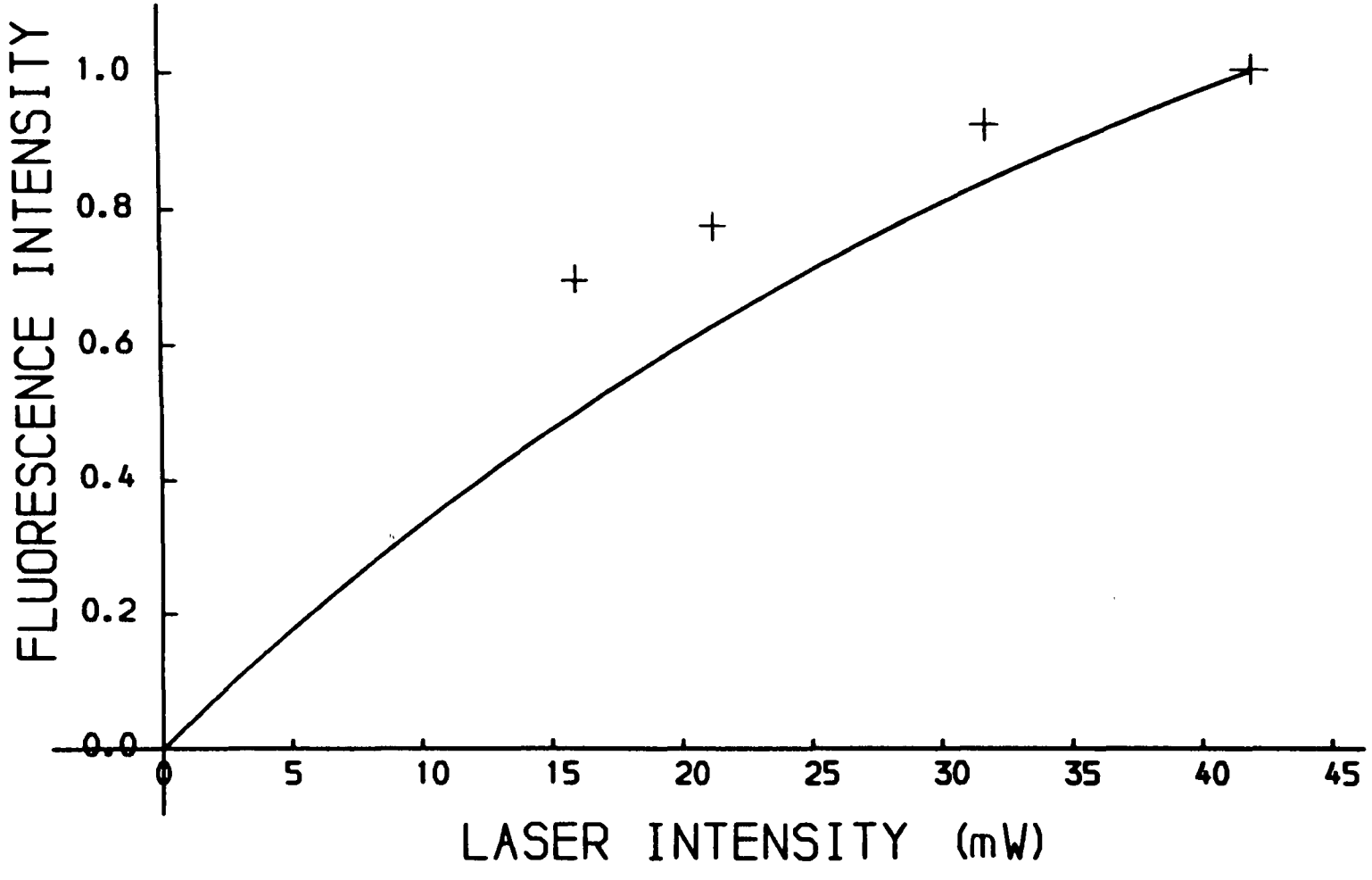

FIGURE 3.17 Fluorescence response of BG in glycerol. Curve gives calculated response, "+" represents observed data. λ = 595nm, spot diameter - 29μm.

linearly, but leave the fluorescence background almost unchanged, thereby increasing the signal/noise intensity in proportion with the laser intensity increase. This of course assumes that no adverse sample decomposition occurs at high laser intensities.

3.3.6.3 Fluorescence response of R6G.

A 10^{-5} M solution of R6G in glycerol was examined in exactly the same way as the BG sample above. Unfortunately, the same depletion of fluorophores that occurred for the BG solution was also evident with the RSG sample, and so any saturation effects that were present were once more masked by the drench quenching effect.

It was not considered worthwhile to randomly select any further samples in the hope of avoiding the problems encountered with R6G and BG, since these dyes are considered to be laser-stable under normal circumstances. Before any serious studies of the saturation response are attempted, it is clearly necessary to construct a sample flow system to continually replenish the fluorophore concentration within the illuminated volume. Such an undertaking was not considered worthwhile for the purposes of the present work.

3.3.7 Conclusions and future work

It is apparent that although calculations indicate that saturation of the fluorescence response should occur under suitable experimental conditions, the apparatus described above is incapable of resolving this effect from that of sample degradation. In order to make sensible progress in this work, it would be necessary to devise a rapid-flow system which would

constantly replenish the fluorophore concentration within the illuminated volume. Such designs have already been successfully employed in fluorescence spectroscopy. It would also be advantageous to arrange microscope-type collection optics, which would only accept light which originated from a small part of the beam path length, *i.e.* the position of tightest focus, and which would also provide a measure of the focussed spot size.

Although it is possible to construct an apparatus to measure fluorescence saturation in liquid samples, this might, at first sight, appear to be a retrograde step in terms of producing a useful Raman spectrometer, since it is highly desirable that depletion of contaminating fluorophores should occur in the laser beam! However, under many circumstances, the fluorophore may be the molecule of interest itself, rather than a contaminant in the sample. In this case, depletion or degradation of the molecule would have to be avoided, and a sample flow system would be beneficial. Under such conditions, fluorescence saturation techniques would be potentially useful and are worthwhile of further investigation. As an additional benefit, the saturation technique could be applied in tandem with a time-resolved detection system, in order to accrue further enhancement in R/N.

If this technique is to be studied quantitatively, it would be desirable to refine the mathematical treatment which has been given above. In particular, allowance for the real laser pulse shape, and the attenuation due to sample absorption, would have to be made. However, the <u>viability</u> of this method could be quickly ascertained if a suitable flow system were obtained, prior to undertaking any intricate mathematical analysis.

Although it would be interesting to pursue these studies further, it was felt that use of time-resolved rejection methods offered more immediate prospects of success, and for this reason no further work was performed upon the fluorescence saturation technique.

REFERENCES - CHAPTER THREE

1. L.A. Woodward, "Introduction to the Theory of Molecular Vibrations and Vibrational Spectroscopy", Oxford University Press, London, (1972).

2. J.A. Koningstein, "Introduction to the Theory of the Raman Effect", D. Reidel Publishing Co., Dordrecht-Holland, (1972).

3. J.R. Lakowicz, "Principles of Fluorescence Spectroscopy", Plenum Press, New York (1983).

4. W.J. Eyring, J. Walter and G.E. Kimball, "Quantum Chemistry" John Wiley, New York (1944).

5. F.A. Cotton, "Chemical Applications of Group Theory", Wiley-Interscience, New York (1971).

6. R.A. Lampert, L.A. Chewter, D. Phillips, D.V. O'Connor, A.J. Roberts and S.R. Meech, Anal.Chem., 55 (1), 68 (1983).

7. C.A. Arguello, G.F. Mendes and R.C.C. Leite, Appl.Opt, 13 (8), 1731 (1974).

8. J.N. Demas and R.A. Keller, Anal.Chem., 57 (2), 538 (1985).

9. D.P. Blair and P.H. Sydenham, J.Phys.E: Sci.Instrum., 8; 62 (1975).

10. M. Trkula and R.A. Keller, Anal.Chem., 57 (8), 1663 (1985).

11. N.J. Dovichi, J.C. Martin, J.H. Jett, M. Trkula and R.A. Keller, Anal.Chem., 56(3), 348 (1984).

12. R.P. Frueholz and J.A. Gelbwachs, Appl.Opt., 19(16),2735 (198

13. A. Zunger and K. Bar-Eli, J.Chem.Phys., 57 (8), 3558 (1972).

14. O. Svelto, "Principles of Lasers", Plenum Press, New York, London (1982).

15. G. Stephenson, "Mathematical Methods for Science Students" Longman, London, New York (1983).

16. B. Di Bartalo, "Optical Interactions in Solids", Wiley, New York (1968).

17. M.R. Spiegel, "Laplace Transforms", Schaum Outline Series in Mathematics, McGraw-Hill, New York (1965).

18. P.P. Yaney, J.Opt.Soc.Am., 62 (11), 1297 (1972).

19. N. Mataga and T. Kubota, "Molecular Interactions and Electronic Spectra", Marcel-Dekker, New York (1970).

20. C.V. Shank, Rev.Mod.Phys., 47 (3), 649 (1975).

21. B.I. Stepanov and A.N. Rubinov, Sov.Phys.Uspeki, 11, 304 (1968).

22. "Continuous-Wave Dye Lasers - Properties and Performance Reports", Spectra-Physics Laser products division (1982).

23. F.G. Smith and J.H. Thomson, "Optics", John Wiley and Sons, London, New York, Sydney, Toronto (1973).

24. A.N. Rubinov and V.A. Mostovnikov, Zhurnal Prikladnoi Spektroskopii, 7 (3), 327 (1967).

25. F.P. Schafer, "Dye Lasers, Top.Appl.Phys., 1", Springer-Verlag, Berlin, Heidelberg, New York (1973).

26. V. Sundström, T. Gillbro and H. Bergström, Chem.Phys., 73, 439 (1982).

CHAPTER FOUR

GENERAL PRINCIPLES OF TIME-RESOLVED FLUORESCENCE REJECTION

4.1 Introduction

The difference in timescale between Raman and fluorescence processes provides a means of distinguishing between the two events. Time-resolution has been one of the most commonly applied techniques in attempting to suppress fluorescence backgrounds in Raman spectra, and the apparatus used in order to achieve this resolution has varied considerably.[1-10] Before going on to discuss the various experimental systems that have been applied, the basic principles of the method will be considered in a more quantitative manner. In this way, it will become apparent what degree of improvement can be expected in using this technique. The general experimental requirements for an efficient system will also be discussed.

4.2 Fundamental aspects of time-resolved fluorescence rejection (TRFR)

4.2.1 The physical basis of TRFR

Figure 4.1 illustrates the physical basis of the TRFR system. For simplicity, we consider an idealised situation in which a Raman active, fluorescing sample is subjected to a laser pulse whose duration Δt is much shorter than the fluorescence limetime, and so constitutes an impulse input.[11] Since the laser used in our work (Chapter Five) produces pulses of picosecond duration, this is a valid approximation for fluorophores with lifetime τ_f of the order of nanoseconds. Furthermore, to simplify the subsequent analysis, we assume that the laser pulse actually approximates to a δ function input.[11]

Raman photons are scattered only for the duration of the laser pulse, whereas fluorescence photons are emitted

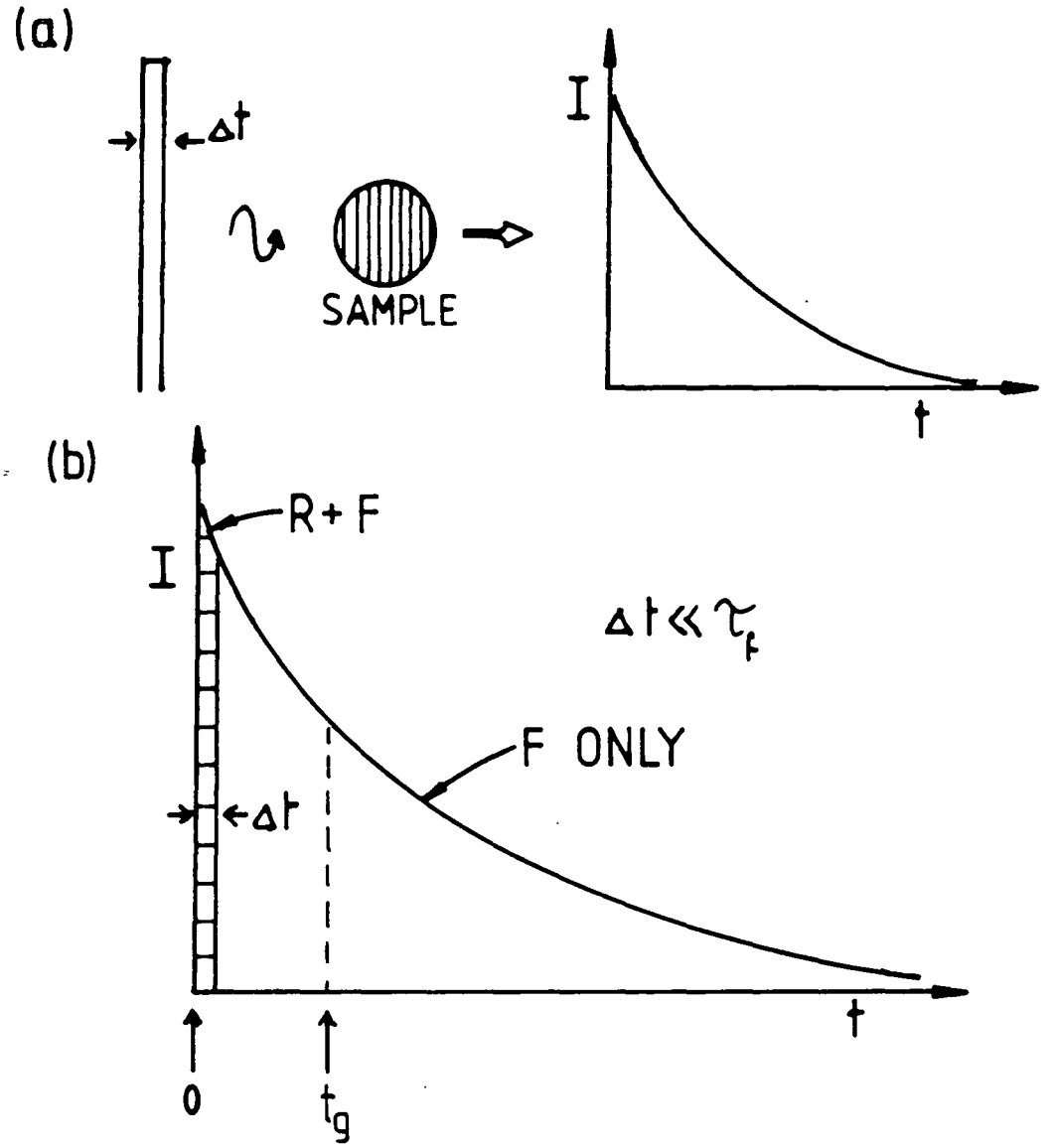

FIGURE 4.1

(a) Laser pulse (width Δt) falls upon Raman active, fluorescing sample. We assume that $\Delta t << \tau_f$ and so comprises an impulse input. Pulse is shown as a rectangle for simplicity, but the actual flunctional form is irrelevant, provided that $\Delta t << \tau_f$.

(b) Details of time distribution. Raman and fluorescence photons occur during Δt, fluorescence only after Δt. Gate is set to accept photons between $0 \rightarrow t_g$. Since $\Delta t \approx 0$, Raman signal is independent of t_g for most practical gate widths.

from the sample according to a specific (often exponential) probability-time distribution (Chapter One). The object of the experiment is only to record photons which arise over the duration of the laser pulse Δt, and so to reject the majority of the fluorescence photons while accepting the full Raman signal. This may be achieved with the use of a suitable detector and timing electronics.

It is necessary at this point to clarify the term "detector". In this work we consider that the detector is in fact the entire detection system, including the actual photosensitive device and any subsequent timing and recording electronics. In principle, time resolution may be achieved in two ways.

(a) By directly gating (switching on and off) the photosensitive device, so as to detect photons only during selected time intervals.

(b) By operating the photosensitive device continuously, but configuring the subsequent counting electronics such as to record only specifically timed pulses. This is referred to as "indirect gating".

Examples of each of these approaches are the gated diode array detector (Chapters Six and Seven), which is physically switched on and off, and the PMT with associated pulse timing electronics, which is operated continuously (Chapters Six and Eight). The choice of either gating system does not affect the general discussion below.

4.2.2 Quantitative efficiency of TRFR in an ideal system

4.2.2.1 Improvement in signal/background (R/F)

A rough estimate of the expected efficiency

of fluorescence rejection may be obtained from an analysis of the ideal system depicted in Figure 4.1. Since the laser pulses are considered to be infinitesimally short, the resultant fluorescence decay will have an infinitesimal risetime (Chapter Three). For simplicity, we assume that the decay is a single exponential of lifetime τ_f. We also assume that the photon detector does not distort this time distribution in any way, *i.e.* it has zero timing error. This restriction is lifted in Chapters Seven and Eight.

Ideally, the detector system would be gated such as to only accept or record photons which arise during the period Δt of the time distribution. In practice, the gate width will be somewhat larger than the laser pulse duration, and so photons are accepted if they arrive between times 0 and t_g, where t_g is the (variable) gate width (Figure 4.1). Then the fluorescence intensity recorded by the detector is a function of the gate width t_g. At any instant in time, the fluorescence intensity I(t) incident upon the detector is given by equation (4.1).

$$I(t) = k_R C e^{-t/\tau_f} \tag{4.1}$$

where k_R is the radiative decay constant (see Chapter One) and $k_R c$ is the fluorescence intensity at t=0. (Note that the fluorescence lifetime, τ_f, is given by $1/(k_R + k_N)$, the reciprocal sum of the radiative and nonradiative decay constants (Chapter One)). Equation 4.2 gives the total fluorescence intensity detected between the gate limits 0 and t_g.

$$F = k_R C \int_0^{t_g} e^{-t/\tau_f} = \phi C (1-e^{-t_g/\tau_f}) \tag{4.2}$$

In this equation $k_R/(k_R+k_N)$ has been replaced by ϕ, the fluorescence quantum yield (Chapter One). If the upper gate limit is infinite, equation (4.2) reduces to ϕC, the total detected intensity for a non-gated detector.

Since Raman photons are only generated during the presence of the laser pulse, the Raman photon distribution also approximates to a δ function, and so all Raman photons will be accepted irrespective of the gate width t_g. This means that in an ideal system, the detected Raman intensity (R) is not a function of gate width. If the detector is not gated, the ratio of the Raman signal to the fluorescence background is given by equation (4.3).

$$R/F = R/(\phi C) \qquad (4.3)$$

If the detector is gated to accept photons from $0 \rightarrow t_g$, the ratio R/F becomes:

$$R/F = R/[\phi C(1-e^{-t_g/\tau_f})] \qquad (4.4)$$

The enhancement in R/F (denoted E[R/F]) on gating the detector is given by the ratio of (4.4) to (4.3) namely:

$$E[R/F] = 1/[1-e^{-t_g/\tau_f}] \qquad (4.5)$$

4.2.2.2 Improvement in signal/noise (R/N)

In order to calculate the enhancement in S/N on gating the detector, we assume that the background noise may be entirely attributed to random fluctuations in the fluorescence signal, *i.e.* detector noise is negligible in comparison. This is valid for the samples studied in our work. Furthermore, for the reasons outlined in Chapter One, we calculate the ratio of the Raman signal to the noise associated with the

fluorescence background (R/N), rather than the signal/noise level at the peak of the Raman band. When F>>R, these two quantities are actually identical.

Proceeding on the assumption of Poisson statistics (Chapter Two), the noise (N) associated with a fluorescence signal of intensity F is given by $\sqrt{F}$. Then, from equations (4.3-4.5), the enhancement in R/N is given by equation (4.6).

$$E[R/N] = 1/[1-e^{-t_g/\tau_f}]^{\frac{1}{2}} \qquad (4.6)$$

Equations (4.5) and (4.6) demonstrate that, in this ideal case, the improvements in R/F and R/N are determined solely by the ratio t_g/τ_f. It is apparent that materials with short fluorescence lifetimes demand narrower gate widths and hence better timing resolution than do more slowly decaying samples.

Figure 4.2 illustrates the magnitude of improvements in R/F and R/N as a function of the ratio t_g/τ_f. Although this represents an idealised situation, it does illustrate two important points which are common to more realistic analyses.

(a) The improvement in R/F is always greater than that in R/N when photon shot noise is the dominant noise source, since reducing the fluorescence by a factor K only reduces the noise by $\sqrt{K}$. This is unfortunate since it is the R/N ratio which must be improved in order to better discern a Raman signal hidden on a noisy background. The improvement in R/F is immaterial in shot-noise limited spectra, unless saturation of the detector occurs with high fluorescence intensities.

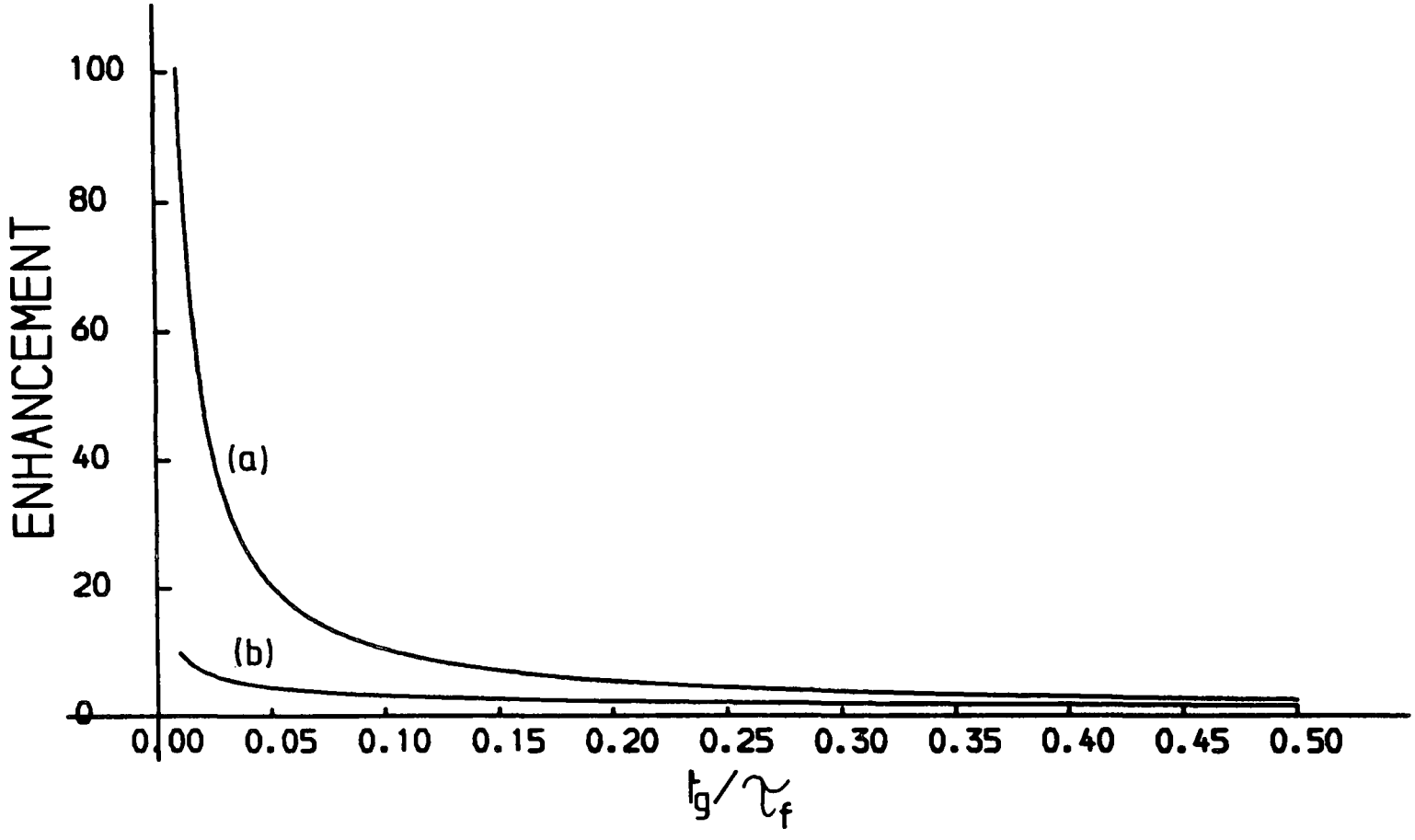

FIGURE 4.2 Fluorescence rejection with ideal δ function Raman input.

(a) Enhancement in R/F. (b) Enhancement in R/N.

(b) No significant improvement in R/N arises until the gate width is less than *ca.* 1/10 of the fluorescence lifetime. For example, a threefold improvement in R/N requires a ratio $t_f/\tau_f = 0.12$, while a fivefold enhancement is obtained for $t_g/\tau_f = 0.04$. It is generally true that obtaining small gate widths is crucial in achieving a viable rejection system.

4.3 Deviation of TRFR system from ideality

This ideal model is unrealistic in that it predicts that one may monotonically narrow the gate while obtaining ever-increasing improvements in R/N. In reality, the detector response to the Raman signal has a finite width, and so the Raman signal in a gated experiment is a function of gate width. A limitingly narrow gate is reached, below which the detected Raman signal is decreased upon further narrowing, and it is this behaviour which determines the limiting performance. The most important criterion in determining the rejection efficiency is, in fact, the timespread of the Raman signal that is produced by the detector, since this determines the narrowest effective gate which can be chosen.

4.3.1 Origin of the timespread of the Raman signal

The finite width of the observed Raman time distribution arises as a result of the two main effects.

(a) The laser pulses actually have finite duration. Even if the Raman response to a single photon is instantaneous, the overall Raman signal (prior to detection) will have a time distribution identical to that of the laser pulse. For narrow laser pulses (picosecond duration) this broadening is negligible compared to that due to factor (b) below.

(b) Even if the laser pulses constitute a delta function impulse, the response of the detector is not instantaneous, and so the output signal is not a faithful reproduction of the input. This has the effect of introducing a finite timing error into the detector response and so the arrival of a single photon gives rise to broadened response from the detector. In the case of a PMT, this results from a random variation in the time taken for a pulse of electrons to propagate through the tube and to generate a pulse at the anode (known as the transit-time spread), and is the fundamental lower limit to the timing resolution that can be achieved.[12,13] This is discussed in greater detail in Chapter Six. The performance of the directly gated diode array detector is somewhat more complex and is described in Chapter Seven.

For most practical purposes, (*i.e.* conventional photomultipliers and gated diode arrays (Chapter Six)), the blurring of the time response is due primarily to the detector rather than the laser pulse. For example, the laser pulses are typically in the region of 10 ps while the timing resolution of the PMT may be several hundred ps.[12,13] The time response of the gated diode array is of the order of nanoseconds.

4.3.2 Effect of finite timing resolution upon rejection efficiency

The finite timing resolution of the system has important consequences in determining the efficiency of fluorescence rejection. Its effect upon the observed photon distributions is illustrated in Figure 4.3. We again assume that the Raman photon distribution constitutes an impulse excitation, while the fluorescence response is an exponential decay. The

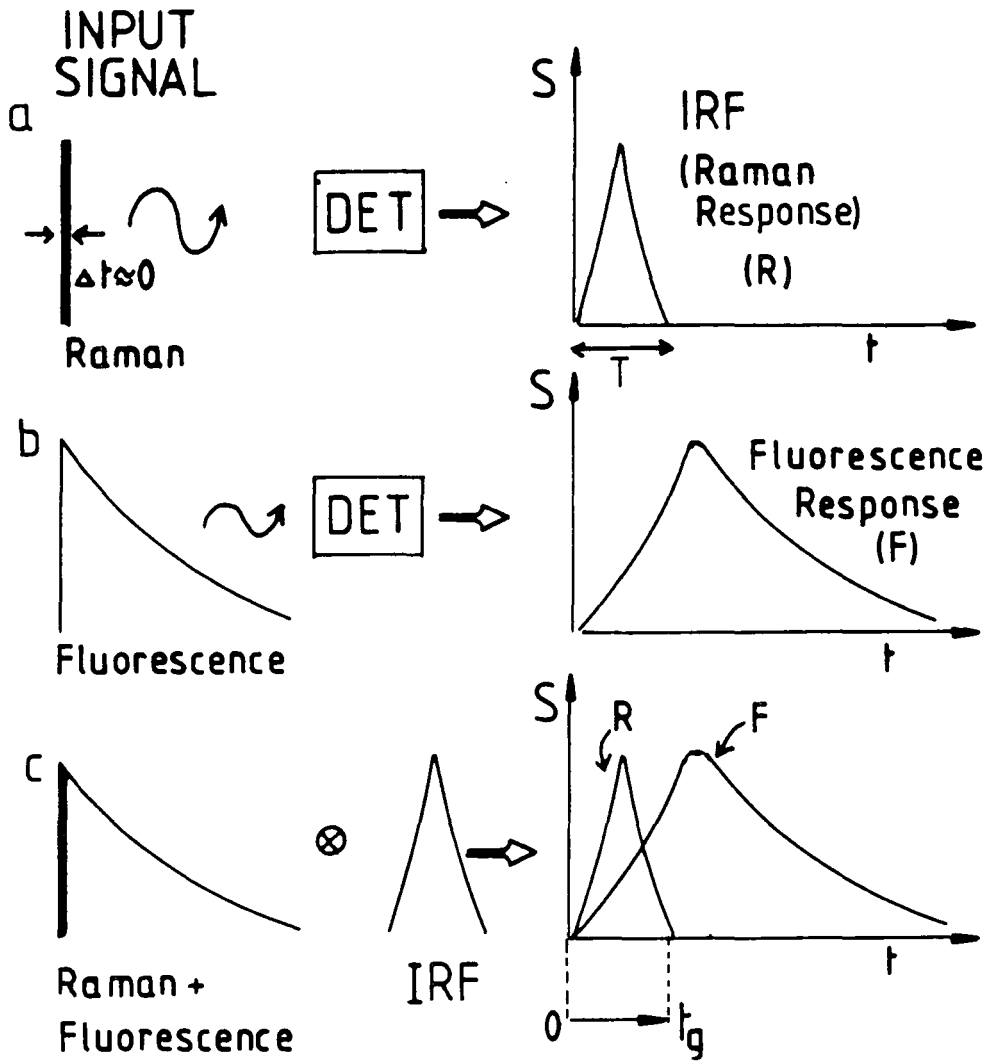

FIGURE 4.3 Effect of detector (DET) response upon observed photon distribution.

(a) Response to Raman impulse - yields IRF of system.

(b) Response to fluorescence - convolution of IRF with exponential.

(c) Raman + fluoresence signal convolved with IRF.
A gate set with $t_g \leq T$ still rejects most of the fluorescence, but Raman signal is lost when $t_g \leq T$, in contrast to the ideal case (Figure 4.2).

situation here is identical to that in Figure 4.1. However, the detector has a finite response time, so the response to an impulse input will have a finite width. The response of the detector to an impulse input is known as the impulse (or instrument) response function (IRF).[11] Therefore, the recorded Raman time distribution represents the IRF of the detection system.

The response of the system to any input is given by the convolution of the IRF with the functional form of the input signal.[11] Figure 4.3 illustrates the Raman and fluorescence distributions as recorded by the timing system. The important factors here are that the observed Raman signal now has a finite width (and a functional form given by the IRF), while the fluorescence distribution is determined by the convolution of the IRF with the exponential decay.

The width of the base of the IRF is denoted T (Figure 4.3). If $\tau_f >> T$, most of the fluorescence photons are still registered after the Raman signal has ended, but the gate cannot be decreased below the width T without attenuating the recorded Raman intensity, *i.e.* the Raman signal is also a function of gate width. This is the most important difference between a real TRFR system and the idealised model considered previously, where the R/N enhancement depended only upon the ratio t_g/τ_f, and so could be improved by monotonically increasing t_g. In general, there will be a gate width at which the R/N is optimised, determined by the ratio of the IRF width and the fluorescence lifetime.

A detection system which displays no timing error would result in the ideal system being obtained (neglecting

laser pulsewidths). It is only by reducing the width of the IRF that more efficient rejection can be obtained. (It is usual to measure the timespread of the IRF by the full width at half maximum height (FWHM)). It will be seen in the review of time-resolved methods that have been applied, (Section 4.4 below), that the steadily improving results that have been obtained have been due entirely to the production of shorter laser pulses and detection systems with higher time resolution, *i.e.* narrower IRFs.

It is worthwhile noting at this stage that other factors can degrade the performance of the apparatus. In particular, if the spacing between laser pulses is not long compared to τ_f, then fluorescence decays stimulated by adjacent pulses will overlap, resulting in an excess of fluorescence photons falling within the gate, degrading the R/N ratio. This effect was first considered and quantified by Van Duyne *et al.*[3] Furthermore, if the output power of the pulsed laser is low compared to that of a conventional cw source, the R/N improvement gained by the gating process may not compensate for the degradation in S/N which results from decreasing the excitation intensity (Chapter Two). This has been a serious drawback in much of the previously published work,[3-9] and is of crucial importance in determining the performance of the gated diode array detector (Chapter Seven).

4.4 Experimental requirements and a review of previously published work

There are two major requirements in constructing a TRFR system, namely a source of short-duration laser pulses, and a detection system with fast-timing capability. The performance

of the monochromator/spectrograph is of secondary importance as far as timing considerations are concerned, (although some broadening of the system IRF does occur during the passage of light through the monochromator (Chapter Eight)), but is obviously critical in determining the overall quality of spectra produced.

The constraints which apply to the choice of laser system are essentially that a source of very short (ps) pulses of variable repetition rate (in order to avoid fluorescence overlap) must be available. It is also important that the power of the beam should be as high as possible, since we expect, (in the absence of the saturation effects discussed in Chapter Three) that the R/N should increase as the square root of the incident power. It is also desirable that the pulses should be wavelength tunable in order that absorption maxima may be avoided (Chapter Two). The laser system which was employed in our work is discussed in Chapter Five.

Time-resolved detection may be achieved in two distinct ways, as was discussed above. We may either directly gate the photon detector such that it is only sensitive to light for short time periods, or the detector may be operated continuously while the output is time-resolved. Direct gating of a variety of detectors is achievable over nanosecond timescales,[14,15] but the maximum repetition rate for triggering the active period is often low (*e.g.* kHz) and so the laser repetition rate must be reduced accordingly. This means that the duty cycle, (the effective photon accumulation time per second) is low, and so poor R/N ratios are obtained.

At present a more viable route lies in time resolving the

detector output, which allows faster data accumulation (100kHz), higher laser pulse rates, shorter gate periods and hence better rejection. Instrumentation for achieving this is described in Chapter Six.

It has already been noted that a variety of experimental configurations have been applied in temporally-resolving Raman and fluorescence photons. However, nearly all of the reported work has involved the use of a PMT (operated continuously) and associated gated counting electronics, in conjunction with a pulsed laser system. The success of these attempts has been governed by three factors, namely:

(a) the width of the laser pulse,

(b) the detector time-resolution,

(c) the repetition rate of the detection system.

In order to appreciate the significance and effectiveness of this work, it is necessary to consider in detail the operation of the laser and detection systems (Chapters Five, Six), as well as a more detailed theoretical treatment of practical TRFR experiments. At this stage it will suffice to indicate the briefly the type of apparatus which has been employed. The published work will be more critically reviewed after the results which were obtained in this laboratory have been presented (Chapters Seven, Eight).

Yaney[1,2] used a Q-switched Nd:YAG laser (120-200ns pulse duration, 10-3000 Hz pulse rate) and gated photon detection, (gate widths from 100ns-1μs) in order to successfully reject phosphorescence backgrounds from Raman spectra of ZnSe and Al_2O_3. The success of these experiments was due entirely to the fact that the luminescence lifetimes were long (μs-ms) compared to the laser pulse/gate widths, as is expected for spin-

forbidden transitions. The apparatus would have failed for fluorescing materials (ns lifetimes). Van Duyne *et al*[3] and Burgess and Shepherd[4] used mode-locked Ar^+ lasers as pulse sources, with time-to amplitude conversion and pulse-height analysis as the pulse-timing technique (Chapter Six). The authors achieved IRF widths of 2.5ns and 1.3ns respectively, but neither group successfully improved R/N ratios in the fluorescing systems studied, even though the R/F ratios were improved. This was due, in part, to the closely space mode-locked laser pulses inducing overlapping fluorescence.

Harris *et al*[5] used a cavity-dumped, mode-locked Ar^+ laser as a variable repetition rate pulse source, and time-resolved the PMT output with a sampling oscilloscope, resulting in a broad IRF of *ca*. 2.7ns width. Unfortunately, the use of the sampling oscilloscope constrained the system to a low repetition rate (42kHz) and hence a poor duty cycle, so the effective laser power on the sample was small compared to cw excitation. This actually resulted in a seven fold decrease in R/N on gating the detector, even though the R/F ratio was increased by more than 100 times! This reinforces the important point that merely reducing the intensity of the background is not sufficient in shot noise limited spectra; the signal/noise must also be improved.

Gustafson and Lytle[6] used a cavity-dumped, synchronously-pumped dye laser (Chapter Five), as a source of tunable wavelength, variable repetition rate 10 ps pulses, coupled with high speed gated photon counting. They observed R/N improvements of *ca*. 2.4 for a solution of rubrene in benzene (τ_f = 16.5ns), but the experimental conditions under which this was obtained are not clear. The work of Gustafson and Lytle is discussed

in more detail in Chapter Eight, in comparison with the results and theoretical analysis presented in this thesis.

Watanabe *et al*[7] reported the use of a microchannel plate PMT[13] in a time-correlated photon counting system, which had an IRF width of only 67 ps. This has been the most successful example of TRFR yet reported. R/N enhancements of *ca.* 4.2 were observed with a solution of R6G (τ_g = 4ns). However, it appears from our own work that the gate width was not optimised, and so the system performance was considerably degraded. This is discussed further in Chapter Eight.

All of the techniques above are based upon essentially the same approach, namely time-correlating a photomultiplier output. It is significant that little work has been reported on directly gated detectors - this is due to the difficulty in efficiently gating a detector for short time periods at high repetition rate. As far as we are aware, the only TRFR studies using a directly gated multichannel detector have been reported by this laboratory,[8,9] and are discussed in more detail in Chapter Seven.

Delhaye *et al*[10] recently discussed a novel method of temporal discrimination, utilising a Fabry-Perot interferometer as the resolving apparatus. Light pulses which are short compared to the round-trip time of the interferometer are passed without interference, while pulses longer than the round-trip time undergo interference, and will be diminished in intensity if destructive interference occurs. This is determined by the wavelength of the radiation, and so a broad fluorescence background is converted into a spectrum where the energy is channeled into discrete wavenumber regions, between which a Raman signal may theoretically be observed.

The method was demonstrated to be successful in resolving Rayleigh lines on fluorescence backgrounds, but it was noted that the optical losses of the interferometer were so great that the Raman lines could not be resolved; the R/N ratio was in fact substantially decreased compared to conventional detection. The authors postulated that the use of more efficient interferometers (such as the Michelson type) might yield better results, but no further work on this technique has been published.

Finally, it should be noted that, apart from the interferometer described above, all of the other methods have relied upon electronic gating. It is also possible to construct fast optical gates, utilising, for example, the Kerr effect[16] or a Pockels cell.[17] Unfortunately, such devices are inefficient for our purposes, since they inevitably attenuate the photon intensity prior to detection, further reducing the R/N. They are commonly used for temporal analysis of fairly intense signals,[16] or for Q-switching lasers.[18] Furthermore, the optical switching time of a Pockels cell is *ca.* 20ns,[18] which is too slow for our application. It seems unlikely at present that these methods would find practical applications in TRFR systems.

4.5 Conclusions

The physical basis of TRFR methods have been outlined in this chapter, and simple calculations have indicated the magnitude of improvements which can be expected from this approach. Factors which cause deviation from ideality have been discussed with regard to optimising instrument design. Several general considerations have emerged; the improvement in R/F is always

greater than that in R/N in a shot-noise limited system, and the finite timing resolution of detection systems means that one cannot monotonically decrease gate widths in order to improve the R/N; in general, the optimum gate width will be determined by the relative width of the IRF and the fluorescence lifetime. Many of the previously reported TRFR systems have succeeded in improving the R/F ratio while degrading the R/N, which is a retrograde step!

Practical experimental configurations which can be used to achieve temporal resolution will be discussed in Chapters Five and Six, and results obtained in this laboratory will be presented in Chapters Seven and Eight, along with a critical comparison with previously published work.

REFERENCES - CHAPTER FOUR

1. P.P. Yaney, J.Opt.Soc.Amer., 62 (11), 1297 (1972).

2. P.P. Yaney, J.Raman Spectrosc., 5, 219 (1976).

3. R.P. Van Duyne, D.L. Jeanmaire and D.R. Shriver, Anal.Chem., 46 (2), 213 (1974).

4. S. Burgess and I.W. Shepherd, J.Phys.E.: Sci.Instrum., 10 617 (1977).

5. J.M. Harris, R.W. Chrisman, F.E, Lytte and R.S. Tobias, Anal.Chem., 48 (13) 1937 (1976).

6. T.L. Gustafson and F.E. Lytle, Anal.Chem., 54, (4)634(1982).

7. J. Watanabe, Shuichi Kinoshita and T. Kushida, Rev.Sci. Instrum., 56 (6), 1195 (1985).

8. N. Everall, J. Howard, R.W. Jackson and K. Hutchinson, "Proceedings of the Second International Conference on Time-Resolved Vibrational Spectroscopy", A. Lauberau and M. Stockburger (Eds.), Springer-Verlag, Berlin , (1985).

9. N. Everall, J. Howard, R.W. Jackson and K. Hutchinson, J.Raman Spectrosc., 17 (5), 415 (1986).

10. M. Delhaye, A. Deffontaine, A. Chapput and M. Bridoux, J.Raman Spectrosc., 15 (4), 264 (1984).

11. D.C. Champeney, "Fourier Transforms and their physical applications", Academic Press, New York, London (1973).

12. R.W. Engstrom, "Photomultiplier Handbook", RCA Corporation, (1980).

13. J.P. Boutot, J. Nussli and D. Valat, Adv.Electron. Electron.Phys., 60, 223 (1983).

14. R.K. Chang and M.B. Long, Top.Appl.Phys., 50, 179 (1982).

15. R. Wardle, "Gating of Photomultipliers", Thorn-EMI Research Publication R/PO61.

16. R.R. Alfano and S.L. Shapiro, Physics Today, 30 (July 1975).

17. G.F. Albrecht, E. Kallne and J. Meyer, Rev.Sci.Instrum., 49 (12), 1637 (1978).

18. O. Svelto, "Principles of Lasers", Plenum Press, New York, London, (1982).

CHAPTER FIVE

THEORY OF OPERATION, PERFORMANCE ANALYSIS AND OPTIMISATION OF THE PICOSECOND PULSED LASER SYSTEM

5.1 Introduction

The laser system is a complex piece of apparatus, the correct use of which demands a thorough knowledge of the theoretical and practical aspects of its operation. During the course of the work described in this thesis, several important aspects of the system performance have been discovered which are not reported by the manufacturer, but which are vitally important in interpreting experimental results. For this reason, this chapter presents a detailed discussion of the operation, performance and optimisation of the laser system.

The following section (5.2) consists of a brief description of the function of the individual components of the laser system. Section 5.3 reviews the basic physics needed to understand the operation of the individual components, in particular the nature of acoustooptic interactions.

Section 5.4 discusses methods of characterising the output of the laser, and includes work performed in this laboratory upon measuring and optimising the laser performance. Finally, Section 5.5 describes our observation and characterisation of spurious wavelength emissions from the dye laser, which lase simultaneously with the main selected wavelength, and which give rise to artifacts in the Raman spectra which may be very confusing to users who are unaware of the problem.

5.2 Brief overview of the function of the laser system

The function of the laser system is to provide a source of variable repetition rate, wavelength-tunable, picosecond duration optical pulses of high peak power. The work described

in this thesis was carried out with a mode-locked, cavity dumped, synchronously-pumped dye laser (Spectra-Physics), a schematic diagram of which is presented in Figure 5.1.

The laser system is modular. Before giving a detailed description of its operation, the function of each component will be summarised. All specifications quoted are taken from the manufacturers literature.

5.2.1 Mode locked Ar laser

An Ar^+ laser was used as a source of continuous wave (cw) or pulsed 514.5 nm radiation. Under cw operation, the laser can deliver *ca.* 3.75 W of radiation,with a line-width of *ca.* 5 GHz (single line). Mode-locking the laser (Section 5.3.2) generates pulsed output, with pulse widths on the order of 180 ps and a (fixed) pulse separation of about 12 ns. Peak pulse powers of *ca.* 100 W are attainable, with an average power of *ca.* 500 mW.

5.2.2 Synchronously-pumped dye laser

The pulses emerging from the mode-locked Ar^+ laser are unsuitable for our applications for three reasons:

(a) they are of rather long duration,

(b) the repetition rate is fixed at *ca.* 82 MHz, which is too fast for our detection systems (Chapter Six),

(c) the wavelength of the radiation is not continuously tunable.

The use of a dye laser enables problems (a) and (c) to be overcome. By carefully selecting the dye laser cavity length such that its round-trip time matches the separation of the Ar^+ laser pulses, the pulsewidth is decreased from 200ps to the order of a few picoseconds. This mechanism is discussed in

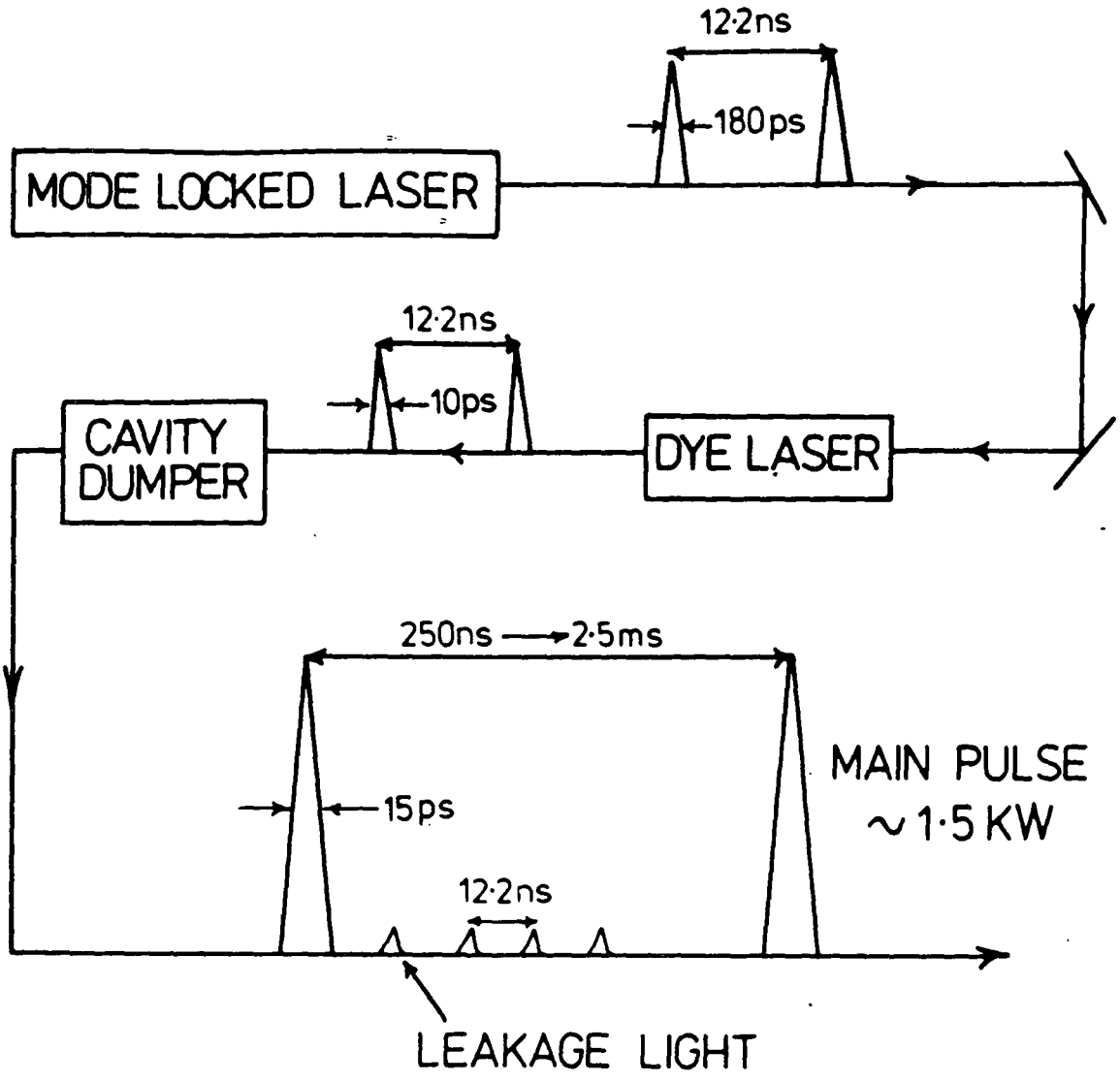

FIGURE 5.1 Schematic diagram of laser system, comprising of a Spectra-Physics model 342 Mode-locked Ar^+ laser, a model 375 dye laser and a 344S cavity-dumper. System performance is indicated briefly on the diagram, and is discussed fully in the text.

Section 5.3.5 below. The broad-band fluorescence of the dye enables tuning of the laser over a range of wavelengths, (560-640 nm for R6G dye), which overcomes problem (c). The pulse separation remains fixed, and the peak power is still *ca.* 100 W.

5.2.3 Cavity-dumper

Insertion of a cavity-dumper into the system is beneficial for two reasons.

(a) The repetition-rate of the pulses may be varied in a stepwise fashion, from single shot to 4 MHz in nine ranges.
(b) The peak power (per pulse) is increased from 100W to several kW, (typically 1.5kW at 800 kHz repetition rate), but the average laser power is decreased to *ca.* 25 mW (800 kHz). Pulse widths remain of the order of 10 ps.

It is worth noting at this point that, alongwith the cavity dumped pulses at the selected repetition rate, the laser also emits a train of pulses, of greatly reduced intensity, at the mode-locked rate (82 MHz). These are referred to as "leakage-light" pulses, and are discussed in detail in Section 5.4.4.

The modular nature of the system allows it to be used in several different configurations, depending upon the application. These configurations are illustrated in Figures 5.2 and 5.3.

It is clear that this system appears to satisfy our criteria for suitability of the pulsed source. However, the results and analysis presented in this thesis show that the system is far from ideal; in particular, the low average

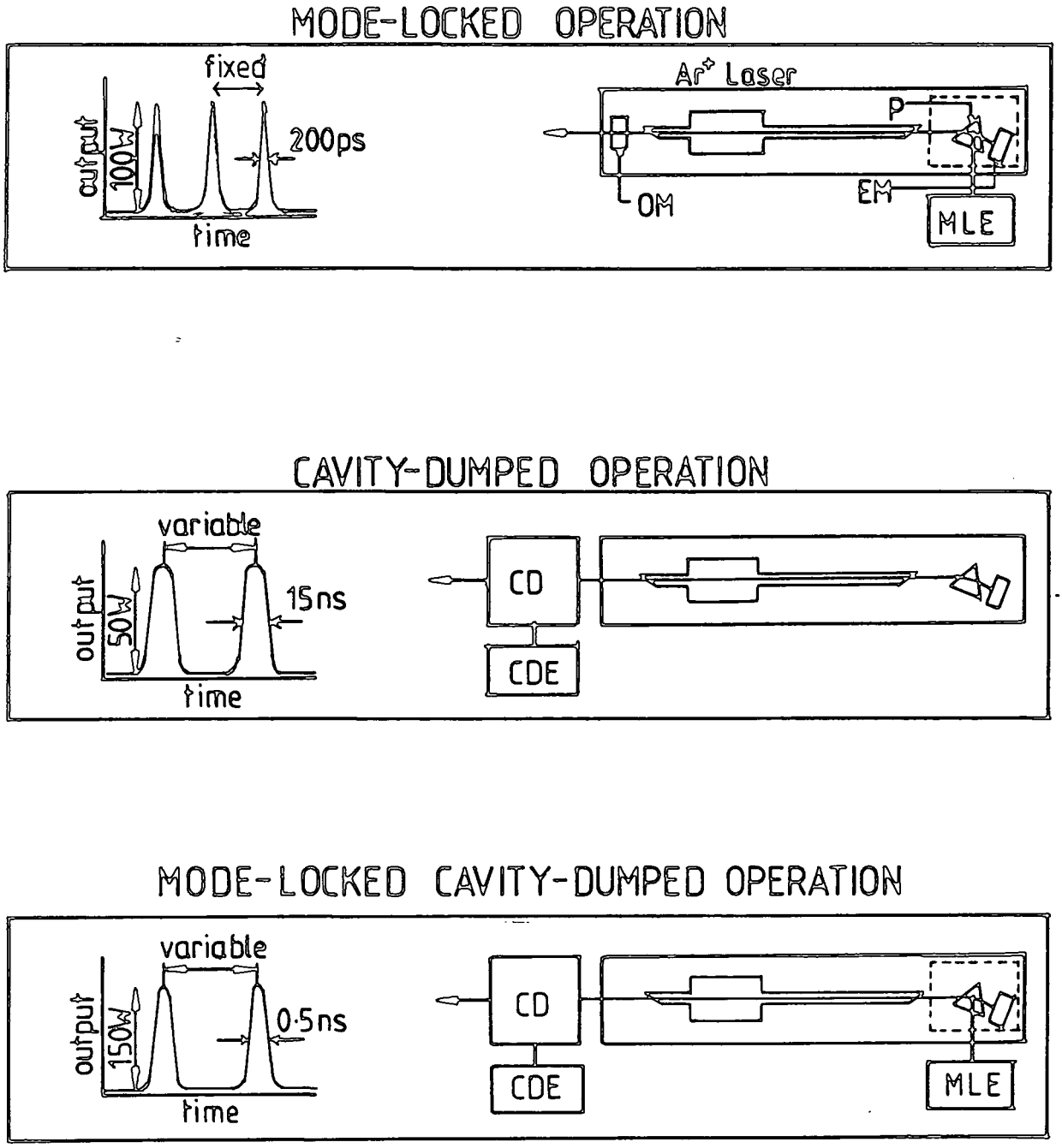

FIGURE 5.2 Mode-locked/cavity-dumped Ar^+ laser configurations. CD = cavity-dumper, CDE = cavity-dumper electronics, EM = end mirror (high reflectance), MLE = mode-locker electronics, OM = output mirror/coupler, P = prism. The cavity-dumped repetition rate is variable from single shot to 4kHz.

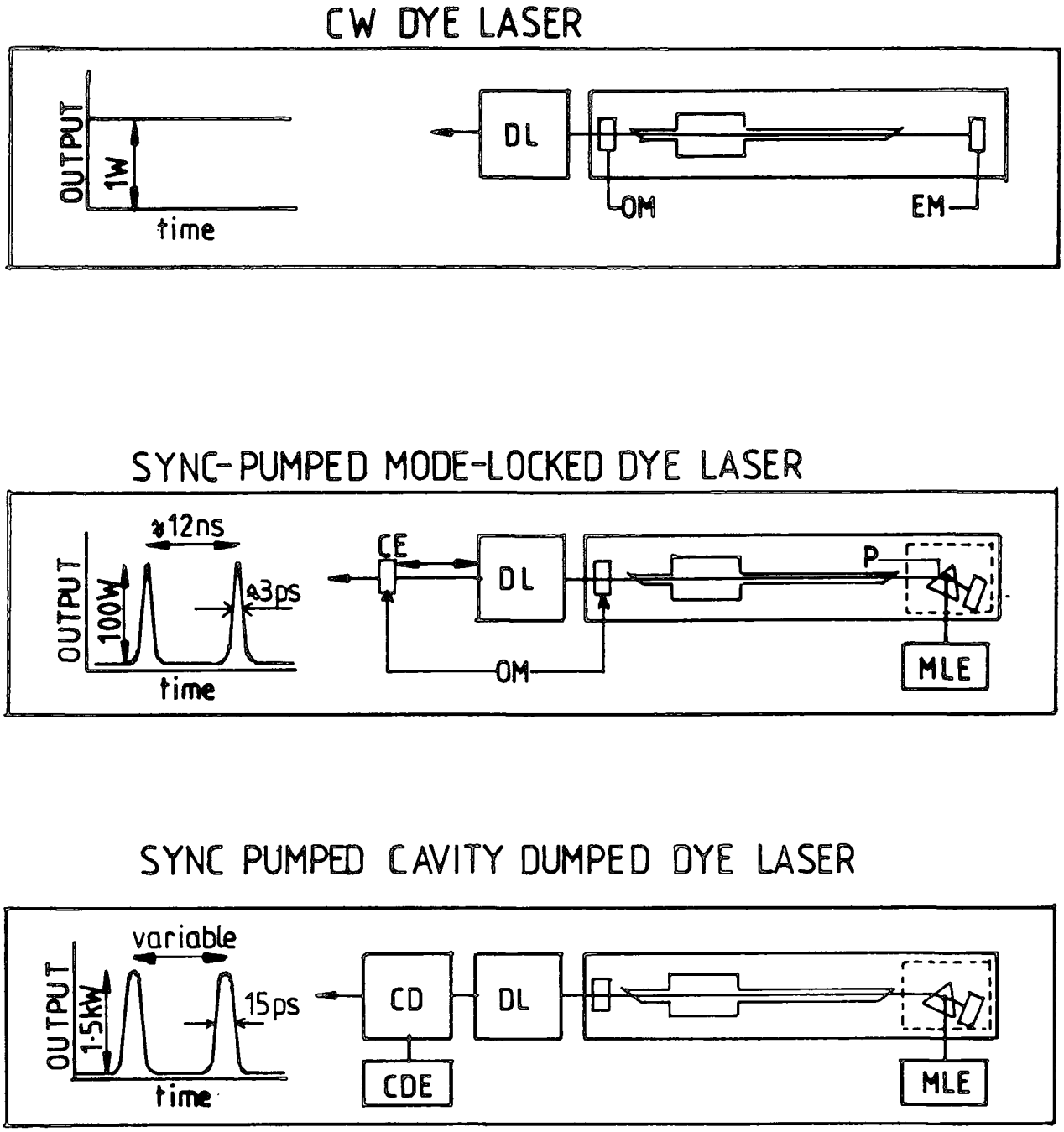

FIGURE 5.3 CW and pulsed dye laser configurations. Specifications depend upon dye type, pump power, lasing wavelength and repetition rate. DL = dye laser, CE = cavity extension. All other symbols were defined in Figure 5.2.

power (compared to cw operation) decreases the Raman signal and R/N (Chapter One) compared to that obtained from a non-fluorescing sample under cw excitation. In practice, the improvement in R/N obtained from time resolved detection is often negated by the low incident laser power. This is particularly critical when the system is operated at the low (4kHz) pulse rate required by the gated diode array detector (Chapter Seven), when the average output power is of the order of 1mW, resulting in a serious degradation in R/N.

It should be remembered that the specifications quoted above will be dependent upon a variety of factors, including ion laser discharge current, dye laser pump power and cavity-dumper repetition rate, and may alter significantly when operating at other repetition rates and pump-powers.

5.3 The physical principles underlying the operation of the pulsed laser system

5.3.1 Multi-mode structure of the single line emission of cw ion lasers

In general, an ion laser cavity is capable of displaying gain over a range of (discrete) wavelengths, each arising from a separate energy transition in the laser medium.[1] For example, the Ar^+ laser oscillates efficiently at both 488.0 and 514.5 nm, and may be operated such that both lines lase simultaneously. Such an output is not useful for most spectroscopic applications, and so a frequency-selective element (usually a prism) is inserted into the cavity in order to restrict the oscillation to a single wavelength. This is commonly referred to as "single-line" operation.

However, even when this is achieved, the output does not consist of a single discrete spectral line, but is actually broadened over a range of frequencies. The minimum possible linewidth is determined by the uncertainty principle or "lifetime broadening", but in practice the major source of broadening in ion lasers is the Doppler effect, where the motion of the ions within the cavity causes slight variations in the frequency of the emitted radiation observed in the laboratory frame of reference.[1] This inhomogenous line broadening is characterised by a Gaussian lineshape, the width (FWHM) of which is specified by equation (5.1).

$$\Delta\nu_0 = 2\nu_0(2kT\ln 2/Mc^2)^{\frac{1}{2}} \qquad (5.1)$$

Here ν_0 is the transition frequency at the band centre, and $\Delta\nu_0$ is the width (FWHM) of the broadened band, k is the Boltzmann constant, T is the absolute temperature, c is the velocity of light and M is the mass of the ion. It may be shown[1] that both spontaneous and stimulated emissions are characterised by the same lineshape when Doppler broadening is the dominant factor, and so the widths of spontaneous and lasing lines are identical.

The frequency of the 514.5 nm line of the Ar^+ laser is *ca.* 6×10^{14} Hz, for which equation (5.1) predicts a Doppler broadening of *ca.* 5 GHz, or 0.001% of the absolute frequency. In comparison, both collisional and lifetime broadening in ion lasers occur in the MHz region[1], and so are negligible in comparison to the Doppler effect. This broadening is small compared to the range of frequencies for which the laser cavity displays gain, and so the overall laser gain profile[1] is identical to the emission lineshape. One might

therefore expect the observed laser line to consist of a simple Gaussian intensity/frequency distribution. However, in order for the system to be in a stationary state, the lasing radiation must be of a wavelength such that a standing wave is formed in the cavity. For a cavity of length L, the lasing frequency must satisfy equation (5.2)

$$\nu_N = Nc/2L \qquad (5.2)$$

where N is an integer.

Therefore, the actual "single line" output of the laser consists of a number of closely spaced cavity modes, separated in frequency by c/2L, and lying within a Gaussian envelope centred upon the transition frequency (Figure 5.4). The intermode spacing of the Ar^+ laser used in this work is *ca.* 82 MHz, so there are about 60 modes oscillating within the FWHM (*ca.* 5GHz) of the gain profile. It is important to note that the modes oscillate independently of each other, *i.e.* with no fixed phase relationship or coherence, so constructive interference does not occur as a result of superposition of the waves.

5.3.2 Mode-locking as a means of pulse formation

It is apparent that if the cavity modes could be forced to assume a fixed phase relationship, then interference between the individual modes would take place to generate a new, periodic waveform. This is known as "mode-locking", (referring to the locking of the phases of the individual modes in a fixed pattern). The consequences of this are best understood through recourse to the equations of the electromagnetic field.

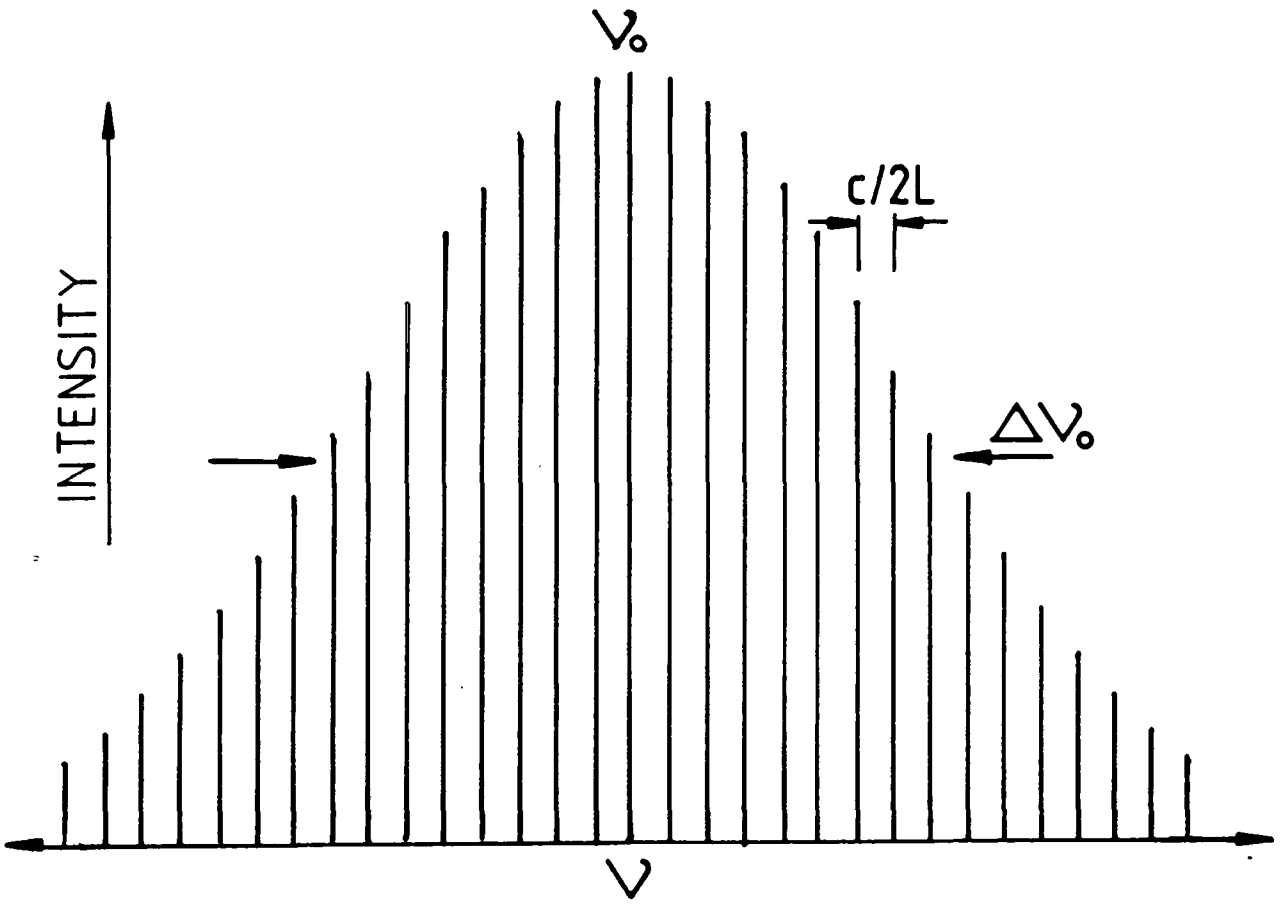

FIGURE 5.4 Inhomogeneously broadened emission lineshape. Several cavity modes, spaced by C/2L, oscillate within the laser gain bandwidth, with a Gaussian amplitude distribution centred upon ν_0. Each cavity mode is not actually a single discrete frequency, but will be homogeneously broadened. This homogeneous broadening is much less than the Doppler broadening, $\Delta\nu_0$.

The electric field E(t) which arises from the superposition of a set of modes, propagating in the positive z direction with no fixed phase relationship, is given[2] by equation (5.3)

$$E(t) = \sum_{-r}^{r} E_r e^{i[\omega_r(t-z/c) + \phi_r]} + C.C. \qquad (5.3)$$

where ω_r is the angular frequency of the r^{th} mode ($\omega_r = 2\pi\nu_r$), ϕ_r is the epoch (phase at t=0) of the r^{th} mode and C.C. denotes the complex conjugate of the summation. From equation (5.2) $\omega_r = \omega_o + r\Delta$, where Δ is the angular intermode frequency separation, $(2\pi c/2L)$, and r may take both positive and negative values. Here r=0 is defined as the central mode (ν_o) of the emission, and the summation extends over values of r sufficient to span the broadened line profile (Figure 5.4). If we assume that it is possible to fix the phase angles ϕ_r at a constant value[1,2] independent of r, then it is possible to always define time t=0 such that ϕ_r=0. Methods for achieving this are discussed below. Under these conditions, equation (5.3) may be recast as:

$$E(t) = e^{i\omega_o(t-z/c)} \sum_{-r}^{r} E_r e^{i[r\Delta(t-z/c)]} + C.C. \qquad (5.4)$$

This can be seen by substituting ϕ_r=0 and $\omega_r = (\omega_o + r\Delta)$ into equation (5.3).

This corresponds[2] to a carrier wave of frequency ω_o, which is amplitude modulated with an envelope which depends upon the values of E_r. The modulation envelope travels with the speed of light, and is periodic with period $T = 2\pi/\Delta = 2L/c$. Therefore, the effect of phase locking the individual modes is to generate pulses of light (of frequency ω_o) which are separ-

ated in time by 2L/c, the reciprocal of the intermode frequency spacing. This is the round-trip time for light circulating in the cavity.

The width of the envelope is approximately the reciprocal of the frequency range over which the E_r have appreciable amplitudes, and so wide gain bandwidths are necessary in order to achieve narrow pulses. In other words, oscillation over a large number of modes is required. This is to be expected from the general properties of Fourier pairs;[3,4] a narrow signal in the time domain requires a wide range of frequency components for it's synthesis.

It can be shown[1] that in the case of a Gaussian mode amplitude distribution, of width $\Delta\omega$, the limiting pulsewidth is given by $0.441/\Delta\omega$. Therefore, the transform-limited pulsewidth of a laser, operating with a single line of *ca.* 5GHz breadth, is of the order of 90 ps, and in order to obtain shorter pulses one needs to use a laser medium with a wider gain profile (*e.g.* a dye laser).

Although the consequences of mode-locking the laser output are easy to appreciate, it is not altogether obvious how phase locking may be achieved in practice. Mode-locking is commonly induced through the use of an acousto-optic modulator; the operation of these devices is briefly summarised below.

5.3.3 Principles of acoustooptic modulation

Acoustooptic modulation arises from the interaction of optical and acoustic waves in a suitable medium, and results in the transfer of momentum between photons and phonons. Adler[5] has given an excellent introductory review upon the inter-

action between light and sound, and much of the discussion below is based upon the contents of his paper.

5.3.3.1 Interaction of optical waves and travelling acoustic waves

The basic source of the acoustooptic interaction is provided by the change in refractive index "n" which occurs when a periodic compressional wave moves through a medium. Modulation of "n" results in a modulation of the velocity (and wavelength) with which an optical wave propagates through a material. This causes a phase modulation of the optical wave which is traversing the medium. Fourier analysis[3,4] of a phase-modulated sinusoidal wave (of frequency ω_o) shows that the wave is composed of a carrier wave at the original frequency ω_o, plus sidebands of frequency $\omega_o \pm \omega_m$ (where ω_m is the frequency of modulation), which are generated in phase with the acoustic wave. The amplitudes of the carrier and sidebands are determined by the amplitude of the modulation, and it is possible to arrange the modulation such that all of the light is carried in the sidebands.

It can be shown[5] that if a light beam is incident upon a slab of material, *e.g.* a quartz crystal, which is being subjected to a compressional wave travelling perpendicularly to the optical beam (Figure 5.5), then the optical carrier wave proceeds straight on in the original direction, but the sidebands are deflected from the original path through an angle of *ca.* $\pm\lambda_o/\Lambda$, where λ_o and Λ are the optical (vacuum) and acoustic wavelengths respectively. (The angle of scattering <u>within</u> the crystal itself is $\pm\lambda/\Lambda$, where λ is the wavelength of light in the <u>unstressed</u> crystal. This angle is increased to *ca.* $\pm\lambda_o/\Lambda$ by refraction upon leaving the crystal). This is

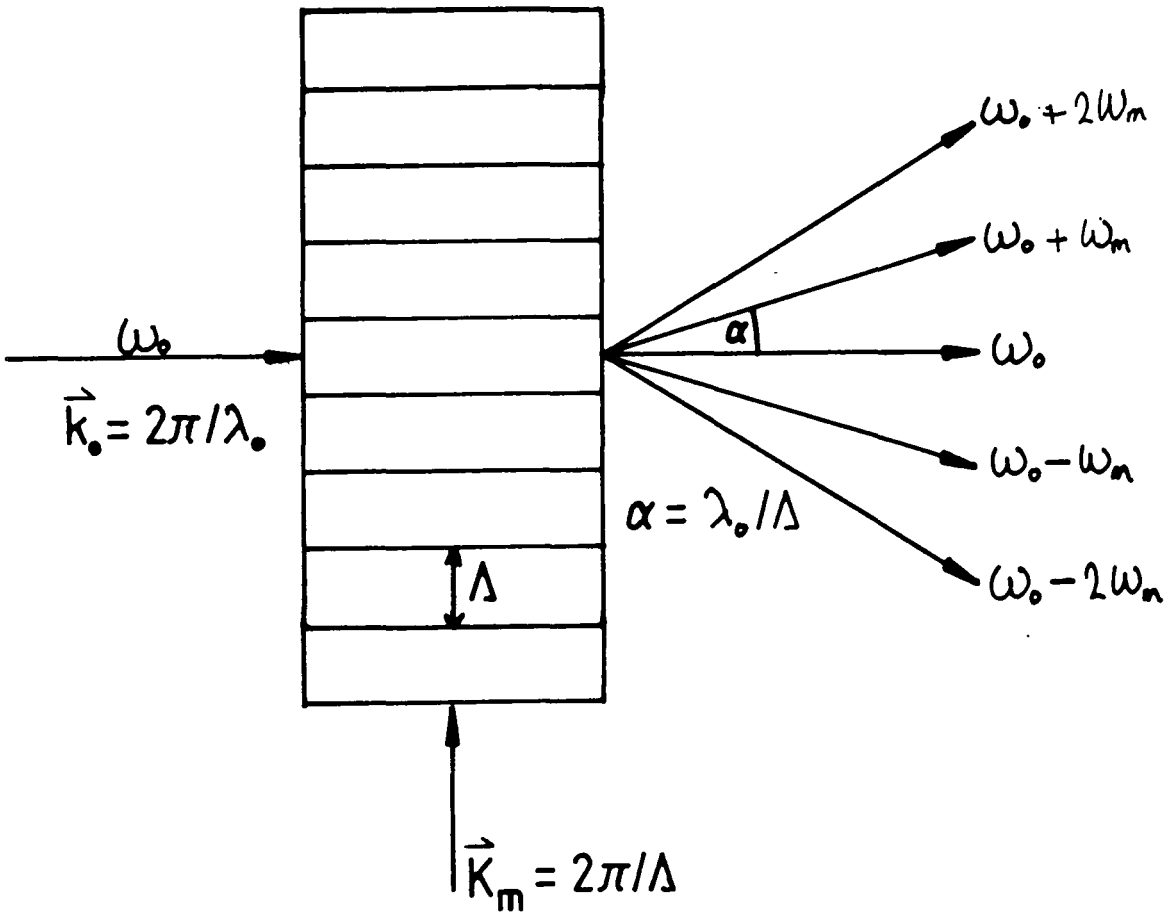

FIGURE 5.5 The Debye-Sears effect. Interaction between an optical wave (wavevector $\vec{k}_o=2\pi/\lambda_o$) and a travelling acoustic wave ($\vec{k}_m=2\pi/\Lambda$). Sidebands are scattered with frequency shifts of $\pm\omega_m$, $\pm 2\omega_m$, *etc*, at angles of *ca*. $\pm\lambda_o/\Lambda$, $\pm 2\lambda_o/\Lambda$, *etc*.

known as the Debye-Sears effect.[6] The acoustooptic device acts in a manner similar to that of an optical diffraction grating, except that it can be arranged that no light is scattered into the zeroth order (*i.e.* the carrier amplitude is zero).

It is found that the light which is scattered with a component along the direction of the acoustic wavevector $\vec{K}_m$, (Figure 5.5), is the sideband of frequency $\omega_o+\omega_m$, while the sideband of frequency $\omega_o-\omega_m$ is scattered with a component antiparallel to $\vec{K}_m$. The intensity of the carrier and sidebands remains constant as long as the acoustic excitation is maintained.

5.3.3.2 Interaction between optical waves and standing acoustic waves

An interesting modification of this effect occurs if, instead of using a travelling compressional wave, a standing wave of frequency ω_m is set up in the crystal. This results in alternating regions of compression and rarefraction, each occupying a length of $\Lambda/2$ in the crystal, which are interchanged twice during each period of the acoustic wave. Instead of the steady-state situation which existed before, where the crystal was continuously strained and therefore always diffracting light, it is obvious that there is now a situation where all strains (compressions or rarefractions) within the crystal disappear twice during each period of the standing wave. When this occurs the light may pass through the crystal without being diffracted; at all other times, the beam will be scattered from its original direction to a certain extent.

The net effect is to create an optical shutter which allows free transmission of a light beam at twice

the frequency of acoustic modulation. If such a device is placed inside a laser cavity, it enables one to modulate the cavity losses at twice the resonant frequency of the crystal; this is in fact a common method of mode-locking a laser (Section 5.3.4).

5.3.3.3 The Bragg Cell

Before going on to relate the use of acoustooptic modulation in mode-locking lasers, we will consider one final application of the acoustooptic effect, namely the construction of a Bragg cell. It can be shown that the effectiveness of the modulator discussed above is limited by the path length of the optical beam through the crystal,[5] such that the width of the crystal must be small compared to $\Lambda^2/2\pi\lambda_o$. When this width is exceeded, destructive interference occurs and the intensity of the diffracted beam is zero. While this does not affect the use of the device as an optical shutter, serious problems arise when it is desired to actually use one of the diffracted beams.

This difficulty may be overcome by rotating the crystal such that the incoming beam makes an angle $\lambda_o/2\Lambda$ with the acoustic wavefronts (Figure 5.6). Under these conditions, the first order diffracted beams are not destroyed by destructive interference, whereas the higher order diffracted beams are. The carrier wave is undeflected. The reason for this is clear from Figure 5.6; the scattering process is analagous to the Bragg diffraction condition for radiation of wavelength λ from a set of crystal planes separated by the acoustic wavelength Λ. The choice of angle $\lambda/2\Lambda$ merely satisfies the Bragg diffraction equation:

$$\sin \alpha = \lambda/2\Lambda \qquad (5.5)$$

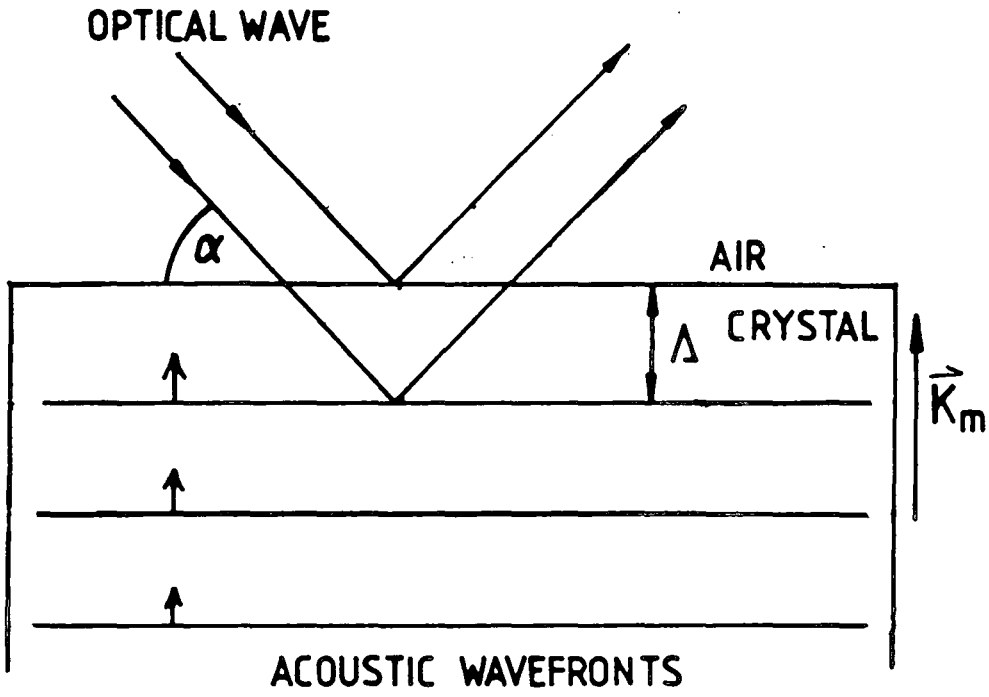

FIGURE 5.6 Bragg reflection of light from moving acoustic waves of wavelength Λ. The Bragg diffraction condition $n\lambda = 2\Lambda\sin\alpha$ must be satisfied for constructive interference to occur. Refraction at the air/crystal boundary modifies this condition to $n\lambda_o = 2\Lambda\sin\alpha$ when observing the rays outside the crystal. This refraction is not indicated on the diagram.

for the limit $\alpha \to 0$, and is simply the necessary condition for observing diffraction into the first order.

The interaction may alternatively be represented[7] on a vector diagram in momentum space (Figure 5.7). A photon of frequency ω_o (wavevector $\vec{k} = 2\pi/\lambda_o = \omega_o/c$) interacts with a phonon of wavevector $\vec{K}_m(2\pi/\Lambda)$, resulting in the creation or annihilation of a phonon. If the former process occurs, the scattered photon loses energy, $(\omega_o - \omega_m)$, whereas the latter process enhances the frequency of the scattered photon $(\omega_o + \omega_m)$. The photon is scattered in a direction such that momentum is conserved in the collision.

5.3.4 Practical attainment of mode-locking

Here we will only discuss mode-locking by modulation of cavity losses, *i.e.* amplitude modulation (AM) of the cavity modes, since this is the strategy used in the Spectra-Physics system. Mode-locking may also be achieved by modulating the frequency of the cavity modes, or by placing a saturable absorber in the cavity; further details are given elsewhere.[1,2,8,9]

Mode-locking can be explained by considering laser operation in either the time or frequency domain. Consideration of the time development of the oscillation is perhaps the more physically enlightening explanation and so will be treated first.

The construction of a fast optical shutter, based upon the Debye-Sears effect, has been described in Section 5.2.3. Typically, the device consists of a fused quartz block or crystal, which is coupled to a piezo-electric transducer driven by

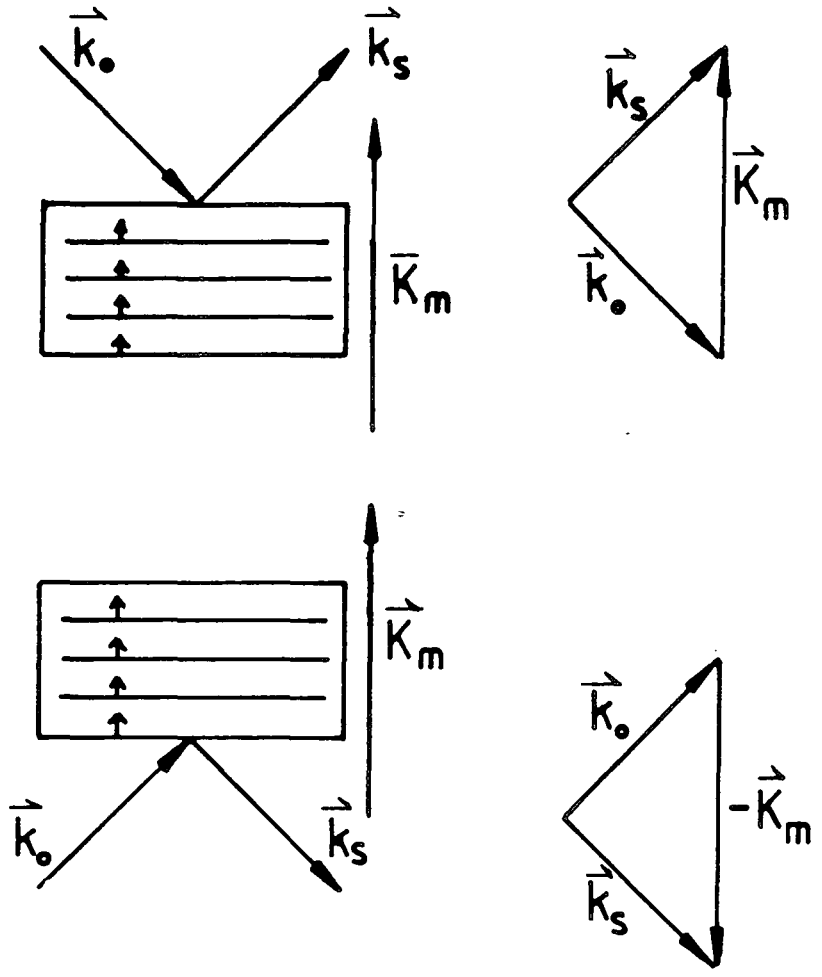

FIGURE 5.7 Momentum-space representation of acoustooptic interaction.

(a) Interaction of photon with incident wavefront yields a scattered photon with higher momentum ($\vec{k}_s = \vec{k}_o + \vec{k}_m$).

(b) Interaction with receding acoustic wave yields a scattered photon of lower momentum ($\vec{k}_s = \vec{k}_o - \vec{k}_m$).

a radio frequency supply. The transducer is driven at a frequency which generates a standing acoustic wave in the crystal, and the crystal dimensions are such that the frequency of the standing wave is approximately c/4L, *i.e.* 1/2 the mode frequency separation. Light passes freely through the block twice per acoustic period, since the "shutter" opens at twice the modulation frequency, *i.e.* c/2L. Therefore, the shutter "openings" are separated by 2L/c, *i.e.* the round-trip time of light in the cavity. In practice, the cavity length L may be adjusted in order to ensure that the acoustic resonance of the crystal exactly matches c/4L.

The device is placed in the laser cavity close to one of the end-mirrors, such that the sidebands will be diffracted off the laser axis and will not oscillate. The carrier wave is not deflected and is returned to the cavity to continue lasing. Since the period of shutter "opening" matches the round trip time of the cavity, a circulating pulse of light develops within the cavity, and arrives at the acoustooptic device so as to coincide with the period of maximum transmission. Obviously, the pulses are separated by 2L/c, the round-trip time of the cavity, in accordance with equation (5.4). This technique was first demonstrated by Hargrove *et al*,[10] who mode-locked the 633 nm line of a He-Ne laser to produce *ca.* 2.5 ns pulses.

The time domain description given above is unsatisfactory for several reasons; it does not indicate the expected pulse duration or powers, and it assumes that the shutter is either open or closed, *i.e.* no allowance is made to account for the variation of carrier amplitude during the acoustic cycle. Furthermore, it does not explain how the phase locking condition

arises other than in an inverse manner, namely that a periodic train of pulses in the time domain may be considered as arising from superposition of a set of harmonics with a fixed phase relationship, and *vice versa*.

The behaviour of the laser may also be analysed in the frequency domain.[1,2,8,11] It is clear that the cavity modes are amplitude modulated (at a frequency c/2L) on passing through the acoustooptic cell. The r^{th} AM cavity mode may be Fourier analysed as a carrier wave of frequency ω_r, plus sidebands at frequency $\omega_r \pm \omega_m$ where ω_r and ω_m are the mode and modulation frequencies respectively. If the modulation frequency matches the separation of the individual modes (*i.e.* $\omega_m = c/2L$) the sidebands of mode r actually overlap with the adjacent mode frequencies ω_{r+1} and ω_{r-1}, and this occurs over the whole oscillating bandwidth. Modes which oscillate within the same homogeneously broadened[1] linewidth are actually competing for the same atomic population, and are strongly coupled together.[8]

The interaction of sidebands with adjacent cavity modes results in a definite phase relationship between the modes, and so the superposition described by equation (5.4) can occur. A full mathematical treatment of AM mode coupling has been given by Yariv,[11] but the important result for our purposes is that modulation of the cavity losses, at a frequency c/2L, induces coupling and a constant phase relationship between all modes, thereby producing a train of pulses separated in time by 2L/c.

5.3.5 Pulse shortening mechanisms in the dye laser

5.3.5.1 Criteria for pulse shortening

The pulses obtained from a mode-locked laser are unsuitable for our TRFR system because they are

(a) too long, and (b) of fixed wavelength. If the mode-locked output is used to pump a dye laser, we find that the dye laser becomes mode-locked, and that under certain conditions, drastic pulse shortening may occur. The design and theory of operation of dye lasers (both cw and pulsed) is a broad and complex field, and only those features especially relevant to pulsed operation will be discussed here. The reader is referred to the literature for a more comprehensive treatment.[1,12,13]

In order to obtain very short pulses, we require the superposition of a large number of cavity modes, and this in turn demands that the gain profile is as wide as possible (Figure 5.4). Doppler and collisional broadening of emission from the Ar^+ ions is only of the order of GHz, which limits the pulsewidth to *ca.* 100 ps (Section 5.3.2). However, the energy levels of organic molecules (such as laser dyes) in solution are broadened by rotational, vibrational and collisional interactions; a 50 nm broadening in an optical absorption/emission line centred at *ca.* 600 nm would be typical of this effect.[12,14] This is equivalent to a frequency broadening of *ca.* 10^{13} Hz, *i.e.* 10000 times the breadth of an atomic line.

Under broadband operation, the variation of laser output power with frequency does <u>not</u> match the dye gain profile, *i.e.* a laser with a broadband optical cavity does not oscillate with a bandwidth equal to that of the dye emission.[12,14] The process of mode-competition[14] results in most of the emission occurring through the modes near the gain maximum, and it is found that the lasing bandwidth is about 2 nm. This corresponds to a breadth of *ca.* 50 cm^{-1} at 600 nm, which is too wide to be a useful source of excitation for Raman spectroscopy.

In order to obtain a tunable, narrow band output it is necessary to insert a frequency-selective element into the dye laser cavity. Early experimenters[15] used a diffraction grating to tune the output, but the system used in our work has a two plate birefringent filter (Section 5.5) as the tuning element. Ideally, this yields an output linewidth of *ca.* 60 GHz (0.07 nm, or *ca.* 2 cm^{-1} at 600 nm central emission). This corresponds to a tenfold increase in the number of modes available for locking compared to the Ar^+ laser.

Therefore, even when the linewidth is sufficiently narrow for use as a Raman source, the lasing bandwidth is sufficient to produce a tenfold reduction in pulsewidth compared to ion lasers, and so the lower limit on pulsewidth is decreased to *ca.* 10 ps. The gain bandwidth of the laser dye enables these transform-limited pulses to be tuned over a range of more than 50 nm. One further benefit of the tuning process is that the power which is distributed over the entire 2 nm bandwidth of the broadband emission is almost totally delivered into the 0.07 nm bandwidth of the tuned output. The mechanism for this transfer is denoted "spectral condensation" and is described in the review by Shank.[13]

5.3.5.2 Synchronous pumping of dye lasers

Although it is clear that the dye laser oscillates with a sufficient number of cavity modes to produce very narrow mode-locked pulses, the cavity lengths of the dye and Ar^+ lasers must be carefully matched in order to achieve the optimum pulse width.[16] This involves extending the cavity of the dye laser (normally *ca.* 35 cm for cw operation) to around 1.8m, and is illustrated in Figure 5.8. The pulses

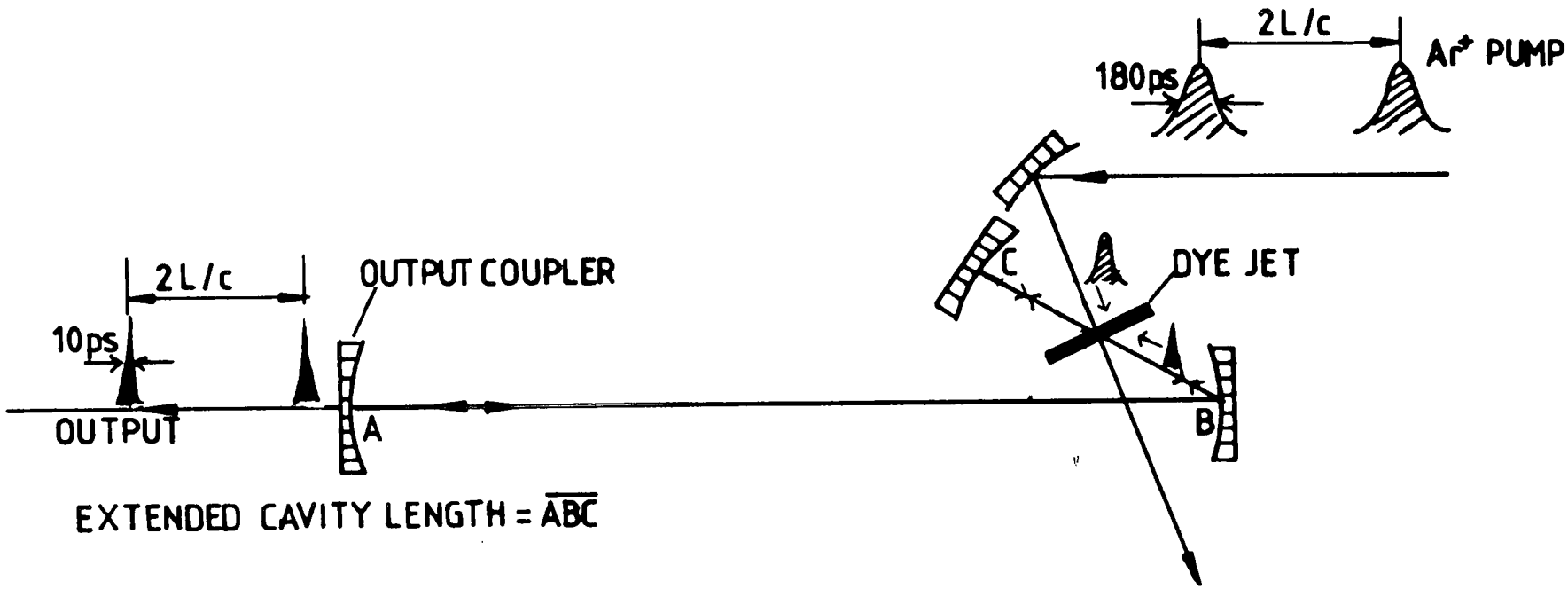

FIGURE 5.8 Pulse shortening mechanism in a synchronously pumped dye laser. The dye laser cavity length is extended and matched to that of the mode-locked Ar^+ laser (L), such that the round trip time (2L/C) matches the Ar^+ pulse separation. The Ar^+ pulse electronically excites the dye molecules, which are then deactivated in a few ps by the synchronous arrival of the pulse circulating in the dye cavity, which causes stimulated emission.

from the Ar^+ laser (separated by 2L/c), pump and excite fluorescence from a thin stream of dye solution. The dye jet is situated near one end of the cavity, which has been adjusted in length so that its round-trip time matches the separation of the mode-locked 514.5 nm pulses.

The birefringent filter passes a narrow bandwidth of the fluorescence emission from the dye, which will lase provided that the standing wave condition (equation 5.2) is satisfied. Since the Ar^+ laser pulse is much shorter than the round-trip time of the dye laser cavity, one might expect the dye pulse to have roughly the same temporal characteristics as the pump pulse, *i.e. ca.* 200 ps width. In practice the dye laser pulses are observed to be shortened to 10 ps or less.[16-19]

This may be understood when one remembers that the round-trip time of the extended dye laser cavity matches the mode-locked Ar^+ pulse separation. The fluorescence emission, which was stimulated by the absorption of one 514.5 nm pulse, completes one round trip of the cavity just as the next pump pulse arrives at the dye stream. The dye molecules which have been pumped into an excited state by the Ar^+ laser pulse are then rapidly deactivated, as a result of the stimulated emission which occurs upon the arrival of the pulse which is circulating in the dye laser cavity. This deactivation is very efficient and results in a very short laser pulse,which then circulates within the cavity to arrive back at the dye jet to repeat the process. This yields a train of picosecond-duration output pulses separated in time by 2L/c.[16-19] The technique of matching the arrival times of the Ar^+ and dye laser pulses is known as synchronous pumping, for obvious reasons.

This process is efficient because of the high cross sections for stimulated emission (σ_e) which are characteristic of laser dyes. Typicall, $\sigma_e \simeq 10^{-16} cm^2$ (Chapter Three). Pulse shortening in an ion laser is not so effective because of the much lower cross sections ($10^{-19} cm^2$), resulting in lower rates of stimulated emission. A high σ_e arises as a result of broadened energy levels (Chapter Three), which is in good agreement with the rationalisation of pulsewidths based purely on consideration of the bandwidth of oscillation (Section 5.3.2 above).

Sync-pumping a dye laser provides a mode-locked train of tunable, short pulses at a fixed repetition rate (that of the ion laser). It is highly desirable that the repetition rate should be variable to some extent, and this is achieved through the use of an acoustooptic device known as a cavity dumper.

5.3.6 Acoustooptic cavity-dumping

Cavity dumping[20,21] refers to the process of deflecting a circulating optical pulse out of the laser cavity at a selected repetition rate. This yields output pulses of much higher peak power than does a simple synchronously-pumped dye laser, where the power is governed by the transmission efficiency of the output coupler. The cavity dumper is based upon a Bragg cell, the operation of which has been described in Section 5.3.3.

Figure 5.9 is a schematic diagram of a cavity dumped laser.[20] The light circulating in the cavity is represented by $E_o(s,t)\cos(\omega_o t)$, where $E_o(s,t)$ describes the pulse shape at a position s along the optical path. $E_o(s,t)$ is assumed to

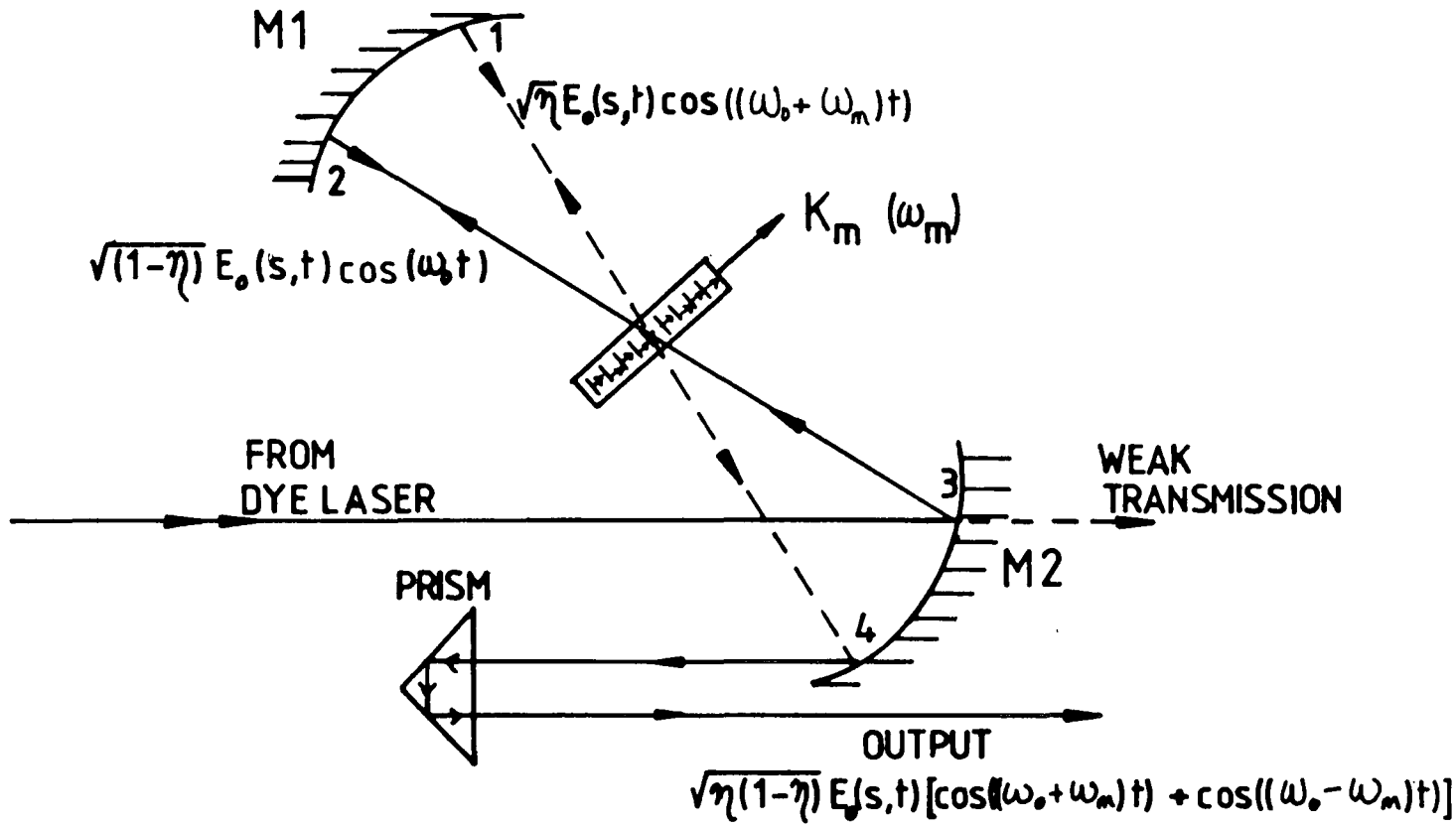

FIGURE 5.9 Schematic of Bragg cell operation. See text for details. Note the weak transmission of mode-locked pulses throygh mirror M2 (Section 5.3.3.1).

vary slowly compared to the optical frequency ω_o. The light passes through a Bragg cell, where it encounters an advancing acoustic wave of frequency ω_m, and part of the beam is diffracted and frequency upshifted. If the diffraction efficiency is η (intensity diffracted/incident intensity), the amplitude of the diffracted beam (first pass) is given[21] by equation (5.6)

$$E_1(t) = \sqrt{\eta}\, E_o(s,t)\cos(\omega_o+\omega_m)t \qquad (5.6)$$

The diffracted portion of the beam travels the path to M1 (point 1) where it is reflected back on itself for another pass through the Bragg cell. Part of the beam is again diffracted and is deflected by mirror M2 (point 3) back into the cavity. The undiffracted part is reduced in intensity by $\sqrt{1-\eta}$, and travels to M2 (point 4) where it is deflected onto an output prism to form <u>part</u> of the output beam, with amplitude $\sqrt{\eta\ (1-\eta)}E_o(s,t)\cos(\omega_o+\omega_m)t$.

The portion of the original incident beam which was <u>not</u> diffracted on the first pass travels to M1 (point 2) and is reflected back into the Bragg cell. Here it encounters a <u>receding</u> acoustic wave and so diffraction results in a frequency <u>downshift</u> to $\omega_o-\omega_m$. The amplitude of this beam is given by equation (5.7)

$$E_2(t) = \sqrt{\eta(1-\eta)}\ E_o(s,t)\cos(\omega_o-\omega_m)t \qquad (5.7)$$

This beam is reflected off M2 and combines with the other diffracted beam to form the output, with amplitude:

$$E_T(t) = E_o(s,t)\sqrt{\eta(1-\eta)}\,[\cos(\omega_o+\omega_m)t + \cos(\omega_o-\omega_m)t] \qquad (5.8)$$

Johnson[21] has shown that the <u>intensity</u> of the output beam is then given by equation (5.9), *i.e.* the intensity is modulated at <u>twice</u> the drive frequency of the Bragg cell.

$$I(t) = 2\eta(1-\eta)E_o^2(s,t)(1+\cos 2\omega_m t) \qquad (5.9)$$

In order to obtain equation (5.9) the expression for $(E_T(t))^2$ must be averaged over an optical cycle to remove terms in ω_o.

Clearly, the transmission of the light pulse depends upon its time of arrival at the Bragg cell with respect to the phase of the modulation function (Figure 5.10(a)). A pulse which coincides with the peak of the modulation function is deflected out of the cavity into the output beam. Careful adjustment of the phase of the modulation function with respect to the cavity pulse is necessary to achieve optimum output.

The selection of the rate of cavity-dumping is controlled by pulsing the rf supply to the Bragg cell such as to coincide with the arrival of the desired optical pulse (Figure 5.10(b)) since, when no acoustic waves are present, the diffraction process does not occur and no light is deflected from the cavity. The rf burst is *ca.* 14 ns wide, which means that two mode locked pulses, (*ca.* 12 ns separation), will always fall inside the rf power envelope. The system is configured to prevent the dumping of both pulses, by fixing the modulation frequency of the Bragg cell, $2\omega_m$ (equation (5.9)), at (n+1/2) times the mode-locked pulse frequency, where n is an integer. This ensures that when one mode-locked pulse is at the peak of the modulation function, the adjacent peak automatically arrives at a trough and is suppressed (Figure 5.10(a)). The other mode-locked pulses fall outside the rf pulse and are automatically suppressed.

In fact, Figure 5.10(b) is a rather idealised description of the cavity-dumper operation. From the discussion

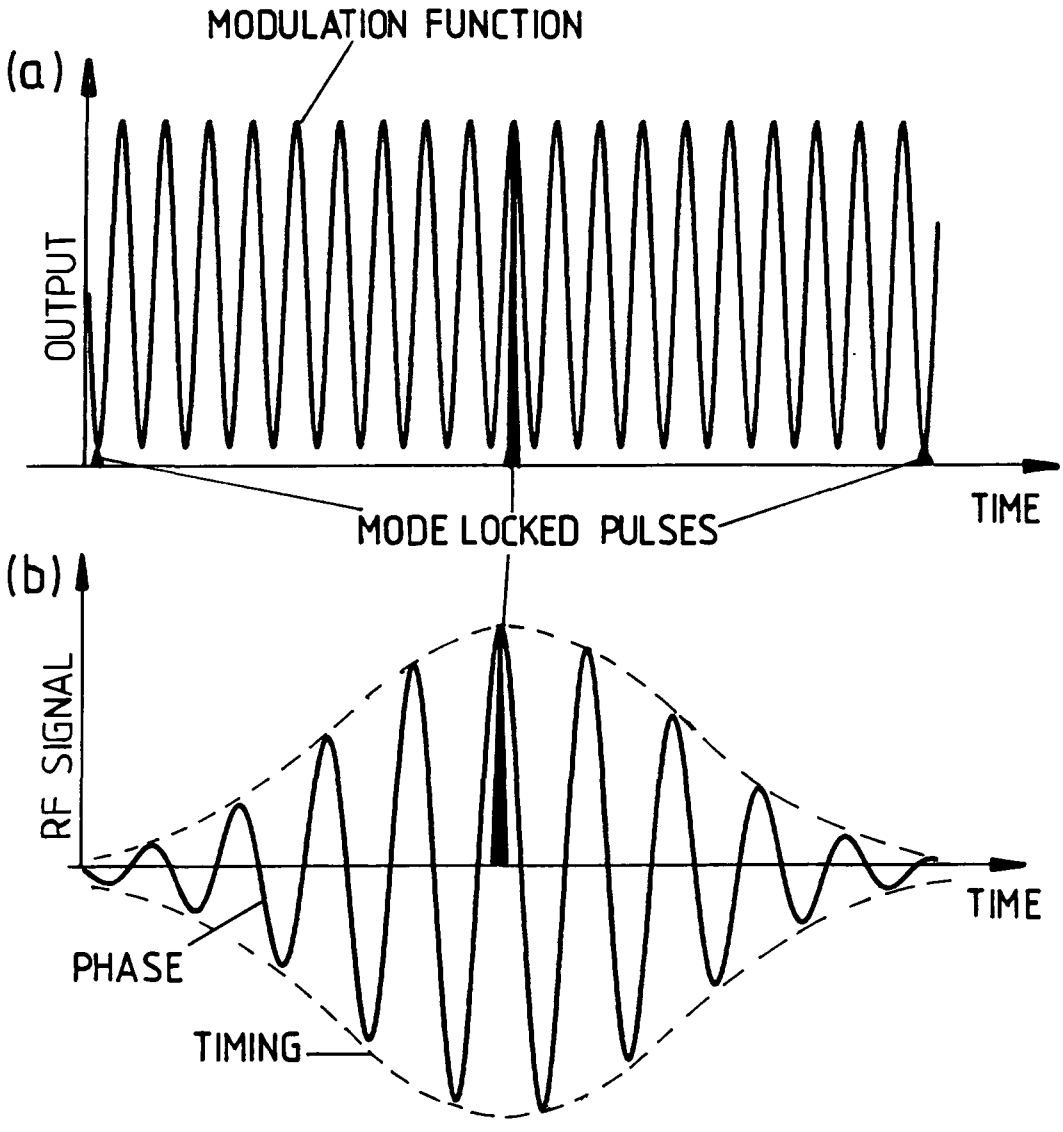

FIGURE 5.10 Temporal characteristics of cavity-dumping.

(a) Integer + ½ timing. When a mode-locked pulse is coincident with a maximum of the cavity-dumper transmission function, it is deflected out of the cavity. The frequency of modulation of the transmission ($2\omega_m$) is 9½ times the mode-locked pulse frequency - therefore pulses adjacent to the main pulse arrive at transmission minima.

(b) To select pulse dumping rates, the rf supply to the Bragg cell is pulsed. The phase of the rf signal (relative to the mode-locked pulse) and the timing (position of the rf envelope) may be adjusted for maximum output and extinction ratio (see text).

above, we would expect the cavity-dumper output to consist of two adjacent pulses, (one very much more intense than the other), at the selected repetition rate. In practice, suppression of the other mode-locked pulses is not complete, and we have observed[22-24] that the cavity dumped output consists not only of the main pulses at the selected repetition rate, but also the mode-locked pulse train (albeit with a greatly diminished intensity). This implies that the modulation function (and hence rf power) is actually nonzero outside the idealised rf envelope, and has important consequences for the laser performance, particularly at low repetition rates. This is discussed in Section 5.4.4.

The direct dumping of power out of the cavity results in higher peak powers than are obtained from a simple sync-pump dye laser, where the output power is governed by the transmission of the output coupler. Also, the desired repetition rate may be selected merely by varying the repetition rate of the rf pulse to the Bragg cell. This is valuable for the study of processes which are long-lived compared to the Ar^+ pulse spacing, or when the detection electronics are limited to slower data acquisition rates.

5.3.7 Conclusions

The laser system is a complex apparatus, which relies upon state-of-the-art technology in order to function satisfactorily. The sections above have presented the basic physical principles of the operation of the system, including the mechanisms of mode-locking, pulse formation and shortening, and cavity dumping, at a level sufficient to appreciate not only how the system works, but also the fundamental limitations (both physical and technical) of its performance.

The following section will consider the actual practical performance and assessment of the system, with particular emphasis being placed upon operational aspects and problems which are not detailed in the manufacturer's literature, but which can seriously degrade the system performance unless suitable precautions are taken.

5.4 System performance and diagnostics

5.4.1 General considerations

There are several parameters to be considered when judging the performance of the laser system. These include, for example, the width, shape, power and reproducibility of the laser pulses, as well as the average power of the beam and its stability with time. While average power levels are easily measured, the properties of individual pulses are more difficult to assess. For the purposes of our work, the exact width and shape of the laser pulse are not important, provided that the width is less than *ca.* 100 ps. If this criterion is satisfied, the pulses constitute impulse inputs to the detectors (Chapters Six, Seven, Eight), and so the exact pulse shape is irrelevant. Of course, other applications may demand much better characterisation of the pulses. The power of each pulse is actually the most important factor in determining the performance of our system, assuming that the pulses are effectively impulse excitations with respect to the timing electronics.

The manufacturer's literature provides guidelines upon optimising the laser performance and checking the output. Unfortunately, the system specifications are not quoted over the whole range of selectable repetition rates, even for fundamental

quantities such as average output power. Specifications tend to be limited to the 800 kHz cavity-dumped rate. When one has access to sophisticated pulse-measuring apparatus (see below) this is not important, but when only basic system diagnostics are available, this is a fundamental difficulty, and there is always the doubt that the performance is not optimised. In addition, we have found that some of the manufacturer's system diagnostics and optimisation procedures are misleading, and can result in a severe degradation in system performance when implemented! This is discussed in detail in the following sections.

5.4.2 Ar^+ laser optimisation

Characterisation of the mode-locked ion laser output is relatively straightforward. The laser pulses were directly observed using a Spectra-Physics model 403B fast-photodiode, and a Tekronix 7904 oscilloscope with a 7S11 plug-in sampling head. The diode has a fast rise time (<50 ps) and as such gives a reasonable representation of the mode-locked laser pulse (*ca.* 200 ps width). This is sufficient to observe the pulse shortening and amplitude changes which occur while the cavity length is adjusted.

Ruddock and Illingworth[25] pointed out that this procedure is not adequate when it is necessary to measure the exact pulse shape, for instance in time-resolved fluorescence measurements. The best method would be the use of a synchronous-scan streak-camera, which is capable of picosecond resolution, but this would be too expensive to be used simply for optimisation of the laser. It is, nevertheless, the only method which gives a direct, accurate measurement of the laser pulse shape. Rapid-scanning second-harmonic autocorrelation[26,27] is not an ideal technique, because interpretation of the data

involves a prior assumption of the form of the pulse shape. Also, there is some difficulty in generating the second harmonic of the 514.5 nm line.[25]

A novel method of optimising the Ar^+ cavity length to yield the shortest pulses was suggested,[25] based upon measurement of the plasma tube discharge current required to maintain a constant output power as the cavity length is adjusted. The discharge current was found to peak in the region of shortest mode-locked pulses, and enabled cavity length optimisation to better than 100μm. Although this provides no information upon pulse shape, it does allow attainment of the shortest pulses on a routine basis, and so might be useful as a general optimisation technique prior to synchronously-pumping a dye laser, or when the exact pulse shape is not of interest.

5.4.3 Cavity-dumped dye laser optimisation

Optimisation of the cavity-dumped pulses is more difficult than the Ar^+ output, because the pulses are an order of magnitude shorter. Second-harmonic autocorrelation is the most common means of determining pulsewidths, and probably represents the most useful routine optimisation technique. Unfortunately, an autocorrelator was not available on a regular basis during the course of this work, and so other system diagnostics had to be employed.

Spectra-Physics[20] recommend three basic diagnostics as a guide to optimising the laser output. These are the average output power, the "extinction ratio", and the variation in output power as the "phase and timing" of the rf signal to the Bragg cell are adjusted. The latter two factors need some explanation.

5.4.3.1 Extinction ratio

Figure 5.10 illustrates the operation of the cavity dumper, and shows how the pulses adjacent to the main dumped pulse arrive at a minimum of the modulation function. If the output of the cavity dumper is observed with the photodiode and oscilloscope, it is possible to observe the main and adjacent pulse intensities simultaneously. The extinction ratio is defined as the ratio of the intensities of the main and adjacent pulse, with a value of 500:1 being quoted as being representative of a well aligned system.

We have found this diagnostic unsatisfactory for two main reasons. Firstly, the time-resolution of the photodiode is insufficient to yield an accurate representation of the cavity dumped pulses, and it seems highly unlikely that the intensity ratio obtained by this technique is in fact accurate. We believe that the technique described in Section 5.4.4 below gives a better estimate of the extinction ratio. Secondly, this method only gives information upon the intensities of the main and adjacent pulses; in fact, it is found in practice that the entire 82 MHz mode-locked pulse train is emitted from the cavity dumper, albeit with a greatly reduced intensity. These pulses are denoted as "leakage light", since they effectively "leak" through the cavity-dumper's suppression system, and were illustrated in Figure 5.1.

It is very important to note that Spectra-Physics also discuss an emission termed "leakage light" in their system manuals,[20] where they refer to intracavity radiation which is weakly transmitted through mirror M2 (Figure 5.9, Point 3) of the cavity dumper. This emission is extremely weak (of the order of μW), since it is not deflected out of the

dumper by the Bragg cell, and is used as a diagnostic in matching the dye and Ar^+ laser cavity lengths. In contrast, the emission which we term "leakage light" actually follows the same path through the cavity dumper as do the main pulses (Figure 5.9), and is of fundamentally different origin to the "leakage light" discussed by the manufacturer.

Clearly, the leakage light referred to by the manufacturer may easily be spatially isolated from the cavity-dumped beam, and does not normally illuminate the sample. The leakage pulses which are a problem in our system are collinear with the cavity-dumped beam, may carry milliwatts of power, and can only be removed by improving the cavity dumping efficiency.

At low repetition rates, there are many more leakage than main pulses, and the situation can arise when nearly all of the laser output intensity resides in this spurious emission. This fact does not appear to have been generally appreciated in the literature. At best, the pulses represent "wasted energy" in the beam, and in the worse case they may constitute a source of excitation competitive with the main beam. The monitoring and significance of leakage light is discussed in greater detail in Section 5.5 below.

5.4.3.2 Phase and timing effects

This refers to the effect of varying the phase of the modulation function, and the timing of the rf pulse envelope (Figure 5.10) with respect to the arrival of the dye laser output pulse at the Bragg cell. Clearly, if all of the intensity of the beam is carried in narrow pulses at the desired repetition rate, then adjusting the phase and timing of the rf

signal will drastically effect the output power. The manufacturers quote a 10:1 variation in output power as being indicative of short (<40 ps) pulses. On the other hand, if most of the power is carried by the leakage-light, then adjustment of phase and timing will have very little effect. We have found this to be a useful guide to the system performance, and compares well with the results obtained with the time-correlated photon counting method described in Section 5.4.4.

5.4.3.3 Pulsewidth measurement *via* autocorrelation - check on laser performance

In order to check the laser alignment, a rapid scanning autocorrelation (Spectra-Physics model 409) was borrowed from the manufacturer. It was observed that the laser, which had been aligned on the basis of output power, phase/timing effects and time correlated photon counting results, was yielding *ca.* 30-40 ps output pulses. The autocorrelator was not available for a sufficient length of time to significantly improve this performance, and so it is assumed that 40 ps is a reasonable upper estimate of the laser pulse duration obtained with this system throughout the work described in this thesis.

5.4.4 Time correlated photon counting (TCPC): measurement of photon-time distributions

We have found that the best way of characterising the overall laser performance is to record photon-time distributions, using the time-correlated photon counting[28] (TCPC) method described in the following chapter. This enables examination not only of the main dumped pulse, but also of the intensity distribution between the main pulses. It is therefore a good method of quantifying the leakage light contribution to the beam intensity. It does not yield an accurate represent-

ation of the laser pulse shape, since the impulse response function of this measuring system is of the order of 1 ns wide (Chapter Six). However, it has been explained that this factor is irrelevant for our purposes; it is much more important to be able to measure the relative intensities of the main and leakage light pulses.

5.4.4.1 Observed Photon distributions - leakage light

Figure 5.11(a) illustrates a typical photon distribution, obtained at a cavity dumping rate of 800 kHz. This data is actually the photon distribution obtained from the Raman scatter from the 992 cm^{-1} normal mode of benzene, since this should have the same temporal characteristics as the laser pulses (Chapter One). The main laser pulse is clearly visible. Immediately following the main pulse, there are several much smaller features, separated by *ca.* 12.2 ns, *i.e.* the mode-locked pulse separation. These are the leakage light pulses.

Figure 5.11(b) shows these features in greater detail. Clearly, the pulses nearest to the main dumped pulse are of greater intensity than the average, but on the basis of Figure 5.10, we would expect to only observe the main and immediately adjacent pulse. It appears that the burst of rf power to the Bragg cell is not as discrete as Figure 5.10 indicates; a low power rf signal must be reaching the cell at all times, since the entire mode-locked pulse sequence is being weakly deflected out of the cavity.

5.4.4.2 Minimising the amplitude of leakage pulses

Although these peakage pulses are very small compared to the main emission (as low as 0.05% in favourable cases), they cannot be ignored since they occur in such

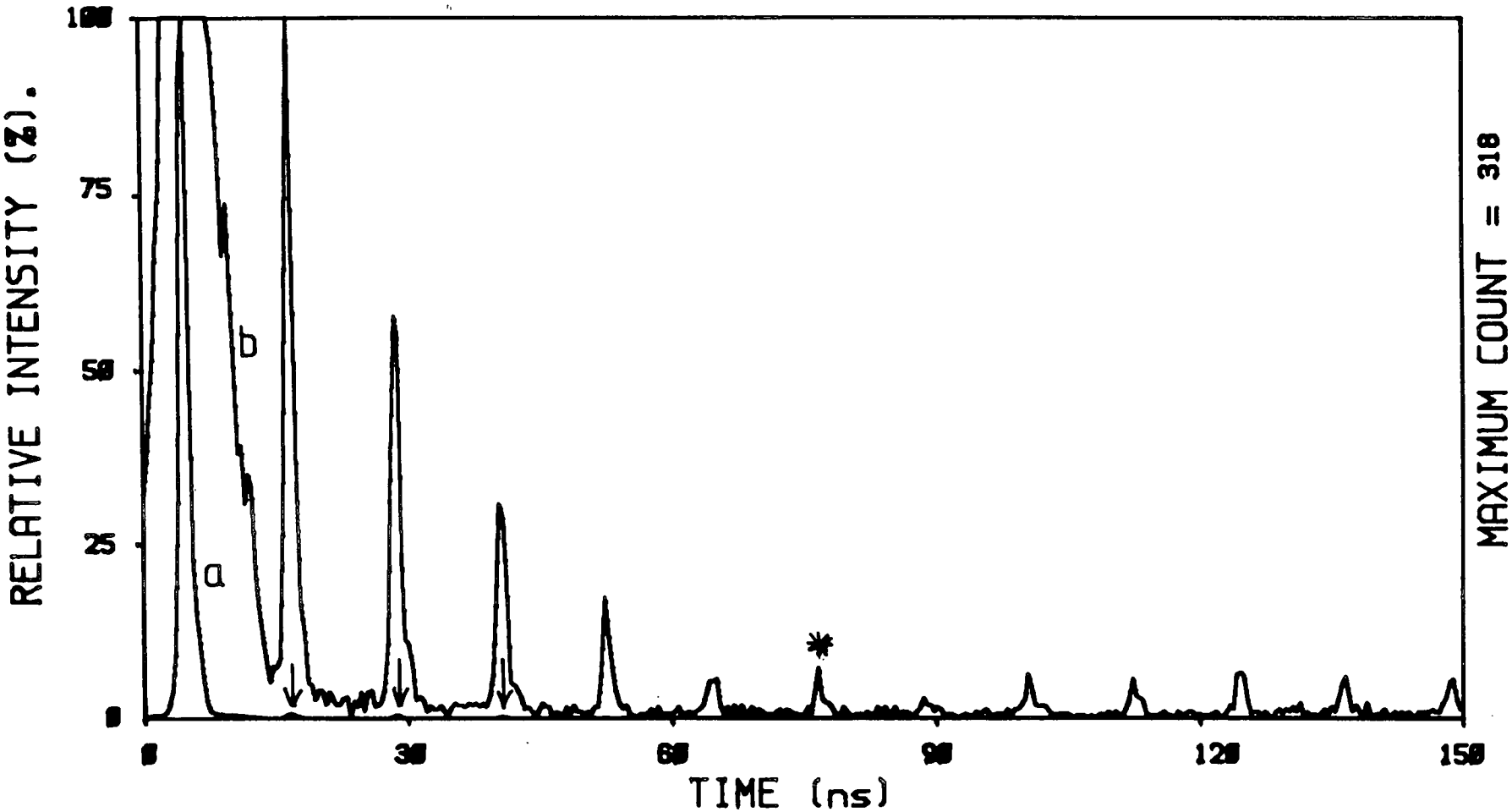

FIGURE 5.11 Photon distribution (800 kHz).

(a) Main pulse, followed by leakage pulses (arrowed).

(b) x143 magnification of (a). Leakage pulses are clearly visible. Average intensity (*) pulse is much lower than those adjacent to main pulse.

large numbers. For instance, at a repetition rate of 4kHz, there are 20,499 leakage pulses for each main one. This would mean that *ca.* 90% of the beam power is carried by leakage emission rather than the main pulses, given the 0.05% intensity ratio! This caused severe problems when a gated diode array detector was used (Chapter Seven), where the maximum trigger rate was 4 kHz, and so the majority of the beam power was effectively wasted.

The manufacturers were apparently unaware of this problem, which only becomes noticeable when photon distributions are recorded, or when systems are operated at very low repetition rates. They did, however, supply a simple solution. If an rf suppressor circuit (Figure 5.12) is inserted between the rf supply and the Bragg cell, most of the leakage emission is eliminated.

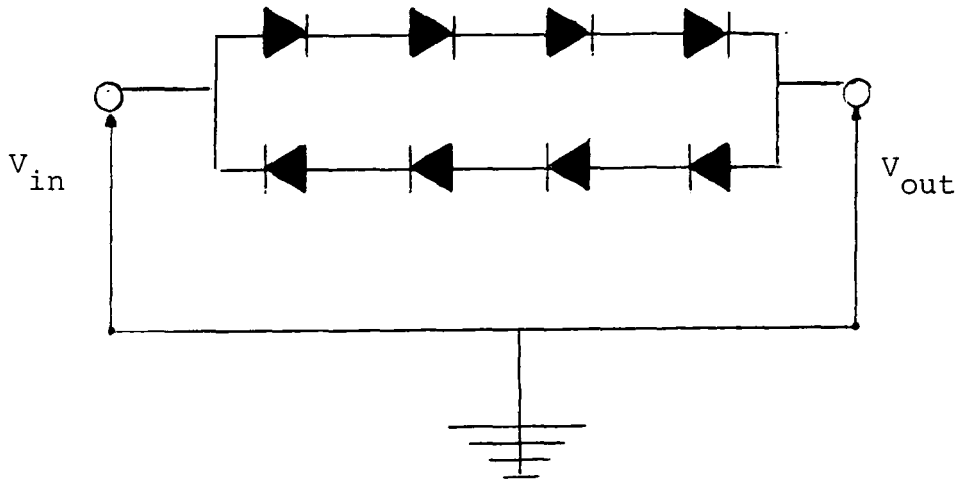

FIGURE 5.12 Rf suppression circuit. All diodes are type IN 196.

Only rf signals above the threshold level of the circuit are passed, so the rf pulse reaches the Bragg cell while the lower level continuous signal is blocked. This circuit improves both the extinction ratio and the main/average leakage pulse ratio (Figure 5.11). Table 5.1 summarises the effect of the suppressor upon the leakage contribution at a variety of repetition rates.

TABLE 5.1 The effect of the rf suppressor in minimising leakage intensity

Rep rate	M/counts	M/Adj	M/Ave	T/s	Int/mW
4MHz	55250	170	2400	100	32
* 4MHz	56667	250	$\simeq \infty$	100	31
800kHz	45578	140	2300	100	32
* 800kHz	47928	280	$\simeq \infty$	100	32
4 kHz	360	30	-	400	1.0
* 4 kHz	778	80	-	400	0.2

M = intensity of main pulse
Int = laser intensity (average)
M/Adj = ratio of main dumped pulse to adjacent leakage pulse (extinction ratio)
M/Ave = ratio of main dumped pulse to average leakage pulse
* = rf suppressor inserted
T = time to accumulate distribution

The S/N ratios of the 4kHz photon distributions were too poor to accurately judge M/Ave. This is discussed in the text.

It is clear that the rf suppressor improves the extinction ratio by a factor of *ca.* 2, while the majority of the leakage pulses are totally eliminated. (This is illustrated in Figure 5.13 for a repetition rate of 800kHz. Compare the average pulse height with that observed without

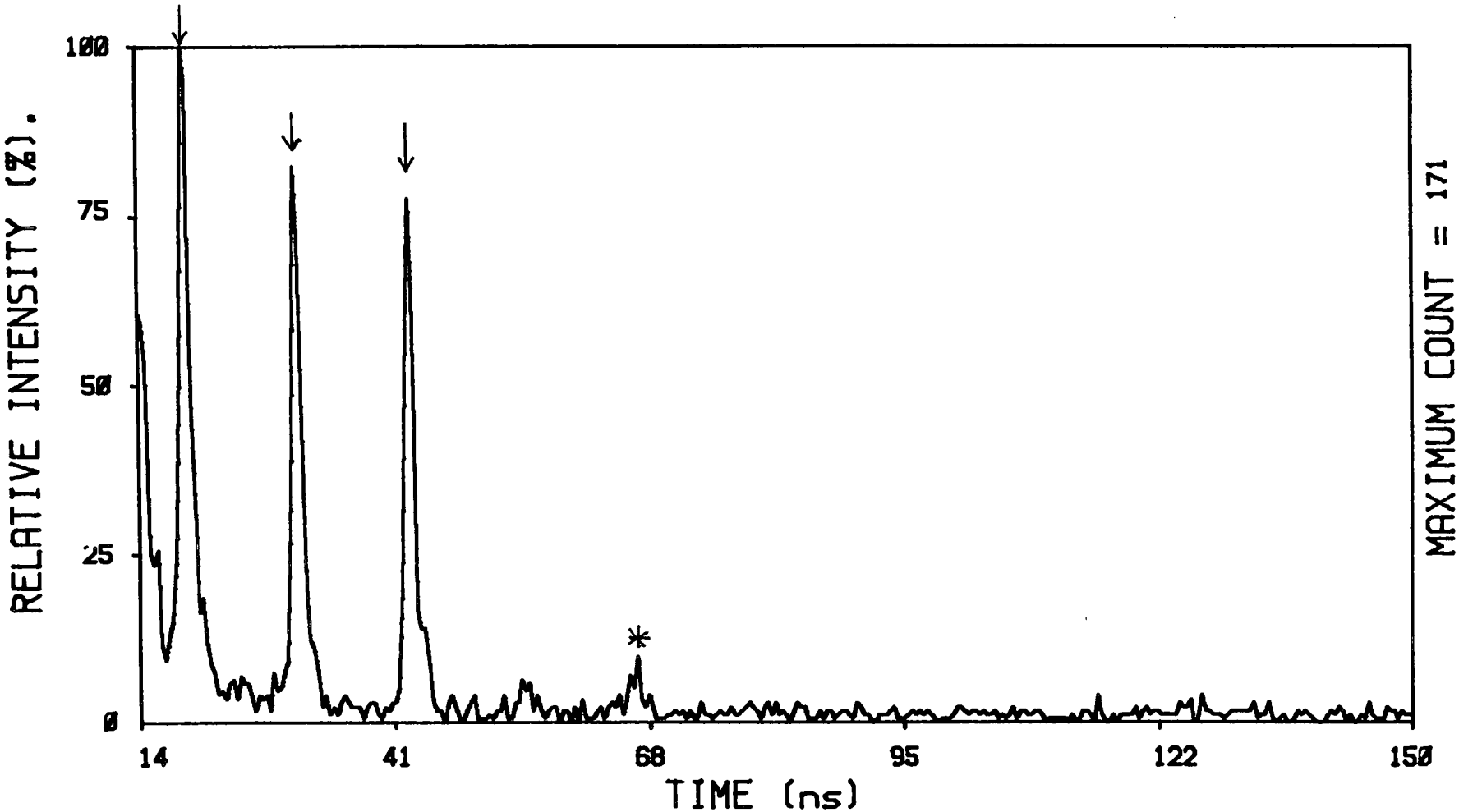

FIGURE 5.13 Effect of rf suppressor circuit. Pulses adjacent to the main dumped pulse are roughly halved in intensity (compare with Figure 5.11(b). The remainder of the pulse train is totally suppressed. Note, the main pulse is not shown on this figure.

the suppressor, Figure 5.11). Also, at 4 MHz and 800 kHz, the intensity which was carried by the leakage light is transferred to the main pulses, according to the laser intensity measurements.

The S/N ratios of the 4 kHz photon distributions were poor because of the low average intensities, and so it was difficult to estimate the average leakage intensity. An estimate of the magnitude may be made from the variation in the laser intensity upon inserting the suppressor.

The intensity of the main pulse (M) was doubled when the suppressor was used, but the total beam power fell from 1 mW to 0.2 mW. Assuming that all of the power was carried by the main pulse when the suppressor was in place, this would indicate that the main pulse carried 0.1 mW in the un-. suppressed case. Therefore, 0.9 mW were carried by the 20,499 leakage light pulses relative to each main pulse, giving an M/Ave ratio of *ca.*2500, in good agreement with the ratios observed at higher repetition rates. No leakage pulses could be observed above the noise levels in the suppressed case.

It is interesting to note that the extinction ratio was much more dependent upon the laser repetition rate than was the M/Ave ratio. The reasons for this are not obvious since it might be expected that <u>both</u> the main and adjacent pulses would be equally dependent upon the cavity-dumping rate. Insertion of the rf suppressor affects the lower intensity leakage pulses much more than those adjacent to the main pulse, as would be expected. It is much more difficult to improve the extinction ratio (M/Adj) than to increase M/Ave.

For the purposes of our work, we require that most of the laser intensity is carried in the main pulses,

simply because we need the highest possible peak powers. Furthermore, merely improving M/Ave is not sufficient; this must be achieved by transferring the power from the leakage pulses to the main pulses. The improvement which was obtained in M/Ave at 4 kHz is largely irrelevant, since the leakage intensity was not transferred to the main pulses but was almost totally lost. This should be contrasted with the experiments at higher repetition rates, where the leakage power was relocated in the main pulses.

It should be remembered that the extinction ratio can be of importance in certain applications, most notably in fluorescence decay measurements,[28,29,30] where an extra excitation *ca.* 12 ns after the main pulse distorts the decay profile. Under these conditions, improving the extinction ratio may be vital, and so an accurate estimate of its value is needed.

We believe that the photodiode/oscilloscope method recommended by Spectra-Physics is inherently inaccurate, and prefer to measure the ratio with the TCPC apparatus. We have found that there is little correlation between the extinction ratios measured using the fast photodiode, and those by TCPC. In practice, we found it extremely difficult to achieved a true extinction ratio of 500:1 (Section 5.4.3.1). The difficulty in achieving this specification, and the inadequacy of the photodiode method for its measurement, has been confirmed by another group using this system.[30]

5.4.4.3 Optimisation of the rf power to the Bragg cell

The effect of varying the phase and timing of the rf pulse to the Bragg cell has been discussed, but another important factor is the actual power of the signal. The power is not fixed, but is user-selectable up to about 10 W. The

manufacturers recommend that maximum rf power be supplied to the cell; in fact such a procedure has disastrous consequences for the quality of the laser output. Selection of maximum rf power does generally yield a cavity-dumped beam of high average intensity, but it is found that the phase and timing of the rf signal has little effect upon the output power. This would inply that the intensity is residing largely in the leakage light pulses, a conclusion that is supported when the photon distribution is recorded.

Figure 5.14 displays the photon distribution of an 800 kHz cavity-dumped beam with full rf power delivered to the Bragg cell, and demonstrates very clearly that the main pulse only contains a small fraction of the total beam energy. It appears that the rf supplied to the Bragg cell is no longer takes the form of discrete pulses, but is instead a continuous, unmodulated 82 MHz signal. Under these circumstances, the TCPC method is superior to autocorrelation function measurements, since it allows more direct observation of the power distribution over longer timescales.

The spectrum in Figure 5.14 is further evidence that the leakage light arises from excess rf power in the Bragg cell; notethe alternating intensities of the pulses as they arrive at maxima and minima of the modulation function (Figure 5.10), which is clearly not constrained to a 14 ns pulse. It is likely that the leakage pulses which were observed at lower rf powers arose through a similar mechanism. It is important to be aware of this problem, since following the manufacturer's recommendations in setting the rf power would yield a virtually useless output beam. In practice, we have found that the most

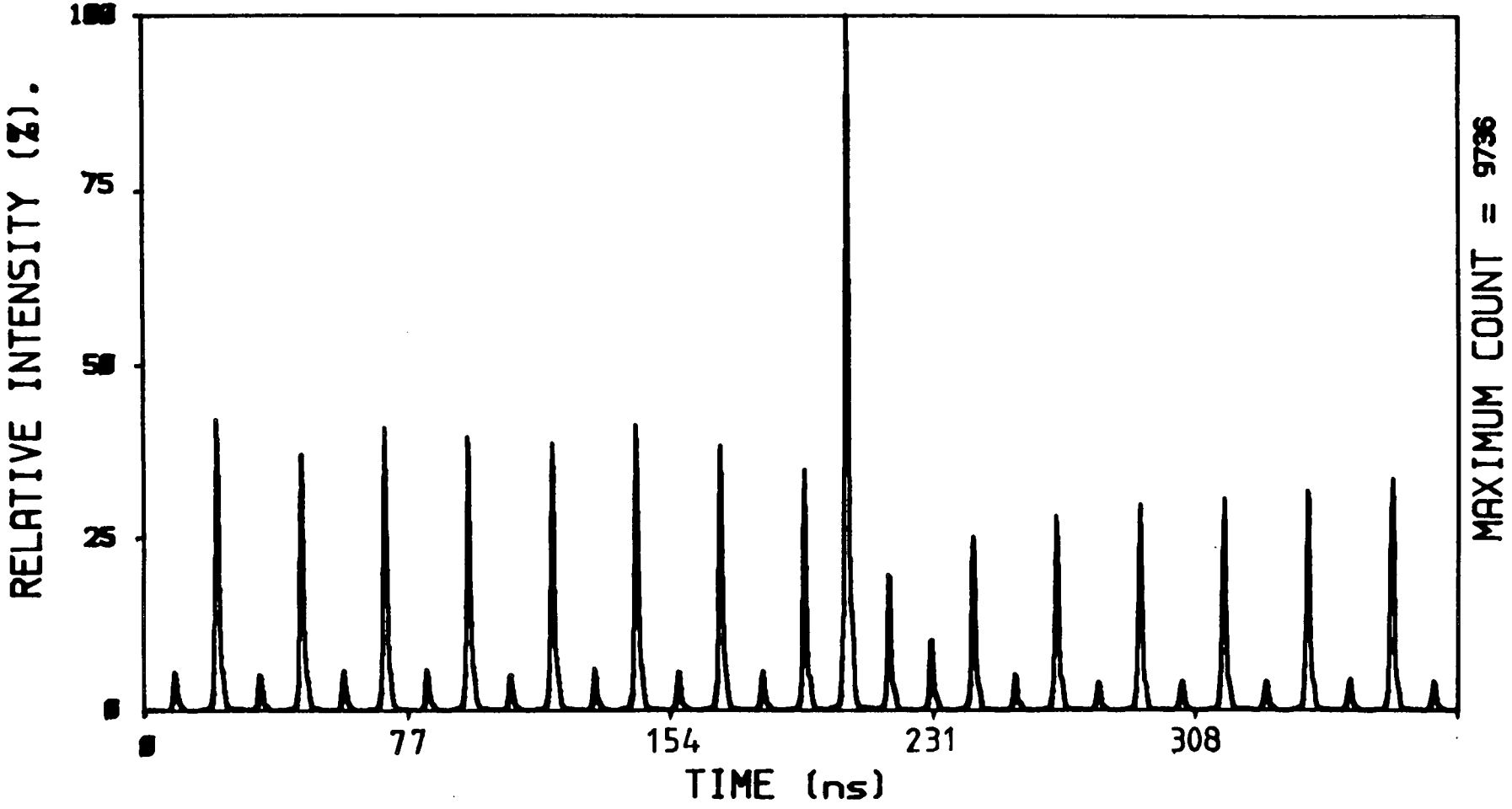

FIGURE 5.14 Effect of supplying maximum rf power to the Bragg cell. The entire 82MHz mode-locked pulse train is dumped from the cavity. Note the alternating pulse heights at maxima/minima of the modulation function (Figure 5.10).

reliable way to set the rf power is to observe the photon distribution as the power is varied. A rough guide to the correct rf power can be obtained from the variation in output intensity as a function of rf power (Figure 5.15).

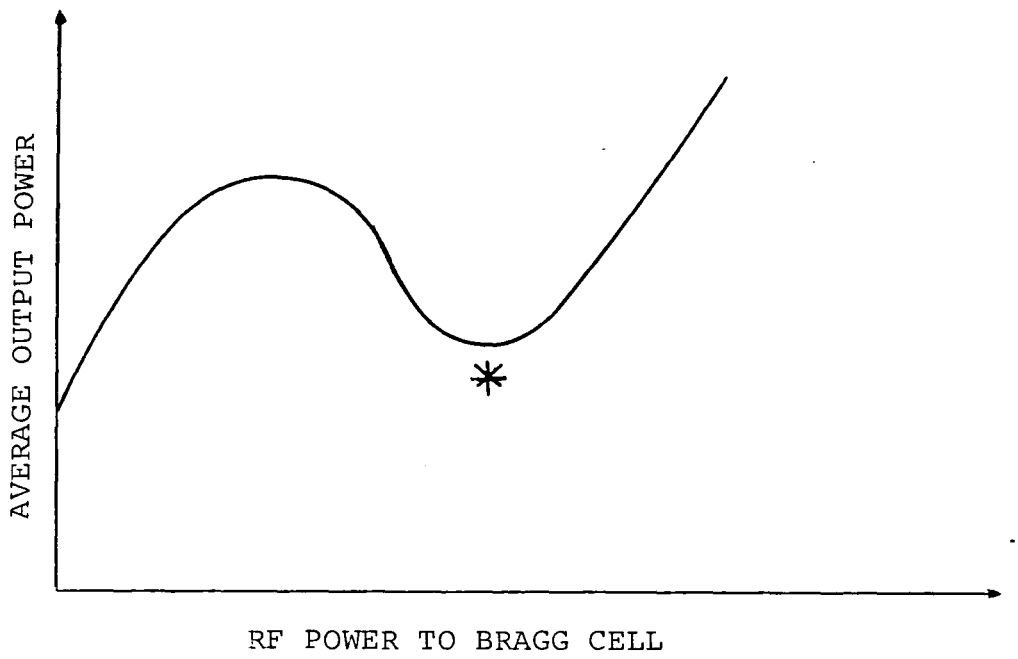

FIGURE 5.15 Optimisation of rf to Bragg cell.
The asterisk marks the optimum point.

We have found that the optimum rf power setting corresponds to the dip in output intensity which occurs on varying the power, in rather stark contrast to the manufacturer's recommendations. Although the shape of the curve in Figure 5.15 was found to vary considerably with the rate of cavity dumping, it appears to be generally true that the best results are obtained when operating the laser at the power dip, which seems to be present under all circumstances when the system is well aligned.

5.4.5 Conclusions

The sections above have related to specific points concerning the operation and optimisation of the laser system. There are, of course, many other diagnostics which are applied when the system is being aligned, and which give an indication of the quality of the output. The ones mentioned above were chosen because they were important with regard to our specific application, or because we believe that the pulse quality could be degraded by blindly following the manufacturer's instructions.

Finally, it should be pointed out that the process of learning to optimise the laser output, and to identify when the system is not functioning correctly, is a slow one. Much of the information in the sections above, particularly concerning the leakage light, was not known when the system was first installed. As a result, some of the work which is described in this thesis, (particularly the diode array experiments), was carried out when the laser was not operating at peak efficiency, *i.e.* low output intensity and poor leakage-light suppression was common. For example, the laser intensity was typically 20-25 mW (4MHz) during the early TCPC experiments, whereas powers of 40-50 mW are now readily attainable at this repetition rate, with very little or no leakage contribution.

5.5 Spurious wavelength emission from the synchronously-pumped dye laser

5.5.1 Introduction

It was stated in Section 5.3 that the dye laser, operating with a two plate birefringent filter, should yield a single emission line of *ca.* 60 GHz width (2 cm^{-1} at 600 nm)

and ought to provide a suitable pulsed source. Indeed, when liquid samples were examined with this laser, reasonable quality Raman spectra were obtained. However, when solid samples were studied, we observed spurious intense, broad features in the spectra, which were independent of the chemical nature of the sample and which apparently originated in the laser beam. These features were more intense than normal Raman bands, and often masked the true Raman signals from the sample.

Although preliminary results of this work have been reported in the literature,[24] more detailed studies have been subsequently undertaken which have provided some insight into the origin of these emissions. It was suggested in the previously published work that the spurious bands may have been generated by a Raman transition within the dye laser cavity rather than at the sample; a more detailed study shows that this is not the case, and it seems highly likely that the features are due to sidebands in the transmission curve of the birefringent filter.

5.5.2 Experimental

The cavity-dumped, synchronously-pumped dye laser which has been described in this chapter was used to excite the Raman spectra of three solid samples (a polymer film, benzoic acid and benzophenone). This variety of samples was chosen to illustrate the fact that the extra emissions do not originate from the compounds under investigation. The polymer film was self-supporting, while the other samples were pressed into self-supporting discs, thereby avoiding complication of the spectra with features due to sample cells. The laser repetition rate was fixed at 4 MHz.

Light scattered at 90° to the incident beam was collected by a Spex 1401 (Ramalog 4) double monochromator, which was equipped with a cooled RCA C31034-05 PMT and associated pulse counting electronics. The detector assembly is described in Chapter Six.

5.5.3 Results

5.5.3.1 General properties of the extra emissions

Figure 5.16 illustrates the Raman spectrum of the polymer film which was obtained with the apparatus described above. The laser was operated at a wavelength of 587 nm (17043 cm^{-1}) with an intensity of 35 mW. A true Raman band of the sample is marked with an arrow. In addition to this feature, much stronger bands were observed at apparent Raman shifts of approximately:

570 cm^{-1} (very intense, 80 cm^{-1} FWHM)
1130 cm^{-1} (less intense, *ca.* 30 cm^{-1} FWHM)
1700 cm^{-1} (weak).

The feature at 570 cm^{-1} is referred to as "band A"throughout the rest of this discussion.

These bands were observed with <u>any</u> solid sample, irrespective of chemical composition, under conditions when a large amount of laser light was reflected off the sample directly on to the entrance slit of the monochromator, but the intensity and shape of the bands varied with sample alignment. Alignment of the sample such as to minimise direct reflection into the spectrometer largely eliminated the features. The bands were unchanged if the detector was temporally gated so as to detect photons over the duration of the laser pulse,

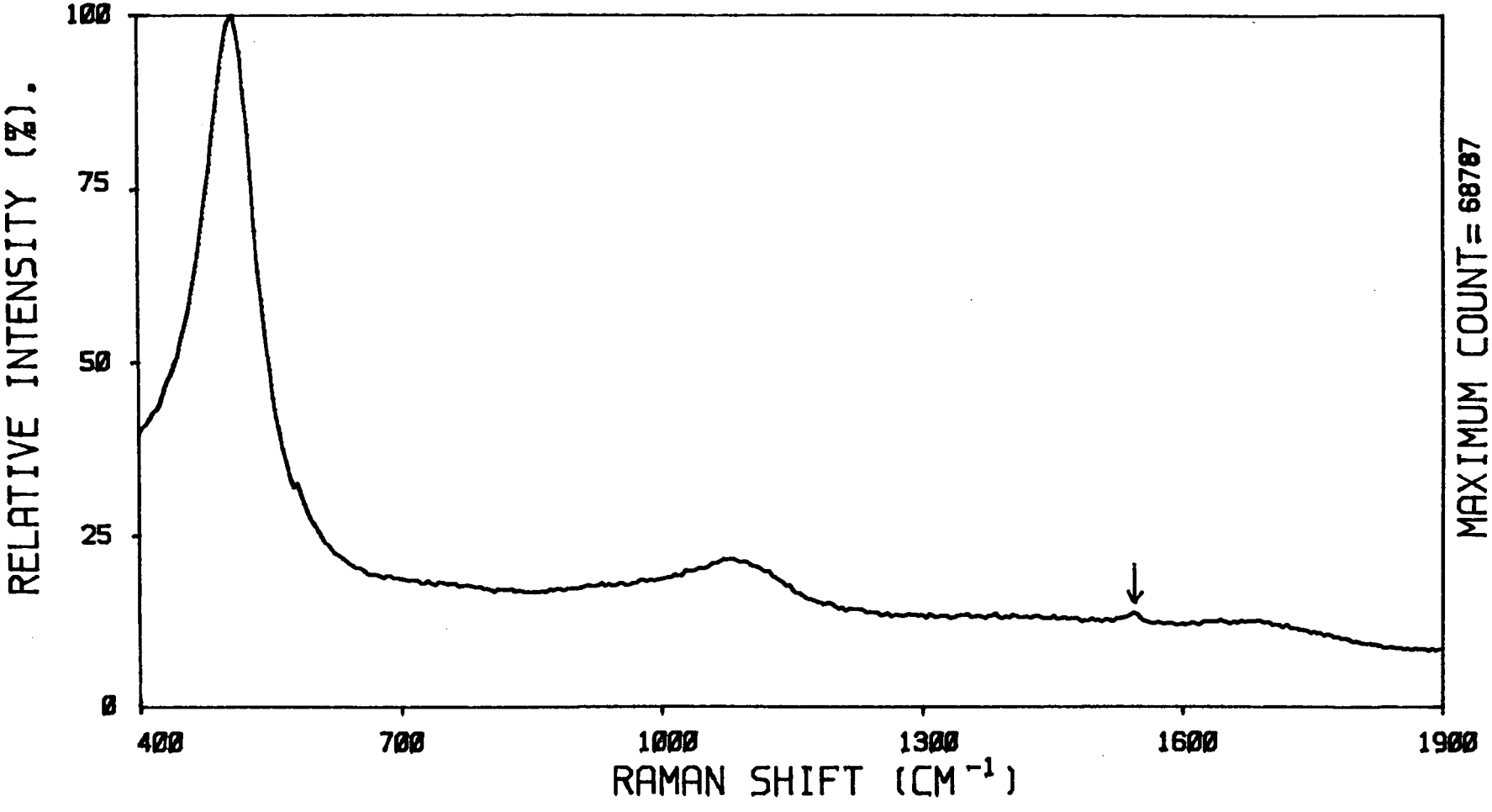

FIGURE 5.16 Raman spectrum of polymer film. Laser wavelength - 587 nm (17043 cm^{-1}) at 35mW (4MHz pulse rate). The arrow represents a true Raman feature.

(Chapter Six), which implies that they have the same temporal characteristics as the laser pulses and Raman scatter.

The bands could have arisen either internally in the laser system, or from external optical components/ stray light within the spectrometer. To determine the source of this emission, a short pass filter (Ealing Optics 35-5628) was introduced at the output of the cavity dumper. This filter has a sharp cutoff, which ensures that while the transmission at 590 nm (the chosen exciting line) is *ca.* 71%, the transmission at more than 550 cm^{-1} from the exciting line is less than 5%.

Figure 5.17 demonstrates the effect of this short pass filter. The Raman spectra of benzophenone were obtained with and without the short pass filter, with an exciting wavelength of *ca.* 590 nm (50mW). Spectrum (a) was collected without the short pass filter, and displays the intense spurious bands. Insertion of the filter (spectrum (b)) totally eliminates the anomalous bands, but the Raman lines are reduced in proportion with the exciting intensity (*ca.* 70%). This strongly indicates that the features do not arise from interaction of the exciting radiation with the spectrometer optics, but are actually genuine emissions from the laser, travelling collinearly with the main dumped beam. It is only when a large amount of laser light is reflected directly into the monochromator (*i.e.* in the study of reflective solid samples) that these emissions are observed, and so spectra of liquid samples do not exhibit these anomalous features.

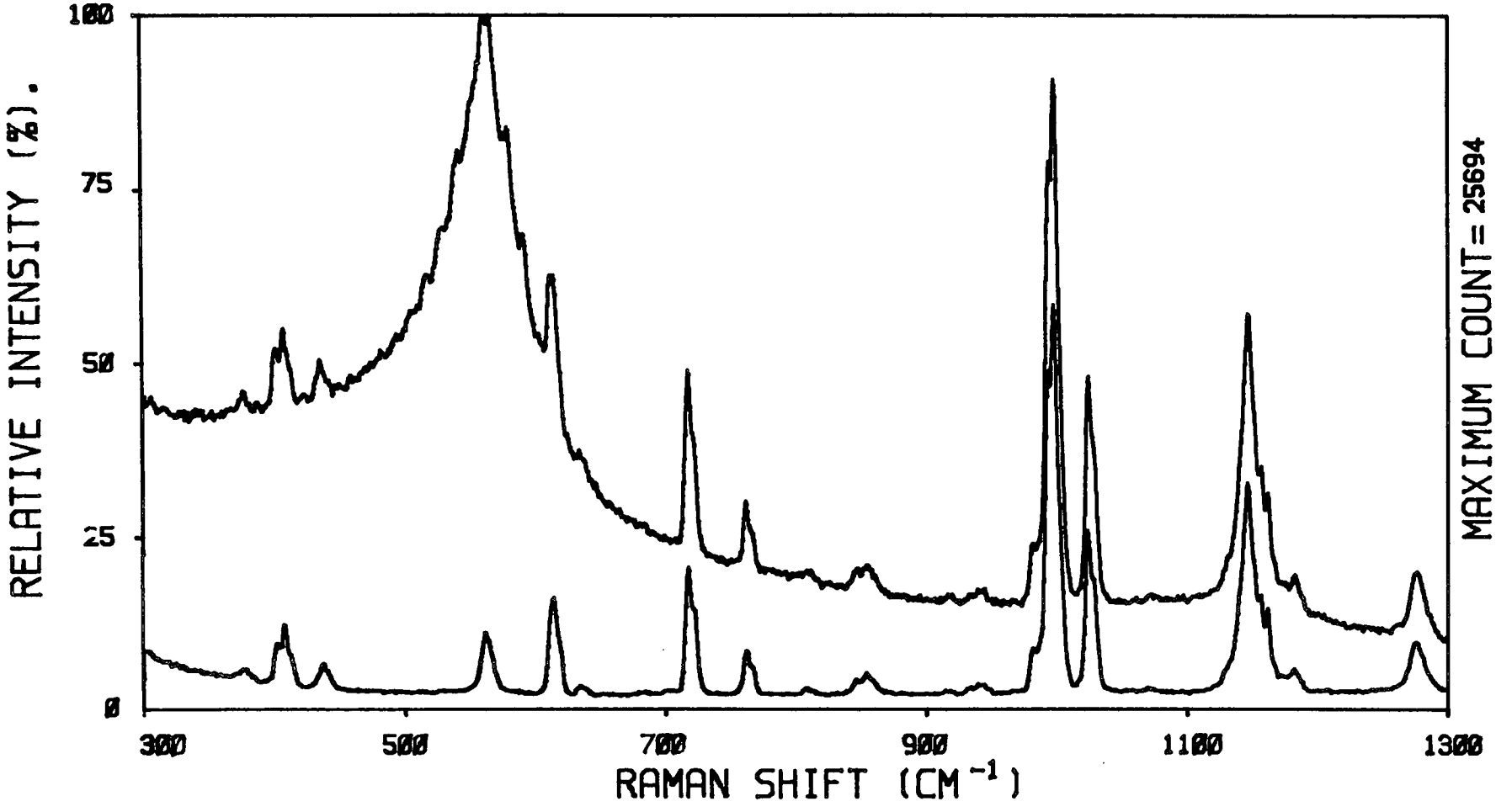

FIGURE 5.17 Raman spectrum of benzophenone. λ_{ex} = 590 nm (16961 cm^{-1}) at 50mW.

(a) No short pass filter, sample illuminated directly by dumped output.

(b) Short pass filter installed at cavity-dumper output (transmission <5% at > 550 cm^{-1} shift). Anomalous feature is totally eliminated, and high background is reduced.

5.5.3.2 Effect of exciting wavelength upon band positions

In the originally published preliminary results of this work, it was implied that the emissions occurred at a constant frequency shift from the exciting line, irrespective of its absolute frequency, *i.e.* they behaved as Raman bands. While this initially appeared to be true for small shifts in the exciting frequency (*e.g.* +/- 5 nm), a more precise measurement of band positions over a wider range of laser wavelengths reveals that the apparent "Raman" shift of the anomalous bands is not constant. Only the variation of the position of band A is considered here, since the other two features are too weak for accurate measurements to be made.

Figure 5.18 illustrates Raman spectra of benzophenone obtained using three different laser wavelengths, namely 572 nm, 590 nm and 614 nm, without the short pass filter in place. The positions of the true Raman bands of the sample, against which the position of the extra feature was calibrated, are revealed in Figure 5.17(b). Clearly, band A is present in all of the spectra obtained without the short pass filter, but careful examination shows its apparent "Raman" shift actually varies with excitation wavelength (Table 5.2).

TABLE 5.2 Variation of the position of band A as a function of exciting wavelength

Laser wavelength		Position of feature		
/nm	/cm^{-1}	"Raman" shift/cm^{-1}	absolute/cm^{-1}	absolute/nm
572	17485	584	16913	591
590	16961	566	16395	610
614	16276	523	15753	635

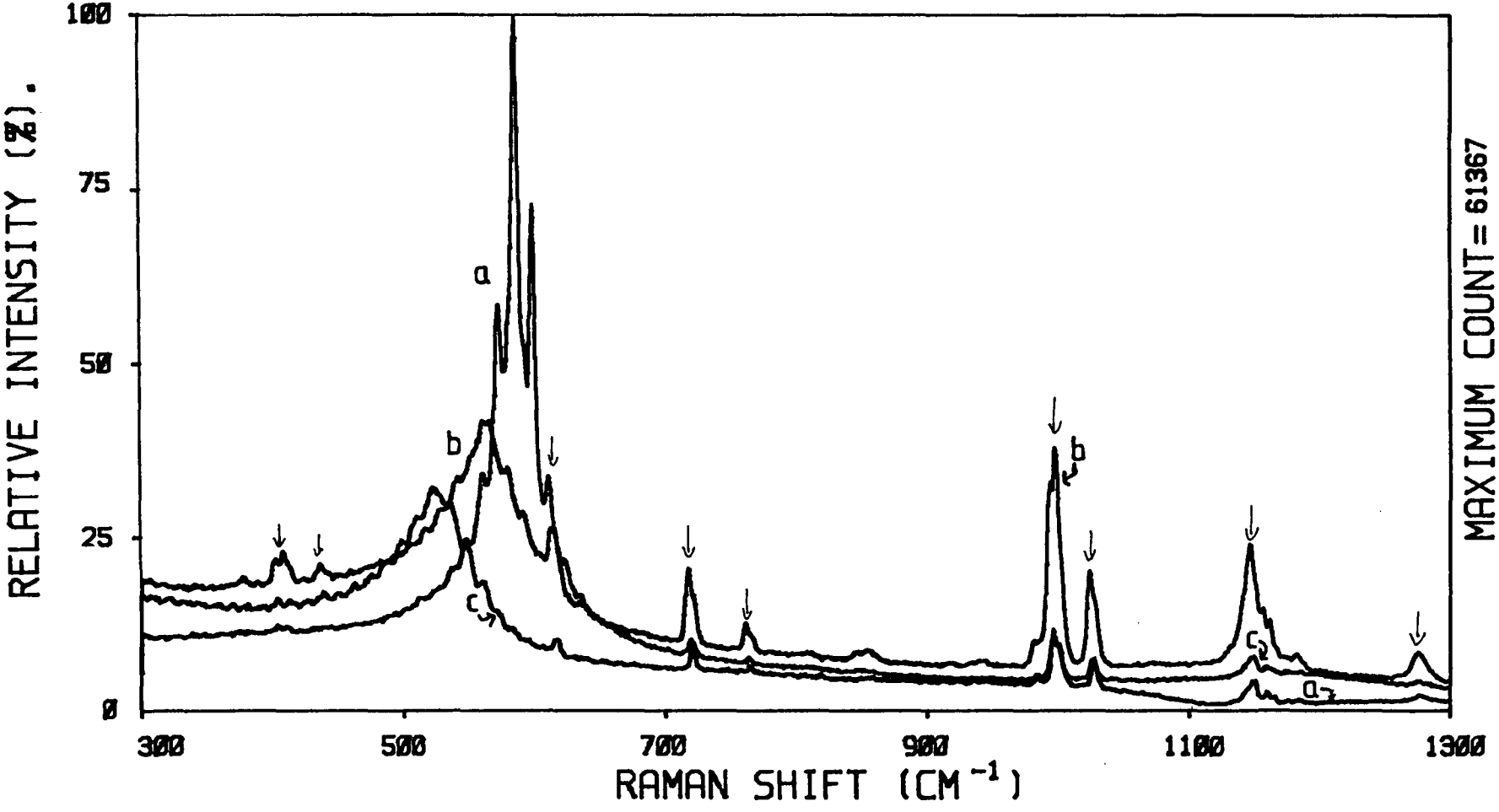

FIGURE 5.18 Variation of band position with exciting wavelength. (a) $\lambda_{ex} \simeq 572$nm, (9mW), (b) $\lambda_{ex} \simeq 590$nm (50mW), (c) $\lambda_{ex} \simeq 614$nm (30mW). Note the unresolved fine structure on the band maxima, and the change in relative intensity/shape as λ_{ex} varies. True Raman bands are arrowed.

Examination of Figure 5.18 and the data tabulated above reveals several points of interest.

(a) A shift in the laser frequency of 1209 cm^{-1} results in a change in apparent "Raman" shift of only 61 cm^{-1}, (5% of the change in absolute laser frequency), and so small changes in the exciting frequency do not yield noticeable movement of the broad band; hence the initial mistaken observation that the spurious bands were Raman features. However, it is clear that the band cannot arise from a Raman transition, or from a simple extra lasing emission at a fixed absolute wavelength.

(b) The absolute wavelength of the spurious feature is *ca.* 20 nm higher than that of the main lasing line, with the separation increasing slightly as the excitation wavelength increases. The separation appears to be roughly proportional and to the exciting wavelength for the (admittedly limited) data set.

(c) The intensity of the band varies with the laser wavelength such that 572 nm excitation yielded by far the most intense band, even though the laser intensity was only 9mW compared to the 50mW (590nm) and 30mW (614nm) excitations. This observation is purely qualitative, since an exact intensity comparison would require calibration of the wavelength-dependent spectrometer/detector efficiency, and allowance must be made for changes in the laser alignment which occur on tuning the wavelength.

(d) Band A is not actually a single, smooth band, but appears to consist of several unresolved overlapping bands, separated by *ca.* 12 cm^{-1}. The resolution of this fine structure varies with excitation wavelength, and it is most pronounced at 572nm.

(e) The overall shape of the band envelope varies with wavelength, with a minimum width at 572 nm excitation. In addition, it should be noted that the shape and intensity of the bands is strongly dependent upon sample alignment, *i.e.* the direction with which light is reflected into the monochromator.

5.5.3.3 Source of the extra emissions

In order to determine the source of the anomalous bands, the laser system was reconfigured so as to excite Raman scattering with the mode-locked Ar^+ laser directly. No spurious bands were observed under these conditions, which implies that the emissions originate in the dye-laser cavity.

The bands were not observed upon replacing the birefringent filter with a tuning wedge (Spectra-Physics model 570), as is illustrated in Figure 5.19. The spectrum of benzoic acid was collected over the region 450 $cm^{-1} \rightarrow 900\ cm^{-1}$ with a tuning wedge and a birefringent filter as the tuning element. Clearly, replacement of the filter with the tuning wedge completely removes band A. This strongly implies that the birefringent filter is responsible for these artifacts. Replacement of the birefringent filter with a tuning wedge is not a satisfactory solution to the problem, since the laser line will be broadened to a certain extent by the wider bandpass of this tuning element (240 GHz as opposed to *ca.* 60 GHz with the birefringent filter). This is indicated by the broadening of the Raman lines (Figure 5.19). Note also that the Rayleigh wing is much more prominent when the tuning wedge is used, and appears to extend out to *ca.* 500 cm^{-1} when light is reflected directly into the spectrometer.

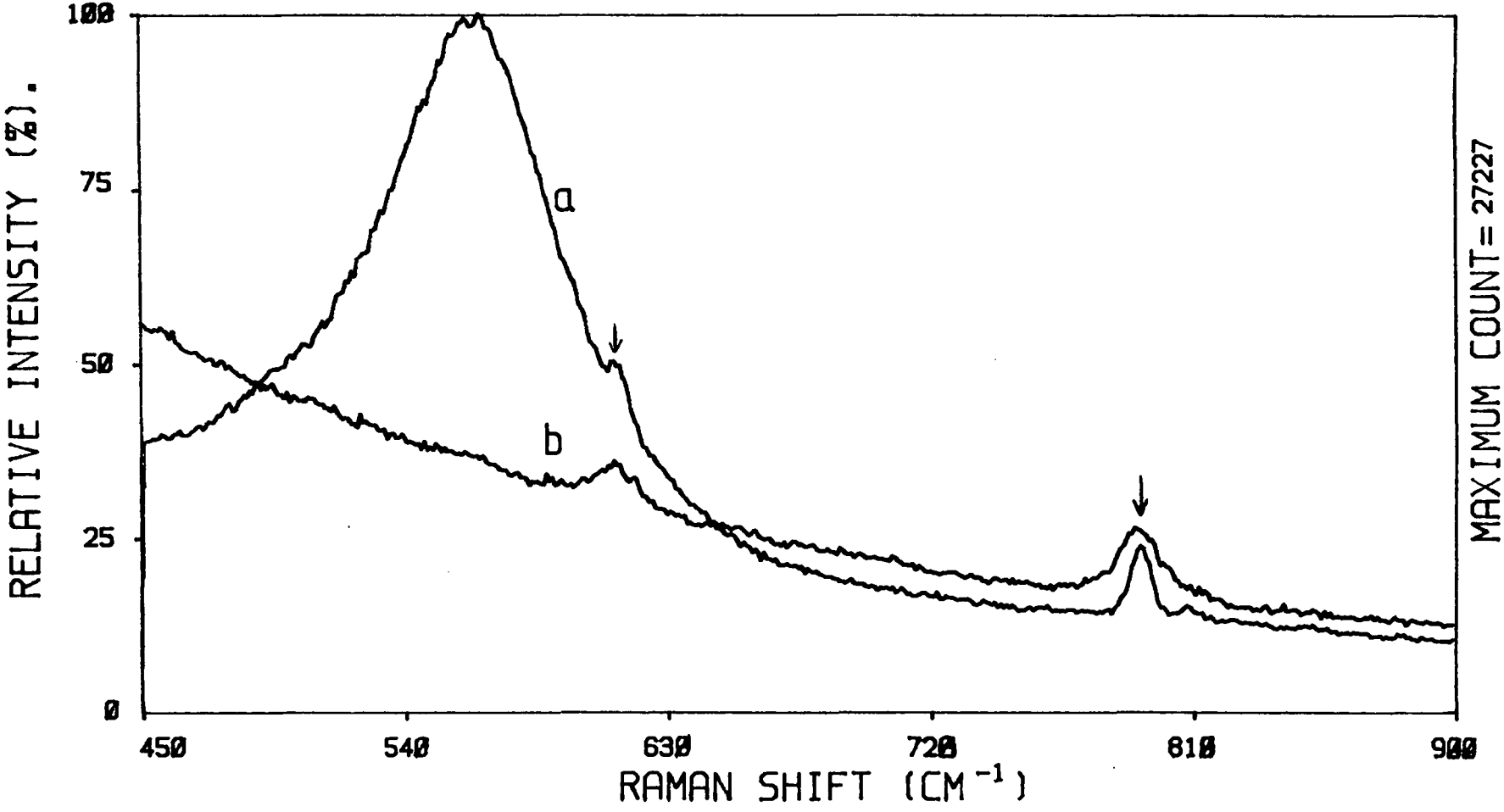

FIGURE 5.19 Raman spectrum of benzoic acid. $\lambda_{ex} \simeq 590$nm.

(a) Laser tuned with birefringent filter, (b) tuned with a tuning wedge. Note the elimination of band A, and the enhancement of the Rayleigh wing, in spectrum (b). The Raman bands (↓) are broadened due to the wider spectral bandpass of the wedge.

5.5.3.4 Effect of plate alignment in the birefringent filter

The birefringent filter actually consists of two parallel quartz discs which are oriented at Brewster's angle with respect to the incident laser beam.[31,32] The plates must be aligned such that the crystal axes of each element have the same orientation in space, and this is achieved by rotating one plate relative to the other about an axis normal to the plane of the disc (Figure 5.20).

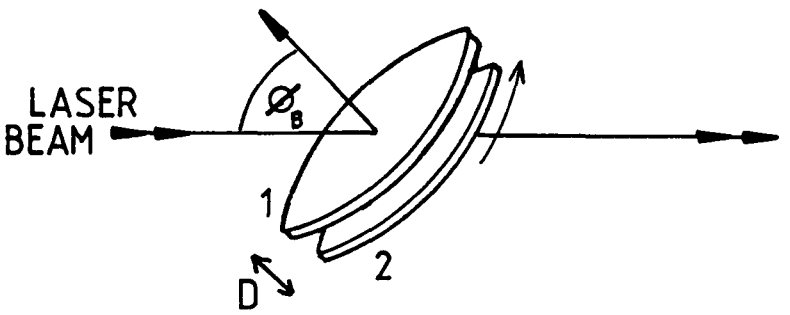

FIGURE 5.20 Internal alignment of the birefringent filter

ϕ_B is Brewsters angle. The distance D is small (plates almost touching). Internal alignment requires rotation of plate 2 relative to plate 1 in order to align crystal axes.

Although the plates are supposed to be factory aligned to ensure optimum operation, it was decided to perform a realignment, since the results recorded above strongly suggest that the filter is responsible for the spurious bands. The plates were aligned according to the manufacturer's recomm-

endations, and it was found that the plates were previously not set in the optimum position. The realigned filter was used to repeat the measurement of the spectrum of benzophenone at three laser wavelengths (Figure 5.21), and the position of the anomalous band is recorded in Table 5.3.

TABLE 5.3 Effect of realignment of birefringent filter upon the position of the spurious band as a function of laser wavelength

Laser wavelength		Band position		
/nm	/cm^{-1}	"Raman" shift/cm^{-1}	absolute/cm^{-1}	absolute/nm
572	17485	640	16845	594
590	16961	627	16334	612
614	16276	605	15671	638

Several interesting points arise from the spectra accumulated with the realigned filter.

(a) The intensity of band A decreases considerably with respect to the true Raman bands, even though the laser beam was being directly reflected off the sample on to the entrance slit of the monochromator. This was observed for all three laser wavelengths. The band is barely visible at 614 nm excitation.

(b) The apparent "Raman" shift of the band increased by *ca.* 60-80 cm^{-1} (according to excitation wavelength) compared to the previous spectra (Figure 5.18) and occurs at a longer absolute wavelength. This is most noticeable for the 614nm excitation.

(c) The total spread in the apparent Raman shifts is smaller (35 cm^{-1} compared to 61 cm^{-1}), than that observed previously (Table 5.2).

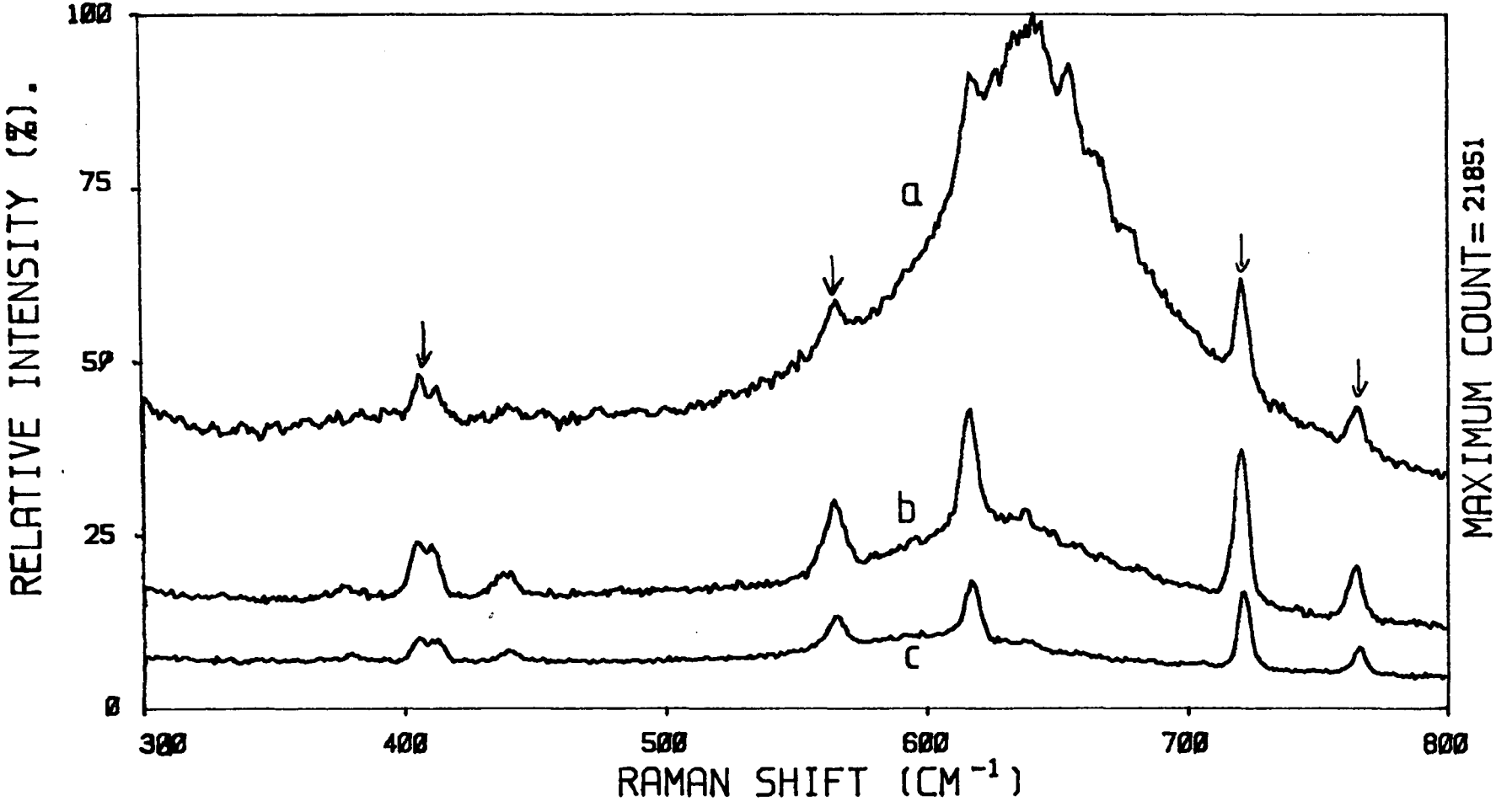

FIGURE 5.21 Realigned birefringent filter. Raman spectra of benzophenone, obtained under conditions: (a) λ_{ex}= 572nm, 45mW, (b) λ_{ex}= 590nm, (50mW), (c) λ_{ex}=614nm (30mW). Band A is greatly diminished in intensity in each case compared to Figure 5.18.

(d) The separation in wavelength of the emission relative to the exciting line ranges from 22-24 nm as opposed to 19-21 nm for the misaligned filter. The separation again increases approximately in proportion to the wavelength of the exciting line.

The above results strongly indicate that the extra bands are due to the transmission characteristics of the birefringent filter, which apparently allow transmission of small sidebands at *ca.* 22 nm longer wavelength than the main laser line. The exact separation of the main line and sidebands depends upon the absolute wavelength of the main line.

It is worth noting at this stage that the intensity of these sidebands is very small compared to the main lasing output, since they are of comparable intensity to the observed true Raman bands. This implies that the spurious emissions are of the order of *ca.* 1/10 of the main line intensity.

5.5.4 Mechanism of generation of the spurious features

Although the quantitative transmission properties of a birefringent filter may be calculated[32-33], the mechanism of generation of the sidebands may be appreciated at a non-rigorous, qualitative level.

In a birefringent crystal, the refractive index depends upon the orientation of the beam polarisation vector relative to the crystal axes, and so the propagation velocity of a light ray depends upon its state of polarisation and direction of travel within the crystal.[34] A monochromatic, linearly polarised ray may be decomposed as the sum of two orthogonally polarised beams with equal phase (Figure 5.22).

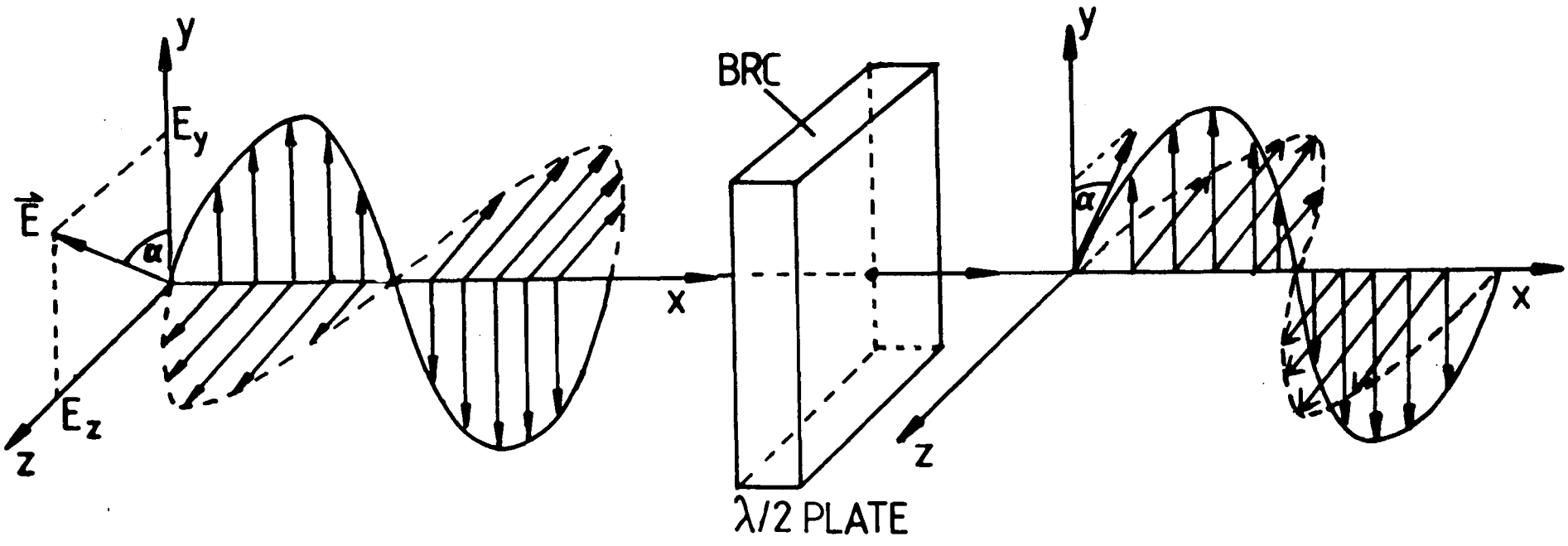

FIGURE 5.22 Polarisation changes of an electromagnetic wave on traversing a birefringent crystal (BRC). The incident, plane polarised wave is polarised at an angle α to the y axis. A BRC which retards one polarisation component by λ/2 compared to the other reverses the sign of α, while a full wave retardation leaves α unchanged. Any other retardation yields an elliptically polarised wave (*i.e.* the tip of $\vec{E}$ traverses an ellipse as the wave progresses).

In general, when such a ray traverses a birefringent crystal, each polarisation component will suffer a different retardation (since they experience a different refractive index). If the retardation of one component relative to the other is a whole number of optical wavelengths, the plane of polarisation of the ray is left unchanged, and the radiation remains linearly polarised upon leaving the crystal. A half wavelength retardation reverses the sign of α (Figure 5.22). All other retardations yield an elliptically polarised ray,[34] *i.e.* the angle α is no longer constant along the path length of the ray after it leaves the crystal. Therefore, it is clear that a birefringent material may be used to manipulate the state of polarisation of a light beam.

The birefringent filter is a rather complex optical component, which utilises the fact that the retardation of the polarisation components depends upon their wavelength, as well as their orientation with respect to the crystal axes of the quartz plates. For a polychromatic, polarised beam incident upon the filter, only certain of the wavelength components will be unaltered in their polarisation properties, while all other components will become elliptically polarised or have the plane of polarisation shifted (Figure 5.22).

The filter is aligned at the Brewster angle with respect to the incident beam, such that only those waves which do not suffer a change in the state of polarisation are passed through the plates without reflection. All other components experience losses on traversing the filter, and are (ideally) suppressed sufficiently to fall below the lasing threshold.[32] Rotation of the filter alters the orientation of the crystal axes relative to the beam, and so allows unattenuated passage

of a different group of wavelengths, thereby providing the tuning action of the element.

Ideally, the transmission characteristics of the filter would resemble Figure 5.23, where the wavelength separation of the adjacent transmission maxima is greater than the fluorescence bandwidth of the dye, allowing free lasing of only one frequency at a time. The manufacturer's literature indictes that this is the case with the two plate filter, with a free spectral range (FSR) of *ca.* 80-100 nm. In fact, Holtom and Teschke[32] have demonstrated that this is unlikely to occur in practice, owing to incomplete polarising action at the surfaces of the quartz plates. This means that wavelength components other than those whose polarisations were unchanged may be transmitted by the filter as sidebands to the main lasing wavelengths.

The amplitude and position of these sidebands will be determined by the design of the filter. In a computer analysis of the performance of a two plate filter (coupled with an extra polarising plate), Holtom and Teschke[32] predicted the existence of two sidebands on either side of each maximum in the transition curve (Figure 5.23). The separation of the sidebands and maximum peak was calculated to increase linearly with exciting wavelength, which tallies well with our observed results. Table 5.4 illustrates the approximate positions of the main peak and lower energy sidebands, as estimated from the transmission curves in reference 32. The second lower energy sidebands are spaced approximately twice as far from the exciting line as the first, adjacent sideband.

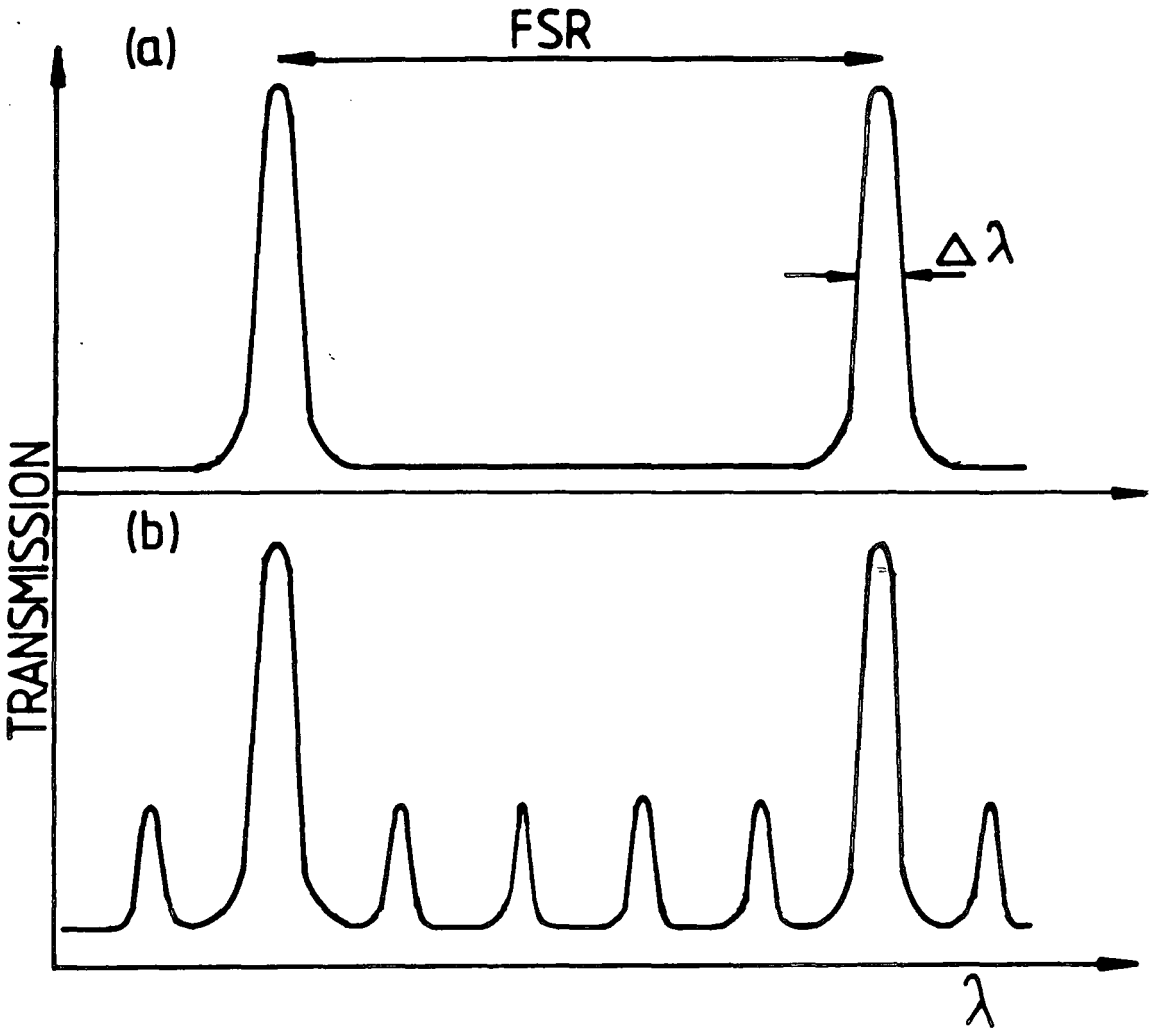

FIGURE 5.23 Transmission characteristics of a birefringent filter as a function of wavelength.

(a) Ideal transmission curve - free spectral range (FSR)=80-100nm $\Delta\nu \simeq 2$ cm^{-1} at 600nm.

(b) Qualitative representation of actual transmission curve. If the sidebands associated with each maximum are above the lasing threshold, extra emissions will be observed. For a qualtitative transmission curve, see reference 32. Note, band spacing actually increases linearly with λ.

TABLE 5.4 Transmission characteristics of a two plate birefringent filter as estimated from the work of Holtom and Teschke.

Main band position Absolute/nm	1st sideband position	
	Absolute/nm	shift/nm
553	568	15
579	595	16
623	643	20

These figures are not too dissimilar to the behaviour which we observed with our birefringent filter. Exact agreement would not be expected, since the sideband position and amplitude is dependent upon filter design. However, they do provide qualitative evidence for the assignment of the spurious bands as being due to transmission sidebands of the filter.

In order to obtain further evidence for this assignment, it was noted that there should also be sidebands on the high energy side of the exciting line, *i.e.* we expect to observe a band in the antistokes region of the Raman spectrum, with roughly the same wavelength shift as the lower energy sideband. This was tested by tuning the dye laser to 16274 cm^{-1} (*ca.* 614nm) and scanning the Raman spectrum over the region -800 cm^{-1} to *ca.* 1100 cm^{-1} (Figure 5.24). The laser beam was attenuated over the region -180 cm^{-1} to +180 cm^{-1} by a factor of *ca.* 10^{-5}, in order to safely scan the exciting line and Rayleigh wings.

The spectrum clearly shows the presence of the sidebands, at *ca.* +605 cm^{-1} and -610 cm^{-1} from the exciting line. In terms of absolute wavelength, this corresponds to a main peak at *ca.* 614nm with sidebands at 592 and 638nm (separations of

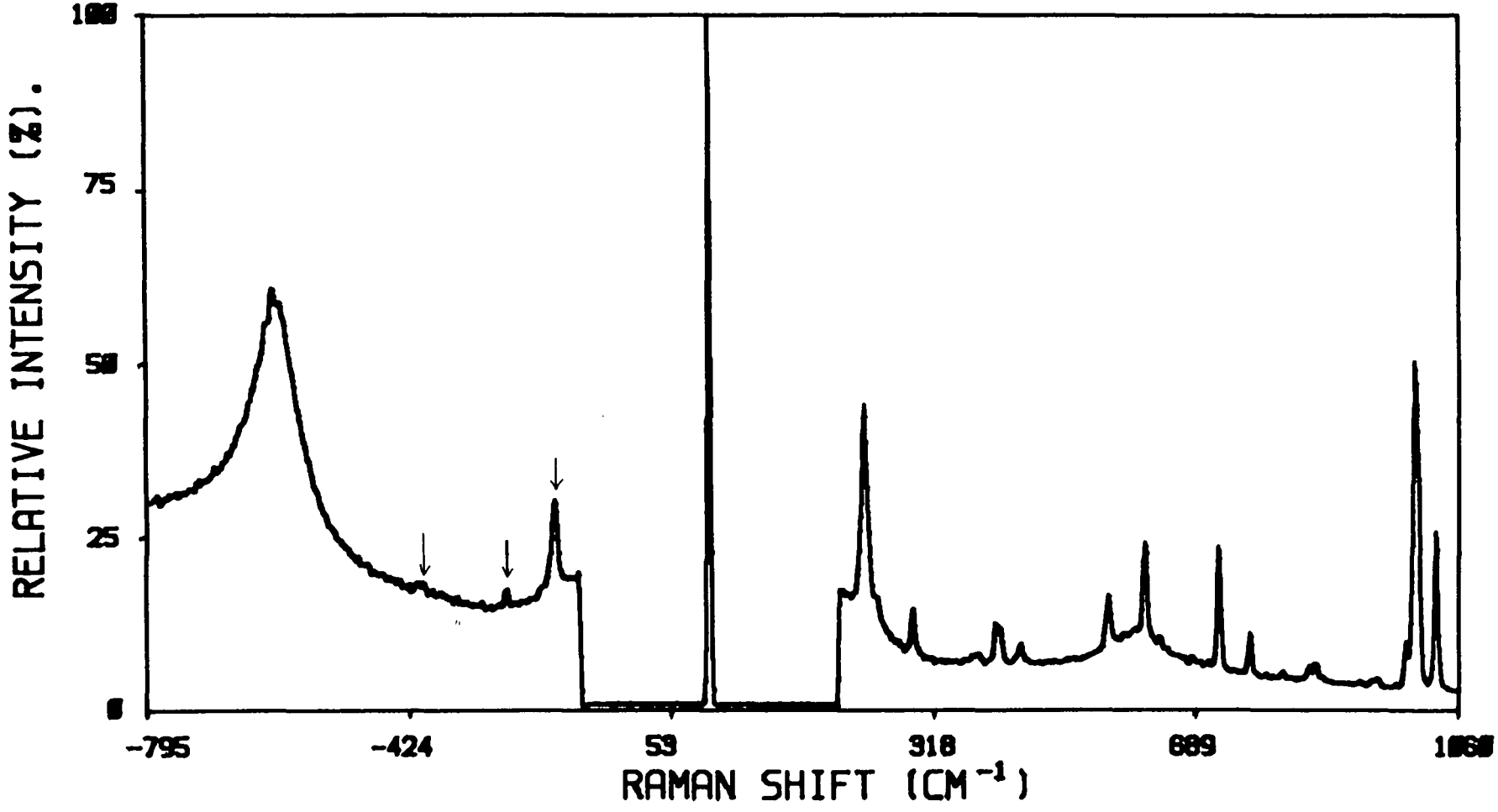

FIGURE 5.24 Spectrum of benzophenone, $\lambda_{ex} \simeq 614$nm (25mW). High energy sideband gives rise to features in antistokes region, at *ca.*-610 cm^{-1}. Laser was attenuated (10^{-5}) to scan Rayleigh line. Bands marked (↓) are antistokes Raman bands.

22 and 24 nm respectively). This is in qualitative agreement with the trends predicted by Holtom and Teschke. The small features observed at *ca.* -218 cm^{-1} and 288 cm^{-1} are antistokes Raman bands arising from the 218 cm^{-1} and 288 cm^{-1} vibrational modes, which are observed in the stokes region. The high energy spurious band (592 nm) is more intense than the 638 nm band because it lies at the peak of the gain curve for R6G dye,[14] whereas the 638 nm band occurs near the cutoff region (Figure 5.25).

This figure also explains the reason why the sidebands in Figures 5.18 and 5.21 increased in intensity as the exciting wavelength was raised. Excitation at 572 nm places the low energy sideband (592 nm) near the peak of the gain curve, while moving to longer excitation moves the sideband towards the gain cutoff region, thereby decreasing its intensity.

Finally, we note that while the evidence above strongly indicates that the transmission curve of the filter is responsible for the observed effects, we would expect that the width of the sidebands would be comparable to that of the exciting line. While this is manifestly not observed in the spectra above, this broadening could be due to an internal alignment problem in the birefringent filter, and is not incompatible with the behaviour postulated above.

5.5.5 Conclusions

The work described above has succeeded in identifying the origin of some puzzling artifacts which were obtained when recording the Raman spectra of highly-reflective solid samples. Whereas these artifacts were initially identified as arising from Raman transitions, more recent studies have provided very convincing evidence that they are in fact due to

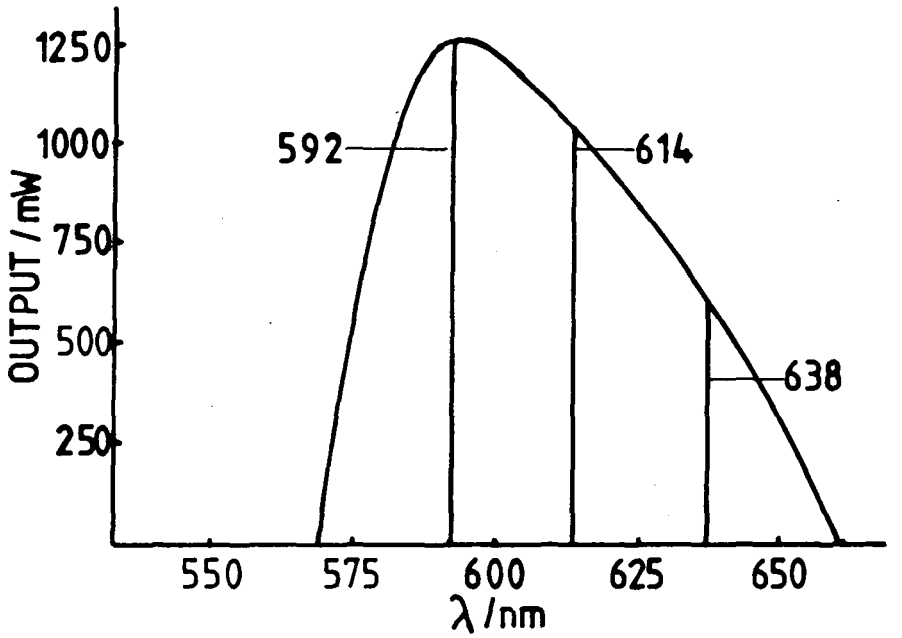

FIGURE 5.25 Transmission of lasing sidebands. Selection of a main lasing wavelength of 614nm results in sidebands at 592nm and 638 nm, which lie within the gain curve and so also lase, giving rise to spurious features in the Raman spectra.

sidebands in the transmission curve of the birefringent filter which is used to tune the dye laser output.

The presence of these sidebands are, in fact, well known to designers of birefringent filters, and have been described in the literature. Correct design of the filter can suppress the sidebands to a very low level, but it appears that, even when our filter is aligned to within the manufacturer's specifications, these extra emissions are still above the gain threshold of the laser. The lasing sidebands are, admittedly, of a much lower power than the main output (*ca.* 10^{-5}-10^{-6} fold decrease), but even this low intensity is comparable to (or greater) than the intensity of the Raman features which are being investigated. This can yield very confusing results if one is unaware of this aspect of the behaviour of the filter. It would certainly be useful if the manufacturers made users more aware of this potential problem in their literature.

5.6 Overall conclusions

This chapter summarises both the theoretical aspects of the operation of the laser system, and the practical experience which has been gained in characterising and optimising its performance. It should be clear that, although the system is a commercial instrument, it has not been thoroughly characterised, and there are several aspects to the performance of which the manufacturers were either unaware, or failed to stress in their literature. Certain of these factors, such as the contribution of leakage light at low repetition rate, are of crucial importance in determining the quality of results obtained in this system. This will become more apparent in the following chapters

REFERENCES - CHAPTER FIVE

1. O. Svelto, "Principles of Lasers", Plenum Press, New York, London (1982).

2. P.W. Smith, Proc. I.E.E.E. 58 (9), 1342 (1970).

3. R.N. Bracewell, "The Fourier transform and its applications", McGraw-Hill electrical and electronic engineering series, McGraw-Hill, New York (1978).

4. D.C. Champeney, "Fourier Transforms and their Physical Applications", Academic Press, New York, London (1973).

5. R. Adler, I.E.E.E. Spectrum, May, 42 (1967).

6. P. Debye, and F.W. Sears, Proc.Nat'l. Acad.Sci.(USA), 18 409 (1932).

7. E.J. Gordon, Proc.I.E.E.E. 54 (10), 1391 (1966).

8. S.E. Harris, Proc. I.E.E.E. 54 (10), 1401 (1966).

9. C.V. Shank, and E.P. Ippen, Appl.Phys.Lett. 24 (8), 373 (1974).

10. L.E. Hargrove, R.L. Fork and M.A. Pollack, Appl.Phys.Lett. 5, (1), 4 (1964).

11. A. Yariv, J.Appl.Phys., 36 (2), 388 (1965).

12. F.P. Schafer, (Ed.), "Dye Lasers, Topics on Applied Physics 1 Springer-Verlag, Berlin, Heidelberg, New York (1973).

13. C.V. Shank, Rev.Mod.Phys., 47 (3), 649 (1975).

14. "Continuous Wave Dye Lasers - Properties and Performance Reports", Spectra-Physics Laser Products Division, Technical Report.

15. B.H. Soffer and B.B. McFarland, Appl.Phys. Lett., 10, 266 (1967).

16. G.R. Fleming, D. Waldeck and G.S. Beddard, Il Nuovo Cimento, 63B (1), 151 (1981).

17. C.K. Chan and S.O. Sari, Appl.Phys.Lett., 25 403 (1974).

18. J.M. Harris, R.W. Chrisman, and F.E. Lytle, Appl.Phys.Lett. 26, 16 (1975).

19. C.K. Chan, "Spectra Physics Technical Bulletin" (8),(1978).

20. Spectra-Physics "Model 3446 High Efficiency Cavity Dumper Instruction Manual".

21. R.H. Johnson, I.E.E.E. J. Quantum.Electron., QE9, 255 (1973).

22. N. Everall, J. Howard, R.W. Jackson and K. Hutchinson, J.Raman.Spectrosc., 17(5), 415 (1986).

23. N. Everall, J. Howard, R.W. Jackson and K. Hutchinson, J.Phys.E:Sci.Instrum., in press.

24. N. Everall, J. Howard, K. Hutchinson and R.W. Jackson, Rev.Sci.Instrum., 56(12), 2335 (1985).

25. I.S. Ruddock and R. Illingworth, J.Phys.E:Sci.Instrum., 18, 121 (1985).

26. J.A.Armstrong, Appl.Phys.Lett., 10, 16 (1967).

27. H.E. Rowe and Li. Tingye, I.E.E.E. J.Quantum Electron., QE-6 (1), 49 (1970).

28. G.R. Haugen, B.W. Wallin and F.E. Lytle, Rev.Sci.Instrum., 50 (1), 64 (1979).

29. A.E.McKinnon, A.G. Szabo and D.R. Miller, J.Phys.Chem., 81 (16), 1564 (1977).

30. Dr. A.G. Szabo, National Research Council of Canada, Personal communication.

31. J.W. Evans, J.Opt.Soc.Am, 39 (3), 229 (1949).

32. G. Holton and O. Teschke, I.E.E.E. J. Quantum Electron., QE10 (8), 577 (1974).

33. M. Born and E. Wolf, "Principles of Optics", Pergamon, New York (1970).

34. F.G. Smith and J.H. Thomson, "Optics", J.Wiley and Sons, London, New York, Sydney, Toronto (1973).

CHAPTER SIX

A COMPARISON OF DETECTORS AND GATING METHODS FOR TIME RESOLVED FLUORESCENCE REJECTION

6.1 Introduction

In this chapter practical arrangements for time-resolved fluorescence rejection (TRFR) are considered. Emphasis is placed upon the physical principles upon which the methods are based; detailed evaluation and specifications are given in Chapters Seven and Eight.

It has already been stated (Chapter Four) that there are two basic approaches to time-resolved detection. The first involves directly gating the photosensitive device itself, such that it only registers the arrival of a photon during specific time periods. The detector is only "switched on" for a selected time interval. The effectiveness of this method depends primarily upon the time evolution of the detector sensitivity during the gating period, *i.e.* the shape of the "gate", and the maximum repetition rate at which the gate may be triggered.

An alternate technique lies in continuously operating the detector while it is exposed to optical pulses, and processing the output with suitable timing electronics. This is referred to as "indirect gating" of the detector, and has been one of the most widely used approaches for time-resolved photon counting. However, it is only comparatively recently that equipment with sufficient timing precision has become available for effective TRFR.

Regardless of which technique is chosen, the ultimate signal/noise of a Raman spectrum attained by TRFR is limited by the timing resolution, the gating repetition rate, and the power of the laser pulses which are delivered to the sample. Only the first two factors are considered in this chapter, while the third is discussed in Chapters Seven and Eight.

Examples of both of the gating techniques have been evaluated in this laboratory. Direct gating has been achieved through the use of an intensified diode array detector (DAD), which may be switched on for periods as short as 5 ns (FWHM sensitivity), at repetition rates of up to 4kHz with a switching speed (on→off), of *ca.* 3 ns. We have also investigated the use of time-correlated photon counting (TCPC), with a PMT and associated fast-timing electronics. This yields a substantially better timing resolution than the gated DAD (IRF widths as narrow as *ca.* 775 ps were achieved), and allowed the use of *ca.* 1000-fold higher laser repetition rates. It is apparent that we would expect superior R/F and R/N improvements with this latter mode of detection, and this is indeed found with the present equipment. However, modifications have been identified which should make the gated DAD a useful system for TRFR, and so this device is treated in some detail in the following sections.

Each of these approaches has specific advantages and disadvantages. However, before a detailed evaluation of the two techniques can be presented, it is necessary to consider the mode of operation of each apparatus. Therefore, the following sections contain a discussion of the construction and operation of the detection systems. Theoretical models for the performance of each detector are presented in Chapters Seven and Eight, along with experimental results illustrating their effectiveness in TRFR.

6.2 An introduction to intensified multichannel detectors and their use in time resolved optical spectroscopy

6.2.1 Introduction

In the following sections we consider the use of directly gated intensified multichannel detectors for time-resolved optical spectroscopy, with particular regard to low light level detection. This section describes the rationale of multichannel detection, and the types of detector which have been employed. Section 6.3 contains a description of the construction and physical operation of a typical intensified diode array detector (DAD), and explains how such a device may be temporally gated. The thermal generation of charge in the array (dark charge), which results in a large background upon which optical signals are superimposed, is also discussed.

We are particularly interested in obtaining Raman spectra of samples where the dominant noise source is a fluorescence background, rather than stray light or detector noise. It is found that the noise contribution of multichannel detectors is very much dependent upon whether or not the device contains an image intensifier. For this reason, Section 6.4 contains a detailed discussion of the effect of image intensification upon the S/N ratio of spectra accumulated with a DAD. This is one of the most important aspects of the operation of the device.

One might naively expect that the action of the image intensifier is to simply increase the optical signal such that it is much greater than the dark charge background. In fact, this is not the case. A detailed examination of the statistics of photoelectron generation and multiplication in an intensified detector reveals that the image intensifier

actually changes the statistics which the optically generated charge in the detector obeys, such that the noise associated with the optical signal is much greater than that of the observed dark background. Thus spectra are photon-noise limited even when the dark charge is *ca.* 100 fold higher than the photoelectric charge.

Although the fact that the intensified detectors can provide photon-noise limited detection is well known, the reason for this behaviour has not been stressed in the spectroscopic literature, and so the derivation of this result is presented in Section 6.4. If this result did not hold the background noise would be determined solely by the dark charge and there would be little point in employing fluorescence rejection techniques, since this would not improve the S/N ratio of the spectra.

Section 6.5 contains a brief consideration of situations where image intensification is not needed or positively degrades data quality. However, since the intensifier provides the means by which gating is achieved, this does not affect the choice of detector for TRFR work.

Finally, after the PMT based rejection system has been described, the relative merits of the directly gated multichannel detector and the indirectly gated PMT are summarised. Quantitative performance details are given in Chapters Seven and Eight.

6.2.2 The advantage of multichannel data accumulation

Multichannel detectors are now widely used in many branches of spectroscopy.[1-8] In this chapter we specif-

ically consider their use as gateable optical detectors, with particular reference to the low light-level quantification which is required in Raman spectroscopy.

In single channel optical spectroscopy, the detector is placed at the exit slit of a monochromator. Only radiation lying within the (narrow) spectral bandpass of the monochromator reaches the detector at any one instant, and so the spectral information at all other wavelengths is rejected. The optical multichannel detection (OMD) system utilises an array (1 or 2 dimensional) of individual photosensitive devices, positioned at the focal plane of a spectrograph. A wide bandwidth of radiation is dispersed across the photosensitive array, such that each discrete detector records data over a specific wavelength range.

The OMD system has the advantage that spectral information over a range of wavelengths (governed by the dispersion of the spectrograph and the size of the array) is accumulated simultaneously. This can greatly enhance the S/N of spectra or reduce the accumulation time required for a given S/N. For example, if we assume that each detector has the same quantum efficiency, a linear array of N elements (usually 512 or 1024), can accumulate an N channel spectrum in $1/\sqrt{N}$ of the time required by a single channel detector to produce a spectrum of equal S/N, assuming Poisson statistics.

The shortest scan time achievable with a DAD is of the order of milliseconds. This rapid data accumulation makes the OMD particularly suitable for recording the time evolution of spectra over relatively long (*e.g.* ms-s) timescales.[9] When the OMD is coupled with a pulsed laser system,

data acquisition on the ps timescale can be achieved. Bridoux *et al*[10] reported Raman spectra obtained from a single 25 ps laser pulse. It is important to note, however, that the OMD records all signals occurring during the entire scantime,and this limits the actual time resolution of the device itself to milliseconds rather than picoseconds (Section 6.3.3). For our work we require time resolution on ns timescales, and so direct gating of the OMD is necessitated.

The relative merits of single and multichannel detection have been reviewed in the literature[1,2,6] and so only characteristics relevant to the time resolution and noise associated with each type of detector are discussed in this thesis.

6.2.3 Types of multichannel detector

There are several types of OMD which are suitable for spectroscopic applications. The simplest example is the photographic plate, which can store a large amount of information (10^8 bits for a single 35mm format exposure). However, this medium is far from ideal in that the sensitivity and dynamic range are poor, and the response is nonlinear. Also, quantification of the stored information is difficult. Photoelectric detectors are much more suitable as multichannel analysers, since they are sensitive, highly linear, have a wide dynamic range and store the information in digitised form, which is convenient for subsequent processing. A wide range of these detectors are now used in optical spectroscopy, including silicon photodiode arrays, charge-coupled devices (CCDs), charge injection devices (CIDs), and Vidicon cameras.[1,2,5]

The operating characteristics of these detectors (*i.e.* noise, dynamic range and data acquisition/transfer rate) vary widely, which affects their suitability for certain applications. These considerations have been well reviewed in the literature.[5] Here it suffices to comment that the arrays may be linear or 2 dimensional, with the latter devices being used to date primarily for image analysis rather than spectroscopic purposes.

The work described in this thesis was performed with an intensified silicon photodiode array detector, which is described fully in Section 6.3.

6.2.4 Intensified multichannel detectors

In optical spectroscopy, the limiting S/N ratio which may theoretically be achieved is that of the photon flux incident upon the detector. This S/N is only attained if the detector has a quantum efficiency of unity, and if the optical intensity is sufficiently high that its shot noise is greater than that generated by the detection system itself (Section 6.4). It may therefore be necessary to amplify the photon flux prior to detection by the array, such that the detector noise is insignificant in comparison. This is achieved through the use of an image intensification stage.

It is important to realise that image intensification is only necessary if the detector noise is comparable to or greater than the photon shot noise (see Section 6.5). The detector noise is device dependent, (for example, readout noise of a typical CCD is an order of magnitude less than that of a silicon diode array[5]), and so a careful choice of device may eliminate the need for an expensive (and easily damaged) intensification stage.

It was pointed out above that the effect of image intensification is not simply to amplify the photon flux, but also to change its statistical behaviour. The effect of intensification upon the S/N ratio of spectra is considered in Section 6.4, where the photoelectron statistics of intensified and unintensified detectors are analysed. A quantitative description of photoelectron noise in detectors is essential to the formulation of a mathematical model of fluorescence rejection.

6.2.5 Direct gating of multichannel detectors

The use of an intensification stage aids time-resolved photon detection over ns timescales,[6] since, when the intensifier is disabled, no photons are recorded and the detector is essentially gated "off". This provides gates of down to *ca.* 6 ns width (FWHM of "on" period) with on/off ratios of $>10^6$. Direct gating of intensification stages is not unique to multichannel detectors; many attempts have been made to gate the dynode-chain electron-multiplier of PMTs.[11-19] In these attempts, resolution has been largely limited to μs timescales, due to the difficulty in switching the gain of the multistage dynode chain multipliers, although switching on ns timescales has been achieved with PMTs containing special focussing electrodes.[11-13,18] Gating performance is somewhat superior (in terms of on/off ratios and gate width) for the channel electron multipliers used with multichannel detectors, compared to dynode-chain PMTs.[6] Even if the gain switching were equally effective for each device, the multichannel data acquisition could make the DAD the more favourable option.

Gated OMDs have been used predominantly for following the rapid (μs-ns) time evolution of spectra by sequentially recording separate spectra at given time intervals.[20-22] It is much more difficult to actually resolve a weak signal (Raman) from a stronger one (fluorescence) which has a similar time response. The work described in Chapter Seven was the first reported attempt to use a directly gated diode array for fluorescence rejection studies.[23]

6.3 Construction and operation of an intensified silicon photodiode array

6.3.1 General construction

Figure 6.1 illustrates the essential components of the intensified silicon photodiode array detector which was used in this laboratory. The detector consists primarily of an image intensifier which is coupled to a linear self-scanned photodiode array.[24] Before considering the properties of the image-intensifier, it is instructive to briefly review the operation of the diode array itself.

The photodiode array is an integrated circuit fabricated on a single silicon chip. It consists of a linear array of 1024 individual silicon photodiodes (SPD), each of which is formed from a p-type silicon bar which has been diffused into an n-type silicon wafer (Figure 6.2). Each diode is 2.5mm high and 13μ wide, with an inter-diode spacing of 25μ. The entire array is covered with a protective layer of SiO_2.

The diodes are reverse-biased (*i.e.* the p-type region is held at negative potential to the grounded n-type wafer). This results in a net accumulation of charge (the

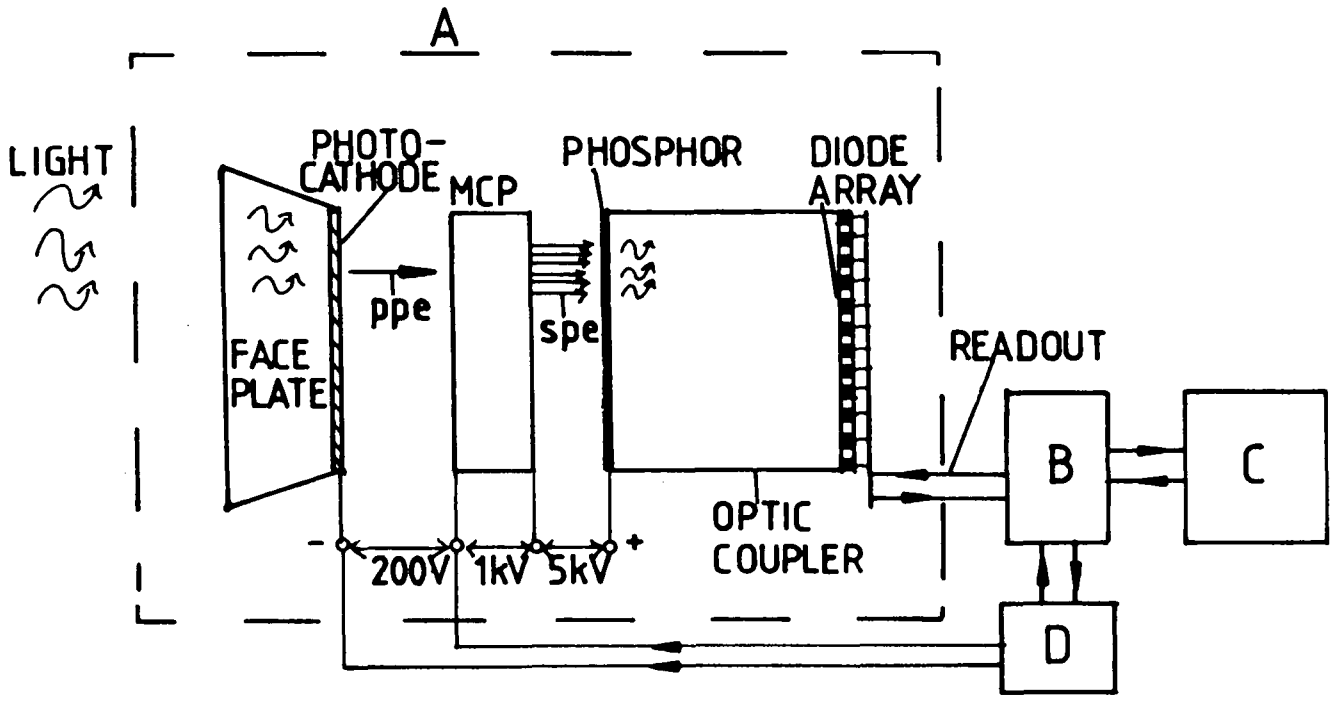

FIGURE 6.1 Schematic of DAD (not to scale).

A. Spectroscopy Instruments (S.I.) model IRY700 diode array detector.

B. S.I. model ST110 controller.

C. LSI 11/23 minicomputer.

D. SI model MD100 fast pulser.

ppe ≡ primary photoelectron, spe ≡ secondary photoelectron.

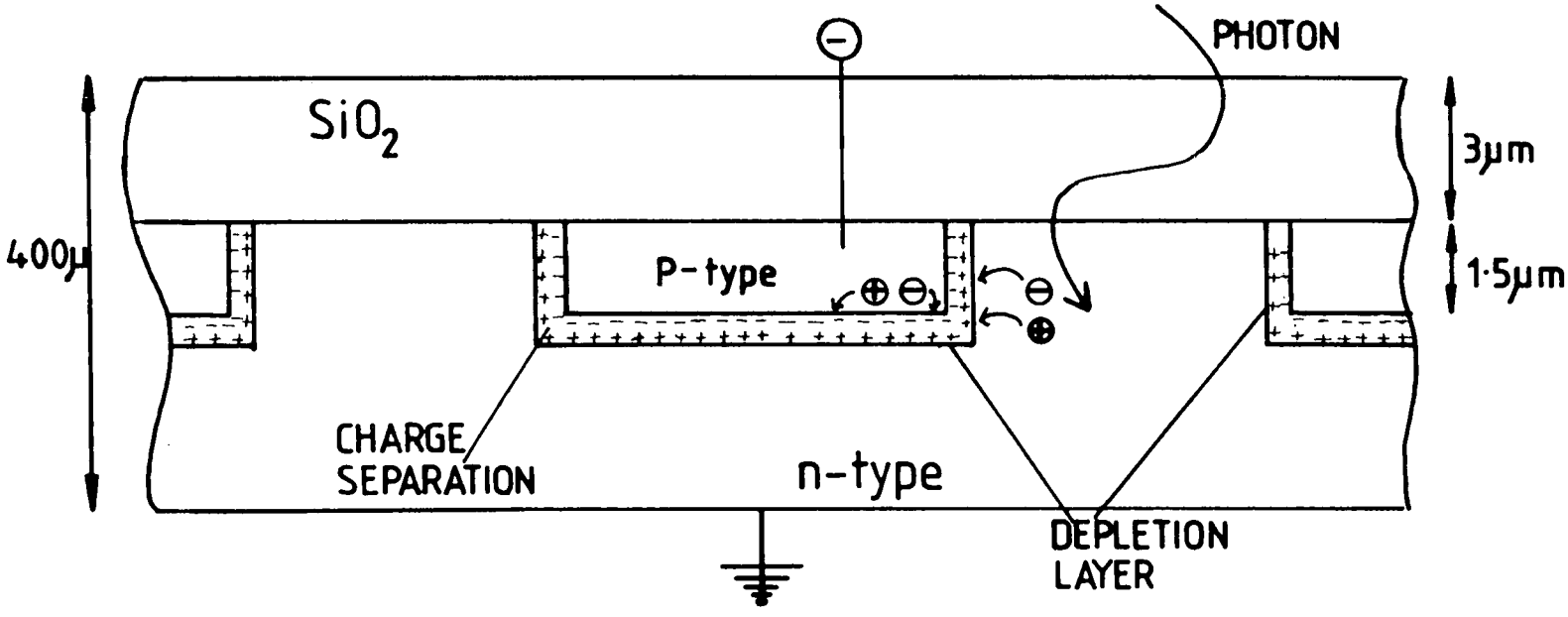

FIGURE 6.2 Photodetection in an SPD array.

Charge is stored at the reverse biased p-n junction, which is then isolated from the voltage source. Thermal or photoelectrically generated-charge diffuses into the p-n junction and discharges the diode. The current required to re-bias the diode to the original potential is measured on readout.

"saturation charge") at the p-n interface, the magnitude of which is determined by the p-n junction capacitance and the reverse bias voltage.

Prior to beginning a charge integration, the diode is biased to a reference voltage and then allowed to "float". Photons which strike the array penetrate into the silicon wafer, inducing the formation of electron-hole pairs which diffuse into the reverse-biased p-n junction, decreasing the charge stored by that particular SPD (Figure 6.2). The magnitude of the decrease in stored charge is proportional to the number of photons which have been absorbed by the SPD. Photons may be accumulated for a variable time period (the integration time) prior to data readout. The maximum integration time is determined by the charge capacity of the SPD, the radiation intensity, and the rate of accumulation of dark charge.

6.3.2 Dark charge and dark noise

Electron-hole pairs are also generated thermally in the array. This is known as dark charge formation, and yields a signal which increases linearly with integration time. When the light intensity is low, the dark current may determine the maximum integration time, and so effectively reduces the useful dynamic range of the detector. Furthermore, the shot noise of the dark charge can mask a weak optical signal unless an image intensifier is used to amplify the photon flux (Section 6.5).

6.3.3 Readout of the diode array

Figure 6.3 is a schematic representation of the circuit used to measure the charge distribution on the array. Each photodiode is individually linked, through an FET (Field

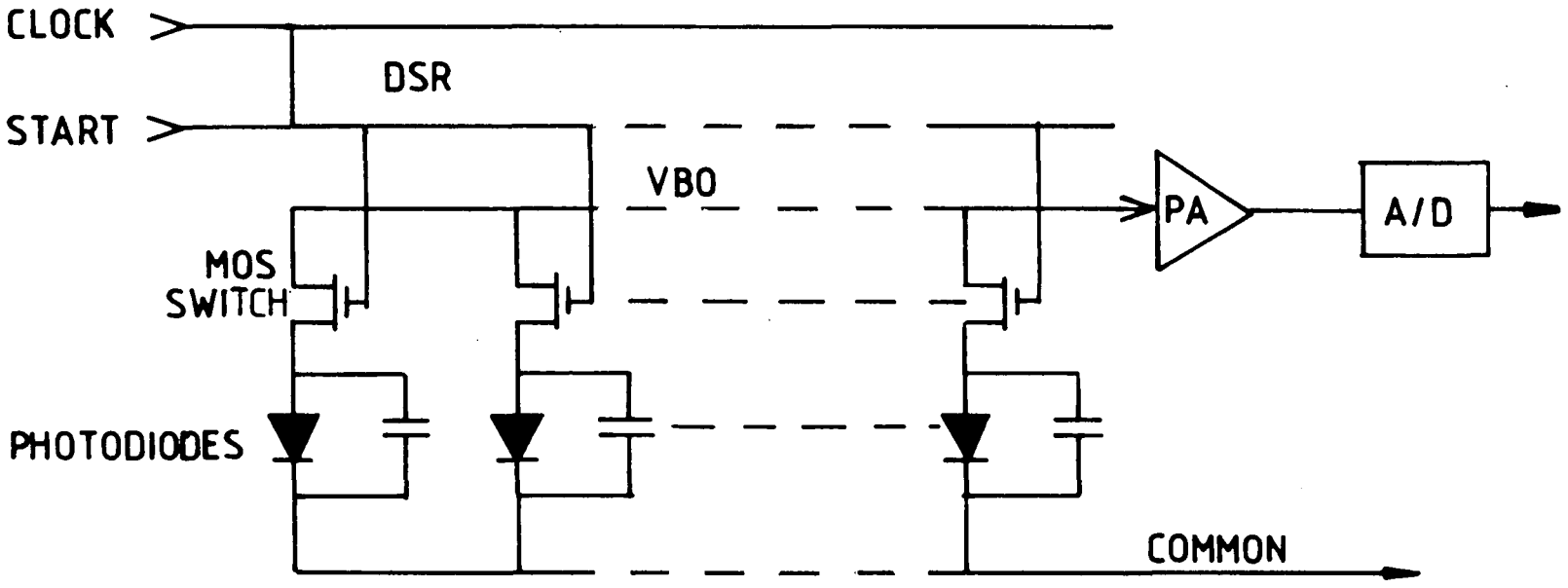

FIGURE 6.3 Readout circuitry for diode array. See text for details.

A/D ≡ analog/digital converter. DSR ≡ digital shift register.

PA ≡ preamplifier. VBO ≡ video bus output

Effect Transistor) switch, to a video-bus and a digital shift register (DSR). In addition, all photodiodes are permanently strapped to a common bus which supplies charging current during the readout cycle.

During readout, the DSR sequentially closes the FET switches, which complete a circuit from the common bus, (Figure 6.3), through the diode to the input of a charge-sensitive preamplifier (video bus). The saturation charge is restored on each photodiode when the switch is closed, and the recharging current for each diode is amplified and input to an A/D converter. The output signal from a complete scan of the array therefore consists of a series of digital values, which represent the state of discharge of each photodiode and therefore may be related to the light intensity over that particular region.

Control of the readout/accumulation cycles is achieved by the ST-100 controller (Figure 6.1). The array is scanned continuously (33.8ns per scan) but the diodes are not necessarily read out (re-biased) on each scan. On target signal accumulation may be performed for up to 4096 scans (138 secs) provided that the A/D dynamic range is not exceeded. The shortest accumulation time is 33.8 ms (1 scan). In memory averaging (*i.e.* numerical averaging of spectra stored in the controller memory) can also be performed. This is useful when adequate S/N cannot be obtained from 1 spectrum with a long accumulation time. Accumulated spectra are manipulated and displayed with a DEC LSI 11 computer.

When the diode array is used in an unintensified configuration, it is simply placed at the focal plane of a suitable spectrograph, such that radiation is dispersed across

the chip. Each SPD then detects radiation lying within a particular frequency range, which is determined by the dispersion of the spectrograph and the spatial response function of the individual diodes.[24] Such a configuration is unsuitable for detection of low intensity signals, because noise from the detector may swamp the signal of interest. Under these circumstances, an intensification stage is required.

6.3.4 Image intensification and MCP operation

The MCP intensifier[5,6,25] consists of a photocathode coated onto a fibre optics faceplate, which is positioned near (300μm) a mosaic of channel electron-multipliers (Figure 6.4). Each channel is a hollow glass fibre, some 10-40 μm in diameter, with an internal resistive coating. The channels are arranged in a regular array (*ca.* 10^6 per cm^2) and are connected in a parallel circuit by electrodes at either end of tubes. The front end is maintained at a positive potential with respect to the photocathode, in order to capture photoelectrons liberated by photons striking the photocathode. Since the microchannel plate is in close proximity to the photocathode, the integrity of the "image" formed by the incident radiation is preserved in the spatial distribution of the primary photoelectrons accepted by the MCP; the electrons cannot move an appreciable lateral distance before capture.

The primary photoelectrons are accelerated down the channels through a potential difference of about 1kV, and collisions with the walls induce secondary electron emission with a gain of *ca.* 10^3-10^4 (controlled by the voltage across the MCP).

The time taken (transit time) for the pulse of

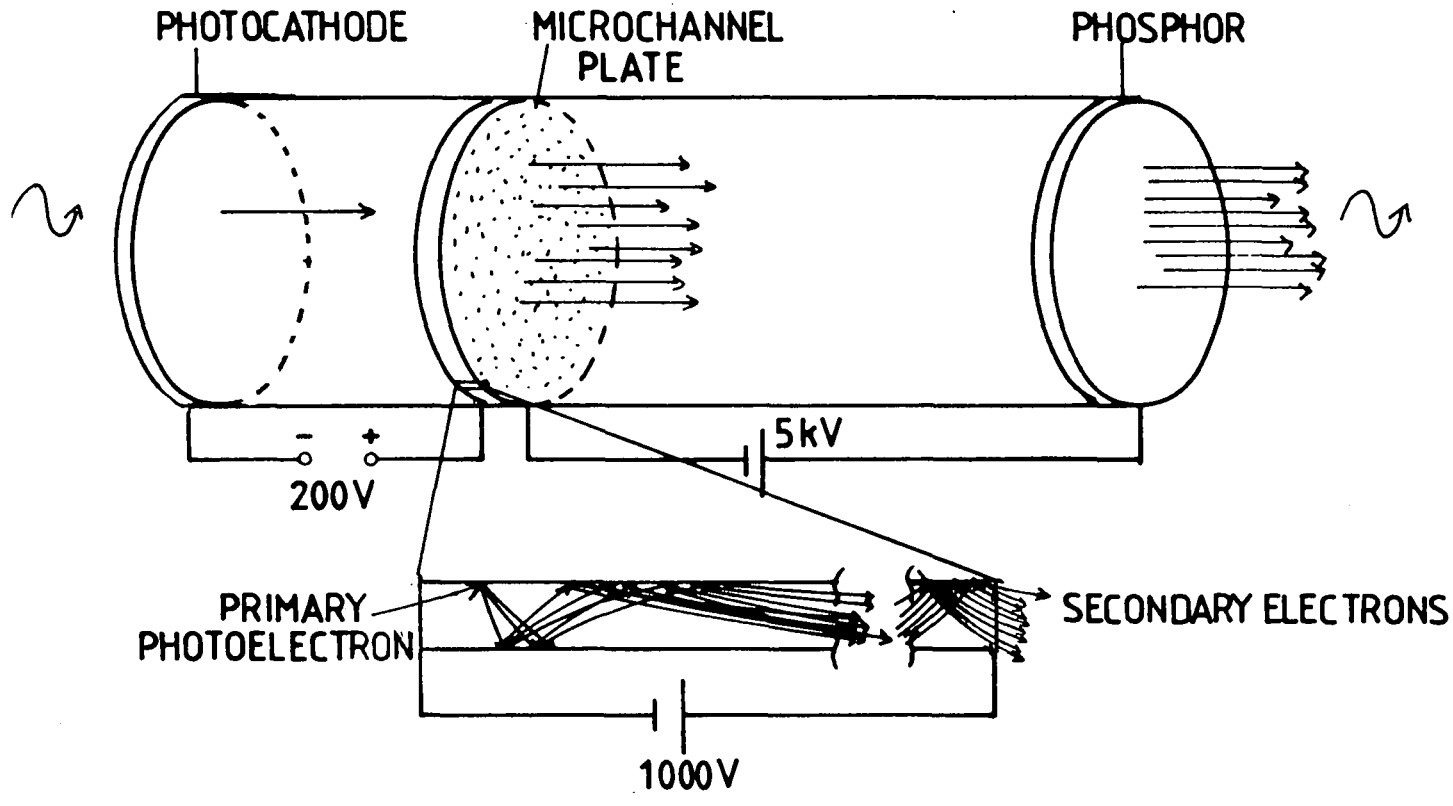

FIGURE 6.4 Schematic of microchannel plate image intensifier (not to scale)

See text for details.

secondary electrons to traverse the MCP is of the order of 1 ns. The proximity of the MCP to the photocathode, and the narrowness of the channel restricts the possible variation in path-lengths traversed by the electrons. This results in the MCP having a very low transit-time spread,[26] (the variation in time taken for a "pulse" of photoelectrons to propagate through the MCP after a photon strikes the photocathode), compared to conventional, dynode-structure electron multipliers.[25,27] While this is not an important factor in determining the timing resolution of the gated diode array, it turns out to be crucial to the performance of the PMT based rejection system (Section 6.7).

The secondary photoelectrons emerging from the MCP are accelerated through about 5 kV and strike a P-20 phosphor screen. The resultant luminescence is an intensified reproduction of the original image on the photocathode. The intensified image is coupled to the photodiode array by fibre optics, whereupon the photon intensity is quantified in the manner already described above. Unfortunately, the MCP has a diameter of 18mm (compared to the diode array length of *ca.* 25mm), which means that only the central 700 of the 1024 photodiodes are subjected to the intensified illumination. This reduces the spectral bandwidth accessible by the array by *ca.* 1/3 compared to an unintensified detector.

Clearly, thermionic emission could occur from the photocathode of the intensifier, which would add to the dark charge thermally generated in the array. According to the manufacturers specifications,[28] the rate of dark charge accumulation is *ca.* 100 counts/sec irrespective of whether the detector is intensified or not, which implies photocathodic emission is not significant. It is observed that temporally

gating the detector (which should reject photocathodic emission) does not appear to affect dark charge levels, and so thermionic emission is unlikely to be a significant background source.

6.3.5 Temporal gating of the detector

In addition to the intensification process, the MCP also provides a means of temporally "gating" the photosensitivity of the DAD.[6] This may be seen by considering Figure 6.4. If the detector is operated without the small accelerating potential (-200V) between the photocathode and the MCP, the primary photoelectrons are not captured and very few photons actually reach the photodiodes. Application of a *ca.* -200 V pulse between the photocathode and the MCP attracts photoelectrons to the MCP, and so the detector responds to incoming photons for the duration of the voltage pulse. Photons arriving at the photocathode at other times are rejected. The efficiency of this process is very high, the sensitivity ratio (pulse on/pulse off) being better than 10^6 for our detector.

Temporal gating does not reduce dark charge accumulation, since this occurs in the SPD and so bypasses the intensifier stage. This contrasts strongly with the indirect gating of a PMT output, where the dark signal is almost totally eliminated from the final spectrum.[29]

The maximum repetition rate at which the detector may be gated is specified by the manufacturer as 5kHz, with an "on" period of 5 ns (FWHM of sensitivity). If the -200 V is continuously maintained, the detector is always "on" and is referred to as being "ungated".

The exact change in detector sensitivity as a function of time during gating is of paramount importance in

our work (Chapter Seven), and is governed by two factors:

(a) A finite time is required for voltage changes to propagate over the whole area of the MCP. The centre of the MCP attracts photoelectrons for a longer period after the termination of the voltage pulse than does the edge of the plate. The transmission of secondary electrons gradually "closes down" towards the centre of the MCP in what has been termed the "iris effect". So even for a voltage pulse of infinitessimal rise and fall times, we cannot expect instantaneous "step-function" changes in sensitivity. The magnitude of the effect will clearly be governed by the capacitance and inductance of the plate.

(b) The second factor poses the most serious drawback at present, namely the shape of the -200 V pulse. Ideally the voltage pulse would be rectangular, with a width equal to the laser pulse duration. However, it is shown in Chapter Seven that both the rise-time and the pulse width are, to a large extent, not important for the purposes of fluorescence rejection. All that is required is to generate a pulse with the fastest possible fall-time. The pulse generator which is presently in use generates pulses with rise and fall-times of greater than 2 ns, and this results in comparable rise and fall-times for the variation in detector sensitivity over the duration of the gating pulse (Figure 6.5).

By varying the width and position of the -200 V pulse, we can gate the detector and selectively record photons which arrive during selected time intervals. (The experimental arrangement for synchronising the detector "on" period with the arrival of the photon pulse is discussed in Chapter Seven).

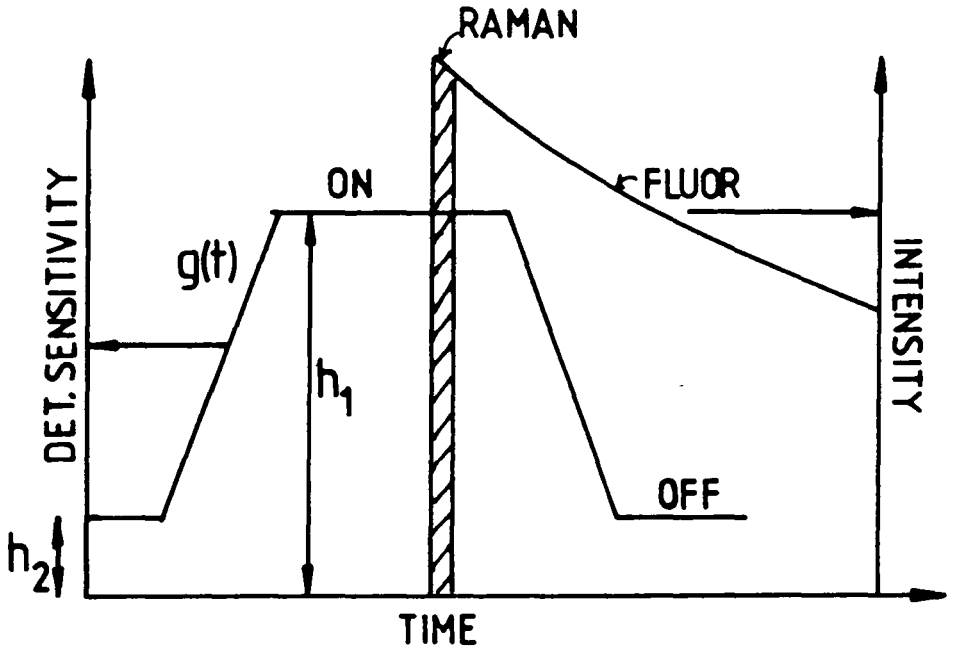

FIGURE 6.5 Observed temporal variation of detector sensitivity g(t) during gating pulse. Note, a trapezoidal rather than rectangular gate is observed, with $h_1/h_2 > 10^6$. The gate must be positioned to accept Raman photons but to reject most of the longer-lived fluorescence emission. The rejection efficiency depends upon the position of the gate and the gradient of the trailing edge, which should ideally have zero falltime for maximum fluorescence rejection.

For our application, we wish to "open" the detector to record the Raman photons, but cut off transmission such as to reject the longer-lived fluorescence emission. The rejection efficiency depends primarily upon the shape of the detector "gate" (Figure 6.5), and is discussed quantitatively in Chapter Seven.

6.4 Photoelectron statistics and noise in intensified/unintensified diode arrays

6.4.1 Introduction

A necessary prerequisite to the formulation of a model of the detector behaviour in TRFR is the quantification of the photoelectron statistics of the DAD. The change in S/N upon gating the detector will obviously depend upon the dominant noise source and its statistics, and so it is obviously important to estimate the contribution of the optical shot and the detector noise to the overall noise of the spectrum. Quantification of the photoelectron statistics of the intensified DAD in fact shows that even for low-light intensities, the spectra are photon shot noise limited. Therefore, the mathematical treatment of TRFR with a gated DAD need only consider the change in intensity of Raman and fluorescence signals, and detector noise may be neglected.

6.4.2 Sources of noise in the detection system

In an unintensified diode array, there are two primary sources of noise which are not correlated with the photon flux.

6.4.2.1 Dark noise (N_d)

Dark noise occurs as a result of thermal generation of charge in the array (dark charge). This is

found to vary in magnitude from diode to diode, and forms a fixed background pattern across the array. (It should be noted that other sources also contribute to the fixed background pattern[7]). Superimposed upon this fixed background there are statistical fluctuations in the charge levels. Although the background may be digitally subtracted from an accumulated spectrum, the associated shot noise (N_d) cannot be removed in this manner. The magnitude of the dark charge may be reduced by cooling the array, and is roughly halved for every 7°C reduction in temperature.[24] The detector employed in this work was Peltier cooled to -20°C, resulting in a dark charge accumulation of *ca.* 1.5×10^5 electrons/diode/sec.[28] The shot noise of the dark charge accumulated in 1 second is *ca.* 387 electrons rms/diode.

6.4.2.2 Readout noise (N_r)

Noise is also generated by the readout/amplification electronics (Figure 6.3) which quantify the stored charge and restore the saturation charge on the individual SPDs. This noise level is independent of integration time, and so its effect (in terms of S/N degradation) may be minimised by accumulating the largest possible charge on the array prior to readout. The noise of one readout is *ca.* 1500 electrons rms.

The magnitude of these contributions will vary according to the design of a particular type of array (and in fact substantial variations occur between devices of the same type), and so the values quoted above are only typical of the RL 1024 S chip used in our detector.[5]

Since the noise sources are not correlated, the total detector noise is given by equation (6.1):

$$N_{det} = (N_d^2 + N_r^2)^{\frac{1}{2}} \qquad (6.1)$$

The preamplifier/A/D converter (Figure 6.3) are adjusted such that 1500 electron/hole pairs in an SPD give rise to 1 output count in the digitised spectrum. The readout noise N_r is then approximately 1 count rms/scan/diode, and the dark charge accumulates at a rate of *ca.* 100 counts/sec/diode.[28] The dark noise increases as the square root of the integration time. If the S/N ratio of the photon flux is not to be degraded significantly by the detector, we require that the shot noise of the photoelectric charge in the array (N_{ph}) is greater than N_{det}. The conditions under which this criterion is satisfied are discussed below.

6.4.3 Statistics related to the generation and multiplication of photoelectrons

The statistics relating to photoelectron generation in optical detectors were originally applied to the analysis of noise in photomultiplier tubes,[26,30] but the same treatment may be extended to intensified/unintensified multichannel detectors. The quantity of interest is the noise associated with the number of photoelectrons formed (as a result of optical absorption) in the photodiode array (N_{ph}), compared with N_{det}, the detector noise.

First consider an unintensified array, subject to a photon flux I for a time t. The statistics of the generation of photoelectrons within the array are identical to those describing ejection of electrons from a photocathode, and are well known.[26]

Assuming Poisson statistics (Chapter Two), the incident optical signal (It) will have a shot noise of $(It)^{\frac{1}{2}}$, and a S/N of $(It)^{\frac{1}{2}}$.

The number of photoelectrons formed in the diode array is $I\phi_u t$, where ϕ_u is the quantum efficiency of the unintensified SPD. The noise (N_{ph}) associated with this signal may be shown[26] to be $(I\phi_u t)^{\frac{1}{2}}$, so the S/N of the photoelectrons formed in the array is $(I\phi_u t)^{\frac{1}{2}}$, *i.e.* a reduction of $\phi_u^{\frac{1}{2}}$ compared to that of the optical signal. Unless ϕ_u=1, the S/N ratio is inevitably degraded by the inefficient generation of photoelectrons.

Since 1500 photoelectrons yield 1 output count (see above), the optical spectrum produced by the DAD consists of a signal of $S = (I\phi_u t)/1500$ counts/diode, with a shot noise of $N=(I\phi_u t)^{\frac{1}{2}}/1500$ counts rms per diode.

6.4.4 The effect of image intensification upon S/N

The treatment of the photoelectron statistics of an intensified array is necessarily more complex than that given above. The processes occurring within the detector are illustrated schematically in Figure 6.6.

An incident photon flux of intensity I strikes a photocathode of quantum efficiency ϕ_1 for t seconds, causing the ejection of $\phi_1 It$ primary photoelectrons (with a shot noise $(\phi_1 It)^{\frac{1}{2}}$. These primary photoelectrons are then multiplied and strike a phosphor screen, resulting in the emission of photons which are absorbed by the diode array.

Typically, the gain of the multiplier is adjusted so that G=*ca.* 10^4. The incident photon signal is amplified to *ca.* $\phi_1 GIt$, and the number of electrons generated in the array is $\phi_1\phi_2 GIt$.

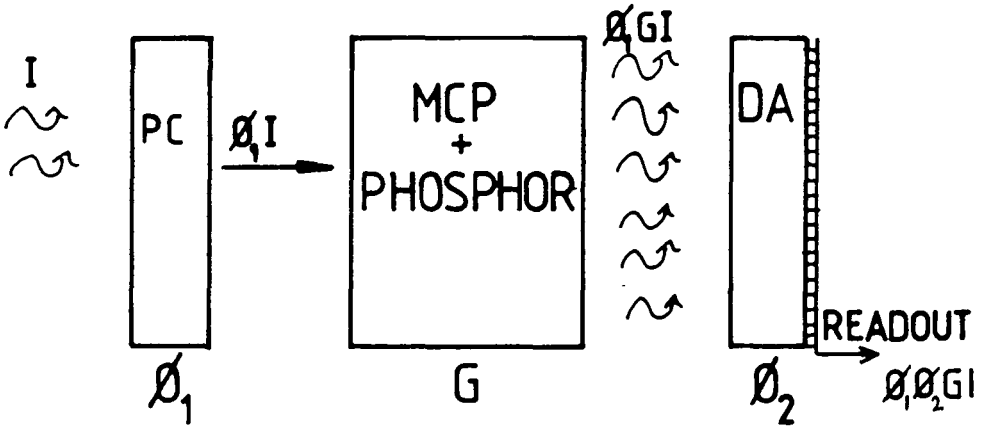

FIGURE 6.6 Statistics of intensification

ϕ_1 = quantum efficiency of photocathode (PC).

G = gain of MCP/phosphor,

ϕ_2 = quantum efficiency of diode array (DA), including the coupling efficiency between phosphor and array.

Incident photon flux I yields $\phi_1 I$ primary photoelectrons, $\phi_1 GI$ photons from the phosphor, and $\phi_1\phi_2 GI$ photoelectrons in the diode array. See text for details.

It has been shown[26] that amplification of a stream of electrons with a high gain multiplier does not significantly degrade the S/N ratio, *i.e.* the noise level of the signal is increased by the same factor (G) as is the signal itself, provided that the fluctuations in the gain (G) follow Poisson statistics. Therefore, the output of the intensifier is a signal of intensity $\phi_1 GIt$ with a shot noise of $G(\phi It)^{\frac{1}{2}}$. This should be compared to a source of photons of intensity $\phi_1 GIt$ which obeys Poisson statistics, *i.e.* has a shot noise of $(G\phi_1 It)^{\frac{1}{2}}$.

Calculation of the noise associated with the electrons generated in the array is most easily performed with the use of probability generating functions.[26,31] By this technique we find that the noise associated with the charge in the array is given by equation (6.2).

$$N_{ph} = (\phi_2{}^2\phi_1 G^2 It + \phi_1 GIt\ (\phi_1 - \phi_1{}^2))^{\frac{1}{2}} \qquad (6.2)$$

Since G>>1, equation (6.2) may be reduced to $N_{ph}=\phi_2 G(\phi_1 It)^{\frac{1}{2}}$ without incurring significant error.

The S/N of the charge in the array is given by equation (6.3).

$$S/N = \phi_1\phi_2 GIt/\phi_2 G(\phi_1 It)^{\frac{1}{2}} = (\phi_1 It)^{\frac{1}{2}} \qquad (6.3)$$

This important result shows that the S/N of the photoelectric charge stored in the array is equal to that of the primary photoelectrons ejected from the photocathode, and so the intensified detector should provide essentially noise free amplification. In practice, non-Poisson fluctuations in the gain will degrade the S/N somewhat, but this is shown to be not significant, and that the spectra are limited by photon shot noise, in Chapter Seven.

The gain of the MCP is adjusted such that 1 primary photoelectron ejected from the photocathode gives rise to 1500 photoelectrons in the diode array, *i.e.* 1 count. Therefore $G\phi_2=1500$ (equation 6.2), and the observed optical signal $S=(\phi It)$ counts/diode, with a shot noise $N_{ph}=(\phi_1 It)^{\frac{1}{2}}$ counts rms/diode. Clearly, with the intensified detector, $N_{ph}=(S)^{\frac{1}{2}}$, which contrasts strongly with the unintensified case of $N_{ph}=(S/1500)^{\frac{1}{2}}$.

6.4.5 A summary of photoelectric and detector noise levels in intensified and unintensified detectors

It is convenient to summarise the results of the statistical treatments performed above.

(a) Unintensified detector

SPD quantum efficiency ϕ_u, photon flux I, integration time t.

Observed photon signal $S = (\phi_u It)/1500$ counts (6.4)

Observed photon noise $N_{ph} = (\phi_u It)^{\frac{1}{2}}/1500 = (S/1500)^{\frac{1}{2}}$ (6.5)

Equations for the observed dark signal and noise may be obtained by replacing $(\phi_u I)$ by the rate of generation of dark charge, *ca.* 1.5×10^5 electrons/diode/sec (Equation 6.4).

(b) Intensified detector

Quantum efficiency of photocathode = ϕ_1.

$S = (\phi_1 It)$ counts (6.6)

$N = (\phi_1 It)^{\frac{1}{2}}$ counts rms $= S^{\frac{1}{2}}$ (6.7

6.4.6 Dark charge statistics for an intensified detector

It is important to realise that dark charge in an intensified detector follows the same statistics as that in an unintensified device, since it is generated directly in the

SPD and does not undergo any intensification. This is very important, since an observed dark background of S counts displays a shot noise of $(S/1500)^{\frac{1}{2}}$ counts, while an optical signal of equal intensity has an observed noise of $S^{\frac{1}{2}}$, *i.e.* $\sqrt{1500}$ times larger! For this reason, a weak optical signal may be resolved in the presence of a much more intense dark background. For instance, an optical signal of 10 counts could be resolved, (neglecting readout noise), with an S/N of 2, on a dark background of 22500 counts (greater than the A/D limit!). If both signals obeyed the same statistics, a dark background of only 15 counts would give the same S/N!

Thus, the function of the image intensifier becomes clear only through an analysis of the photoelectron statistics. The function is not merely to amplify the photon signal so that it is much larger than the dark charge (and indeed this rarely occurs when the detector is gated). The result of intensification is to change the statistical behaviour of the accumulated optical signal relative to the dark charge, such that $N_{ph} >> N_d$ irrespective of the relative size of the two signals. This point has not been widely appreciated in the literature.

The main problem with dark charge accumulation is actually that the A/D limit can be exceeded within *ca.* 160 seconds. This limits the maximum integration time and so reduces the effective dynamic range of the detector when optical signals accumulate slowly compared to dark charge.

It is interesting to note that if thermionic emission from the photocathode were responsible for the dark signal, the dark background would follow the same statistics as the optical signal and so the relatively small optical bands would be swamped by dark noise. In fact, we must expect some

contribution from this thermionic emission, which would imply that we require the photon rate to exceed the rate of thermal emission from the photocathode. This is in fact only true when operating in ungated mode; under gated detection, the vast majority (99.998%) of random, thermally emitted electrons are not detected, and so make no contribution to the dark charge.

6.4.7 Actual photon intensities required to give observable optical signals in intensified and unintensified devices

The quantitative effect of intensification is best seen by considering 2 simple examples.

6.4.7.1 1 second integration

(a) Unintensified array.

ϕ_u = *ca*. 0.7 at 600 nm.

At short integration times, the dominant noise source in the detector is the readout noise, *ca*. 1 count rms. The photon flux required such that $N_{ph}=N_r$ is given by $I = (1500)^2/(0.7)$ (Equation 6.5), or *ca*. 3.2×10^6 photons/diode/sec.

(b) Intensified array.

The quantum efficiency of an S-20 photocathode at 600 nm is only *ca*. 0.1, compared to 0.7 for an SPD. In order for $N_{ph}=N_r$, a flux of $I = 1/(0.1) = 10$ photons/sec/diode is required (equation 6.7), clearly much lower than the unintensified DAD.

6.4.7.2 60 second integration

(a) Unintensified array

At long integration times, N_d is significant. From

equation (6.5), $N_d = (1.5\times10^5\times60)^{\frac{1}{2}}/1500 = 2$ counts rms/diode, and $N_{det} = (1^2+2^2)^{\frac{1}{2}} = \sqrt{5}$. For $N_{ph} = N_{det}$, we require $I = (\sqrt{5}\times1500)^2/(0.7\times60) = 2.7\times10^5$ photons/diode/sec.

(b) Intensified array.

From equation (6.7), for $N_{ph} = N_{det}$, we require $I = 5/(0.1\times60) = 0.8$ photons/diode/sec.

The above calculations illustrate the fact that with an unintensified detector, the spectra will be detector noise limited unless $I>>2\times10^7$ photons/sec/diode. With an intensified detector, however, photon signals of a few counts/diode are sufficient to ensure that the spectral S/N is determined by that of the incident optical signal rather than the detector. This implies that the detector noise may be disregarded in the construction of any mathematical model to describe the S/N improvement obtained by TRFR.

6.5 Conditions under which image intensification is not necessary

The need for image intensification is determined by the relative values of the detector noise and the photon noise. If the detector noise were zero, the S/N of an unintensified DAD would be given simply by $(\phi_u It)^{\frac{1}{2}}$. The S/N of an intensified DAD would be $(\phi_1 It)^{\frac{1}{2}}$, which is actually lower than that of the unintensified array because $\phi_1<\phi_u$. Therefore, image intensification can actually degrade the S/N of low noise detectors! In practice this is worsened by the finite noise of the intensification stage (gain fluctuations).

The detector noise is device dependent.[5] For example, the readout noise associated with a DAD is an order of magnitude higher than that of CCDs (Section 6.3), and our detector is

only cooled to -20C, so dark charge accumulates at a significant rate. A CCD cooled to liquid N_2 temperature generates a negligible dark charge, and the "quiet" readout of data means that low-light levels can be measured without the need for any image intensification. We have used such a device (Wright instruments model AT1 CCD system) to collect Raman data[32] which is of better quality (S/N) than that obtained with our intensified diode array. The CCD has the advantage that it is not damaged by high light levels (*e.g.* room lights) since there is no electron multiplier, and so is more robust and cheaper than intensified detectors. However, the absence of the intensifier prevents fast gating of the device with the minimum time resolution being of the order of milliseconds, and so all of the work involving TRFR with multichannel detectors was performed with an intensified DAD.

6.6 Summary of important operating characteristics of the intensified DAD

The sections above have described the construction, physical operation and properties of gateable, intensified silicon photodiode arrays. The most important factors which have arisen are:

(a) An optical multichannel detector is available which may be gated for periods as short as *ca.* 5 ns, at repetition rates up to 5kHz. The detector is physically switched on and off to coincide with the periods of interest.

(b) The accumulated spectra are photon-noise limited, even when the optical signal is orders of magnitude weaker than the dark background, and so the Raman R/N ratio of fluorescing materials is determined by the fluorescence shot noise.

(c) The major problem associated with the dark charge is that it accumulates rapidly and can overflow the A/D limit on long integrations. This reduces the effective dynamic range of the device for weak optical signals and could be a serious limitation for some applications.

6.7 Indirect gating of a PMT as a means of achieving time-resolved fluorescence rejections: basic principles

6.7.1 Introduction

The following sections describe the time correlated photon-counting (TCPC) method,with the aim of providing insight into the operation and limitations which apply to this particular technique. A detailed performance analysis, and comparison with direct gating methods, is given in Chapter Eight.

There are two basic methods for making time-resolved optical measurements with an indirectly gated detection system. The first, and perhaps most obvious route, is to expose the sample to a laser pulse of sufficient intensity to produce thousands of photons at the detector, spanning the entire photon/time distribution. The output of the detector is resolved in the time domain to yield the entire photon distribution in a single shot. The success of this method is determined by the time resolution of the detector; for instance, a streak camera[33] is a popular (but expensive) method of obtaining photon time distributions over picosecond timescales.

Direct recording on this timescale is not possible with a PMT, since the output pulse generated after detection of a single photon is typically several ns wide.[26] Photons arriving within this "dead time" are not resolved as separate events and the observed distribution is broadened.

Fortunately, there is an alternative to accumulating the entire photon distribution in one shot. This relies upon the concept that the probability distribution for the emission of a single photon (*e.g.* fluorescence) is identical to the intensity-time profile of the photon burst which is emitted following excitation by a single intense light pulse. A photon emission probability distribution may be accumulated by repeatedly exposing the sample to optical pulses, and recording the time of arrival of the first detected photon after each laser shot. A histogram of the frequency of photon arrival times may be built up over many laser pulses to reveal the photon probability distribution.[34] This technique may be applied to any photon distribution, *e.g.* a fluorescence decay or scattered optical pulse.

The advantage of this technique is that it places less severe demands upon the timing resolution of the photon detector. The width of the signal produced upon detecting a photon no longer limits the timing resolution, since we are only interested in the variation of the time of arrival of the pulse, recorded over many (typically 10^7-10^8) laser shots. This is the basis of all time correlated photon counting schemes.

6.7.2 Response of a photomultiplier tube to optical pulses

Consider a PMT illuminated by an infinitessimally short optical pulse, which is attenuated such that only one photon per pulse ejects an electron from the photocathode. An approximation to such an optical pulse might arise from the Raman scatter of a synchronously-pumped dye laser pulse (Chapter Five). The primary photoelectron is accelerated and multiplied down the dynode chain until an avalanche of secondary electrons

is collected at the anode (Figure 6.7). The pulse shape depends upon the tube design and may vary in width from 2-50 ns.[26]

A finite time (10-100 ns) is taken for the electrons to cascade down the phototube and produce the anode pulse. The time is determined by the tube geometry and the accelerating potentials within the tube. Even with a δ function input optical pulse, the time taken to traverse the tube is not constant from pulse to pulse. If a frequency distribution of travel times is plotted, the mean value is referred to as the transit time, and the FWHM of the distribution is called the transit-time spread[26] (Figure 6.7), jitter[35] or difference.[36] Note, the transit-time spread should not be confused with the <u>width</u> of the anode pulse, which is governed by the arrival time of the individual electrons at the anode rather than that of the whole pulse.

The spread in transit times arises from the fact that the primary photoelectrons are ejected from the photocathode with a range of velocities and trajectories, and so the travel-time from photocathode to first dynode can vary considerably. This introduces a range of times at which a primary photoelectron initiates secondary emission from the first dynode, causing a timing variation in the ultimate production of the anode pulse. The time of arrival is determined largely by the variation in trajectory of the single photoelectron between photocathode and first dynode.[37] Variation in electron trajectory over the rest of the tube is not so important, since the large number of secondary electrons actually sample a range of trajectories for each PMT pulse. The net effect of the dynode chain is to broaden the shape of the anode pulse, rather than to change the time of arrival.

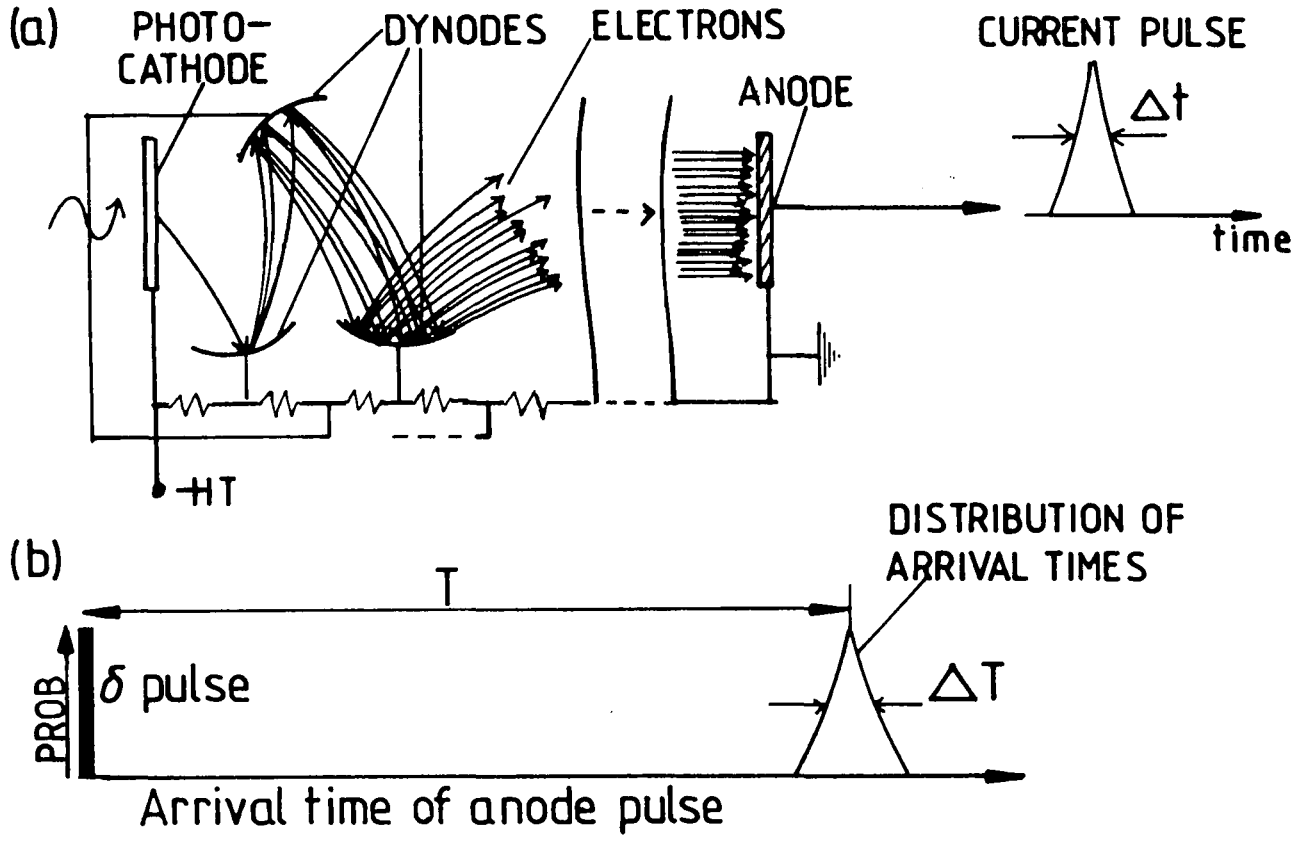

FIGURE 6.7(a) Production of anode current pulse. Width of pulse (Δt) may be 2→50 ns, depending upon tube design.

(b) Definition of transit-time and spread. Transit time (T) is mean time for generation of pulse at anode after incidence of δ function light pulse of cathode. Transit-timespread (ΔT) is the variation (FWHM) of T, averaged over many optical pulses. Note, $\Delta T << \Delta t$, and the timing resolution is determined by ΔT.

The transit time spread sets the lower limit of time resolution which can be achieved and varies widely according to tube design.[25,26] Designs for reducing the timespread have been discussed extensively in the literature,[36-40] and are examined in detail in Chapter Eight.

Since the optical pulse is of much shorter duration than the timing resolution of the tube, it is effectively an impulse input, and so the functional form (g(t)) of the transit time distribution represents the impulse response function (IRF) of the PMT. If the tube is illuminated with a photon distribution of another functional form (*e.g.* a simple exponential fluorescence decay, E(t)), then the observed time distribution of PMT output pulses is given by the convolution[41] of the instrument response g(t) with E(t) (equation 6.8).

$$I(t) = \int_{-\infty}^{\infty} E(t')g(t-t')dt' \qquad (6.8)$$

If the detector is exposed to a series of optical pulses, consisting of instantaneous Raman scatter and a fluorescence decay E(t), the PMT pulses generated by the Raman and fluorescence photons will be characterised by different time distributions (Figure 6.8).

The object of TRFR is to accept a photon which occurs within the duration of the IRF and to reject photons occurring at greater time delays. It is important to realise that the rejection efficiency depends upon the distorted time distribution produced by the PMT, and is critically affected by the PMT time resolution (*i.e.* the transit-time spread). In contrast, the directly gated DAD "sees" the undistorted photon distribution, and records all photons which arrive during the preset gate. Therefore, the transit time spread of the MCP

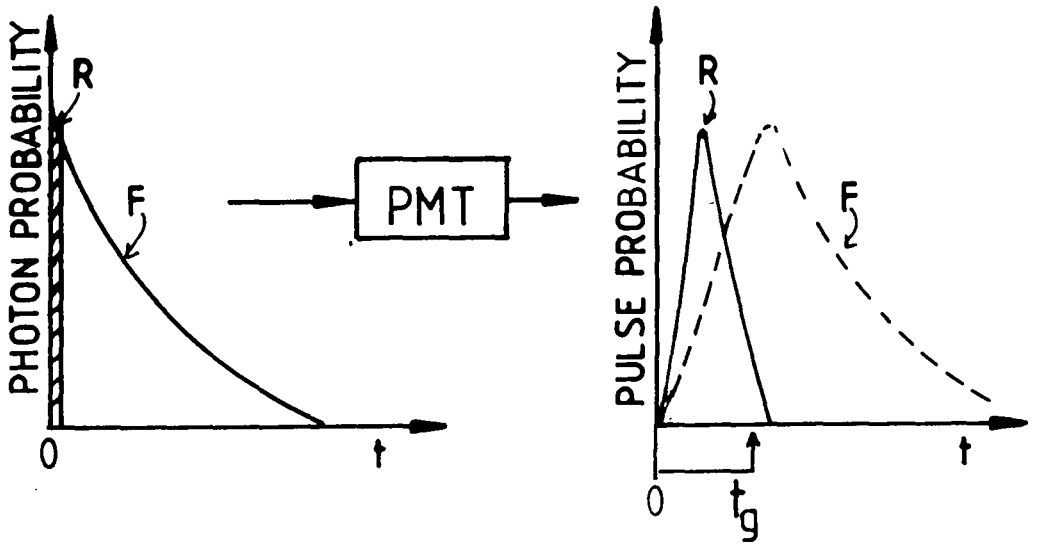

FIGURE 6.8 Response of PMT to Raman (R) and fluorescence (F) photons.

Accepting pulses within the (variable) gate t_g will reject many fluorescence events while accepting any desired fraction of the Raman signal.

of the gated DAD does not affect the TRFR performance, which is determined solely by the shape of the detector gate (Chapter Seven).

6.7.3 Physical method of timing the PMT output

So far, we have only examined the time response of the tube itself, and have not considered how the anode pulses are practically timed. The current pulse at the anode is pre-amplified and input to a fast timing discriminator, which generates a timing signal for each anode pulse. This step is necessary because the anode pulses vary in amplitude and shape, and may not be suitable inputs for the actual time-measuring electronics. Generation of the timing pulse introduces further timing error, which is very much dependent upon the discriminator design.[42] The simplest discriminator (leading edge) triggers when the anode pulse exceeds a certain preset voltage. Both this method, and a more complex discriminator, which triggers at a constant fraction of the anode pulse height, were evaluated in this laboratory. Further details are given in Chapter Eight.

It is necessary to time the arrival of a pulse from the PMI anode with respect to the incidence of the optical pulse at the sample. This may be achieved in a number of ways,[29,34,42-46] but here only one of the most popular methods is considered, that of time-to-amplitude conversion (TAC) followed by pulse height analysis (PHA). This has been widely used in a number of fields, for example fluorescence decay kinetics,[43,47] fast timing of nuclear events,[42] and also fluorescence rejection studies.[48-50]

Figure 6.9 is a schematic illustration of this technique. In a typical experiment, a sample is subjected to laser pulses and the scattered/fluorescence photons are delivered to the PMT. The PMT will produce a series of pulses, (<<1 per laser shot), at times described by a specific probability distribution (Figure 6.8). The timing pulse generated by the PMT is input into the START channel of a time-to-amplitude (TAC) converter. This triggers the TAC to generate a voltage (stored internally) which increases linearly with time. Arrival of a reference timing pulse (synchronised with the laser pulse) at the STOP channel halts the voltage increase. The TAC now contains a voltage which is proportional to the difference in time of arrival between the START and STOP pulses, and depends only upon the time of arrival of the PMT pulse since the STOP signal is fixed in time (relative to the incidence of the laser pulse at the sample). Low voltages correspond to a short time difference and so are indicative of a "late" PMT pulse, *i.e.* a fluorescence event.

The TAC pulse can be collected by a multichannel analyser (MCA) with a PHA facility, which digitises and stores the magnitude of the pulse. The next PMT pulse which triggers the TAC will probably arrive at a different time (with respect to the STOP signal) and so will yield a TAC output of a different voltage. After many laser shots, a frequency distribution of pulse heights is obtained, which directly reflects the time distribution of the PMT pulses (Figure 6.8). The timescale of the distribution may be calibrated by inputting two pulses, of variable (known) time separation, and observing the position of the digitised TAC output on the MCA as a function of separation. Time resolution as low as *ca.* 21 ps per channel may

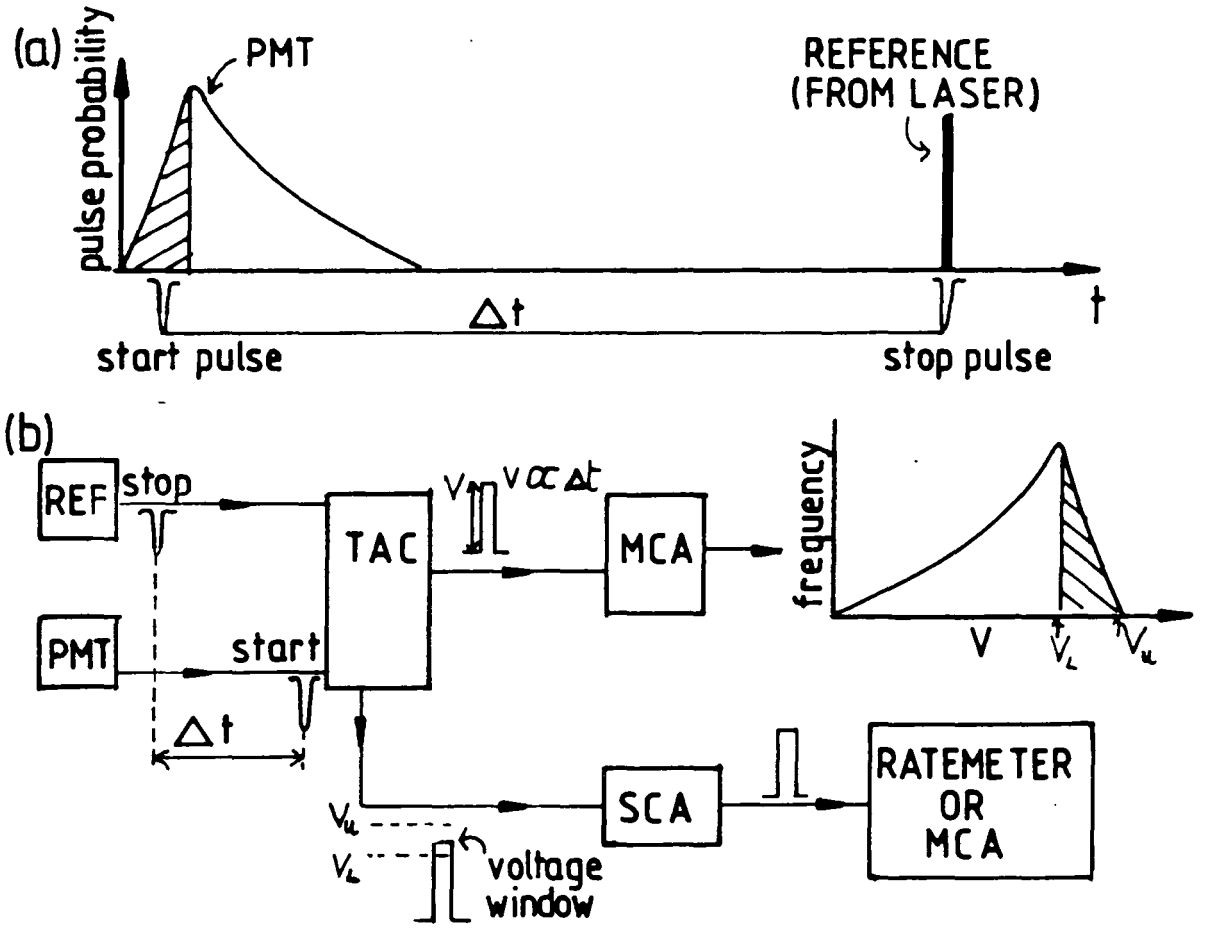

FIGURE 6.9 Schematic of TCPC operation

(a) START pulses may originate anywhere on PMT pulse probability distribution. 'Early' START pulses (shaded) correspond to a Raman event, and generate large START-STOP separations (Δt).

(b) TAC measures Δt and yields output voltage V ($V \alpha \Delta t$). MCA plots frequency distribution of V over many (10^7-10^8) laser shots. Note, early START pulses yield high voltages, so MCA plots reversed time distribution. SCA accepts pulses only when $V_L < V < V_u$, where $V_u \rightarrow V_L$ corresponds to shaded region (the Raman events).

be obtained with our TAC-MCA system.

The PMT time distribution is inevitably further distorted by the timing jitter introduced by the TAC, (*ca.* 10 ps), but this is generally insignificant compared to the transit-time spread of conventional PMTs (hundreds of ps). The time distribution observed on the MCA for the Raman scatter of a dye-laser pulse represents the IRF of the entire detector/laser system, including the jitter from the timing apparatus. It will be seen in Chapter Eight that the IRF width determines the fluorescence rejection efficiency which may be obtained with the apparatus.

In order to accept pulses occurring within a certain time interval, the TAC voltage is examined by a single channel analyser (SCA), which has a voltage acceptance window set to coincide with the desired portion of the MCA pulse height distribution (Figure 6.9). The SCA only accepts pulses lying within this voltage range, and generates an output voltage pulse for each accepted TAC pulse. Therefore, the SCA output consists of a stream of pulses, each of which originates from the detection of a photon within a preset time interval. If the time distribution of the Raman scatter from a nonfluorescing sample is analysed, we obtain the IRF of the PMT/timing system, and can set the SCA acceptance window to count photons occurring within this time range. The Raman spectrum may then be obtained by scanning the monochromator, while recording the rate of emission of the SCA pulses with a chart recorder or with the MCA in pulse-counting mode. This yields the fluorescence rejected Raman spectrum.

The efficiency of fluorescence rejection is determined by the relative areas of the Raman and fluorescence pro-

bability distributions which lie within the gate acceptance window, t_g, (Figure 6.8). This is governed by the fluorescence decay constant and the width of the IRF. Quantification and optimisation of the rejection efficiency is discussed in Chapter Eight.

6.8 Experimental

6.8.1 Experimental configuration

The above sections indicate the principles of single photon counting by the TAC method. Here we consider a basic (instrumental) arrangement for a TCPC experiment, constructed from commercially available components.

Figure 6.10 shows the components of the system used in our laboratory. The laser system has been previously described (Chapter Five), and is not considered further, except to note that the cavity dumper electronics module furnishes a reference voltage pulse which is synchronised (in time) with the dumped optical pulse. This signal (termed the cavity dumper synchronised output, or CDSO) provides a reference against which to time PMT output pulses.

The cavity dumped output (4 MHz pulse repetition rate, *ca.* 590 nm wavelength) is focussed onto a sample which is placed at the focus of the collection optics of a double monochromator. The resultant photons (Raman scattered or fluorescence) are collected by the monochromator, analysed according to wavelength, and delivered to the integrated detector assembly (IDA). The IDA consists of a cooled RCA C31034A-05 PMT and an amplifier/leading edge discriminator, which yields one fast NIM output pulse each time a photon successfully ejects an

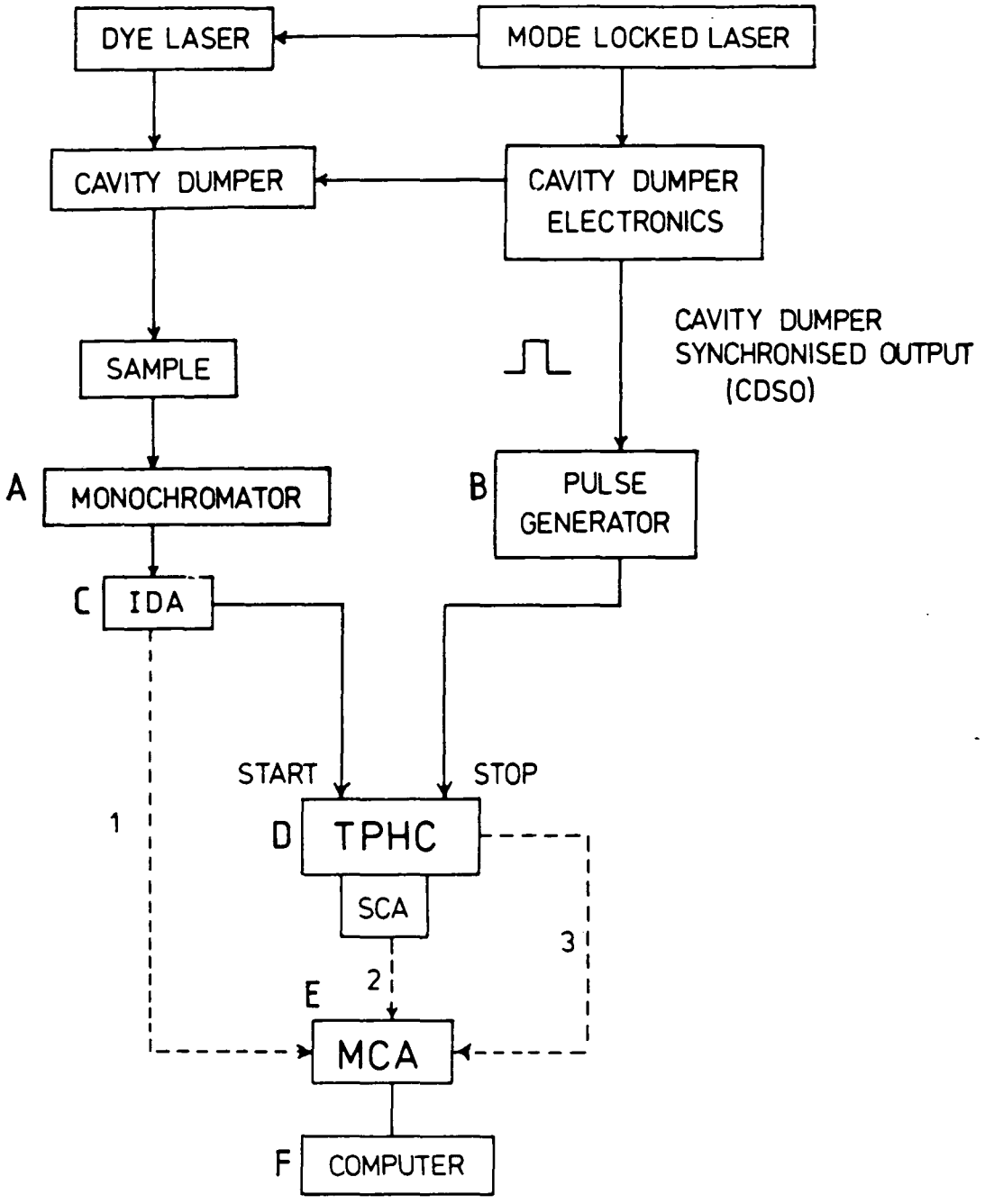

FIGURE 6.10 Basic TCPC configuration. Laser components are described in Chapter Five. Other components are:
A. Spex 1401 double monochromator (from "Ramalog 4" spectrometer)
B. Phillips PM5712 pulse generator, C. RCA Integrated Detector Assembly (cooled C31034-A-05 PMT and amplifier/discriminator,
D. EG & G-ORTEC, model 467 Time-to-Pulse-Height Converter/ Single Channel Analyser, E. Norland Inotech-5300 Multichannel Analyser, F. Sirius Microcomputer.
System may be configured for normal photon counting (route 1), time-resolved photon counting (route 2) or photon-time distribution measurement (route 3). Full details in text.

electron from the photocathode. The photon count rate is kept low (<40kHz, and usually <10kHz) in order to avoid saturation of the timing electronics.[51] In fact, under normal operating conditions <1% of the incident laser pulses actually give rise to a photon (Raman or fluorescence) which triggers the PMT.

In order to measure the PMT time distribution, the NIM pulse is fed into the START channel of a combined TAC/SCA. A reference timing pulse for the STOP channel is provided by the CDSO, which triggers a pulse generator to produce a NIM pulse. This step is necessary for two reasons. Firstly, the CDSO is of the wrong polarity (+) to trigger the TAC, and secondly, the pulse generator incorporates a variable delay, by which the position of the NIM STOP signal may be altered to ensure that it arrives at the TAC after the START pulse.

The TAC and SCA putputs are analysed on a multi-channel analyser, which has both a PHA and pulse counting facility, enabling both photon distributions and Raman spectra to be recorded. Finally, MCA data is transferred to a micro-computer for subsequent plotting and analysis.

Efficient fluorescence rejection may only be achieved if the acceptance gate is accurately set over the Raman photon distribution (Figure 6.8). Setting of the SCA gate with this equipment is easy because of the combined nature of the TAC/SCA unit. The TAC output pulses are only furnished for user-analysis <u>after</u> the SCA has compared their magnitude with its acceptance window. The SCA can inhibit the output of the TAC pulse if it falls outside the gate. Therefore, by examining the TAC pulse height distribution on the MCA while the SCA gate is adjusted, it is possible to observe the exact portion of the photon time distribution which is accepted by the SCA, for any

given gate setting.[48] Once the gate is set, the SCA output pulses are accumulated in the MCA (operating in pulse counting mode rather than PHA) while the monochromator is scanned, thereby recording the time-resolved Raman spectrum (route 3, Figure 6.10).

Alternatively, the SCA inhibit facility may be disabled, and the entire TAC pulse height distribution analysed on the MCA (route 2, Figure 6.10). This procedure is adopted in obtaining fluorescence decay data. A conventional, ungated Raman spectrum may be obtained by counting the IDA NIM pulses directly on the MCA (pulse counting mode), thereby bypassing the gating electronics.

This experimental arrangement is attractive, since the SCA gate can be set by observing the Raman distribution of a non-fluorescing sample, and then the sample of interest may be substituted and the gated Raman spectrum recorded as described above. Therefore, configuration of the timing electronics is easy irrespective of sample nature.

6.8.2 Timing precision achievable with this apparatus

Although the overall timing resolution of the system is determined by the transit-time spread of the PMT, it is of interest to consider the timing precision of the TAC/SCA/MCA combination, *i.e.* the error which would be incurred in determining the separation of pulses which undergo no timing jitter. The TAC output voltage is given by equation (6.9).

$$V = (\text{time}/\text{range}).\ 10 \text{ volts} \qquad (6.9)$$

where "range" is a selectable parameter on the TAC which determines the maximum acceptable time to be measured, and "time" is the START-STOP separation. On our unit the range is switch

selectable from *ca.* 50 ns - 80μs, which governs the timescales which can be studied. The timing accuracy depends upon the selected range, and for the 50 ns range (the only one used in the TRFR experiments) the resolution is *ca.* 10 ps.[52]

The MCA digitisation can be arranged to give a time resolution (over 1024 channels) of *ca.* 21, 42 or 84 ps per channel with this TAC range. The SCA gate may be reduced such that only data in one channel is accepted, which sets the minimum achievable gate width at *ca.* 21 ps. This is very favourable compared to the DAD minimum gate of *ca.* 5 ns. However, the smallest selectable gate width is rarely the most effective one for TRFR, unless the transit-time spread of the PMT (and hence the IRF) is of a comparable width.

The apparatus described above yields an IRF of *ca.* 1.75 ns width, and was used to obtain the majority of the results presented in Chapter Eight. Modifications were made to the wiring of the PMT, the timing discriminator and the focussing of light onto the PMT photocathode which reduced the width to *ca.* 775 ps, and these are discussed in Chapter Eight.

6.9 Important operational aspects of the TAC method

Here we briefly note some of the more important factors which must be considered in order to obtain meaningful results from the TAC method.

6.9.1 Repetition rate

The TAC used in our work actually suffers a dead time of *ca.* 6μs after the generation of an output pulse, during which time the device is reset to accept the next START pulse.

The total dead time of the TAC is given by the START-STOP separation plus the reset time, during which all other START pulses are ignored. This sets the maximum useful repetition rate of the START channel at *ca.* 170 kHz.

Deriving a START trigger from the laser CDSO (4MHz) would saturate the START channel. However, since in our work we ensure that the PMT pulse rate never exceeds 40 kHz, it provides a valid START trigger without causing saturation. The STOP channel may be safely triggered by the CDSO, since it only accepts an input once the START channel has been triggered, and so cannot be saturated provided that the START rate <170 kHz. This configuration is known as the "inverted configuration" and is the usual operating mode when the laser pulse rate is high.[51]

6.9.2 Nonlinearity of SCA output rate with PMT START rate

The inverted configuration discussed above merely ensures that the START channel is not saturated. Haugen *et al*[51] have pointed out that this does not ensure that the TAC output rate increases linearly with START rate. The reason for this is that 24 laser pulses are emitted (4MHz) during the 6μs TAC dead time, and although, on average, <1% of laser shots yield a PMT pulse (*i.e.* one every 25μs), there is a finite probability that two or more PMT pulses might be generated within a 6μs period. This probability increases as the PMT pulse rate is raised, and results in START pulses being rejected until a valid STOP has been accepted.

In our work, the nonlinearity arising from such events depends upon the SCA acceptance gate, that is, only pulses which arrive both within the system dead time and within the

SCA gate contribute towards the nonlinearity. No other START pulses would give rise to an SCA output anyway. The probability of pulse pile-up may be calculated if the distribution of START pulses is assumed to follow Poisson statistics.

First consider a non fluorescing Raman sample. In our work the Raman count rate rarely exceeds 10kHz, which corresponds to an average START separation of 100μs, well outside the system dead time. However, it is possible that on some occasions, more than one of the 24 laser pulses occurring within the system dead-time could give rise to a PMT pulse. We wish to calculate this probability. If the average pulse rate is R, then the average number of pulses occurring within an interval of t seconds is Rt. The probability of n pulses occurring within this interval is given by the Poisson distribution, equation (6.10):

$$P(n) = \frac{(Rt)^n}{n!} e^{(-Rt)} \qquad (6.10)$$

Using R = 10kHz and t = 6μs, P(2) = 0.002, *i.e.* the probability of two PMT pulses arriving within 6μs is less than 1%. Assuming that the SCA gate is set to accept *ca.* 70% of the Raman photon distribution (Chapter Eight), the probability of two pulses arriving within 6μs and the SCA gate is 0.7 x 0.002 = *ca.* 0.001. Nonlinear response of the Raman count rate is therefore very small.

The situation is more complex for a fluorescor, since the fraction of fluorescence photons which fall within the gate depends upon the fluorescence lifetime as well as the gate width. For the samples examined in this work, the probability of arrival within the dead time is always <1%, and so no corrections for non-inearity were made to any of the results obtained.

Nonlinearity of response has not been considered in any of the previous reports on the use of TAC systems for TRFR. It is found[51] that the nonlinearity increases rapidly with START rate, and so unless care is taken to limit the PMT count rate, the time-resolved Raman spectrum may be distorted.

Haugen *et al*[51] have considered in detail the performance of various instrumental configurations based upon the TAC approach. Although their report is solely concerned with obtaining fluorescence decay data rather than time-resolved rejection, it is a useful guide to optimising data accumulation rates to avoid nonlinear effects.

6.10 Conclusions

This chapter contains a technical description of the operation of two distinct time-resolved detection systems, namely a directly gated device (DAD) and a detector which is operated continuously while the output is time-resolved (PMT). Although a quantitative comparison of the techniques is given after the results obtained with each have been presented, the essential differences can be stated succinctly:

(a) The DAD can only be gated for periods down to 5 ns, compared to the 21 ps achievable with the TAC/SCA. However, the minimum effective gate width with the TAC system is found to be of the order of the PMT transit-time spread, which amounts to hundreds of ps with conventional PMTs, (Chapter Eight).

(b) The laser system is constrained to 4kHz pulse rate with the gated DAD, while MHz pulse rates can be employed with the TAC system, provided that PMT pulses trigger the START channel. Thus the effective laser power on the sample is much higher with

the TAC system, thereby improving the spectral S/N.

(c) The intensified DAD can accumulate *ca.* 700 spectral elements simultaneously, a S/N improvement of *ca.* 26 compared to a PMT operated for the same time, assuming equal sensitivity for each detector.

(d) The efficiency of the PMT rejection system is determined by the transit-time spread of pulses propagating down the tube. The DAD timing resolution is not affected by the transit-time spread of electrons through the MCP, but rather by the speed with which the gain of the device is switched. This means that the mathematical models which are required to describe the performance of each detector are fundamentally different.

(e) Gating the PMT system almost totally eliminates the dark background in spectra, while the dark charge in gated DADs is unchanged. Elimination of the dark charge in DADs (by cooling to liquid N_2 temperatures) would greatly increase the maximum integration time and effective dynamic range for weak optical signals, but would barely affect the overall noise. Removal of dark signal from PMTs can increase the spectral S/N, but does not affect the effective dynamic range.

The following chapters contain the results which were obtained with each detector, and the mathematical models which were developed to both describe the performance and identify modifications which would improve the system.

REFERENCES - CHAPTER SIX

1. "Multichannel Image Detectors", Y. Talmi (Ed.), ACS. Symp. Series 102, ACS, Washington, D.C. (1979).

2. "Multichannel Image Detectors", Vol.2, ACS Symp. Series, 236, ACS, Washington, D.C. (1983).

3. D.G. Jones, Anal.Chem., 57 (9), 1057A (1985).

4. D.G. Jones, Anal.Chem., 57 (11), 1207A (1985).

5. J.G. Timothy, Pub.A.S.P., 95, 810 (1983).

6. R.K. Chang and M.B. Long, Top.Appl.Phys., 50, 207 (1982).

7. S.S. Vogt, R.G. Tull and P. Kelton, Appl.Opt., 17(4),574, (1978).

8. Y. Talmi, Appl.Spectrosc., 36(1), 1 (1982).

9. G. Atkinson in "Advances in infrared and Raman Spectroscopy" 9, R.E. Hester and R.J.H. Clark (Eds.), Heyden, London, Philadelphia, Rheine (1982).

10. M. Bridoux, A. Deffontaine, M. Delhaye and F. Grase, Il Nuovo Cimento, 63B, (1), 91 (1981).

11. U. Farinelli and R. Malvano, Rev.Sci.Instrum., 29(8),699 (1958).

12. N. Klein and T.J. Rock, Rev.Sci.Instrum., 41 (11)1671 (1970).

13. K.B. Keller, B.M.K. Nefkens, Rev.Sci.Instrum., 35 (10). 1359 (1964).

14. F. de Marco, and E. Renco, Rev.Sci.Instrum., 40 (9), 1158, (1969).

15. F. de Martini, and K.P. Wacks, Rev.Sci.Instrum., 38 (7). 866 (1967).

16. M. Rossetto and D. Mauzerall, Rev.Sci.Instrum., 43 (9), 1244 (1972).

17. T.D.S. Hamilton, J.Phys.E.:Sci.Instrum., 4, 326 (1971).

18. B.L. Elphick, J.Phys.E. Sci.Instrum., 2, 953 (1969).

19. S.G. Ballard, Rev.Sci.Instrum., 54 (11), 1473 (1983).

20. E.P.L. Hunter, M.G. Simic and B.D. Michael, Rev.Sci.Instrum., 56 (12), 2199 (1985).

21. J.D. Oxman and F.D. Lewis, J.Phys.Chem., 88, 2308 (1984).

22. G.F. Albrecht, E. Kallne and J. Meyer, Rev.Sci.Instrum., 49 (12), 1637 (1978).

23. N. Everall, J. Howard, R.W. Jackson and K. Hutchinson, J.Raman.Spectrosc., 17 (5), 415 (1986).

24. Y. Talmi and R.W. Simpson, Appl.Opt., 19 (9), 1401 (1980).

25. J.P. Boutot, J. Nussli and D. Vallat, Adv.Electron.Electron. Phys., 60, 223 (1983).

26. R.W. Engstrom, "Photomultiplier Handbook", R.C.A. Corporation (1980).

27. I. Yamazaki, N. Tamai, H. Kume, H. Tsuchiya and K. Oba, Rev.Sci.Instrum., 56 (6), 1187 (1985).

28. Y. Talmi, "Description of O-SMA detector heads and their performance", Spectroscopy Instruments GmbH (1983).

29. J.M. Harris, R.W. Chrisman, F.E. Lytle and R.S. Tobias, Anal.Chem., 48 (13), 1937 (1976).

30. W. Shockley and J.R. Pierce, Proc.IRE, 26, 321 (1938).

31. T. Jorgensen, Am.J.Phys., 16, 285 (1948).

32. N. Everall, J. Howard, J. Wright - unpublished data.

33. G.W. Walden and J.D. Wineforder, Spectrosc.Lett., 13 (11), 793 (1980).

34. B. Leskovar, IEEE Trans.Nucl.Sci., NS-32(3), 1232 (1985).

35. "Photomultipliers", Thorn-EMI Electron Tubes Ltd. (1986).

36. F. de la Barre, Nucl.Instr. and Meth., 102, 77 (1972).

37. B. Sipp and J.A. Miehe, Nucl.Instr. and Meth., 114 249 (1974).

38. B. Leskovar and C.C. Lo, Nucl.Instr.and Meth. 123, 145 (1975).

39. C.C. Lo and B. Leskovar, IEEE Trans.Nucl.Sci., NS-28 (1), 698 (1981).

40. S. Canonica, J. Farrer, U.P. Wild, Rev.Sci.Instrum. 56 (9). 1754 (1985).

41. R.N. Bracewell, "The Fourier transform and its applications" McGraw Hill electrical and electronic engineering series, McGraw Hill, New York (1978).

42. T.J. Paulus, IEEE Trans.Nucl.Sci., NS-32(3), 1242 (1985).

43. J.R. Lakowicz, "Principles of Fluorescence Spectroscopy", Plenum Press, New York (1983).

44. E. Campini, G. Gorini and G. Massetti, J.Phys.D: Appl.Phys. 14, 2189 (1981).

45. A. de Wilton, L.V. Haley and J.A. Koningstein, Can.J. Chem., 60, 2198 (1982).

46. T.L. Gustafson and F.E. Lytle, Appl.Spectrosc. 34(2), 185 (1985).

47. R.A. Lampert, L.A. Chewter, D. Philips, D.V. O'Connor, A.J. Roberts and S.R. Meech, Anal.Chem., 55(1), 68 (1982).

48. S. Burgess and I.W. Shepherd, J.Phys.E:Sci.Instrum., 10 617 (1977).

49. R.P. van Duyne, D.L. Jeanmaire and D.R. Shriver, Anal.Chem. 46(2), 213 (1974).

50. J. Watanabe, S. Kinoshita and T. Kushida, Rev.Sci.Instrum. 56(6), 1195 (1985).

51. G.R. Haugen, B.W. Wallin and F.E. Lytle, Rev.Sci.Instrum. 50(1), 64 (1979).

52. "Model 467 Time to Pulse Height Converter and SCA Operating and Service Manual", EG and G ORTEC Ltd., (USA).

CHAPTER SEVEN

EVALUATION OF A GATED INTENSIFIED SILICON DIODE ARRAY DETECTOR FOR FLUORESCENCE REJECTION IN RAMAN SPECTROSCOPY

7.1 Introduction

The previous chapter outlined the essential characteristics of gated multichannel detectors, and indicated how they may be used to suppress fluorescence in Raman spectra. In this chapter, the results of a theoretical and practical evaluation of the performance of one particular gated DAD are presented. It is found that, at present, the instrument successfully suppresses the background due to moderately long-lived fluorescors (τ_f = 10ns), but does not improve the R/N ratio of the spectra relative to those obtained by ungated detection with a conventional cw laser source. This is not due to poor timing resolution, but rather to the low average power of the laser when operated at kHz pulse rates.

Since the R/N ratio determines the actual quality of the spectrum, this is a somewhat unfortunate result. However, the theoretical analysis of the performance, (which is in good agreement with experimental results), has identified modifications to the detector and laser system which should produce an effective instrument. The performance of the gated DAD is compared with that of the PMT-based apparatus in Chapter Eight.

7.2 Theory describing the efficiency of fluorescence rejection

7.2.1 Calculation of the detected Raman and fluorescence intensity as a function of gate position

In order to calculate the expected improvements in R/F and R/N upon gating the DAD, we must first calculate the variation in detected fluorescence intensity as a function of fluorescence lifetime and detector gate position. This variation is governed by the impulse response function (IRF)

of the gated array, *i.e.* the response of the detector to a signal which is of infinitessimally short duration compared to the timing resolution of the system (*ca.* 5ns). The pulses from our laser system are less than 1/100th of this duration, and so the Raman scatter which they produce represents an impulse input with which to measure the IRF. The variation in intensity as the detector gate is scanned temporally across the pulsed Raman signal yields the IRF, which is found (Section 7.3) to be well represented by a trapezium.

Figure 7.1 illustrates the IRF and defines the parameters which are used to describe it. The functional form of the IRF is denoted g(t), and is subdivided into three discrete regions, namely $g_1(t)$, $g_2(t)$ and $g_3(t)$. The base and peak widths are denoted 2L and 2W respectively, and the maximum detector quantum efficiency is ϕ_g. The relative quantum efficiency is given by $\phi(t) = g(t)/\phi_g$. We first consider the gate to be opened at time (t-L) with respect to an exponential decay ($E(t) = e^{-kt}$) beginning at t=0 (Figure 7.2). Here t is defined as the time from the origin (beginning of fluorescence decay) to the centre of the IRF, and so photons will be detected for a range of gate positions (t) from $-L \rightarrow \infty$. A gate positioned at t=0 therefore has the centre of the IRF coinciding with the origin, and actually opens at time -L.

The total intensity detected by a gate positioned at time t is given by equation (7.1).

$$I(t) = \int_{-\infty}^{\infty} E(t')g(t'-t)dt' \qquad (7.1)$$

This equation represents the cross correlation of the functions E(t) and g(t).[1] It may be noted that in the case of a symmet-

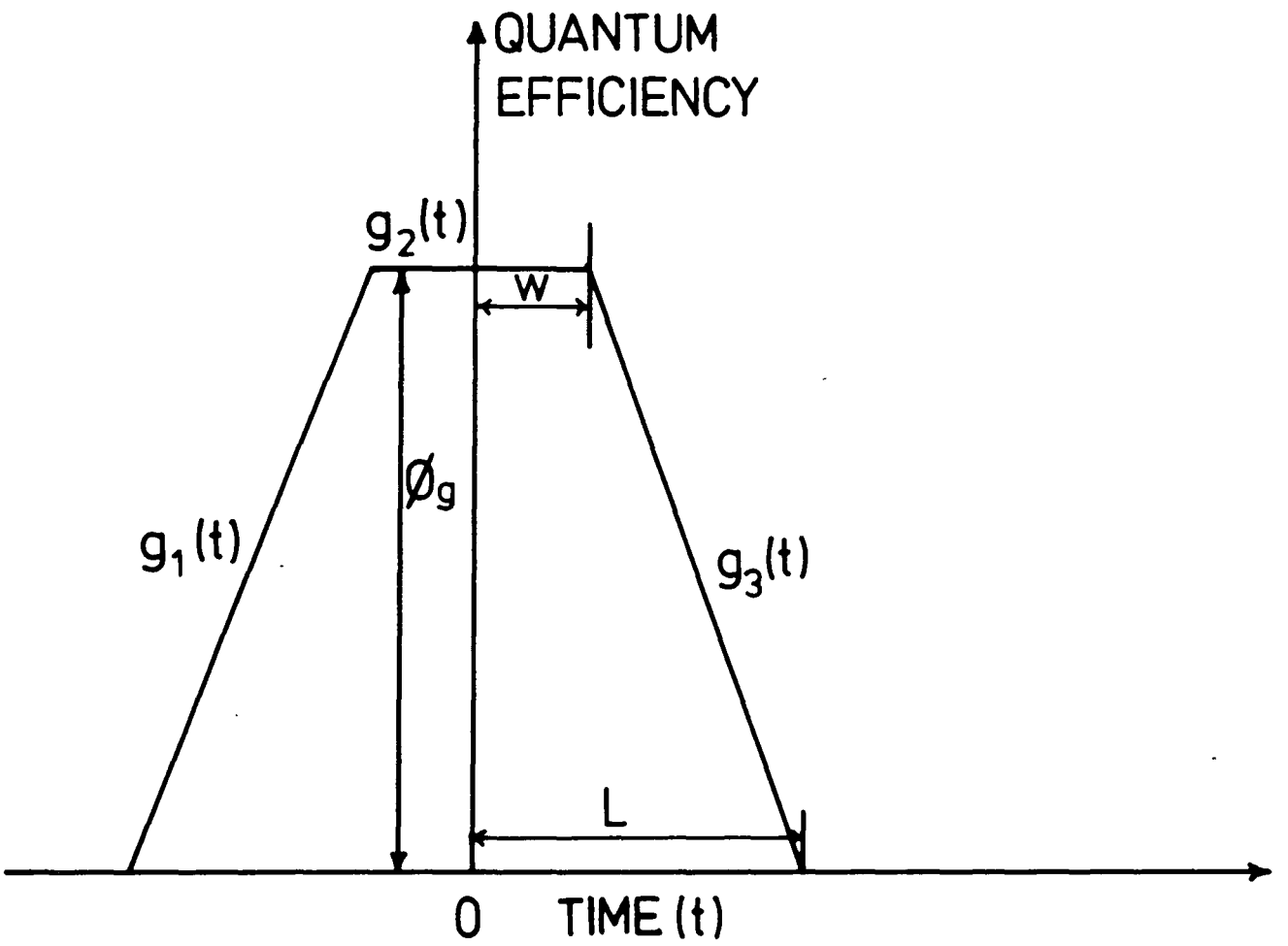

FIGURE 7.1 Parameters defining the IRF of the gated DAD. ϕ_g is the maximum quantum efficiency during the "on" period. The relative quantum efficiency at time t is defined by $\phi(t) = g(t)/\phi_g$.

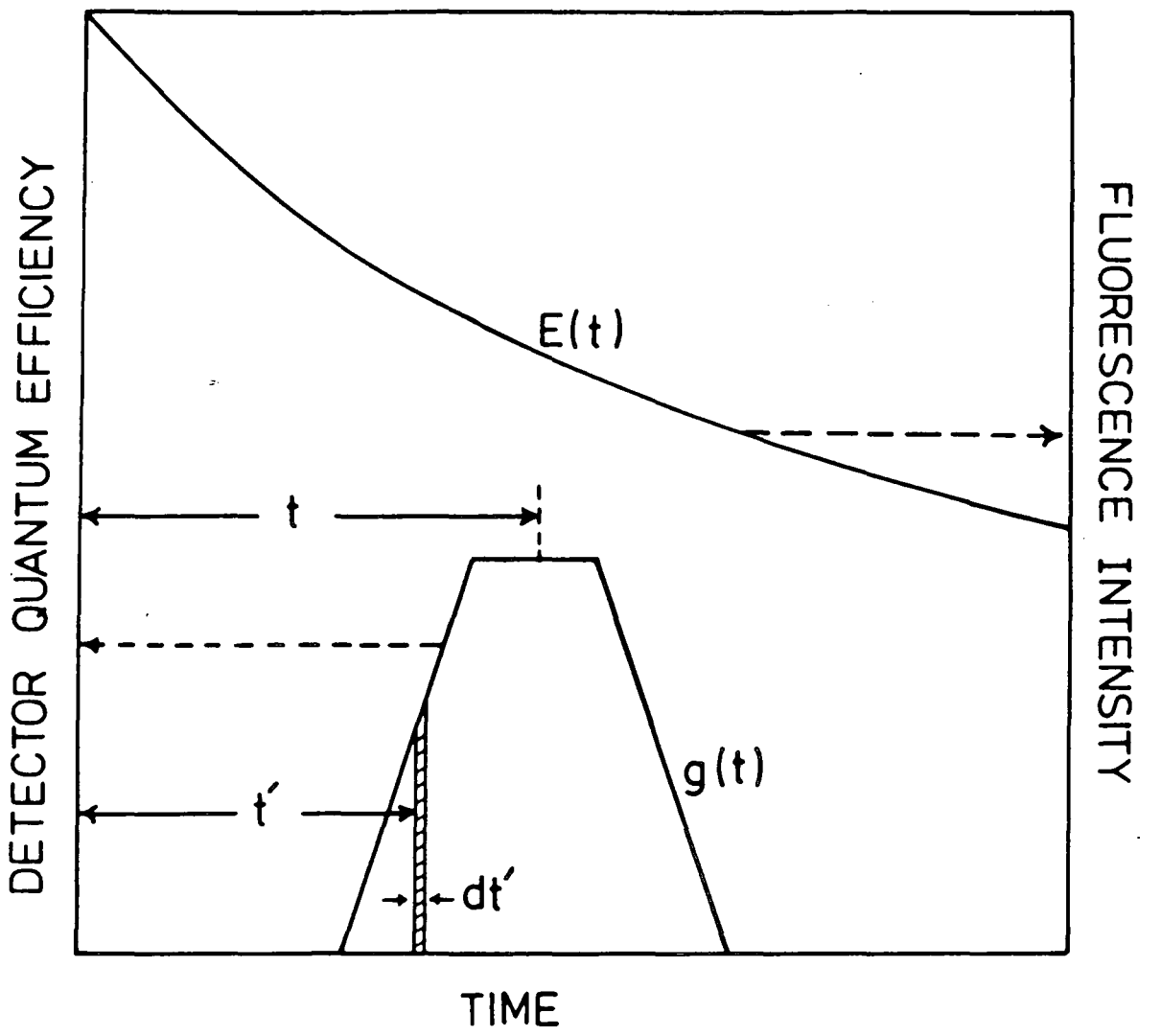

FIGURE 7.2 Parameters used in the calculation of the observed fluorescence intensity from a pure exponential decay (E(t)). See text for details.
Note that the parameter t is subsequently redefined (Figure 7.4) to ensure that only positive time values occur.

rical g(t) (such as a trapezium) equation (7.1) is identical to the convolution integral[1] (7.2).

$$I(t) = \int_{-\infty}^{\infty} E(t')g(t-t')dt' \qquad (7.2)$$

Since we know the forms of g(t) and E(t), it is possible to evaluate equation (7.1) analytically, and we may therefore derive an exact functional form for the detected intensity as a function of fluorescence lifetime, gate position (t), and the dimensions L and W. Evaluation of (7.1) is not difficult. Defining time zero as the midpoint of g(t) (Figure 7.1), g(t) is described by:

$$g_1(t) = \phi_g(L+t)/(L-W) \qquad (7.3)$$

$$g_2(t) = \phi_g \qquad (7.4)$$

$$g_3(t) = \phi_g(L-t)/L-W) \qquad (7.5)$$

The cross correlation of g(t) with E(t) must be performed over four separate time regimes (Figure 7.3). We obtain the general result $I(t) = \phi_g H(t)$, where H(t) is given (according to the time regime) by:

(a) $-L<t<-W$

$$H(t) = \frac{1}{\phi_g}\int_{0}^{t+L} E(t')g_3(t'-t)dt'$$

$$= C[e^{-k(t+L)} + k(L+t)-1] \qquad (7.6)$$

(b) $-W<t<W$

$$H(t) = \frac{1}{\phi_g}\int_{0}^{t+W} g_2(t'-t)E(t')dt' + \frac{1}{\phi_g}\int_{t+W}^{t+L} g_3(t'-t)E(t')dt'$$

$$= C\{e^{-kt}[e^{-kL}-e^{-kW}] + k(L-W)\} \qquad (7.7)$$

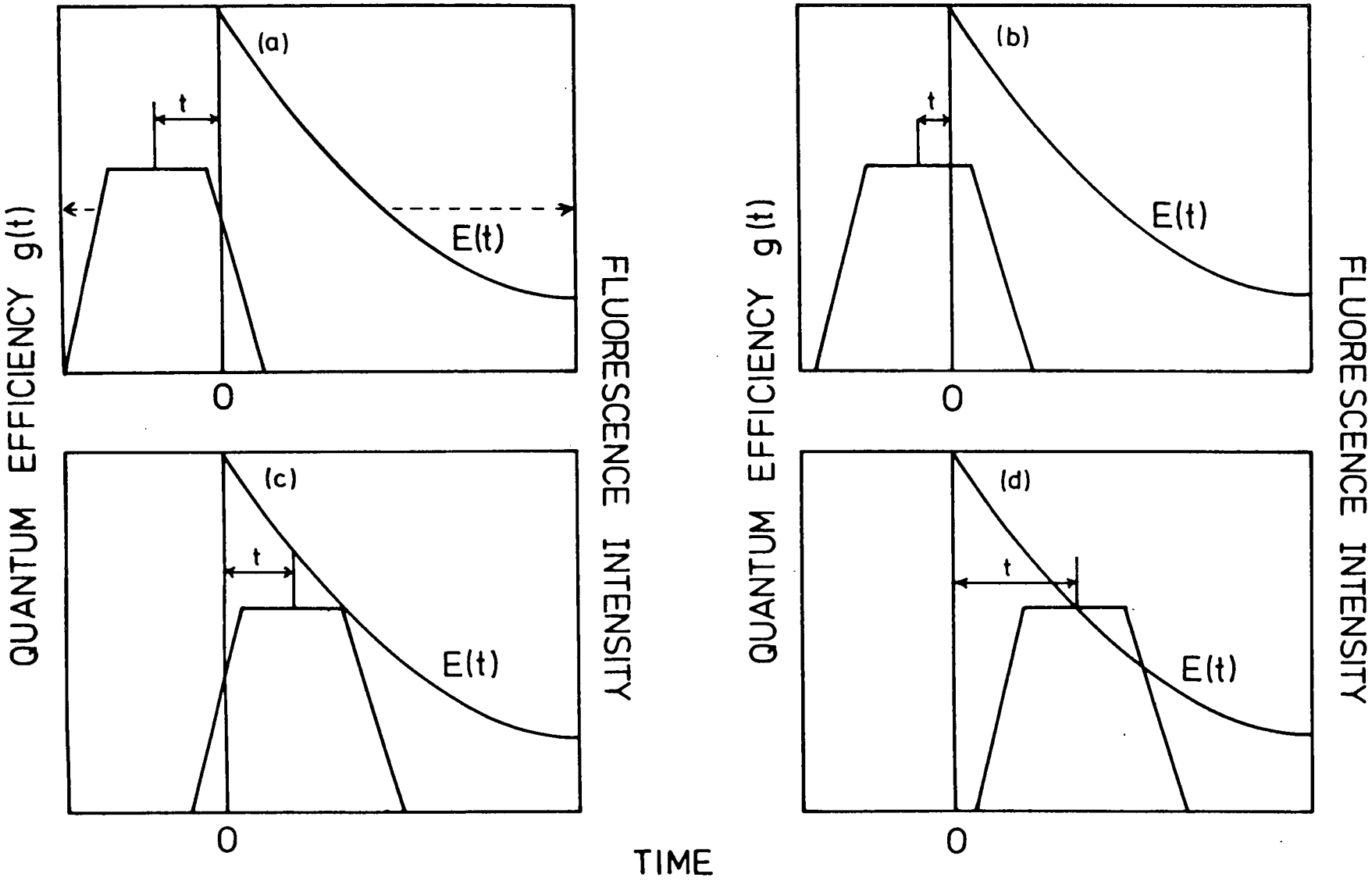

FIGURE 7.3 Cross correlation of trapezium g(t) with E(t). Correlation is performed over four time regimes, according to gate position t. (a) $-L<t<-\omega$, (b) $-\omega<t<\omega$, (c) $\omega<t<L$, (d) $t>L$.

(c) $W<t<L$

$$H(t) = \frac{1}{\phi_g}\int_{o}^{t-W} g_1(t'-t)E(t')dt' + \frac{1}{\phi_g}\int_{t-W}^{t+W} g_2(t'-t)E(t')dt'$$

$$+ \frac{1}{\phi_g}\int_{t+W}^{t+L} g_3(t'-t)E(t')dt'$$

$$= C\{e^{-kt}[e^{-kL}-e^{kW}-e^{-kW}] + k(L-t) + 1\} \qquad (7.8)$$

(d) $t>L$

$$H(t) = \frac{1}{\phi_g}\int_{t-L}^{t-W} g_1(t'-t)E(t')dt' + \frac{1}{\phi_g}\int_{t-W}^{t+W} g_2(t'-T)E(t')dt'$$

$$+ \frac{1}{\phi_g}\int_{t+W}^{t+L} g_3(t'-t)E(t')dt'$$

$$= C\{e^{-kt}[e^{kL} + e^{-kL}-e^{-kW}-e^{kW}]\} \qquad (7.9)$$

In the expressions above, $C = 1/[k^2(L-W)]$, and k is the decay constant $(1/\tau_f)$ for the fluorescence (Chapter One).

7.2.2 Time axis shift

The above equations allow the time t to take negative values (down to -L). This arises because of the way in which the zero time position was defined, *i.e.* at the centre of g(t). If a time axis shift is performed such that $t \rightarrow t-L$, equations (7.6)-(7.9) become:

(a) $O<t<(L-W)$

$$H(t) = C[e^{-kt} + kt - 1] \qquad (7.10)$$

(b) $(L-W)<t<(L+W)$

$$H(t) = C\{e^{-k(t-L)}.[e^{-kL}-e^{-kW}] + k(L-W)\} \qquad (7.11)$$

(c) $(L+W)<t<2L$

$$H(t) = C\{e^{-k(t-L)}.[e^{-kL}-e^{-kW}-e^{kW}] + 1 + k(2L-t)\} \qquad (7.12)$$

(d) $t>2L$

$$H(t) = C\{e^{-k(t-L)}.[e^{kL}+e^{-kL}-e^{kW}-e^{-kW}]\} \qquad (7.13)$$

Equations (7.10-7.13) are only defined for t>0, with the point t=0 corresponding to the time t=L in the previous unshifted time coordinate (Figures 7.2 and 7.4). In the shifted time coordinate, a gate positioned at time t with respect to an impulse of photons in fact closes t seconds after the photons reach the detector, and so the calculated fluorescence decays all begin at t=0 (Figure 7.4). This is less confusing than the time coordinate used in equations (7.6)-(7.9), where the calculated decay curves begin at t=-L (Figure 7.2). The shape of the curve is obviously the same in both cases, but the position on the time axis is different.

Equations (7.10)-(7.13) perhaps require some explanation. H(t) represents the photon intensity which would be detected by a detector of unit quantum efficiency positioned at time t. The actual detected intensity is given by $I(t)=\phi_g H(t)$, and so only differs by the constant ϕ_g. In general, we are only concerned with the shape of the curve of H(t), and the absolute magnitude is irrelevant. It is shown below that the absolute value of ϕ_g is not required for our calculations since we only ever calculate relative improvements rather than absolute R/F and R/N values.

7.2.3 Calculation of the Fluorescence Decay Constant

Figure 7.4 defines the position of the gate with respect to a pulse of photons, we use this time coordinate

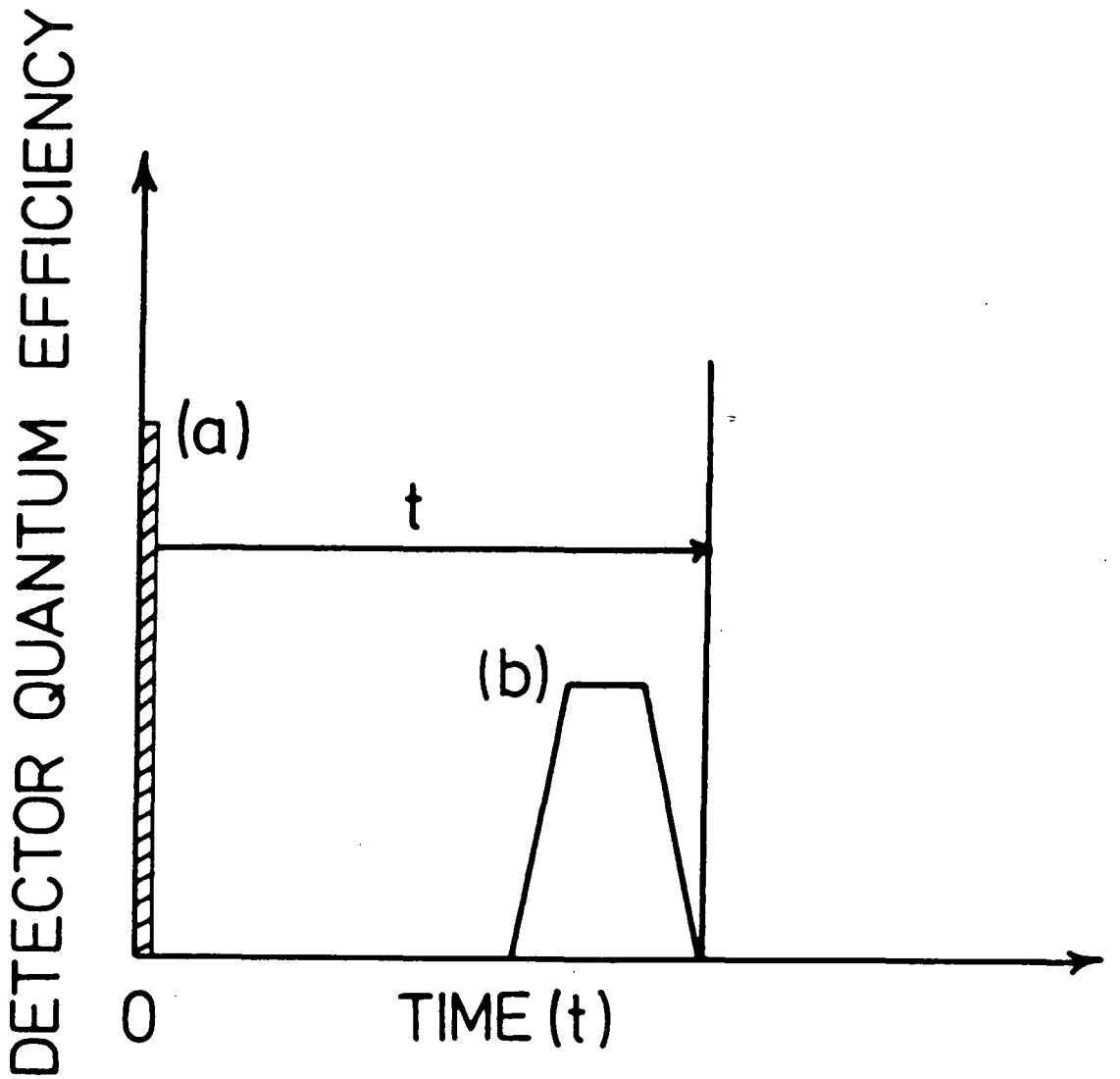

FIGURE 7.4 The position of the detector gate (b) relative to the Raman photon pulse (a). This diagram defines the parameter "t":- the gate position.

throughout the rest of this discussion. Figure 7.5 illustrates the form of H(t) (equations (7.10)-(7.14)) for two different rate constants. Curve (a) represents the calculated response to a decay with k=0.095 ns^{-1} (τ_f=10.5 ns), while (b) depicts the IRF of the detector, obtained by letting $k \to \infty$ in equations (7.10)-(7.13) above. In these calculations, L and W were chosen as 4.5 and 1.75 ns respectively (see Section 7.3.3).

It is apparent that once L and W are known, the decay constant k of any sample may be calculated by obtaining the best fit of equations (7.10)-(7.13) to the observed fluorescence decay curve. A computer program was written to iteratively cross-correlate g(t) with E(t), varying k such as to obtain the best fit (least-squares assessment) to the observed data. This yields the best value of the decay constant, within the constraint imposed by the idealised functional forms of g(t) and E(t). This procedure would not be suitable if it were desired to obtain accurate fluorescence lifetimes, but provides estimates of k which are adequate for testing the model for fluorescence rejection efficiency which is developed below.

7.2.4 Calculation of the expected improvements in R/F and R/N upon gating the detector

In order to assess the performance of the gated detection system, we must compare the R/F and R/N levels of spectra which are obtained by both gated and ungated detection. It is informative to first derive expressions for the expected improvements in R/F and R/N upon gating the detector, compared to ungated detection with the pulsed laser as the excitation source. The inprovement compared to a spectrum obtained by

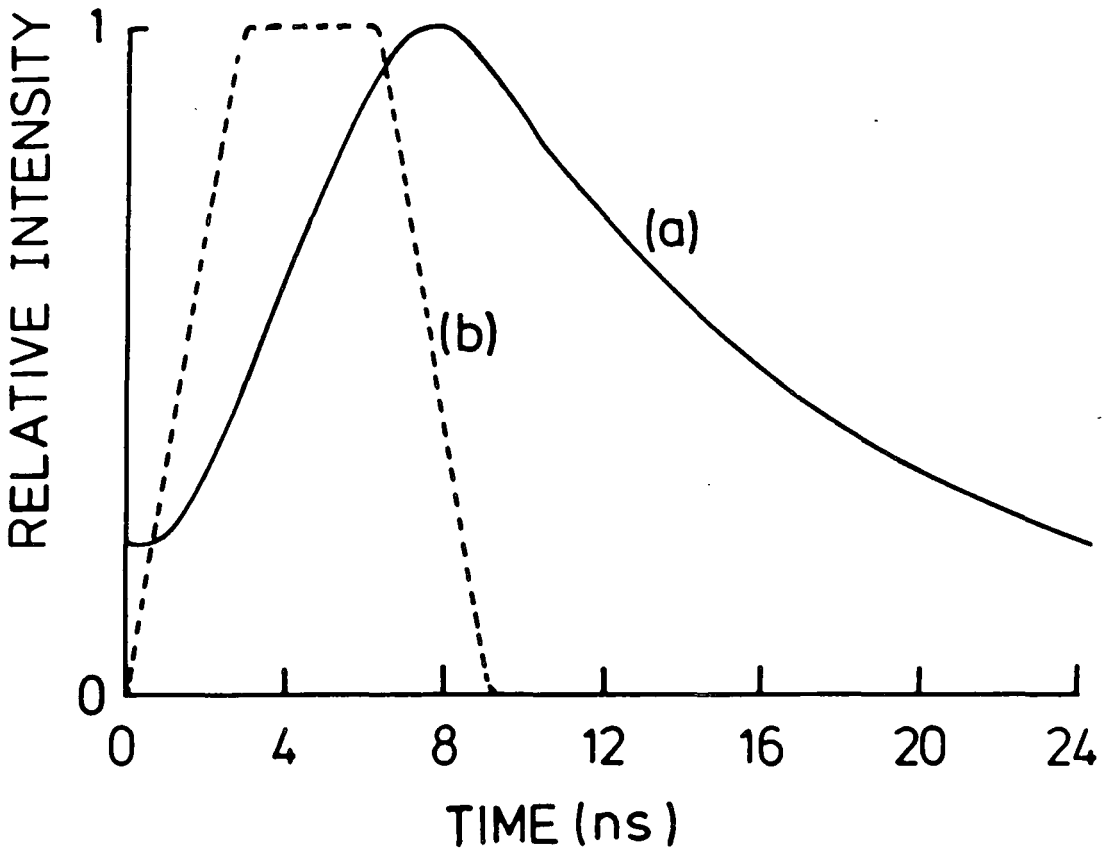

FIGURE 7.5 Calculated response of detector as a function of gate position (t). (a) Response to exponential e^{-kt}, with k=0.095 ns^{-1}. (b) Response to impulse ($k \to \infty$). Curve (b) is the IRF of the gated DAD.

ungated detection with high power cw laser excitation is considered in Section 7.6.6.

7.2.4.1 Enhancement of the R/N ratio upon gating (E[R/F]).

Consider the laser output as illustrated in Figure 7.6, where I_m is the integrated intensity of a cavity dumped pulse and I_L is likewise the intensity of a "leakage-light" pulse (Chapter Five). If there are "n" leakage pulses for every main dumped pulse, then to a good approximation (neglecting non-linear effects) the total intensity of the Raman scattered radiation falling upon the detector is given by:

$$I_R = C_R(I_m+nI_L) \qquad (7.14)$$

where C_R is a constant incorporating the efficiency of the inelastic scattering process and the collection optics.

The fluorescence intensity is also proportional to the incident laser intensity (again assuming a linear response, *i.e.* that the fluorescence is not saturated (Chapter Three)). Each laser pulse (main or leakage) is assumed to generate an electronically excited population which decays exponentially. The intensity of fluorescence photons falling on the detector during one laser cycle is given by:

$$I_F = C_F \int_0^\infty (I_m+nI_L)e^{-kt}dt \qquad (7.15)$$

where C_F is a constant determined by the fluorescence quantum yield, the collection optics efficiency and the spectrometer throughput. Over small wavelength regions around the position of the Raman band, the quantum efficiency of the detector in ungated mode (ϕ_u) is constant, so the observed intensities of the Raman band and of the immediately adjacent fluorescence

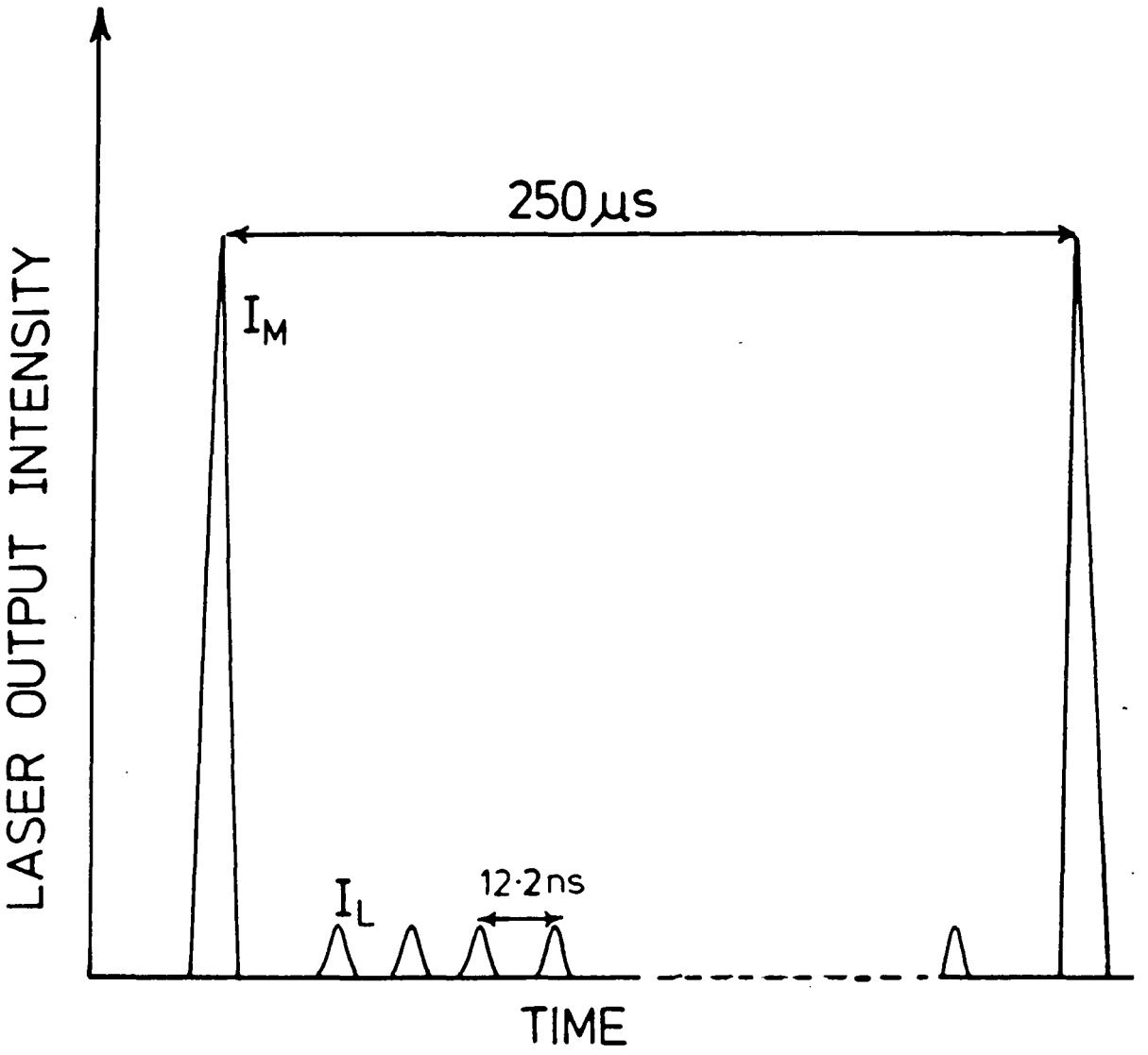

FIGURE 7.6 Nature of laser output (ex cavity-dumper) at 4kHz. The intensity of the leakage pulse (I_L) is greatly exaggerated. When these experiments were performed, I_M/I_L = *ca.* 100.

background are given by:

$$R = \phi_u C_R (I_m + nI_L) \quad (7.16)$$

$$F = \phi_u C_F (I_m + nI_L)/k \quad (7.17)$$

Therefore the ratio of the Raman band intensity to that of the fluorescence background, recorded by an ungated detector, should be:

$$(R/F)_u = kC_R/C_F \quad (7.18)$$

The subscript "u" denotes that the detector is ungated, *i.e.* "open" throughout the laser cycle (one main pulse plus "n" leakage pulses).

If the detector is gated, such as to detect only radiation (scattered + emission) resulting from the main cavity dumped pulse, the detected Raman intensity is given by equation (7.19):

$$R = g(t) C_R I_m \quad (7.19)$$

This equation holds since g(t) represents the quantum efficiency of the detector at the time of arrival of the Raman photons. The relative fluorescence intensity recorded by a detector positioned at time "t" is given by the cross-correlation integral I(t). In general, the detected fluorescence intensity is:

$$F = I_m C_F I(t) \quad (7.20)$$

Therefore, using the relations $I(t) = \phi_g H(t)$ and $g(t) = \phi(t)\phi_g$,

$$(R/F)_g = \phi(t) C_R/(C_F H(t)) \quad (7.21)$$

where the subscript "g" denotes gated detector operation. Now C_R and C_F are not easily determined, but the enhancement in the R/F ratio (E[R/F]) on going from ungated to gated mode is

given by the ratio of equations (7.21) and (7.18).

$$E[R/F] = (R/F)g/(R/F)_{\bar{u}} = \phi(t)/(kH(t))) \qquad (7.22)$$

and so it is not necessary to know the constants C_R and C_F in order to calculate the improvement in R/F on going from ungated to gated mode. According to equation (7.22), fast decaying samples should show the least improvement in R/F on gating, as would be expected intuitively.

7.2.4.2 Raman signal/fluorescence noise enhancement (E[R/N])

It is important to remember that the object of the experiments is to improve the R/N ratio of the spectra, rather than simply the R/F ratio. For the reasons outlined in Chapter One, we only calculate the noise on the fluorescence background adjacent to the Raman band, rather than the noise at the band maximum.

The analysis is based on two main assumptions:

(a) The noise arises mainly from statistical fluctuations in the fluorescence photon flux, *i.e.* detector noise is small by comparison. This assumption was justified in Chapter Six and will be confirmed in the following results section.

(b) The photon intensity is adequately described by a Poisson distribution, *i.e.* $N = \sqrt{F}$

From equations (7.16) and (7.17), the R/N ratio in ungated mode is:

$$(R/N)_u = C_R.[(\phi_u.k.(I_m + nI_L)/C_F]^{\frac{1}{2}} \qquad (7.23)$$

For gated operation, equations (7.19) and (7.20) yield:

$$(R/N)_g = g(t)C_R[\frac{I_m}{C_F I(t)}]^{\frac{1}{2}} \qquad (7.24)$$

The improvement in R/N ratio (E[R/N]) on gating the detector is obtained from the ratio of equations (7.23) and (7.24) above

$$E[R/N] = (R/N)_g/(R/N)_u = \phi(t)\left(\frac{I_m}{(I_m+nI_L)} \times \frac{\phi_g}{\phi_u} \times \frac{1}{kH(t)}\right)^{\frac{1}{2}} \quad (7.25)$$

7.2.5 Effect of integration time

If (T_g/T_u) represents the ratio of integration times in gated/ungated modes, and the total laser intensity is $I_T = I_m+nI_L$, equation (7.25) may be recast as:

$$E[R/N] = \phi(t)\left[\frac{T_g}{T_u} \times \frac{I_m}{I_T} \times \frac{\phi_g}{\phi_u} \times \frac{1}{kH(t)}\right]^{\frac{1}{2}} \quad (7.26)$$

Again, it is not necessary to know the values of C_R and C_F in order to calculate E[R/N]; all that is required is a knowledge of the IRF parameters L and W, the fluorescence decay constant k, and the ratio of the detector quantum efficiencies in gated/ungated mode (ϕ_g/ϕ_u). The latter factor can be measured by comparing the intensity of a continuous source of emission as recorded by a detector in gated and ungated operation, assuming that the shape of the IRF and the gate repetition rate are known. Calculation of the absolute R/N ratio is a much more difficult problem, demanding a knowledge of the absolute Raman scattering cross-section, which is unlikely to be available except in very special cases.[2]

It should be emphasised that equation (7.26) relates to the expected improvement in R/N on going from an ungated detector with pulsed excitation to gated detection, while maintaining identical (pulsed) laser conditions. Comparison with high power cw excitation and ungated detection is very important and is made in Section 7.6.

7.3 Experimental Details

7.3.1 Instrumental configuration, monochromator design and stray-light problems

The physical operating principles of the gated DAD were covered in Chapter Six. We now consider the method of synchronising the detector "on" period with the arrival of photons.

A block diagram of the instrumentation is shown in Figure 7.7. In the experiments reported below, the laser was operated at 4kHz repetition rate, at a known wavelength of *ca.* 590nm. The average laser power was of the order of a few milliwatts, and the leakage-light suppression module (Chapter Five) was not installed. We therefore would expect a large power contribution from the leakage light at this repetition rate, and this was in fact observed.

The laser beam was focussed onto the sample, and the scattered/emitted light was collected at 90^{o} to the incident beam, and focussed onto the entrance slit of a Spex Ramalog 4 double monochromator. The detector head was mounted at the exit slit of the spectrometer, where the dispersed light was focussed onto the photocathode of the image intensifier. In all of the work reported below, a dark background (obtained with no laser illumination but otherwise identical conditions) was subtracted from each accumulated optical spectrum, in order to display the photon-noise limited spectrum.

This particular spectrometer was not well suited to this type of work for several reasons.

(a) The monochromator was designed for use with a conventional single channel analyser, (*i.e.* a PMT), and as such should be

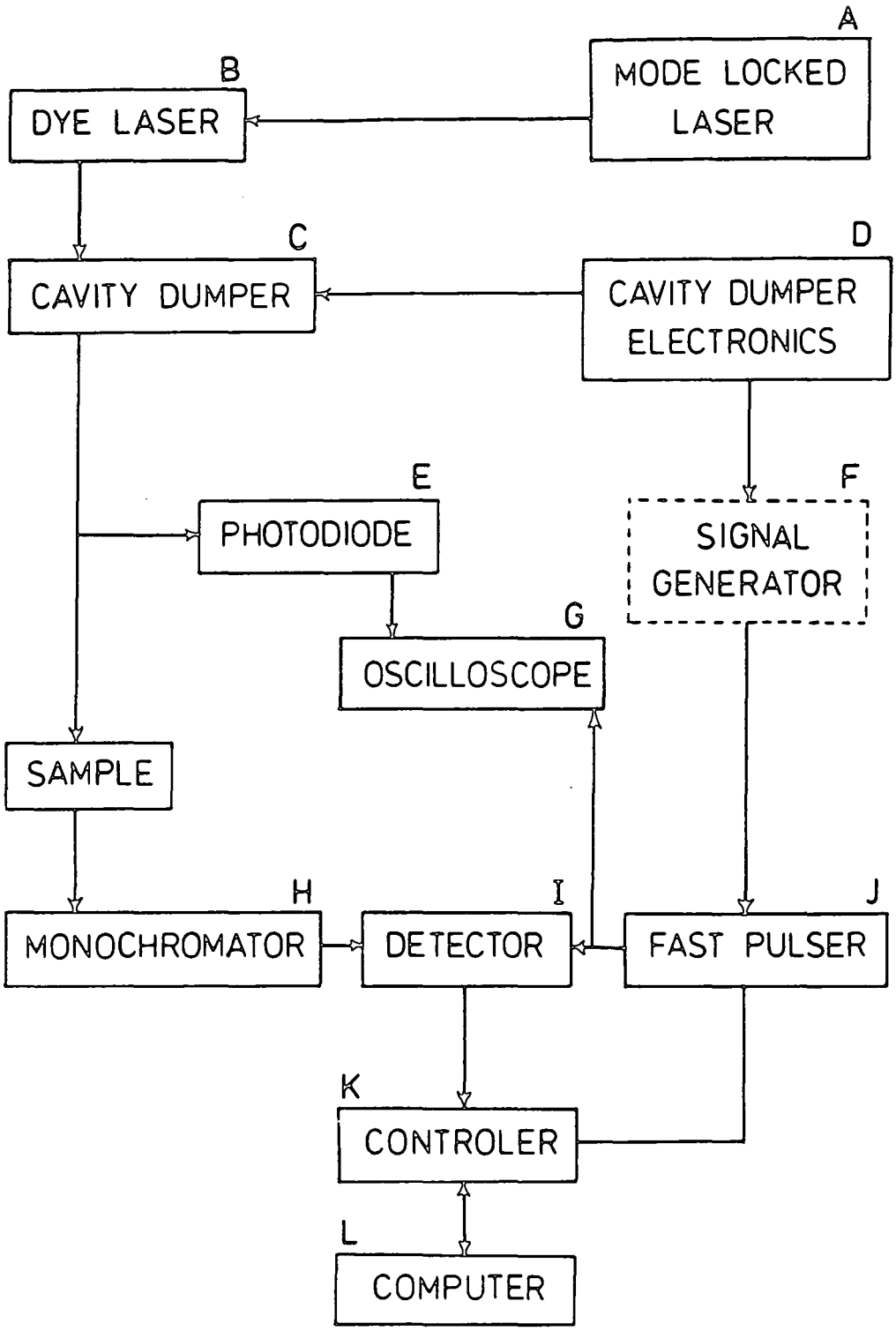

FIGURE 7.7 Experimental arrangement for the measurements. (A) Spectra Physics model 342 Mode-Locking argon ion laser, (B) 375 Dye laser, (C) 344S Cavity-Dumper, (D) 454 Cavity-Dumper driver, (E) 403B photodiode, (F) Phillips PM5712 Pulse Generator, (G) Tektronix 2215A oscilloscope, (H) Spex Ramalog 4 Raman spectrometer, (I) Spectroscopy Instruments model IRY700 Diode Array Detector, (J) MD100 Fast Pulser, (K) ST110 controller, (L) LSI11/23 computer.

used with narrow slits throughout. Normally this would entail use of entrance and exit slit widths of 100-200μ, and intermediate slits at double this value. However, in order to attain a reasonable wavelength dispersion over the array, the central slits had to be opened to about 1cm and the exit slits totally removed. This resulted in very poor stray light rejection characteristics.

(b) The spectrometer gratings were ruled at 1200gr/mm, which limited the dispersion over the array to approximately 300 cm^{-1}. This seriously limited the spectral information which could be simultaneously accessed, but was sufficient to allow the fluorescence rejection performance to be assessed.

(c) The monochromator is not designed to focus the dispersed radiation in a plane, *i.e.* not all spectral features are focussed simultaneously onto the photocathode, which will affect the relative intensities.

It has been pointed out previously[3,4] that merely opening the slits on a conventional single-channel spectrometer in order to allow installation of a multichannel detector is a tempting but inefficient approach, and what is really required is a purpose designed spectrograph. This is discussed in Chapter Nine.

In our work, factor (a) was the most serious constraint. The problem of poor stray light rejection was so severe that solid samples could not be studied below 800 cm^{-1}, owing to the large amount of light reflected directly into the spectrometer. This resulted in an excessively intense Rayleigh wing. Liquid samples were much easier to study since reflected light was minimised, and therefore the background noise could be assigned to fluorescence alone. This greatly facil-

itated the theoretical analysis of the signal/noise improvements obtained on gating the detector.

7.3.2 Synchronisation of the detector gate with the laser pulse

The -200V pulse which is required to gate the array was supplied by an S.I. model MD 100 Fast Pulser. The pulses are generated with durations shown to *ca.* 5ns FWHM, at repetition rates up to 5kHz (manufacturers specifications). For this region, the laser repetition rate was initially constrained to less than 5kHz. This constraint was later relaxed (Section 7.7).

Obviously the gating pulse must be synchronised with the time of arrival of the Raman photons, *i.e.* $0<t<2L$ (Figure 7.4). Figure 7.7 illustrates how this was achieved. The laser cavity dumper driver provides an output voltage pulse (CDSO, Chapter Six) which is synchronised (in time) with respect to the laser pulse. The amplitude of the CDSO pulse is not sufficient to activate the fast pulser, and so it was first used to trigger a Phillips PM 5712 pulse generator, the TTL output of which activated the Fast Pulser. The time of triggering was controlled both by a continuously variable coarse delay in the PM 5712 generator (10ns - 100ns) and a 0-256ns delay (1ns increments) which is incorporated in the Fast Pulser. By adjusting the delays in both pulse generator and the Fast Pulser, it is possible to ensure that the gate is opened at the required time with respect to the pulsed Raman/fluorescence photons.

The output of a Spectra physics model 403B fast photodiode, sampling a small portion of the cavity-dumped laser output, was used to provide a point of reference against which

to measure the separation of the photodiode pulse and the -200 V pulse (x10 attenuated) on a dual trace oscilloscope (Tektronix 2215A). The correct delay settings were then established by recording the intensity of the 992 cm^{-1} band of benzene (<40ps time duration) at different delays (Figure 7.8). The accumulation time of each gated spectrum was 135 s in total, during which the detector was gated "on" for a total of *ca.* 3ms!

7.3.3 Measuring the IRF of the gated DAD

Since the Raman photon distribution comprises an impulse input with respect to the DAD gate width, the "time scan" of the scatter (Figure 7.8) reveals the IRF of the gated DAD. In this figure the time axis has been calibrated such that the delay setting at which a Raman signal was first detected is defined as t=0. This corresponds to the definition adopted in the theoretical treatment (Section 7.2.2), namely the time at which the detector has just closed (Figure 7.4). The observed IRF is approximately trapezoidal, with a base of *ca.* 9ns (2W) and an apex of *ca.* 3.5ns (2L).

When t>9ns, the Raman photons arrive before the gate has opened, and so none are detected, whereas negative values of t correspond to the gate having closed before the Raman photons arrive, and again no photons are detected (Figure 7.4). Therefore, by noting the delay settings which corresponds to the time t=0, it is possible to position the gate at any desired position relative to the Raman/fluorescence photons, and so collect Raman photons in preference to fluorescence photons.

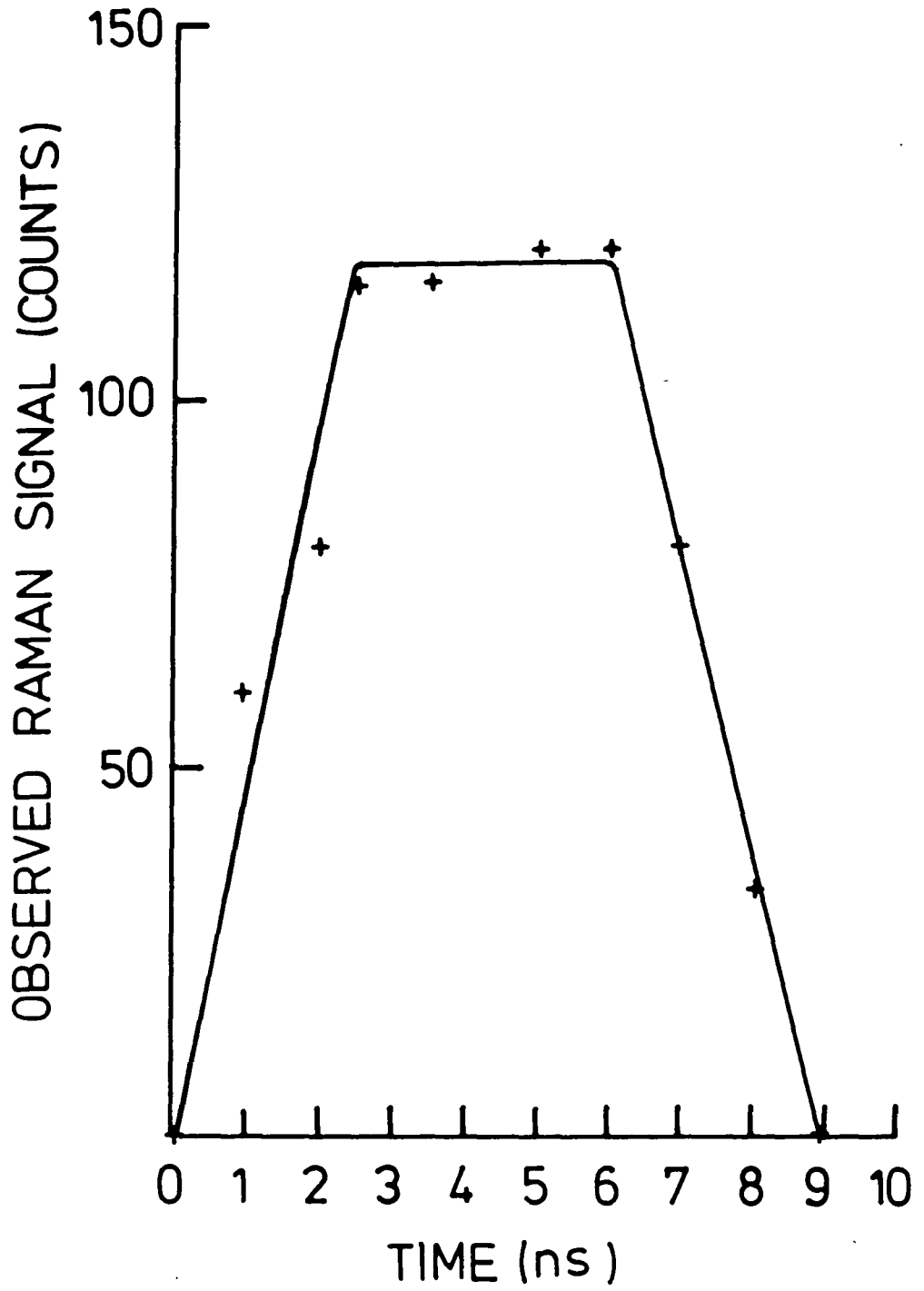

FIGURE 7.8 The observed response of a gated diode array detector to a Raman signal excited using laser pulses of less than 40 ps duration. Data (+) were obtained by changing the gate position "t". The solid line is the trapezium used to represent these data in subsequent calculations.

7.4 The "ringing effect"

7.4.1 Observation of multiple fluorescence decays

When a sample is illuminated by the pulsed laser, the fluorescence decay may be obtained merely by recording the intensity of the fluorescence background of a Raman spectrum as a function of gate position. Figure 7.9 shows the observed decay for a 0.005 M solution of rubrene (Aldrich Chemical Co.) in benzene. No sample purification or degassing was performed. Rather than the expected single fluorescence curve, we actually observed several decay curves of decreasing intensity, separated by intervals of *ca.* 15ns. This is a very surprising, and highly significant, result.

Since the laser pulse separation is 250μs at 4kHz, these extra features cannot arise from excitation by adjacent laser shots. Also, the separation of the decays is greater than the mode locked pulse separation (*ca.* 12.2 ns), so the effect is not due to leakage light. If we assume that the "true" decay curve is the one of highest amplitude, and set t=0 at the start of this curve, then Figure 7.9 indicates that the extra features are detected at earlier gate positions, which correspond to negative time values (Figure 7.4).

In order to study this effect in more detail, a series of measurements were made in which all of the run-time parameters were kept as for the previous experiment, but using pure benzene as a sample. The variation of the intensity of the 992 cm^{-1} band was measured as a function of t, but in this case the gate was positioned to cover negative time values as well as positive ones (in contrast to Figure 7.9). The results (Figure 7.10) again show a series of maxima, separated by

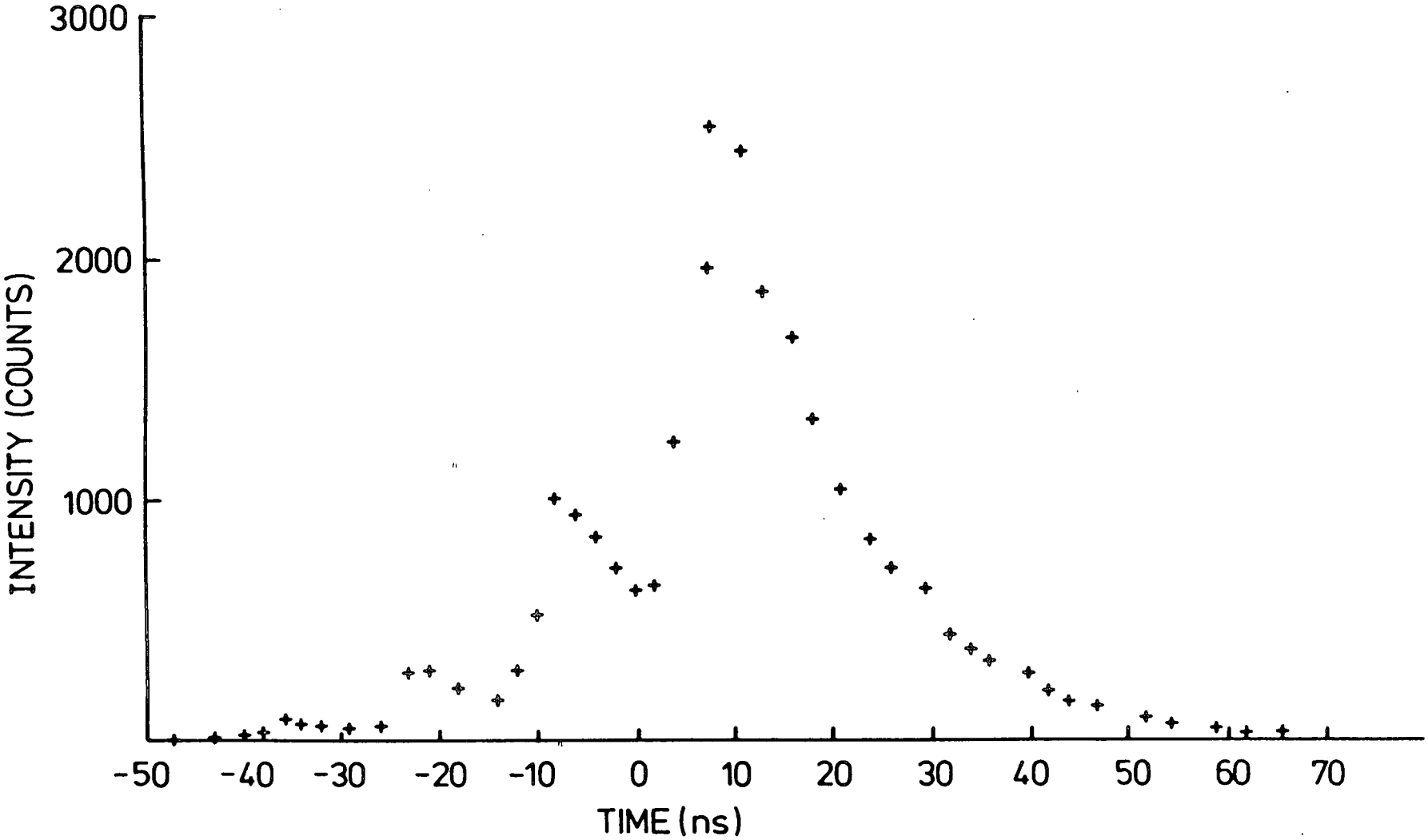

FIGURE 7.9 Fluorescence intensity as a function of the gate position "t" for a wavenumber shift of 992 cm^{-1}. The sample was 5 x 10^{-3}M solution of rubrene in benzene. Negative time values indicate that the gate is positioned prior to the arrival of the photon pulse.

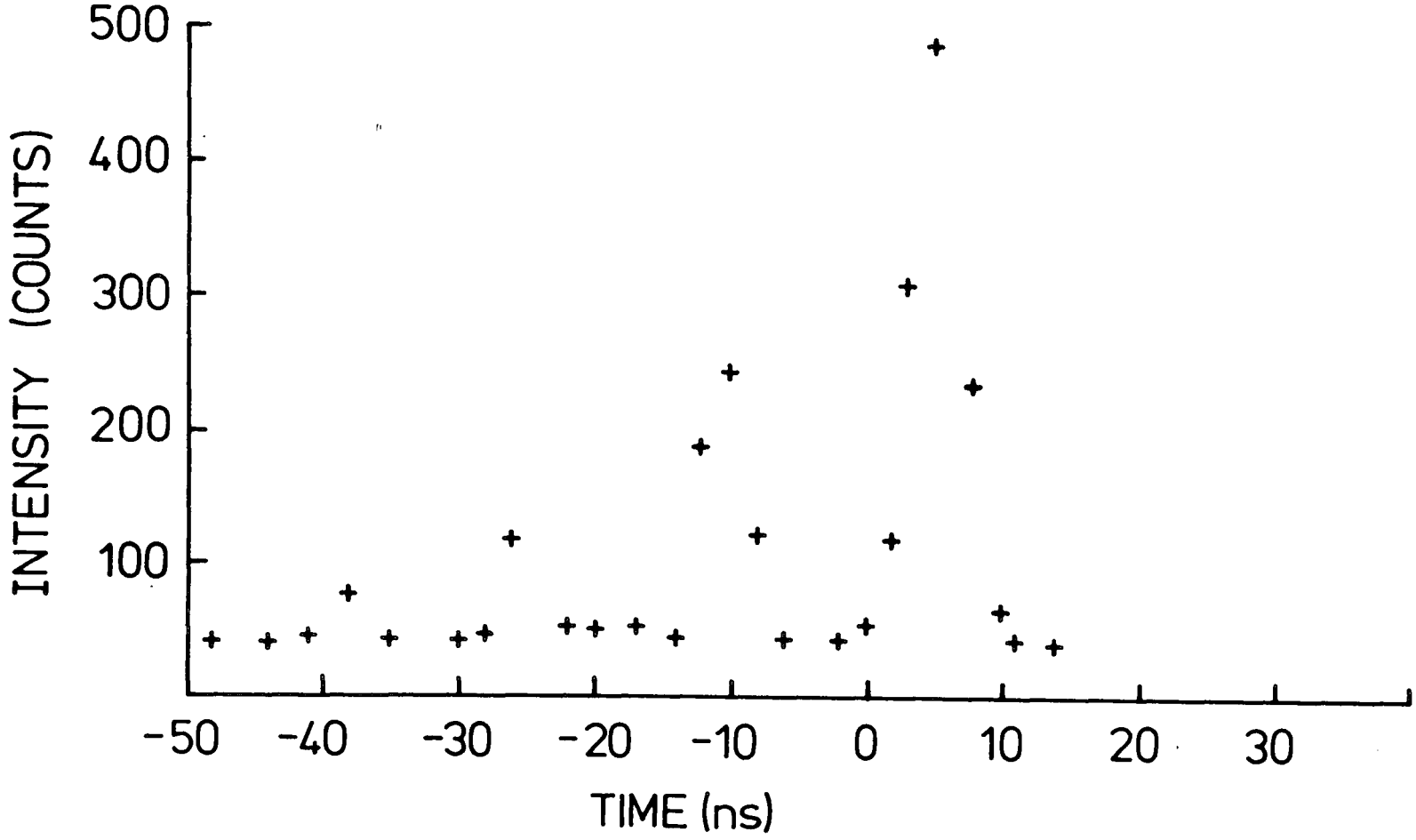

FIGURE 7.10 Intensity of 992 cm^{-1} band of benzene as a function of gate position. The multiple opening of the gate (see text) is clearly illustrated.

ca. 15.5 ns, which diminish in intensity as the gate is shifted to earlier times.

The most likely explanation for this observation is that the detector is not opening just once, at the selected t value, but is in fact re-opening with a period of *ca.* 15.5 ns, (Figure 7.11). Under these conditions, a gate which was nominally set to close at t=0 would in fact reopen at t=6.5 and close at t=15.5ns (first echo), and so the gate would actually be open while the fluorescence photons were incident, giving a nonzero detected intensity. Subsequent reopening apparently occurs at multiples of this interval, although the detection efficiency decreases with each echo.

This explanation has been confirmed as being plausible by the manufacturers, and as yet no other suggestion as to the cause of this effect has been made. Therefore, we proceeded on the assumption that the gate <u>was</u> re-opening, and this assumption was justified to a certain extent by the fact that adapting the model (equations (7.10)-(7.14)) to include the effect of the first echo gave a reasonable representation of the observed behaviour (Section 7.6).

This multiple opening of the detector probably arises as a consequence of ringing of the -200 V pulse applied to the MCP. Examination of the pulse on the oscilloscope showed no sign of multiple pulsing, therefore the multitriggering is most probably a result of an impedance mismatch between the fast pulser and the MCP, causing reflection and ringing of the voltage pulse. The amplitude of the pulse is attenuated on each "echo" such that the maximum detector efficiency is decreased by a factor of 1/2 (Figure 7.11).

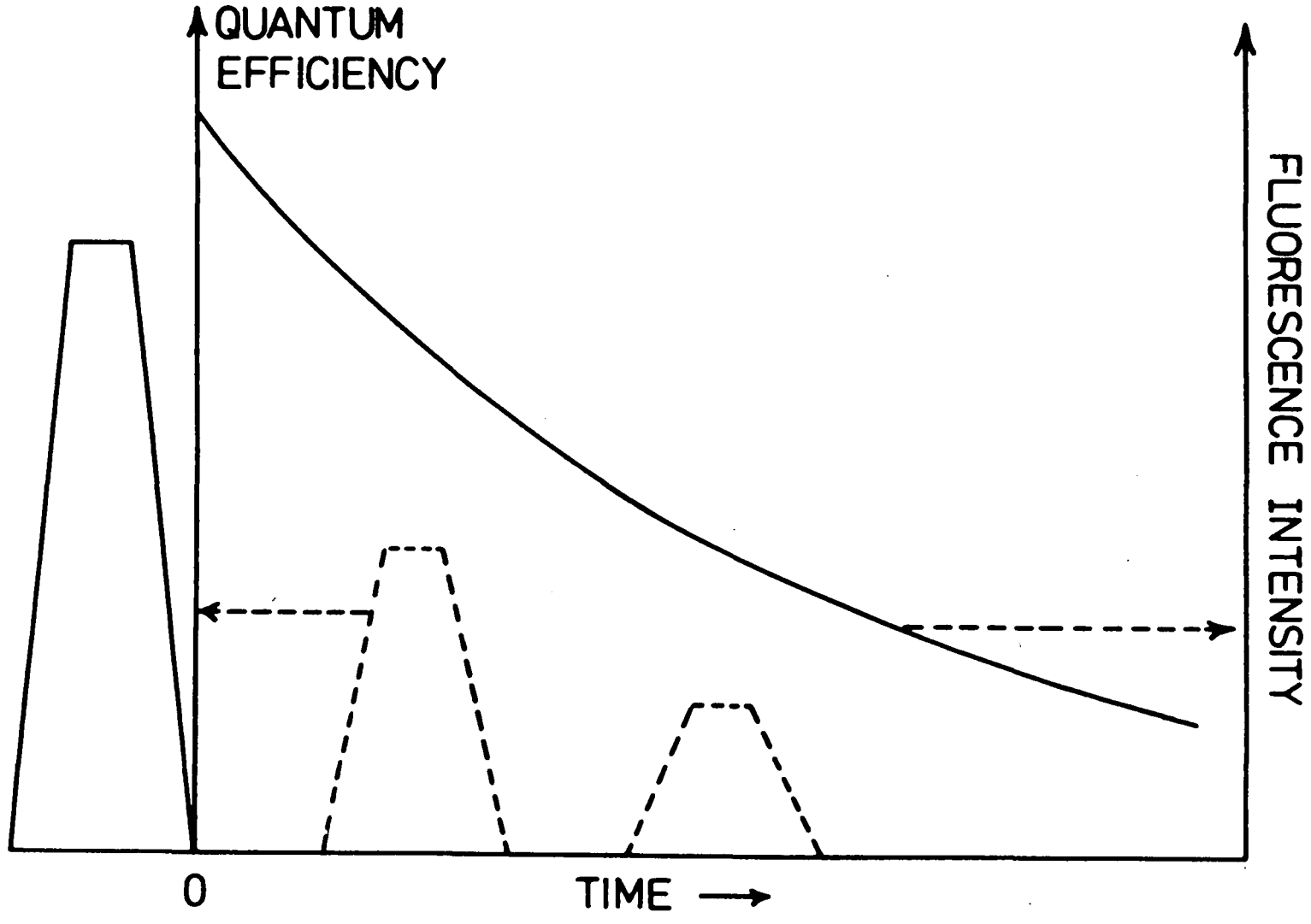

FIGURE 7.11 Schematic representation of the multiple gate opening (ringing) effect.

The ringing effect is important for three reasons:

(a) It is clearly possible for a user who is unaware of the problem to operate the detector away from the main "on" period, *i.e.* on one of echoes. This would result in a reduced quantum efficiency for the detector and a poorer R/N ratio.

(b) The ringing effect increases the fluorescence intensity which is detected. A gate positioned at t=2.75 ns will capture all of the Raman photons ($g(t)=\phi_g$) and a certain fraction of the fluorescence; however, when reopening occurs some 15ns later, there are no Raman photons present, but there may be a substantial fluorescence intensity (depending upon the decay time). Therefore the first echo captures only fluorescence photons, and so decreases both the R/F and R/N ratios in gated mode.

(c) The multitriggering actually occurs at MHz repetition rates, which implies that it is possible to gate an MCP at this rate. Therefore the rate determining step for gating is not imposed by the MCP, but rather by the rate of production of the -200 V pulses, and the speed of data handling. This is discussed in greater detail in Section 7.7.

The ringing effect can be allowed for in the theoretical analysis given in Section 7.2. The computer program was modified such that when the value of H(t) is calculated, an additional component of 0.5xH(t+15.5) is evaluated and added to H(t), assuming that the quantum efficiency is reduced by 1/2 on the first echo. Only the first echo was included in the treatment.

7.5 Analysis of the observed decay kinetics

Figure 7.12 depicts the main fluorescence decay curve observed for 5 x 10^{-3}M solution of rubrene in benzene. Experimental conditions are given in the figure legend. Also shown are the best fits obtained by the computer program, both with and without an allowance for the ringing effect. The ringing has the largest effect in the region t→0 ns, where a substantial fluorescence intensity is detected as opposed to the ideal value of zero intensity. This signal is entirely due to photons arriving during the 1st "echo".

The agreement between calculated and observed behaviour is good considering the unsophisticated nature of the model employed. The deviations between the observed and calculated curves are not random, which indicates that the model is not a very good representation of the true behaviour.[5] However, the accuracy is certainly sufficient to allow evaluation of the possibility of using this device for fluorescence rejection.

The best fit was obtained for a decay constant k of 0.095 ns^{-1} (τ_f = 10.5 ns). Literature values are reported for decay times of *ca.* 16 ns for solutions in degassed benzene. In our work, no attempt was made to correlate solution concentration or solvent quality, and the solution was not degassed, so the lifetime discrepancy is not surprising. The calculated decay constant was in reasonable agreement with that calculated by the TCPC method, (Chapter Eight), and was sufficient for evaluation of the theoretical model developed above.

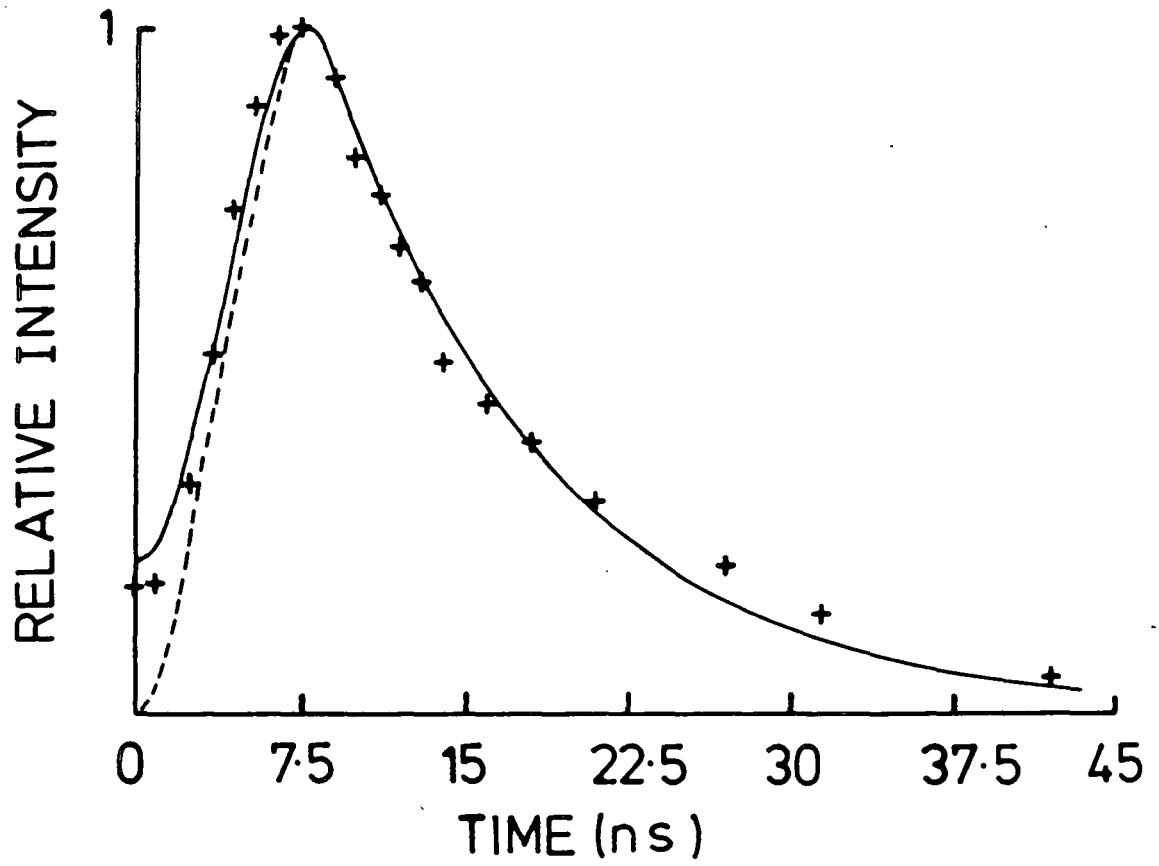

FIGURE 7.12 The cross correlation of an exponential function ($k = 0.095\ ns^{-1}$) with a trapezoidal impulse response. The broken line is the result obtained when detector ringing is ignored and the solid line when this effect is included. (+) represents the measured intensity.

7.6 Fluorescence rejection results

7.6.1 Quantification of detector noise

Prior to making any measurements on accumulated spectra, a dark background (*i.e.* taken with no laser illumination) was subtracted from each spectrum, in order to remove the signal due to thermal charge generation in the array. This background subtraction does not remove the noise associated with the dark charge/readout, and so this noise must be quantified.

The discussion in Chapter Six indicated that the noise of the dark charge/readout cycle should be insignificant compared to that originating from the fluorescence. To check this, dark spectra were accumulated for various time periods (34 ms - 135 s), two for each integration time. One spectrum from each pair was then subtracted from its partner, and the noise (rms) on the resulting spectrum was measured (Table 7.1).

TABLE 7.1 Quantification of detector noise

Time/s	Noise on subtracted spectra/rms counts
0.034	1.3
0.34	1.2
3.4	1.3
34	2.2
135	2.2

The results show that dark spectra obtained over long time periods give rise to low noise (*ca.* 2 counts). This is in reasonable agreement with the value calculated on the assumption that dark charge collects at 100 counts/sec, (*ca.*

3 counts rms after 135 seconds). Also, the data demonstrates that the detector noise is dominated by the readout contribution for short integration times, as would be expected.

It is shown below that the fluorescence backgrounds observed in our work are sufficiently intense for the detector noise to be negligible, and so we are justified in simply considering the variation in fluorescence and Raman intensities during gating.

7.6.2 Observed fluorescence rejection efficiency of the gated DAD

7.6.2.1 Experimental details and results

In order to determine the effectiveness of the gated DAD in TRFR, the Raman spectra of benzene, doped with rubrene (5×10^{-3} M) were obtained over a range of gate positions, and were compared with spectra taken with the detector in ungated mode. The laser was operated at 4kHz, (*ca.* 590 nm, average power *ca.* 3mW) for both the gated and ungated spectra; only the mode of detection was changed during these experiments. The accumulation time was 6.76 s (ungated) and 135.2 s (gated), *i.e.* $T_g/T_u = 20$. The reason for this change in accumulation time is discussed in Section 7.6.4.

In order to quantify the rejection efficiency, the Raman signal was measured as the peak height of the 992 cm^{-1} band, and the fluorescence signal as the height of the background immediately below the Raman band. The noise was measured by performing a linear regression over a region of the fluorescence background near to the Raman band, and calculating the rms deviation from the best line. These quantities are depicted on Figure 1.3.

Figure 7.13 illustrates the effect of gating the detector with a gate positioned at t=2.5 ns. Clearly, the R/F ratio is enhanced significantly, which indicates that fluorescence rejection is occurring, but the R/N ratio is barely altered. Table 7.2 quantifies the R, F and N levels observed over a wide range of gate positions.

TABLE 7.2 Effect of gate position upon Raman, fluorescence and noise levels

Gate position/ns	R/counts	F/counts	N/rms counts
UNGATED	1614	7216	86
1	84	76	10
2.5	160	138	12
3.5	194	204	14
4.5	211	285	19
5.5	206	344	20
6.5	168	383	22
7.5	95	388	20
9.0	0	360	19

Again, it must be emphasised that the above data refer to the noise on the fluorescence background. Since the Raman signal is of a similar magnitude to the fluorescence, the total noise at the top of the Raman band will be somewhat higher than the N values given above, *i.e.* the Raman signal actually makes a significant contribution to the total noise. This does not affect our analysis which deals specifically with the fluorescence noise. For all of the above gate positions N>10 counts, which indicates that the detector noise (*ca.* 2 counts) does not make a significant contribution and so may be ignored.

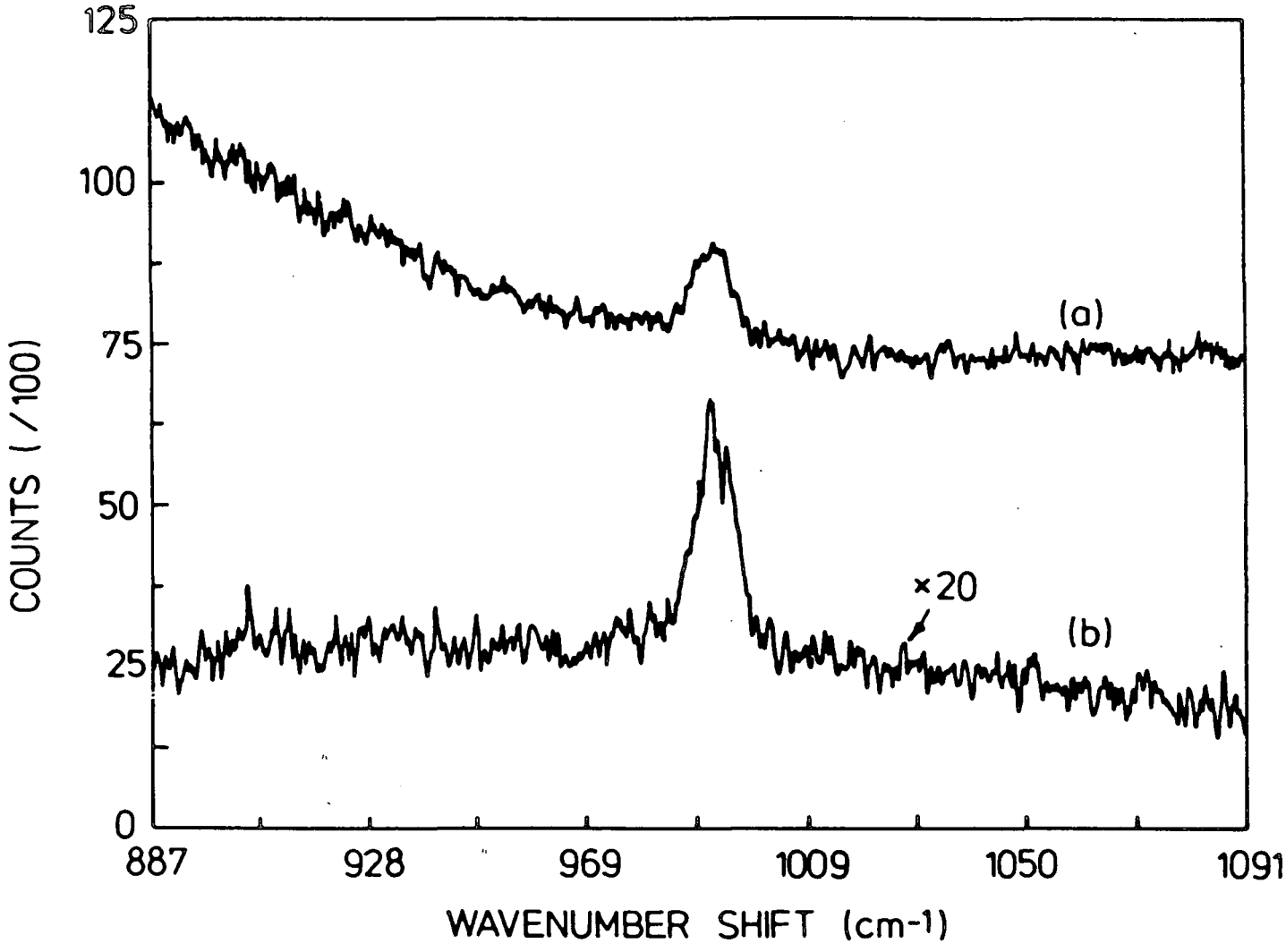

FIGURE 7.13 A typical example of the effect of gating.

(a) Ungated spectrum of benzene doped with rubrene (5×10^{-3} M). 4kHz laser rep. rate.

(b) Gated spectrum, (t=2.5 ns), identical laser conditions. Note the improvement in R/F and negligible effect on R/N of gating the DAD.

Knowing the values of k, L and W it is possible to calculate the improvements in R/F and R/N as a function of gate position, using equations (7.22) and (7.26). In order to use these equations, we must know ϕ_g/ϕ_u, the ratio of maximum detector quantum efficiency in gated/ungated mode. This was estimated by recording the intensity of an attenuated He/Ne laser (cw source) in both gated and ungated mode, using a pulse generator to trigger the fast pulser at 4kHz for gated detection. By calculating the effective "on" time of the gated detector (including an allowance for the ringing effect), and comparing the detected intensity with the ungated result, the ratio ϕ_g/ϕ_u was estimated to be *ca.* 1.3.

7.6.2.2 Comparison of theoretical and experimental R/F and R/N enhancements

Table 7.3 compares the calculated and observed enhancements in R/F and R/N, both with and without an allowance for the ringing effect. It is clear that, on the whole, the calculated values are in good agreement with the observed behaviour. The errors on the observed values were estimated at *ca.* ±15%. No attempt was made to increase the accuracy of the data, since it was adequate to demonstrate that the theoretical model gives a reasonable representation of the detector response.

In terms of the calculated values, the ringing effect induces sharp deviation from ideality in the region $t<2.5$ns, where the improvements are much less than would be expected from Figure 7.12. Over the region $2.5<t<7.5$ ns, the agreement between calculated and observed values is good for both E[R/F] and E[R/N], if ringing is taken into account.

TABLE 7.3 Comparison of calculated and observed rejection efficiencies

Gate Position	E[R/F]			E[R/N]		
t/ns	Non-Ringing*	Ringing*	Observed	Non-ringing*	Ringing*	Observed
1	21.7	3.2	5.0	1.0	0.4	0.5
2.5	9.1	5.0	5.3	1.0	0.8	0.7
3.5	5.5	3.9	4.3	0.8	0.7	0.7
4.5	3.9	3.1	3.4	0.7	0.6	0.6
5.5	3.1	2.6	2.7	0.6	0.6	0.6
6.5	2.4	2.1	2.0	0.5	0.5	0.4
7.5	1.3	1.2	1.3	0.3	0.3	0.3

* denotes a calculated value.

E[R/F] has a maximum value of 5.3, as opposed to a calculated magnitude of 5.0, while E[R/N] has a maximum value of 0.7, with a calculated value of 0.8.

At t=1 ns, the calculated values are too low; this is probably because at this position the Raman signal coincides with a sharply rising region of the gate response, Figure 7.5, and so a slight inaccuracy in gate positioning (to the extent of 0.5 ns, the estimated resolution of our timing equipment) would account for the discrepancy between calculated and observed values.

Although we see significant improvements in the R/F ratio, which indicates that fluorescence photons are rejected relative to the Raman photons, it is clear that the R/N ratio is not enhanced by gating the detector. In fact the R/N is actually decreased compared to ungated detection with the same pulsed source. As the object of the work is to improve the R/N ratio, (the R/F ratio being largely irrelevant), this is a rather unfortunate result! The situation is made somewhat worse by the fact that the ratio of counting times in gated/ungated modes was x 20; in a fair test of the performance we would naturally ensure that $T_g/T_u = 1$. This would further reduce E[R/N] by a factor of $1/\sqrt{20}$, giving E[R/N] = 0.2 for a gate in the t=2.5 ns position. The reasons for this degradation in R/N are discussed in Section 7.6.4.

7.6.3 Optimisation of gate position

From Table 7.3, it is obvious that the gate must be correctly positioned in order to obtain optimum performance. The optimum gate position depends upon the magnitude of the ringing effect and the decay constant k. Furthermore, the R/F

ratio is, in general, optimised at a different position to R/N. The results which are quoted below were obtained by calculating the improvements in R/F and R/N for a range of gate positions and fluorescence decay constants.

7.6.3.1 Non-ringing detector

For a non-ringing detector, it is found that E[R/F] is maximised as $t \to 0$, whilst E[R/N] is greatest at t=2.75, irrespective of the magnitude of τ_f. The improvement in R/F is of no consequence except under two special circumstances.

(a) The dynamic range of the A/D converter might be exceeded by intense fluorescence levels, in which case it may be desired to reduce the background level irrespective of the deleterious effect on R/N when $t \to 0$.

(b) The noise level might not be governed by Poisson statistics. It is sometimes found[6,7] that the background is not shot noise limited, but in fact consists of sudden jumps or steps in the background level, of much greater amplitude than the rms shot noise. Under such circumstances, this noise is often reduced in proportion to the reduction in the fluorescence signal F, rather than $\sqrt{F}$, which then favours earlier gate positions. Such circumstances were not countered with the samples studied in this work, but were found to be important in one of the systems studied with the PMT-based rejection system (Chapter Eight).

7.6.3.2 Ringing detector

When ringing occurs, E[R/N] is again maximised at the beginning of the IRF plateau (t=2.75 ns). However, the position which maximises E[R/F] is determined by τ_f. When

τ_f is short (1 ns) the ringing has little effect, since no fluorescence photons are present at the position of the first echo. The results are then identical to those for a non-ringing detector. As the lifetime increases, the fluorescence intensity detected at the first echo increases, and the optimum E[R/F] is obtained with gates positioned at higher time positions. For example, E[R/F] is maximised at t=1.5 ns when τ_f = 5 ns, and t=2.75 when τ_f = 10 ns. When τ_f>10 ns, E[R/F] is always optimised at t=2.75 ns. Again, the consideration of E[R/F] is only important under the circumstances outlined in Section 7.6.3.1.

7.6.3.3 Conclusions on optimisation of gate position

Under most conditions, the optimum gate position will be that which maximises R/N, and this position should always be t=2.75 ns, irrespective of the ringing effect and the fluorescence lifetime. If it is desired to maximise R/F, the corresponding gate position is dependent upon the magnitude of the ringing effect and the fluorescence lifetime. For samples with τ_f>10 ns, both E[R/N] and E[R/F] are maximised at the same position. These conclusions are confirmed by the experimental results (Table 7.3).

7.6.4 The reason for the observed decrease in R/N upon gating the detector: the effect of leakage-light

The low values of E[R/N] arise primarily as a result of the nature of the laser output. As was discussed in Chapter Five, the laser output consists not only of the main cavity dumped pulses at the selected repetition rate, but also of the smaller leakage-light pulses. At the time at which the experiments were performed, the ratio of main pulse/leakage intensity

was approximately 100:1 (estimated by measuring the relative intensity of a Raman feature in gated and ungated detection modes).

At 4kHz dump rate there are 20,499 leakage pulses for each main pulse in the beam. This means that only (1/205)th of the total laser intensity was actually carried by the main pulses; the rest was "wasted" in the leakage pulses and was not utilised by the gated detector. This behaviour is of vital importance when the system is used at low repetition rates. Of course, the problem is less severe when operating at higher pulse rates since there are less leakage pulses present for each main pulse (Chapter Eight).

This effect may be quantified by recourse to equation (7.26). The factor I_m/I_T was very low (0.005 at 4kHz), since only the main pulse intensity was utilised in the gated experiment. Raman scatter induced by the leakage pulses was not detected in the gated experiment. In the ungated experiment, Raman scatter arising from the entire laser output was detected. This means that the effective laser intensity was reduced *ca.* 205 times in the gated as opposed to the ungated spectra. This reduced the R/N ratio observed in gated mode to a factor of $(1/205)^{\frac{1}{2}} = 0.07$ of that which would have been obtained with a perfect laser output, *i.e.* one in which all of the power was carried by the main pulses ($I_m/I_T = 1$).

7.6.5 Improving the R/N enhancement of the gated DAD by suppression of the laser leakage pulses

It was shown above that if the laser output were perfect, *i.e.* there was no leakage contribution and so the total beam energy was carried in the main cavity dumped pulses, the E[R/N] ratios would be increased by a factor of *ca.* $\sqrt{205}$, *i.e.*

the maximum improvement would increase to *ca.* 14.3x0.8=11.5 (T_g/T_u=20). Since the original work was performed upon the gated DAD, the laser performance has been substantiallv improved such that at present *ca.* 0.2 mW is delivered, (4kHz pulse rate), with almost no leakage contribution. This was achieved by inserting an rf suppression circuit between the cavity-dumper driver and the Bragg cell (Chapter Five).

With this improvement in laser output, we would now expect to observe R/N improvements of *ca.* 2.6 (assuming T_g/T_u=1), whereas previously the R/N ratio was degraded by a factor of *ca.* 0.2 under identical operating conditions. Figure 7.14 illustrates the expected improvements in R/F and R/N for our present ringing detector as a function of lifetime τ_f. The results were calcualted for a gate position t=2.75 ns, under the assumption that $T_g/T_u=I_m/I_T$=1.

7.6.6 Comparison with cw excitation

Up to this point all calculations have related to the effect of gating the detector while operating the laser at the same repetition rate, namelv 4kHz. This does not give a true representation of the usefulness of the system, since under normal (ungated) conditions we would operate a cw laser at the highest output power compatible with sample stability. We should therefore compare the performance of the gated detector and 4kHz pulsed laser to that of the ungated detector and a cw laser operating at the same wavelength.

In order to make this comparison, I_m/I_T (equation (7.26)) is replaced by P_m/P_{CW}, where P_m is the average power carried by the main cavity-dumped pulses alone, and P_{CW} is the corresponding power of the dye laser, operating in cw mode, at

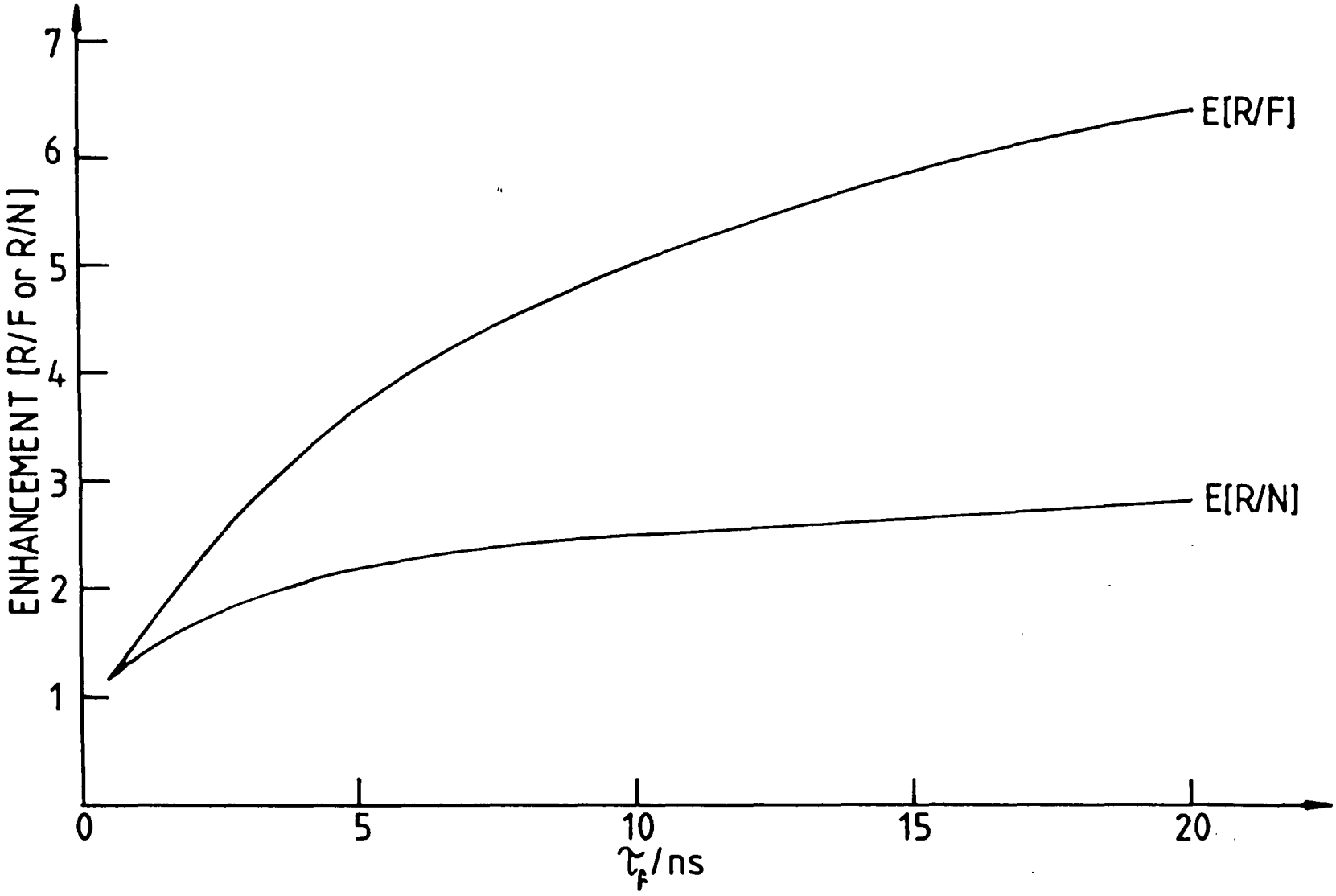

FIGURE 7.14 Calculated variation of E[R/F] and E[R/N] as a function of τ_f. Gate position is fixed at t = 2.75ns. Zero leakage intensity is assumed ($I_M=I_T$), and $T_g/T_u=1$.

the same wavelength as the pulsed laser. An output of *ca.* 100mW would be a typical power level employed in Raman spectroscopy, although lower powers might be necessitated for the study of photosensitive materials.[8] With the improved laser performance at 4kHz, the ratio P_m/P_{CW} = 0.2/100=2×10^{-3}, and so the R/N improvement is reduced by a factor of $(2\times10^{-3})^{\frac{1}{2}}$. For a lifetime of *ca.* 10 ns this yields a calculated E[R/N] of *ca.* 0.1, *i.e.* a tenfold degradation in signal/noise upon gating the detector! In fact, with the present system, cw irradiation of intensity >1.4mW,coupled with continuous operation of the DAD,would yield a superior R/N ratio than the gated detector and 4kHz pulsed laser!

It must be emphasised that this degradation does not arise because of inefficient fluoresence rejection by the gated DAD, but is rather due to the fact that we are constrained to operate the detector/laser at low (kHz) repetition rate. The low power delivered by the laser at these pulse rates causes severe degradation in the R/N ratio compared to that obtained at much higher cw laser powers. Increasing the power of the pulsed laser source would immediately transform the system into a useful TRFR apparatus (Section 7.7.1).

It is obvious that in its present form, the gated DAD/pulsed laser configuration is not suitable for obtaining Raman spectra of strongly fluorescing compounds, and that conventional cw excitation and detection yields far superior results. In order to obtain any benefit from the gating process, several modifications will have to be made to the system.

7.7 Modifications which should improve the TRFR performance of the gated DAD/pulsed laser system

7.7.1 Modifications to the laser system

It is clear from the calculations above that the gated DAD yields a significant improvement in R/N compared to ungated detection at the same laser repetition rate. Unfortunately, the pulse power of our present laser system (kW) is too low to produce spectra of reasonable R/N at low (kHz) pulse rates. If the power of the laser pulses could be increased significantly, a very effective fluorescence rejection system would result.

Ideally, the average power of the pulsed laser would be equal to or greater than that of the cw laser which was used for comparison, in our case 100 mW. Assuming a pulse rate of 5kHz, this would demand an energy of *ca.* 20 μJ per laser pulse. For comparion, the average energy in one pulse from our system is *ca.* 30 nJ, *i.e.* a thousand times lower than that required! Furthermore, in order to preserve the timing resolution of the system, the laser pulse width must be less than 100 ps.

At present, most studies of picosecond phenomena are based upon two extreme types of laser source, namely systems which produce kW pulses at high repetition rates (MHz), or which amplify picosecond pulses to very high power (gigawatt) but at low repetition rates (1-10Hz).[9,10] High pulse powers at medium (kHz) repetition rates are usually achieved by Q-switching,[11] but the resulting pulses are usually of the order of 10-100 ns duration, which is far too long for our work. Many examples of each type of system have been published in the

literature, but comparitively few studies have been reported upon generation of medium (megawatt) pulses at kHz repetition rates.

The very intense picosecond pulses which can be produced at 1-10kHz are unsuitable for our work for several reasons, such as the onset of nonlinear effects[12] and the possibility of sample degradation. However, a variation of the picosecond pulse amplifier utilised by Ippen and Shank[13] might prove useful in obtaining medium power pulses (10^6-10^7W) at kHz rates, rather than GW pulses at 10 Hz. Their system involved pumping a dye amplifier[11] with an amplified, frequency doubled Nd:YAG laser, Q-switched at 10 Hz to coincide with the arrival of a mode-locked dye pulse at the dye amplifier. Increasing the repetition rate of the Q-switched laser would decrease amplification of the dye pulse, but might allow successful production of medium intensity pulses at kHz rates.

As an alternative to amplifying the output of our present cavity-dumped system, an entirely different type of laser could be employed. One possible route would be to utilise a frequency-doubled, mode-locked, Q-switched Nd:YAG or Nd:Glass laser. The output of such a device consists of a short burst (*ca.* 150 ns) of mode-locked pulses at 532 nm wavelength. As a typical example, the Quantronix model 416 Q-switched, mode-locked Nd-YAG produces bursts of mode-locked pulses of *ca.* 100 ps individual duration. Each mode-locked pulse carries *ca.* 50 μJ of energy (0.5 MW), while each Q-switched pulse (containing *ca.* 15 mode-locked pulses) delivers *ca.* 0.6 mJ of power. The Q-switched repetition rate is of the order of 1kHz, which matches the repetition rate of the gated DAD.

In order to use such a device with a gated DAD, it is necessary to select one single mode-locked pulse from each Q-switched burst. This is most commonly achieved by using a Pockels cell.[11] For example, Matsushima *et al*[14] described a pulse switchout system, which can selectively pass single modelocked pulses from the output of a Q-switched laser, at repetition rates of up to 2 kHz. Such a system would be an almost ideal source for the gated DAD system, and would allow significant R/N improvements to be attained over the use of a comparable power cw source with ungated detection.

Thus it seems likely that a kHz repetition rate picosecond pulse source could be obtained with an average power of *ca.* 100 mW. Such a source would allow the full benefits of the gated detection system to be realised, namely E[R/N]=2.6 compared to cw excitation and detection (τ_f=10 ns). Further modification of the detector characteristics (see below) should result in very substantial (*e.g.* 7 fold) improvements in the R/N ratio of spectra of samples containing moderately long-lived fluorescors (τ_f 10 ns).

7.7.2 Modifications to the detection system

It should be possible to substantially improve the system performance by modifying the operating characteristics of the gated DAD. Here we consider what improvements could be made to the detection system, and neglect the possibility of obtaining high power, low repetition rate laser pulses. For simplicity, we consider that an rf suppressor circuit is used, so that the laser performance is ideal (I_m/I_T=1), and that the accumulation times are equal in both ungated and gated detection modes. All R/N improvements are

calculated relative to the R/N expected for ungated detection with a cw laser source of *ca.* 100 mW.

7.7.2.1 Increase of gateable repetition rate

It is clear that one way of improving the ratio P_m/P_{CW} is to operate the laser/gated DAD at a higher repetition rate. For instance, a tenfold increase in pulse rate would yield an average pulsed power of *ca.* 2 mW, and so the observed E[R/N] values should increase by a factor of $\sqrt{10}$.

Figure 7.10 shows that the MCP appears to be gateable at MHz rates, and we have observed the fast pulser itself to function satisfactorily up to 40 kHz, so it would be expected that the tenfold improvement in gating rates should be easily achieved. Unfortunately, we have as yet been unable to obtain satisfactory gated spectra at 40 kHz, since the data stored in the controller appears to become corrupted (Figure 7.15). Furthermore, the observed intensity of the optical signal does not appear to increase linearly with repetition rate.

Extensive consultations with the manufacturer have failed to reveal the reason for this result, but since the hardware appears to function correctly at these rates, it is possible that the problem lies in the data handling performed by the controller. For instance, the incorrect synchronisation of the readout cycle with the application of the -200 V pulse could well cause problems. Even so, there is no fundamental reason to suppose that the detector cannot be successfully gated at this repetition rate, and this is an area worthy of further investigation.

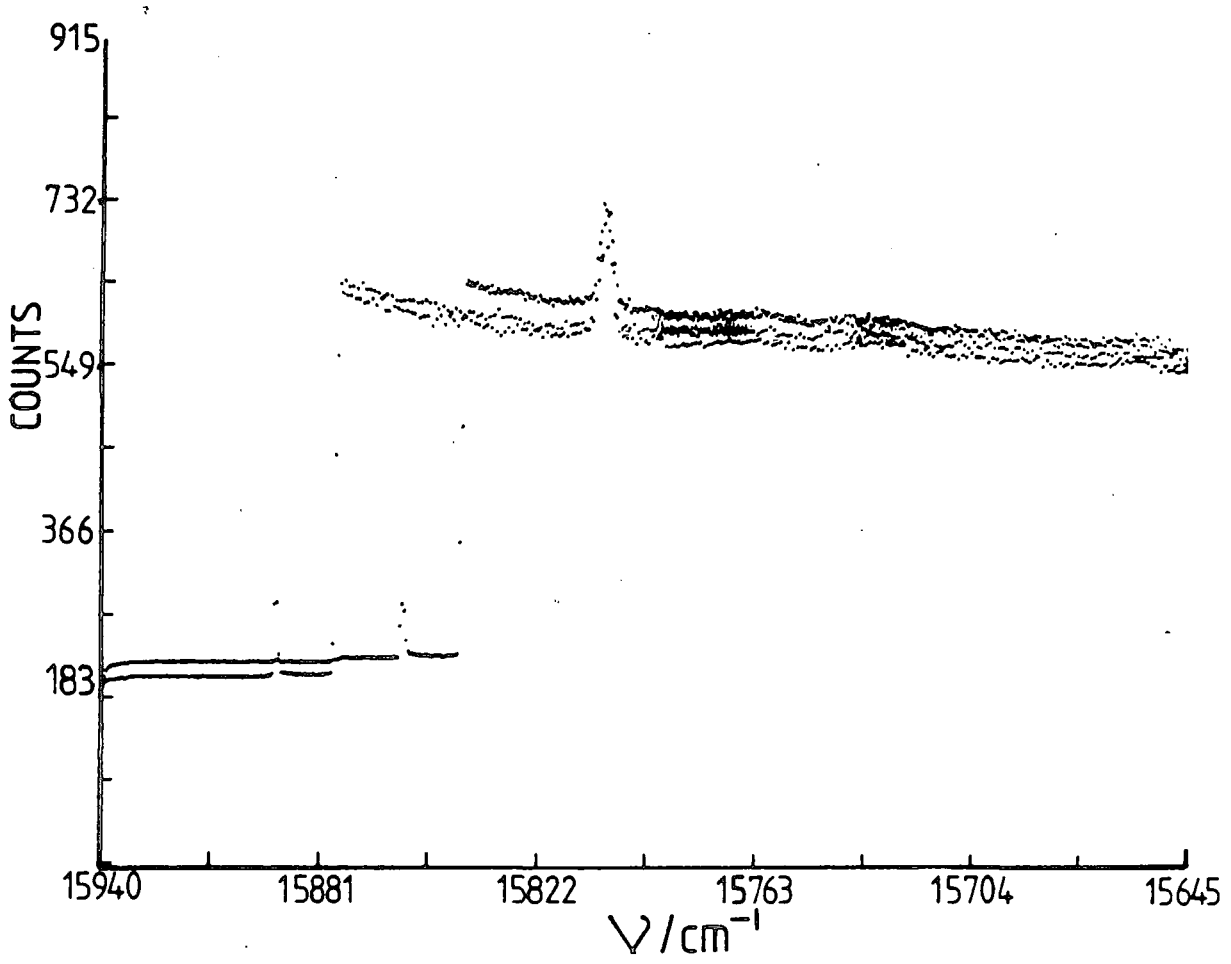

FIGURE 7.15 Effect of increasing gate repetition rate upon the observed spectrum of a cw HeNe emission (632.8nm). Detector was not cooled for these experiments. Repetition rate was 40kHz - note loss of data over left hand region of spectrum.

7.7.2.2 Elimination of the ringing effect

It is clear from the data in Table 7.3 that ringing has a larger effect upon the R/F ratio than upon the R/N ratio, and the effect upon the R/F is only pronounced in the region of t=1 ns (Table 7.3). When the gate is positioned at t=2.5 ns, the ringing decreases the E[R/N] value by a factor of 0.8 and E[R/F] by a factor of 0.5. So the effect is not large. Elimination of the ringing is only important if it is desired to operate the detector in the t=1 ns region, where E[R/F] and E[R/N] are decreased by factors of *ca.* 0.15 and 0.4 compared to a nonringing detector. Circumstances under which it might be desirable to operate in this region were discussed in Section 7.6.3. When the fluorescence lifetime is short compared to the ringing period (*e.g.* τ_f<3 ns), the reopening of the gate does not degrade the fluorescence rejection efficiency at all.

Although the ringing does not appear to seriously degrade the performance of the present system, it is shown in the next section that it has a much more detrimental effect as the detector gate shape approaches an idealised "top-hat" function, *i.e.* with instantaneous rise and fall times. It is therefore important that the ringing is suppressed, but at the present time, the manufacturer has been unable to provide any advice as to how this may be achieved.

7.7.2.3 Effect of gate shape

The shape of the IRF is an important factor in determining the fluorescence rejection efficiency. For our work, the ideal shape would have a trailing edge of infinitessimal falltime and would not exhibit ringing, thus allowing the

gate to be moved to very early positions (approaching t=0) without diminishing the detected Raman intensity (Figure 7.16). Although the IRF width may be many nanoseconds, the effective gate width is simply the overlap between the IRF and the Raman/fluoresence signal, which is decreased as the gate is moved to t=0. Under these circumstances, the ideal detector (Chapter Four, Figure 4.2) is obtained, where the gate may be monotonically narrowed to t=0, and the behaviour depicted in Figure 4.2 would hold.

The occurrence of detector ringing would seriously degrade the performance of this ideal detector, since the gate would reopen at t=15.5 ns, and so the shape of the entire IRF would then be important. This is illustrated quantitatively in Figure 7.17 for three IRFs, with trailing-edge fall-times of 0.5, 1.5 and 2.75 ns. Ringing clearly has a greater effect upon the results for the gate with the sharper cut-off and narrower width, and so elimination of ringing would be an important consideration if the shape of the IRF could be improved.

It is clear from Figure 7.17 that even if the detector gate falltime is reduced to *ca.* 0.5 ns, and the ringing effect eliminated, an E[R/N] ratio of only *ca.* 0.3 is obtained compared to ungated detection and 100 mW excitation (τ_f = 10 ns). If the maximum repetition rate were increased by a factor of 10, the E[R/N] value is only increased to *ca.* 1.0, *i.e.* virtually no improvement in the R/N would be obtained. Making the suggested modifications to the laser system would increase the R/N improvement to *ca.* 7.4 at 4 kHz pulse rate, but it is doubtful whether the required pulse energies could

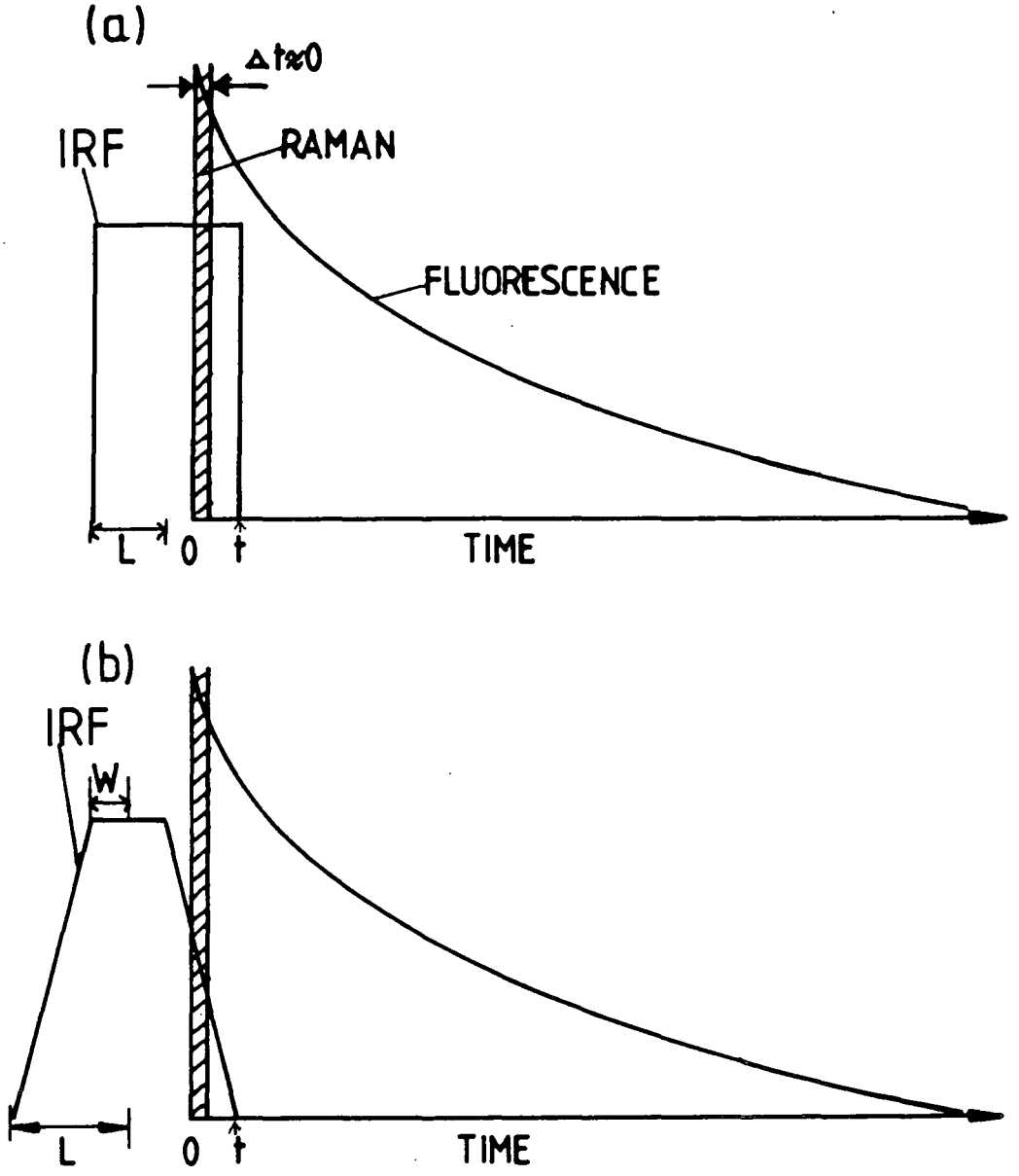

FIGURE 7.16 Effect of IRF (gate) shape for DAD. Note, an impulse Raman input ($\Delta t \simeq 0$) is assumed.

(a) "Top Hat" gate response - effective gate width = t (time at which detector "switches off". Actual width (2L) is irrelevant. The position t may be reduced without decreasing detected Raman signal, provided that $t > 0$ (ideal detector).

(b) Actual observed response - reduction of t below (L-W) causes a decrease in the detected Raman signal, and so limits the practical R/N improvement which may be obtained.

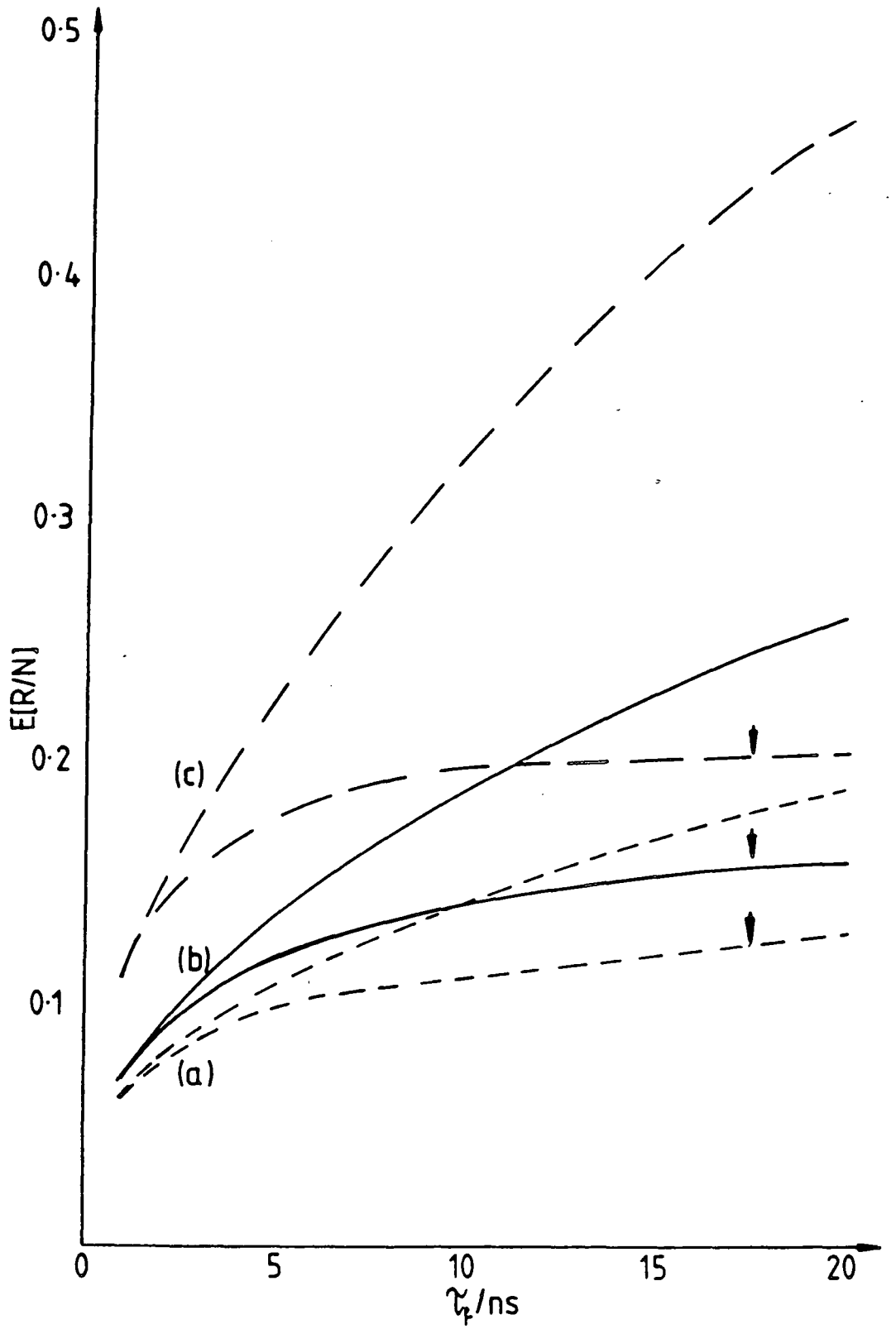

FIGURE 7.17 Effect of gate shape and ringing upon signal/noise enhancement. $T_g/t_u=1$, $P_m/P_{cw}=2\times10^{-3}$.

(a) w = 1.75, L = 4.5 (2.75 ns falltime for trailing edge).

(b) w = 1.75, L = 3.25 (1.5 ns falltime).

(c) w = 1.75 ns, L = 2.25 ns (0.5 ns falltime).

Arrow = indicates ringing is included in calculation.

be delivered at 40 kHz to give a further improvement of $\sqrt{10}$.

In order to improve the switching response of the gate, it would be necessary to decrease the fall time of the -200 V pulse supplied to the MCP. Benzel and Pocha[15] have described a pulse generator which can generate kV pulses with rise-times of 300 ps, at rates of up to 5kHz, but unfortunately the fall times of the pulses are several ns. Work is being carried out by the same authors in order to shorten the trailing edge, but as yet no results have been published. Also, even if δ function voltage pulses were supplied to the MCP, the capacitance of the system would result in a broadening of the observed IRF. At this stage it is not possible to state the lowest IRF width which might be achieved.

It is apparent from the above calculations that merely modifying the DAD response function, and increasing the maximum gateable repetition rate, will not yield a useful system for TRFR, simply because of the very low output power of the laser. A substantial improvement would only be obtained if the repetition rate could be increased to the order of MHz, and this is unlikely to be achieved owing to the difficulty in gating the MCP and in generating high voltage pulses at this rate. Therefore, both the laser system and the DAD response must be modified.

7.8 Conclusions

In this chapter we have evaluated the feasibility of employing a gated DAD and cavity-dumped, synchronously-pumped dye laser for TRFR studies. The most important point to arise is that the pulsed laser and gated DAD, even in the present

configuration, actually allows efficient fluorescence rejection, compared to ungated detection and a cw laser operating at the same average power. The timing resolution of the system is sufficient to efficiently discriminate against the fluorescence. However, the low gateable repetition rate of the DAD means that the pulsed laser system is constrained to operate at very low average powers, (*ca.* 0.2 mW), and so the signal/noise of the gated spectra is degraded compared to ungated detection and high power excitation. The fluorescence photons are efficiently rejected, but the R/N is reduced to a very poor level by the low laser power.

With this fact in mind, it is apparent that the most sensible way to proceed is to actually modify the laser system rather than the detector. In order to obtain useful results, the power of the individual laser pulses needs to be increased by a factor of *ca.* 1000. This could be achieved by either amplifying the cavity dumped pulses from the present system, or by employing a Q-switched mode-locked laser. If this were achieved, the system would yield R/N improvements of *ca.* 2.6 (compared to ungated detection, with 100 mW cw excitation, of a fluorophore with τ_f = *ca.* 10 ns). Making the modifications to the detector IRF suggested in the previous section should raise this figure to *ca.* 7.4 (4kHz repetition rate). Until these modifications are made, the gated DAD is not a suitable detector for TRFR.

It is of interest to compare the performance of the gated DAD with that of the indirectly gated PMT, since many interesting parallels may be drawn between the two methods. This comparison is given in Chapter Eight, where the theoretical and

experimental performance of the time-correlated photon counting method are analysed.

REFERENCES - CHAPTER SEVEN

1. R.N. Bracewell, "The Fourier transform and its applications", McGraw-Hill electrical and electronic engineering series, McGraw-Hill, New York (1978).

2. J.G. Skinner and W.G. Nilsen, J.Opt.Soc.Am., 58(1),113 (1968).

3. R.K. Chang, Top.Appl.Phys., 50, 207 (1982).

4. M. Bridoux, A. Deffontaine, M. Delhaye, B. Rose and E. da Silva, J.Raman Spectrosc., 11(6), 515, 1981.

5. A. Grinvald and I.Z. Steinberg, Analyt.Biochem., 59, 583 (1974).

6. S. Burgess and I.W. Shepherd, J.Phys.E:Sci.Instrum., 10, 617 (1977).

7. J.M. Harris, R.W. Chrisman, F.E. Lytle, and R.S. Tobias, Anal.Chem., 48(13), 1937 (1976).

8. T. Hirschfeld and B. Chase, Appl. Spectrosc. 40(2), 133(1986)

9. "Picosecond Phenomena", C.V. Shank, E.P. Ippen and S.L. Shapiro, (Eds.), Springer Series in Chemical Physics, 4, Springer-Verlag, Berlin, Heidelberg, New York (1978).

10. V.N. Smiley, Adv.Electron.Electron.Phys. 56, 1, (1981).

11. O. Svelto, "Principles of Lasers", Plenum Press, New York, London (1982).

12. "Chemical Applications of Nonlinear Raman Spectroscopy", A.B. Harvey (Ed.), Academic Press, New York, London, Toronto, Sydney, San Francisco (1981).

13. Reference 9, pages 103-107.

14. I. Matsushima, T. Kasai and M. Yono, Rev.Sci.Instrum., 52(12), 1860 (1981).

15. D.M. Benzel and M.D. Pocha, Rev.Sci.Instrum., 56(7), 1456 (1985).

CHAPTER EIGHT

FLUORESCENCE REJECTION BY TIME-CORRELATED PHOTON COUNTING USING A PHOTOMULTIPLIER TUBE AND FAST TIMING ELECTRONICS

8.1 Introduction

In this chapter, we consider the use of the indirectly gated, PMT-based detection system which was discussed in Chapter Six. The use of this apparatus in obtaining estimates of fluorescence lifetimes and in improving the R/N ratio of spectra is demonstrated, and it is shown that a simple theoretical model gives a reasonable representation of the TRFR performance. Improvements in R/N of *ca.* 2.8 (τ_f=11.8 ns) and 2.0 (τ_f=3.9 ns) were obtained for solutions of rubrene and R6G in benzene. When the fluoresence background exhibited non-Poisson noise statistics (rubrene in degassed benzene) the R/N improvement was much larger (7.2).

The response of the system is derived as a function of τ_f, the gate-width and position, the width of the IRF and the laser power. Modifications are suggested which should give a seven-fold improvement in the R/N enhancements which were observed with the present apparatus, and so which should result in a rejection system which is useful for short lived fluorescors (τ_f<5 ns). The importance of comparing the gated R/N ratios with those expected for high-power cw laser excitation is stressed, since this is the condition under which most Raman spectra are normally obtained. Finally, the performance of the DAD and PMT based systems (both present and optimised configurations) are compared and contrasted.

8.2 Measurement of fluorescence lifetimes and the efficiency of fluorescence rejection

The construction and operation of the basic time-correlated photon counting (TCPC) apparatus which was used in this work was described in Chapter Six. Here the analysis of results

which were obtained by this technique are discussed. The results which are presented below were obtained with the system configuration illustrated in Figure 6.10; hardware modifications which were later introduced to improve the performance are discussed after the theoretical analysis has been given (Section 8.5).

8.2.1 Measurement of Raman and fluorescence photon distributions

It was explained in Chapter Six how the TCPC apparatus can be used to measure photon probability-time distributions. If the Raman scatter excited by an ultrashort optical pulse is temporally analysed, one obtains the IRF of the detection system, while the observed fluoresence photon distribution is given by the convolution of the IRF with the true fluorescence function. In Figure 8.1 an observed Raman photon-time distribution, obtained from the 992 cm^{-1} vibrational mode of benzene (Analar), is compared with the fluorescence distribution from a $4x10^{-4}$ M solution of rubrene (Aldrich Chemical Co.) in degassed benzene. The benzene was degassed by 3 freeze-pump-thaw cycles.

The FWHM of the observed IRF is *ca.* 1.75 ns (average taken from three measurements), which is at least forty times the duration of the laser pulses which excite the scatter. Since our PMT should have a transit-timespread of well below 1 ns[1], we concluded that there was appreciable timing jitter in the rest of the system (*i.e.* the timing electronics, generation of the CDSO pulse, (Chapter Six), *etc.*). This jitter was later successfully reduced to yield an IRF of *ca.* 775 ps width; the methods by which this was achieved are described in Section 8.5.

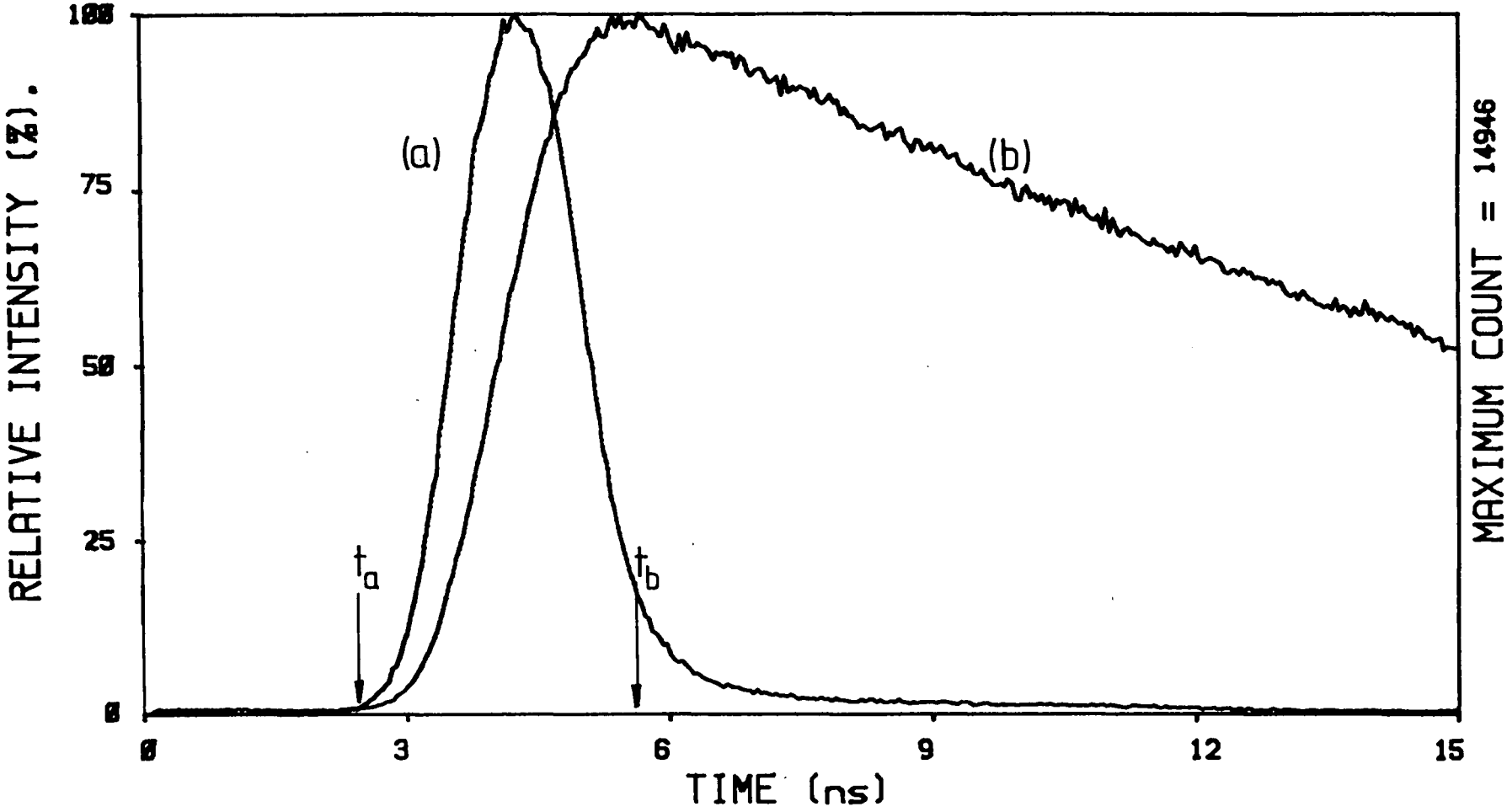

FIGURE 8.1 Comparison of Raman and fluorescence photon distributions.

(a) Raman scatter (992 cm^{-1} mode of benzene) - represents IRF of system, (b) fluorescence emission (τ_f=662 nm) of dissolved rubrene. In a gated experiment, only photons between limits t_a and t_b are accepted ($t_g=t_b-t_a$) where t_a and t_b are variable. The laser limit is normally fixed in the position shown, *i.e.* at the start of the Raman distribution.

A further important feature of the IRF is its pronounced trailing edge, which contains a significant (*ca.* 10%) proportion of the total probability distribution.

Curve (b) shows that the majority of the fluorescence photons are observed after the termination of the Raman events, as would be expected. An unusual feature of the distribution is the presence of a non-zero background prior to the fluorescence pulse, at a level of *ca.* 0.5% of the peak probability. This magnitude is too great to be accounted for by dark counts or stray room light, and is in fact due to the fluorescence stimulated by the leakage pulses occurring before the main laser pulse (Chapter Five). This "leakage fluorescence" overlaps the main fluorescence pulse, and so will fall within the time gate set to capture the Raman photons, raising the detected fluorescence level and so decreasing the R/F and R/N ratios. The "leakage fluorescence" intensity is determined by the amplitude of the leakage pulses, and the lifetime of the fluorphore.

8.2.2 Observed fluorescence rejection efficiency

Fluorescence rejection measurements were made in the manner described in Chapter Six, over a range of gate-widths and positions, (t_a, t_b (Figure 8.1)), for two fluorescing samples, (a) $1x10^{-3}$ M solution of rubrene in benzene (not degassed) and (b) $4x10^{-4}$ M solution of rubrene in degassed benzene. While different solvent treatments were performed to vary the fluorescence lifetime of the solute, this actually led to further complications which are discussed in Section 8.3.4.

Figure 8.2 (a) shows the spectrum obtained for the $1x10^{-3}$ M solution, with a time-gate set to accept photons

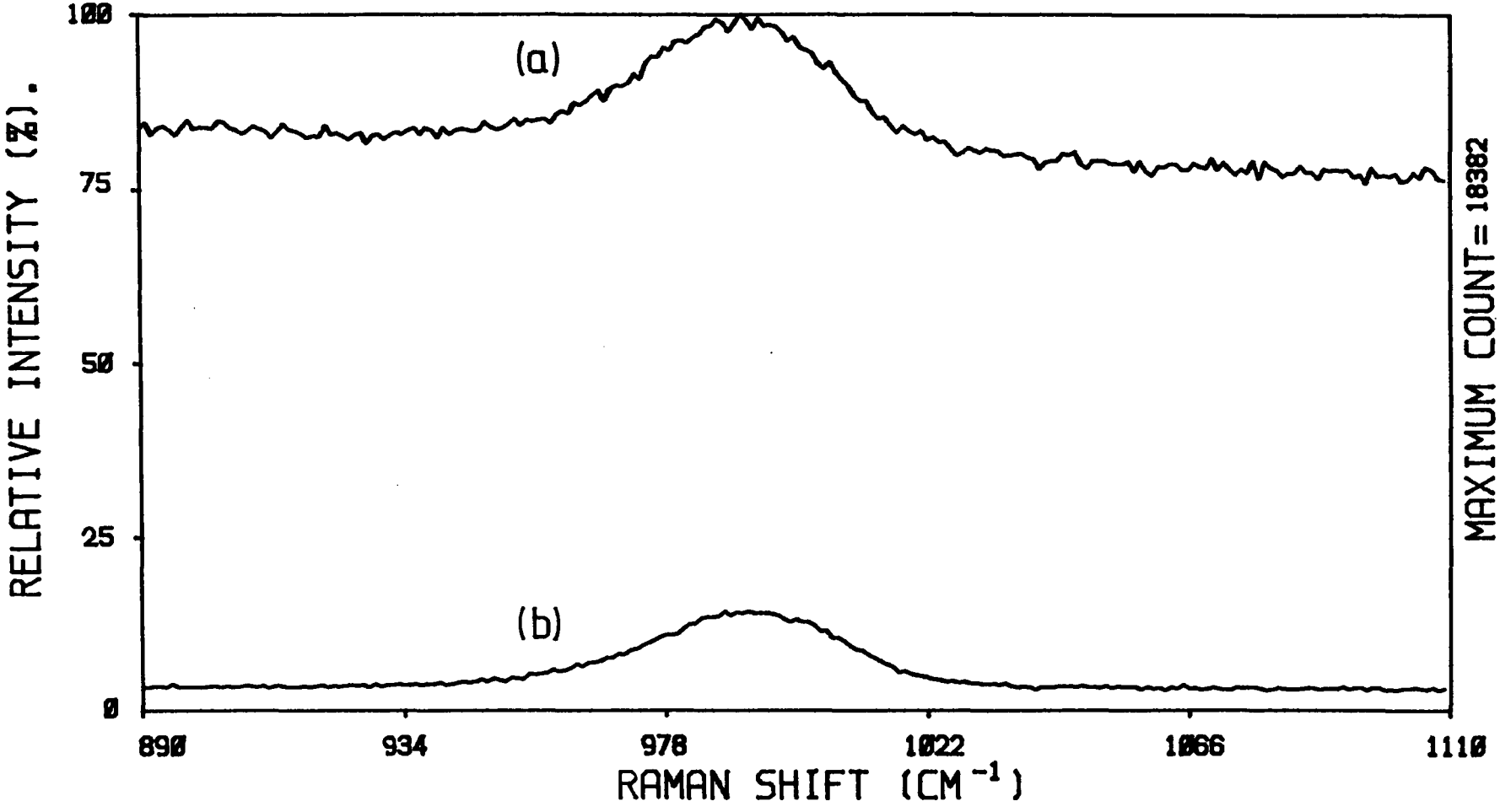

FIGURE 8.2 Effect of gating detector. 4MHz laser pulse rate (28mW, λ=586nm, $I_m/I_T \simeq ca.100$), (a) ungated spectrum, (b) gated spectrum (2.20 ns gate), Laser conditions held constant for both spectra. Sample was 10^{-3} M rubrene in benzene (τ_f = 11.8 ns).

occurring during the first 2.20 ns of the Raman photon distribution, (t_b-t_a = 2.20, t_a fixed at position shown in Figure 8.1) This is compared with a spectrum (b) obtained with ungated detection (*i.e.* simply monitoring the PMT output pulse rate). The laser conditions were identical for each spectrum (4 MHz pulse rate, 28 mW average power, λ = 586 nm, and I_m/I_L = ≈100). The low ratio of main/leakage intensity (I_m/I_L) arose because at the time at which these experiments were performed, the laser output had not been optimised and, more importantly, the leakage suppression module (Chapter Six) was not installed. Figure 8.3 shows the results of a similar experiment on the 4×10^{-4} M solution, with slightly different conditions (2.28 ns gate width), λ = 587 nm, 22 mW average power, I_m/I_L = ≈170). It is immediately apparent that the two solutions behaved rather differently, in that the ungated spectrum of the degassed sample is much noisier than that of the untreated solution, with large and erratic jumps in the background level. An explanation of this behaviour is given in Section 8.3.4.

It was found with the 10^{-3} M solution that on gating the detection system, R/F was enhanced by 14.6±0.9, but R/N was only improved by 2.8±0.2, relative to ungated detection. The corresponding improvements for the degassed solution were *ca.* 14.1±1.3 and 7.2±0.6. In each case the noise levels (N) required for the R/N ratio determination) were determined by performing a linear regression over a region of the background adjacent to the Raman band and calculating the rms value of the residual deviations. Again, only the noise on the fluorescence background ($N=\sqrt{F}$) was considered.

Clearly, gating the detector substantially improved the R/F and R/N ratios of the spectra of both solutions, with a

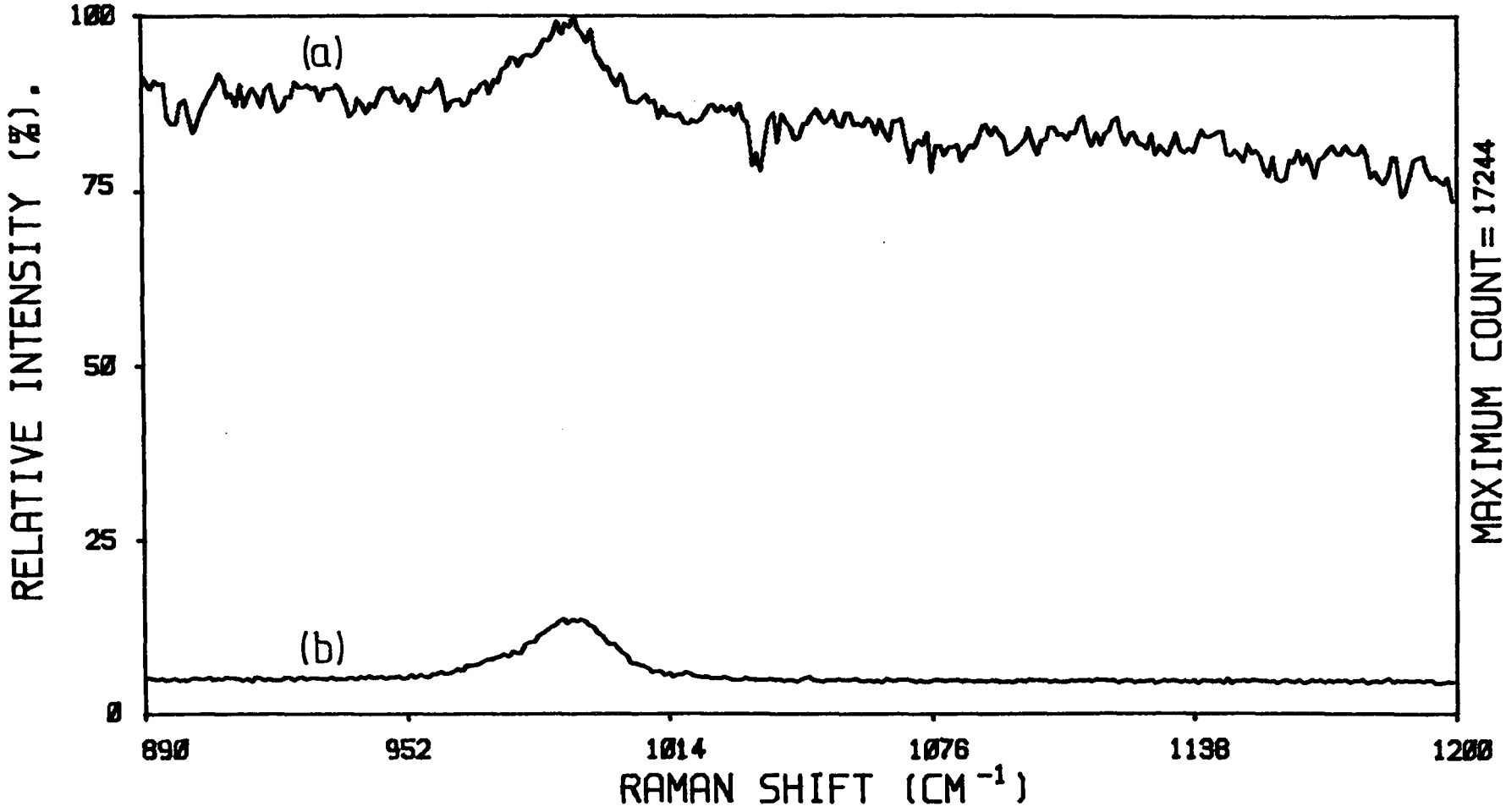

FIGURE 8.3 Repeat of experiment in Figure 8.2 with 4×10^{-4}M rubrene in degassed benzene (τ_f=14.8 ns), (a) ungated spectrum, (b) gated spectrum (2.28 ns gate). 22mW laser power (λ=587nm, I_m/I_T=170). Note noisy, erratic background of ungated spectrum relative to Figure 8.2a.

particularly dramatic improvement in the R/N ratio of the degassed solution. The erratic features which occurred in the ungated spectrum of the degassed solution were completely removed by the gating process.

Enhancements in R/F and R/N were obtained with a variety of gate widths and positions for each solution, and this data allowed us to test the validity of the theoretical model which is presented below. The model was then used to compute the optimum experimental configuration for any fluorescing species, knowing only τ_f and the width of the IRF, and to suggest suitable hardware modifications to improve the performance.

8.3 Theoretical analysis of the system performance

8.3.1 General

Although fluorescence rejection *via* TCPC has been a widely studied technique, and has been theoretically analysed by previous authors,[2-7] it is somewhat surprising to find that equations which fully describe the R/F and R/N improvements have rarely been published. Instead, only the results of calculations have been referred to in the reported work, which is somewhat unsatisfactory for the reader who wishes to check the analysis and the assumptions involved.

The major exception to this statement lies in the work of Yaney,[2] where full equations describing the performance of his system were given. Unfortunately, owing to the duration (100 ns), power (3 kW), and focussing (10μ radius) of the laser pulses produced by his Q-switched Nd:YAG laser, Yaney was forced to consider the population dynamics (Chapter Three) of the fluorescing system (Mn doped ZnSe). This necessitated

several approximations about the magnitude of various rate constants, and led to a set of equations which are not applicable to the performance of a picosecond laser/detection system. For this reason, the equations describing the performance of our system are derived below. Comparison of the practical and theoretical evaluation of our system with the work of other authors is made in Section 8.4, where it will become apparent that fundamental concepts appear to have sometimes been misunderstood and experimental configurations therefore not optimised.

In order to calculate the R/F and R/N improvements expected with our system, it is necessary to know the fluorescence decay constant k ($1/\tau_f$), and the functional form of the IRF (g(t)). In order to simplify the analysis, the actual IRF was approximated as an isosceles triangle, of FWHM (L) equal to that of the observed function (Figure 8.4). This approach allows simple analytic expressions for the change in R/F and R/N on gating to be obtained. A full numerical solution, based upon the exact observed form of the IRF, would yield more accurate results, but would probably not be as physically enlightening as to the processes occurring, and so was rejected for this reason. Watanabe *et al*[7] published the results of a numerical analysis of a similar system, with an IRF which was approximated as a Gaussian function. The results of their calculations were found to be rather similar to those obtained in this simplified model (Section 8.6.4), and they stated that the system performance was insensitive to the exact form of the IRF. For this reason no attempt was made to increase the complexity of our model, particularly as it will be seen that the calculated

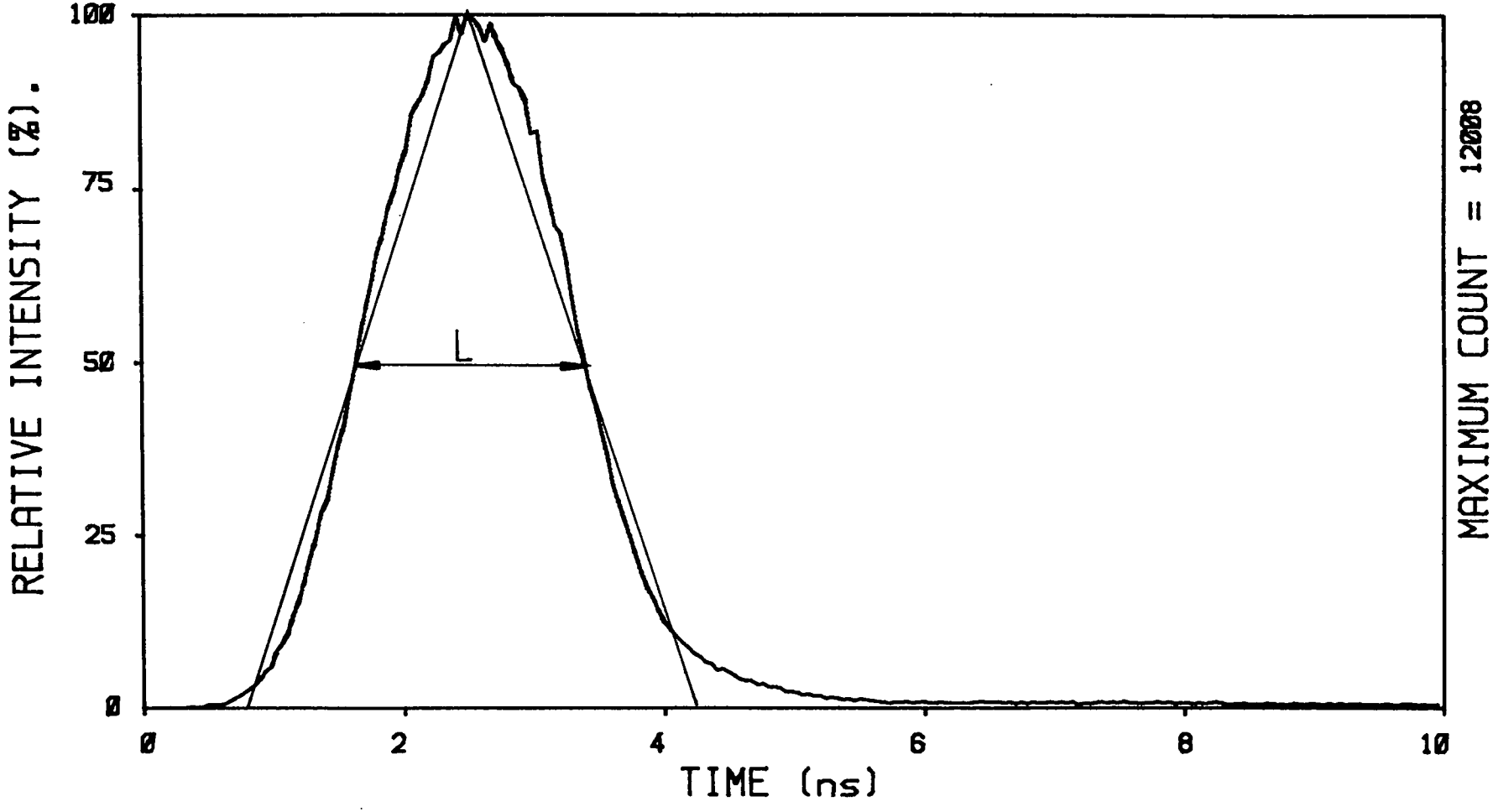

FIGURE 8.4 Representation of IRF as an isosceles triangle of width L. This is a poor model compared to that of the gated DAD as a trapezium (Chapter Six).

behaviour is in reasonable agreement with the observed performance.

8.3.2 Calculation of fluorescence lifetimes from observed data

The observed fluorescence response is given by the convolution of g(t) with the true fluorescence decay (E(t)):

$$I(t) = \int_{-\infty}^{\infty} g(t-t')E(t')dt' \qquad (8.1)$$

where g(t) is approximated to an isoscles triangle of half width L. Clearly, a triangular IRF is actually nothing more than a special case of the trapezoidal IRF discussed in Chapter Seven, but with the apex width W set equal to zero. Therefore, it is not necessary to evaluate equation (8.1), since the required expressions may be obtained merely by setting W=0 in equations (7.10)-(7.13). When this is done, we obtain the analytic form of I(t) over the three relevant time domains.

$0<t<L$

$$I_1(t) = C_1[e^{-kt} + kt - 1] \qquad (8.2)$$

$L<t<2L$

$$I_2(t) = C_1\{e^{-k(t-L)}.[e^{-kL}-2] + k(2L-t) + 1\} \qquad (8.3)$$

$t>2L$

$$I_3(t) = C_1\{e^{-1(t-L)}.[e^{kL}-e^{-kL}-2]\} \qquad (8.4)$$

where C_1 is a constant. It is important to realise that I(t) here describes the pulse-probability distribution of the PMT output, whereas in the analysis of the gated DAD (Chapter Seven) it defined the actual intensity detected by a gate positioned at time t. Although the mathematical analysis is

identical in each case, the actual physical processes described are totally different.

Equation (8.4) may be recast in the form:

$$I_3(t) = C_2 e^{-kt} \qquad (8.5)$$

Therefore, we expect a simple exponential decay of lifetime $\tau_f(1/k)$, over the region t>2L. A plot of $\ln(I_3(t))$ *versus* t should yield a straight line of gradient -k. Figures 8.5 and 8.6 illustrate the results of such an analysis for the fluorescence emission from the 10^{-3} and 4×10^{-4} M rubrene solutions. Clearly, first order kinetics do appear to be obeyed when t>2L. The plots yield fluorescence lifetimes of *ca.* 11.8±0.1 ns (10^{-3} M solution) and 14.8±0.1 ns (degassed 4×10^{-4} M solution) respectively. The value of 11.8 ns is in reasonable agreement with the 10.5 ns lifetime determined by the gated DAD, which was subject to substantial error (*ca.*±2ns) owing to the limited number of data points which were recorded.

It must be emphasised that the object of the work is not the accurate analysis of decay kinetics, and it is shown (Section 8.3.7) that the expected enhancements in R/N are actually rather insensitive to the exact lifetime of the fluorescing species, particularly when τ_f>5 ns. The accuracy of our lifetime determination is sufficient to test the model developed here; if accurate lifetimes were required it would be necessary to deconvolve the observed decay, using the exact form of g(t). Such a sophisticated treatment is not necessary for our present work.

8.3.3 Calculated improvements in R/F and R/N

The analysis given here is based on that given by Van Duyne *et al*[3] and Burgess and Shepherd,[4] but the treatment

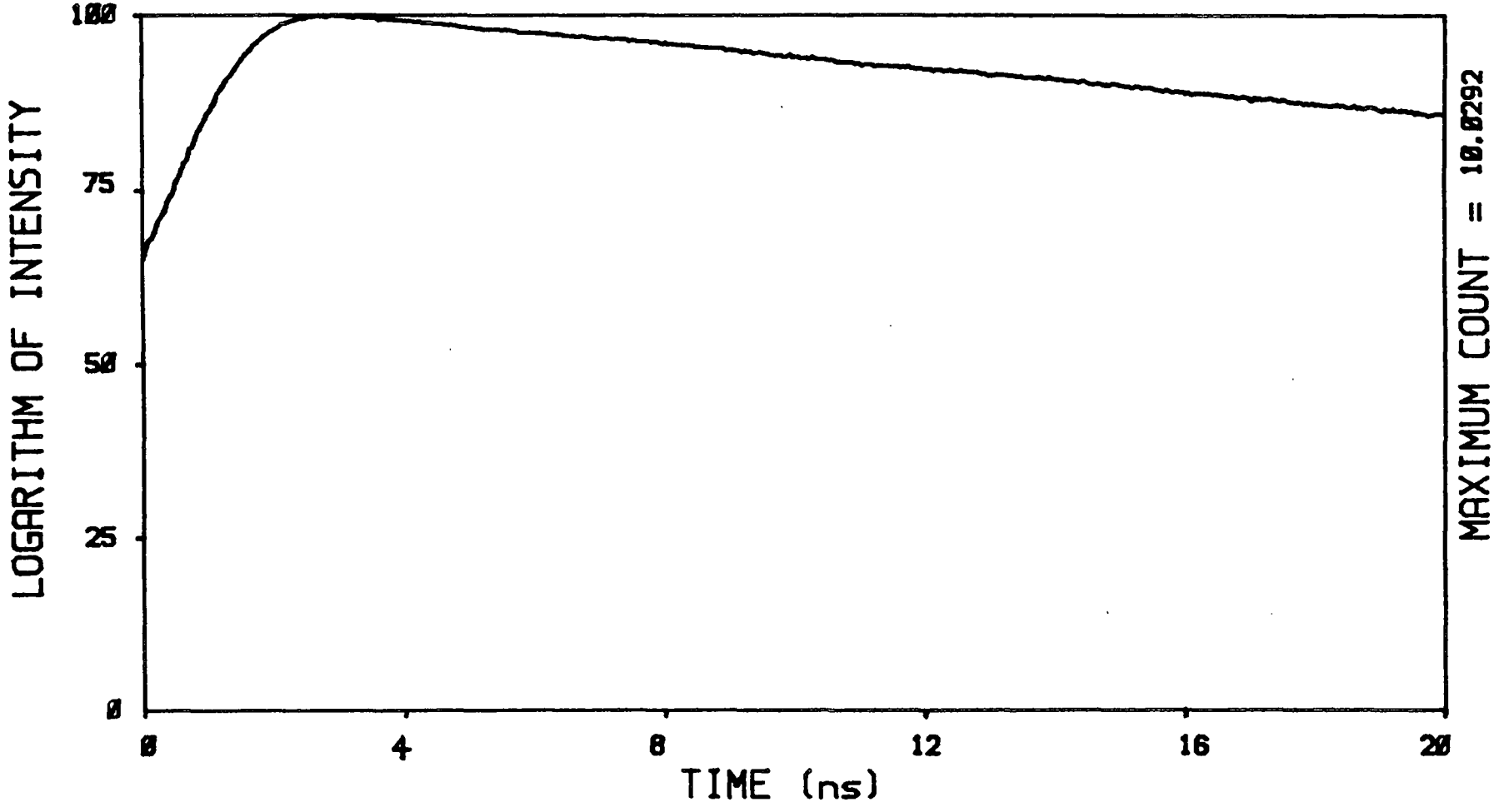

FIGURE 8.5 Fluorescence lifetime analysis of 10^{-3} M rubrene in benzene. Gradient of linear region of plot = $-1/\tau_f$. (τ_f = 11.8 ± 0.1 ns).

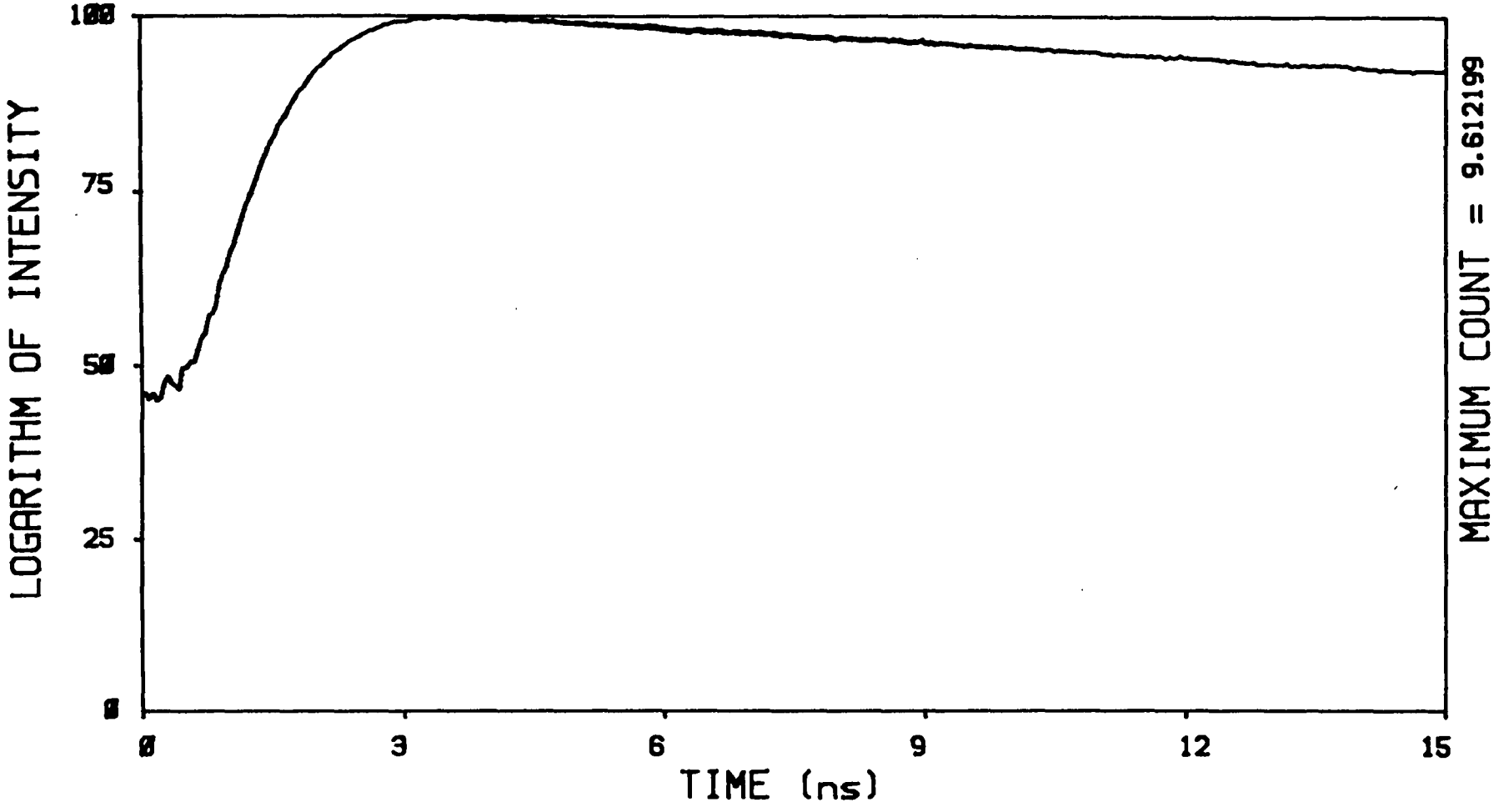

FIGURE 8.6 Lifetime analysis of 4 x 10^{-4} M rubrene solution (degassed benzene). τ_f = 14.8 ns ± 0.1 ns.

is made somewhat simpler by the narrow width of our laser pulses (compared to τ_f), which allows us to neglect convolution of the laser pulse shape with the true fluorescence profile. The large separation of the main pulses (250 ns at 4MHz) prevents the severe overlapping of adjacent fluorescent decays which can occur when using a mode-locked laser to excite the sample,[3] and so further simplifies our treatment. Neither Van Duyne *et al*[3] nor Burgess and Shepherd[4] reported the actual equations which they derived on the assumption of a triangular IRF, and so these results are derived below.

The analysis is based on our usual assumptions of the noise being dominated by (Poisson) fluctuations in the fluorescence background. We also assume that the laser intensity (pulsed or cw) is not sufficient to saturate the fluorescence response (Chapter Three).

We wish to calculate the relative values of R/F and R/N in gated and ungated detection modes, under identical laser conditions. In ungated mode, any one Raman or fluorescence photon over the entire distribution may give rise to an acceptable PMT pulse. The R/F value is then given by the ratio of the total number of Raman to fluorescence photons, and this is proportional to the ratio of the total areas below the curves g(t) and I(t).

$$(R/F)_u = C_3 \int_o^\infty g(t)\,dt \Big/ \int_o^\infty I(t)\,dt \qquad (8.6)$$

In gated mode, only a photon occurring between the gate limits t_a and t_b may trigger an acceptable pulse (Figure 8.1) - R/F is then given by equation (8.7).

$$(R/F)_g = C_3 \int_{t_a}^{t_b} g(t)\,dt \Big/ \int_{t_a}^{t_b} I(t)\,dt \qquad (8.7)$$

The subscripts g and u refer to gated and ungated detection modes. The enhancement in R/F (E[R/F]) obtained on gating the detector is given by equation (8.8).

$$E[R/F] = (R/F)_g/(R/F)_u = \{\int_{t_a}^{t_b} g(t)dt / \int_0^{\infty} g(t)dt\} \times \{\int_0^{\infty} I(t)dt / \int_{t_a}^{t_b} I(t)dt\} \quad (8.8)$$

Equation (8.8) may be simplified as:

$$E[R/F] = Z(R)/Z(F) \quad (8.9)$$

where Z(R) is the fraction of the Raman probability distribution falling within the gate limits, and Z(F) is the fraction of the fluorescence distribution within the same period. This equation requires modification, since fluorescence stimulated by the leakage light will also fall within the gate limits, and so increase Z(F). This contribution may be calculated from first principles, but it is simpler to measure it from the photon distribution curve and then correct Z(F) accordingly. The quantitative effects of this correction are considered at a later stage.

The approximation of g(t) to a triangle must also be modified, since *ca.* 10% of the Raman events were observed to lie within the tail of the distribution (Figure 8.1). A gate-width of 3.5 ns would therefore only accept *ca.* 90% of the Raman photons, and so the Z(R) values should be multiplied by 0.9 in order to yield a more accurate Raman collection fraction. Thus equation (8.9) becomes:

$$E[R/F] = Z(R)_c/Z(F)_c \quad (8.10)$$

where $Z(R)_c$ = 0.9 Z(R) and $Z(F)_c$ is the fluorescence fraction corrected for the effect of leakage fluorescence. The enhancement in R/N is obtained by a similar procedure, but a further

effect of the leakage light must be considered. Since only Raman scatter from the main cavity dumped pulses can be detected in gated mode, the effective laser power on the sample is reduced by I_m/I_T, (where I_T represents the total beam intensity and I_m the intensity carried by the main pulses (Chapter Seven)), compared with ungated mode. Therefore, R/N is reduced by $[I_m/I_T]^{\frac{1}{2}}$ on going to gated mode (This reduction of intensity has no effect on the R/F value). The enhancement in R/N is then given by equation (8.11).

$$E[R/N] = [I_m/I_T]^{\frac{1}{2}} Z(R)_c [Z(F)_c]^{-\frac{1}{2}} \qquad (8.11)$$

The efficiency of fluorescence rejection may be calculated for any fluorescing system, provided that both τ_f and I_m/I_L are known. $Z(R)_c$ and $Z(F)_c$ are calculated from the analytic forms of I(t) and g(t), in contrast with the numerical methods employed by Van Duyne *et al*[3] and Watanabe *et al*[7].

8.3.4 Comparison of calculated and observed enhancements

8.3.4.1 Non-degassed solution

Equations (8.10) and (8.11) were applied to calculate the rejection efficiencies for the two rubrene solutions previously described, for a variety of gate-widths. The results for the 1×10^{-3} M solution are summarised in Table 8.1. The lower time limit for the gate (t_a) was zero (namely the instant at which the first Raman events were observed) in each case.

Clearly, for gate-widths of 2.20 and 1.69 ns, there is good agreement between the calculated and observed R/F enhancements. The agreement for lower gate-widths is less satisfactory. This is a result of the repres-

TABLE 8.1 Fluorescence rejection efficiency for 1×10^{-3} M solution of rubrene in benzene (τ_f=11.8 ns, I_m/I_L=100).

Gate Position/ns	$Z(R)_c$	E[R/F]		E[R/N]	
		Calculated	Observed	Calculated	Observed
0-2.20	0.65	13.2	14.6±0.9	2.7	2.8 ± 0.2
0-1.69	0.42	17.5	17.3±1.3	2.5	2.7 ± 0.3
0-1.10	0.19	23.4	18.9±1.3	1.9	2.0 ± 0.2
0-0.69	0.07	28.1	14.6±2.6	1.3	1.0 ± 0.2

---

entation of g(t) as a triangle, which is a poor model over the initial *ca.* 0.5 ns of the distribution, where a faster rise in Raman intensity (and hence larger Z(R)) is predicted than is observed (Figure 8.4). Also the magnitude of the detected fluorescence is very low for short gates, and so small errors in calculating the fluorescence level lead to large errors in $Z(F)_c$. In general, it is noted that the accuracy of calculated enhancements for the TCPC system are poorer than those for the gated DAD, and this is a direct result of the much poorer representation of the IRF as a triangle compared to that of the DAD gate as a trapezium (Chapter Seven).

The increase in the value of R/F is of no value unless the R/N ratio is also improved. We do in fact observe much closer agreement of calculated and observed E[R/N] values. The most important feature is the decrease in E[R/N] as the gate is narrowed, which occurs because the fraction of Raman photons accepted (Z(R)) is a function of gate width, in contrast to the ideal situation discussed in Chapter Four. The most effective gate-width was observed to be 2.20 ns, with an increase in R/N of 2.8, although the statistics are not reliable

enough to distinguish this from the enhancement obtained with a 1.69 ns gate.

8.3.4.2 Degassed solution - Non-Poisson background fluctuations

Table 8.2 shows the results of similar calculations for the degassed 4×10^{-4} M solution (τ_f *ca.* 14.8 ns). A wider range of gate-widths was included in the calculation, including a gate set to capture the FWHM of the Raman distribution rather than the leading edge. This position would be intuitively expected to give poor results, but was included for comparison with previously reported work (Van Duyne *et al*,[3] and Burgess and Shepherd[4]).

TABLE 8.2 Fluorescence rejection efficiency for 4×10^{-4} M solution of rubrene in benzene (τ_f=14.8 ns, I_m/I_L=170)

Gate Position/ns	$Z(R)_c$	E[R/F]		E[R/N]	
		Calculated	Observed	Calculated	Observed
0-2.67	0.80	12.9	11.4±1.0	3.0	5.3±0.4
0-2.28	0.68	16.4	14.1±1.3	3.2	7.2±0.6
0-1.94	0.54	20.5	19.0±1.7	3.2	6.8±0.6
0.1.69	0.42	23.9	22.7±2.3	3.0	6.4±0.7
0.88-2.64	0.68	11.8	9.3±0.8	2.7	4.2±0.4
0-1.46	0.31	27.0	24.0±2.0	2.8	5.8±0.5
0-0.97	0.14	38.5	32.7±3.4	2.2	4.1±0.4
0-0.49	0.04	61.2	23.2±3.1	1.4	1.8±0.2

Tables 8.3 and 8.4 illustrate the effect of inclusion of the correction for leakage induced fluorescence upon the calculated enhancements in R/F and R/N, and show the higher sensitivity of the R/F value than R/N to this parameter.

The sensitivity is affected by the gate-width, fluorescence lifetime and the relative intensity of the leakage pulses, and for narrow gate-widths the effects may be large owing to the low amount of main-pulse fluorescence falling within the gate. In this case a small error in leakage-light correction can cause a large error in E[R/F] calculations.

TABLE 8.3 Effect of leakage induced fluorescence ($1x10^{-3}$ M rubrene in benzene, τ_f=11.8 ns I_M/I_L=100)

Gate Position	E[R/F]		E[R/N]	
	Calculated	Leakage Corrected	Calculated	Leakage Corrected
O-2.20	14.2	13.2	2.8	2.7
O-1.69	19.5	17.5	2.6	2.5
O-1.10	29.6	23.4	2.1	1.9
O-0.69	48.2	28.1	1.6	1.3

TABLE 8.4 Effect of leakage induced fluorescence $4x10^{-4}$M rubrene in benzene, τ_f=14.8 ns I_M/I_L=167)

Gate Position	E[R/F]		E[R/N]	
	Calculated	Leakage Corrected	Calculated	Leakage Corrected
O-2.67	13.0	12.9	3.1	3.0
O-2.28	16.7	16.4	3.2	3.2
O-1.94	20.9	20.5	3.2	3.2
O-1.69	24.5	23.0	3.1	3.0
O-1.46	28.1	27.0	2.8	2.8
O-0.97	41.9	38.5	2.3	2.2
O-0.49	82.2	61.2	1.6	1.4

Returning to Table 8.2, the same pattern of R/F enhancements was calculated (and observed) as for the $1x10^{-3}$ M solution, namely a steady improvement as the gate is narrowed, and good agreement except in the $t_g<1$ ns region. When the acceptance window was set at the FWHM of g(t), a much poorer enhancement was obtained than when an equivalent width gate was positioned to open at $t_a=0$. The same trend was found for the R/N improvements.

The calculated E[R/N] values show a maximum of *ca.*3.2 for a gate-width of 2-2.28 ns, followed by a steady decrease as the gate is narrowed. The observed enhancements follow the same general behaviour, but in this case are all much higher than the calculated values - more than double for the large gate-widths.

Examination of the ungated spectrum (Figure 8.3) reveals the source of this discrepancy - the background noise is in fact much greater than can be accounted for by fluorescence shot noise, *i.e.* the assumption of Poisson statistics is inadequate in this instance. The background consists of high frequency shot noise, together with regular, non-reproducible structure which is totally removed on gating.

This effect has been noted previously - Harris *et al* referred specifically to observation of large background fluctuations in a rubrene solution, and discussed the possibility of developing non-fluorescing species in the path of the laser beam, the concentrations of which would be modulated by solvent motion. In agreement with this, we note that in our experiments the effect was only observed in degassed solutions - *i.e.* when a major triplet quenching agent (O_2) had

been removed, which may otherwise prevent these accumulations of non-fluorescing species. Aerated solutions exhibited only shot noise, irrespective of the concentration of dye. Thus the concentration of potentially fluorescent molecules in the path of the beam may vary as solvent convection proceeds, causing random shifts in the fluorescence background. This effect, and experimental designs for its prevention, was discussed recently by Pearlstein.[8]

Since the magnitude of the observed modulation will depend upon the detected fluorescence intensity, the noise will vary with $Z(F)_c$ and so the gating procedure should reduce its amplitude. This does occur and the enhancement in R/N is substantial. The improved rejection confirms the effectiveness of the time-resolved method for studying solutions which are prone to large, non-Poisson fluctuations in fluorescence intensity.[4,5]

8.3.5 Rejection efficiency with a fluorophore of shorter lifetime (4 ns)

Table 8.5 summarises the results obtained on studying a faster decaying sample (10^{-4}M Rhodamine 6G in a benzene/ethanol 9:1 mixture, τ_f=3.9±0.1 ns). The laser performance was substantially improved for these experiments in (*i.e.*($I_m/I_r \simeq 1$). Again, good agreement between observed and calculated improvements was obtained.

TABLE 8.5 Fluorescence rejection efficiency for a 10^{-4} M solution of R6G in benzene/ethanol 9:1 mixture ($I_m/I_L=\infty$, τ_f=3.9 ns)

Gate Position	E[R/F]		E[R/N]	
	Calculated	Observed	Calculated	Observed
0-2.41	4.8	4.2±0.6	2.0	2.0±0.3
0-2.03	6.1	5.5±0.9	2.0	2.0±0.3
0-1.69	7.4	5.3±1.1	1.9	1.5±0.3

8.3.6 Suppression of phosphorescence

All of the previous experiments have related to suppression of backgrounds due to fluorescing contaminants, which limits the lifetime of the emission to the picosecond-nanosecond region. Obviously, superior improvements would be expected for samples with longer lived (μs-ms) emissions, *i.e.* phosphorescing species.

8.3.6.1 Phosphorescence from Alumina

In his work upon adsorbed species on alumina, Yaney[9] observed very efficient suppression (>36 fold) of the background at an absolute wavelength of *ca.* 614 nm. Unfortunately, no Raman lines were present in this region to enable an assessment of R/N or R/F. This level of improvement was much greater than that which would be expected for species emitting over ns timescales, since the IRF of the system was *ca.* 100 ns! This indicates that the background was due to phosphorescing rather than fluorescing species. Yaney made no suggestion as to the origin of the background, but it appeared to vary amongst different crystal forms and individual samples of alumina (*i.e.* he only observed it for a particular sample of α Al_2O_3). With all of his samples there was a component with a much shorter (ns) lifetime, indicating that at least 2 luminescent species were present.

8.3.6.2 Observed Phosphorescence rejection

Since our system has roughly 100 fold higher time resolution than that of Yaney, we would expect somewhat superior performance and so decided to examine similar samples. Initially, the Raman spectrum of an untreated sample of α alumina

(unknown origin) was obtained. Since alumina gives rise to weak Raman bands, a small quantity of benzophenone was mixed with the sample, in order to provide strong reference Raman bands at *ca.* 1597 cm^{-1}, 1650 cm^{-1} and 3060 cm^{-1}.[10] The benzophenone made up *ca.* 1/3 of the total volume of the mixture.

Figure 8.7 is the Raman spectrum of the mixture which was obtained using ungated detection and pulsed excitation (30mW, 4MHz, λ=596 nm). The position of the Raman bands of benzophenone are marked with arrows. The spectrum is dominated by an intense doublet (Raman shifts 2363 and 2392 cm^{-1}. There are also several broader features of greatly reduced intensity, marked by asterisks in the spectrum.

The benzophenone bands are swamped by the background noise (in fact the C-H bands in the 3060 cm^{-1} region are not visible at all). However, gating the detector (*ca.* 4ns gate to accept the entire Raman distribution) yielded the spectrum shown in Figure 8.8 . The doublet was reduced to *ca.* 1/58th of the original intensity, and the Raman bands became clearly visible. The broad background features were totally removed. Clearly, the doublet was not due to a Raman effect, but was a radiative emission at a fixed wavelength.

The improvement is better illustrated in Figure 8.9, where the region 2700 $cm^{-1} \rightarrow 3200$ cm^{-1} is expanded. The Raman feature at *ca.* 3060 cm^{-1} is clearly visible in the gated spectrum, but was totally swamped by noise in the ungated spectrum. The R/N improvement on gating is at least x10 in this case.

This degree of improvement strongly indicates that phosphorescing species were present in the α Al_2O_3, and were responsible for the doublet and the broad background

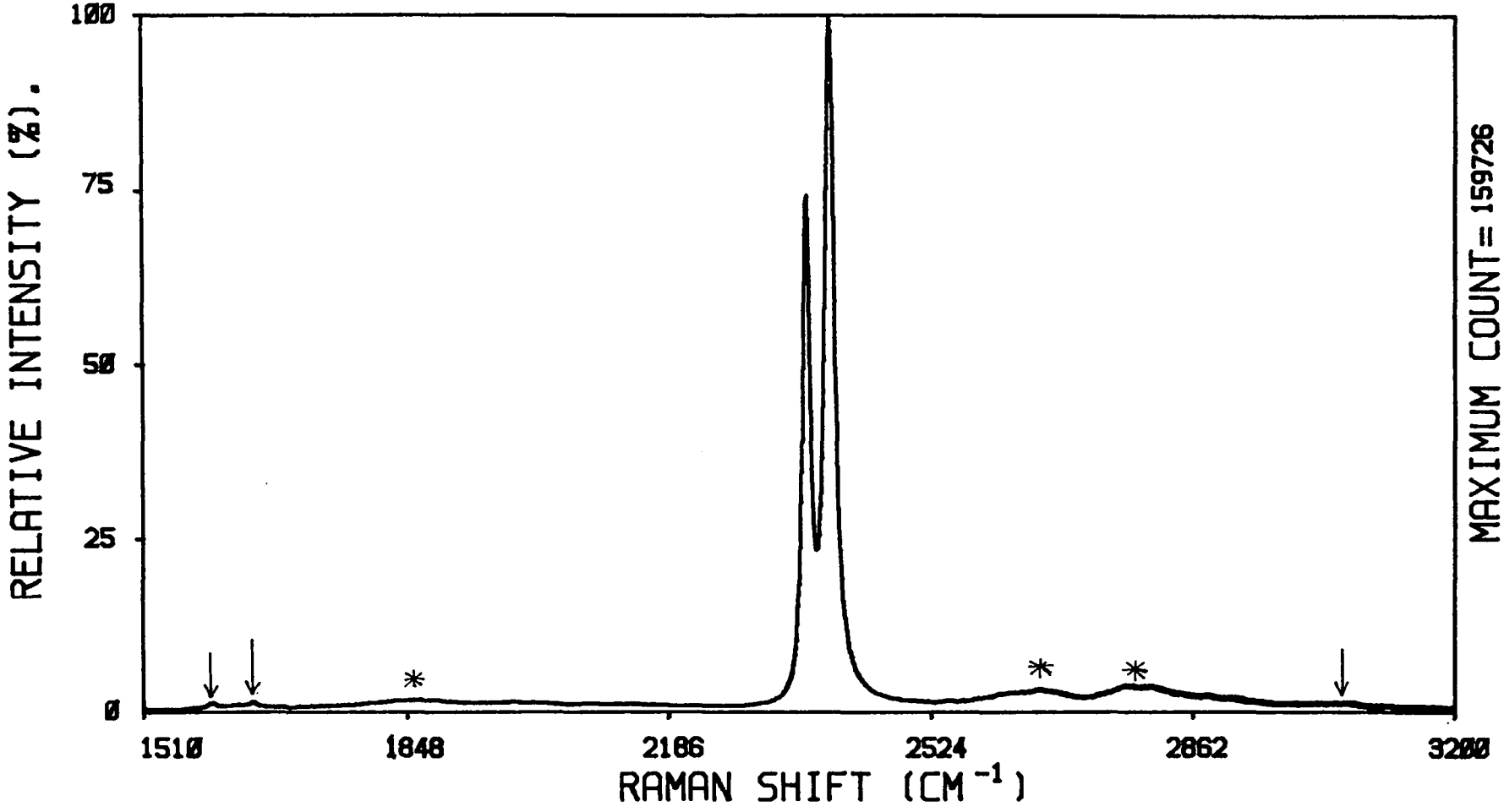

FIGURE 8.7 Ungated Raman spectrum of a 3:1 mixture of αAl_2O_3 and benzophenone. Raman bands are marked with arrows. Note the intense doublet and the broad background features (*), none of which correspond to true Raman transitions.

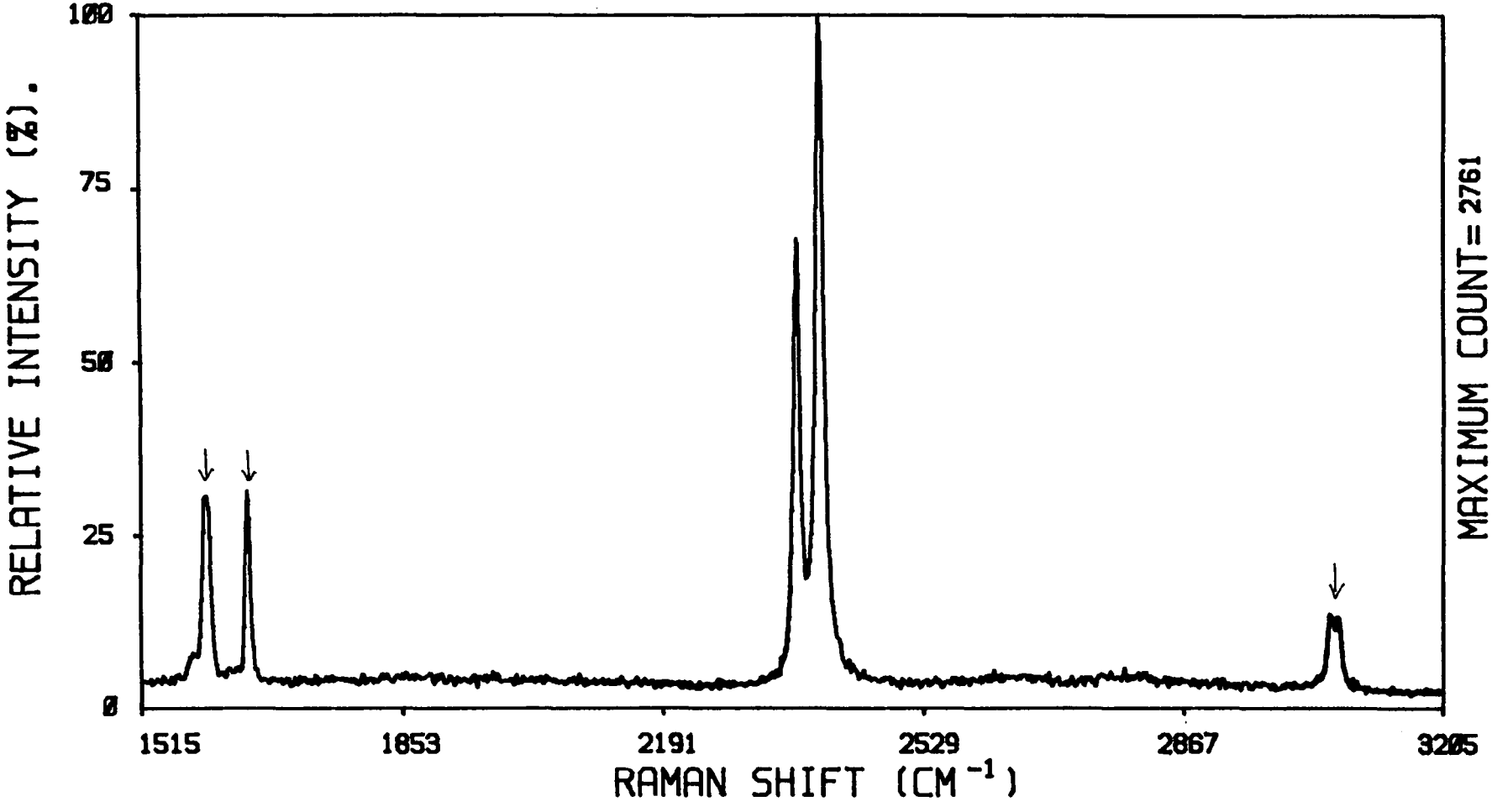

FIGURE 8.8 Gated spectrum of Al_2O_3/benzophenone mixture (*ca.* 4 ns gate). The Raman bands (↓) are clearly revealed, while the doublet and background features are greatly reduced in intensity.

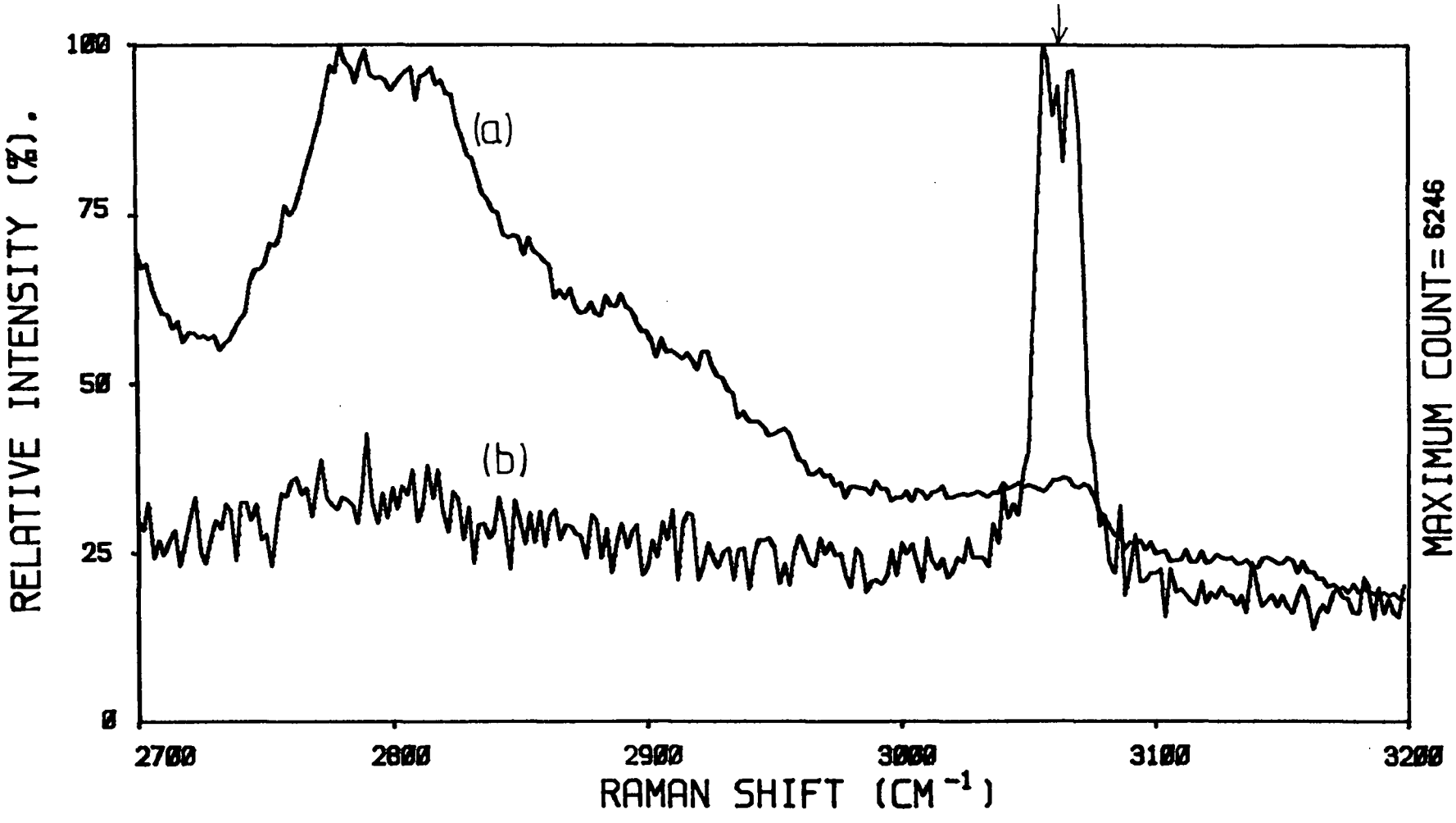

FIGURE 8.9 Expansion of Al_2O_3/benzophenone spectra. (a) = ungated, (b) = gated spectrum. Both spectra are normalised to same scale for ease of comparison. Raman band (↓) is greatly enhanced in gated spectrum.

features. The source of this phosphorescence was easily determined, since a great deal of work has been published upon the optical properties of alumina.[11,12] One of the commonest impurities to be found in this material is Cr^{3+}, which resides in a trigonally distorted octahedral interstice (Figure 8.10).[11] This distortion lowers the symmetry of the ^2E level to give 2 states separated in energy by *ca.* 29 cm^{-1}. Radiative transitions from these levels to the ground $^4A_2$ state are spin forbidden, and so give rise to two phosphorescence lines separated by *ca.* 29 cm^{-1}. This is exactly what we observed in our spectra. The broad features in the background are phonon sidebands,[11] *i.e.* they arise from electronic transitions which are coupled with creation or annihilation of lattice phonons.

The lifetime of these transitions is *ca.* 3 ms[10,11] and so at 4MHz pump rate the phosphorescence intensity reaches a steady state. The intensity of the doublet should therefore be reduced according to the duty cycle of the system, which, assuming a 4MHz repetition rate and a 4 ns gate width, is *ca.* 1.6×10^{-2}S. We therefore expect a reduction in intensity of *ca.* 1.6×10^{-2} on gating the system, *i.e.* a 63 fold decrease. A 58 fold decrease was actually observed.

It therefore seems likely that the sample which Yaney studied contained Cr^{3+} impurities. The Cr^{3+} doublet was not observed because he used a frequency doubled Nd:Yag laser (532nm), which would place the features at a Raman shift of *ca.* 4400 cm^{-1}, well outside the normally-scanned range. The intense background which was so effectively removed was most likely a phonon sideband of the doublet.

Although this experiment serves to demonstrate the effectiveness of the system in suppressing long-lived

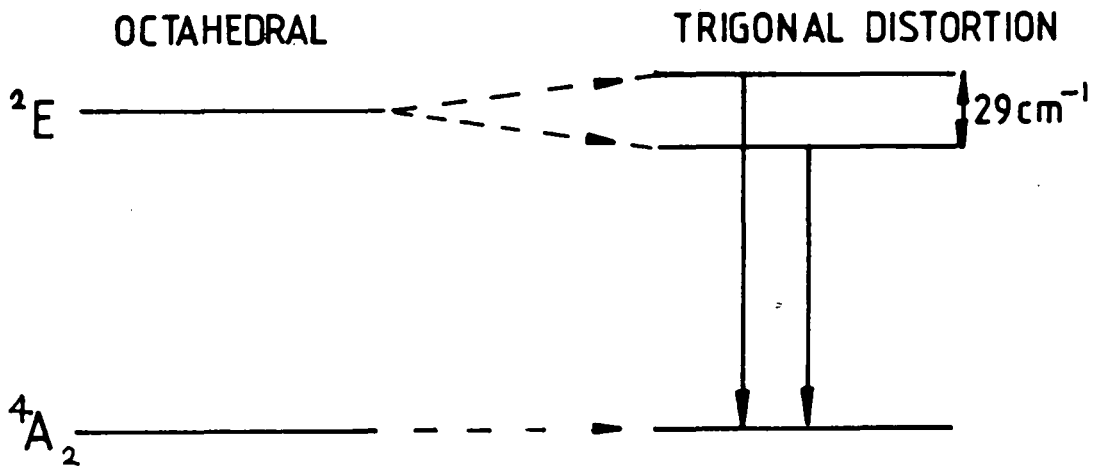

FIGURE 8.10 Origin of the intense doublet in the Raman spectrum of αAl_2O_3. Cr^{3+} impurities reside in trigonally distorted octahedral interstices in the Al_2O_3 lattice. The distortion lifts the degeneracy of the ^2E level to give 2 states separated by *ca.* 29 cm^{-1}. Optical transitions between the upper and lower levels are spin forbidden, and so give rise to phosphorescence bands with correspondingly long (ms) lifetimes.

emissions, it should be noted that a situation will rarely arise where the background arises from phosphorescence rather than fluorescence. For example, we studied many samples of alumina which were not contaminated by Cr^{3+}, but which still exhibited an intense fluorescence background. Suppression of this short-lived emission requires substantially better timing resolution than that which has been described above. Hence modifications to the system are needed to study such samples (Section 8.5).

8.3.7 Calculation of optimum gate width and position

It is obviously important to be able to calculate the most efficient position and width for the photon acceptance window. Harris *et al*[5] stated that the gate should accept *ca.* 67% of the Raman distribution, but do not discuss the variation of this fraction as a function of τ_f or of the FWHM of the IRF. As far as we are aware, this information has not been previously reported and is discussed in detail below.

In order to simplify the calculation of the optimum fraction, we assume that the leakage-light induced fluorescence has a negligible effect upon E[R/N]. We then calculate the value of $Z(R)/[Z(F)]^{\frac{1}{2}}$ as a function of the upper gate limit t_b, while keeping the lower gate limit t_a fixed at zero, (Figure 8.1). A perfect triangular IRF is assumed, *i.e.* no correction is made to Z(R). The maximum enhancement occurs when:

$$\frac{d(E[R/N])}{dt_b} = \frac{d(Z(R)/[Z(F)]^{\frac{1}{2}})}{dt_b} = 0 \qquad (8.12)$$

Since the functional form of Z(R) and Z(F) depends upon the value of t_b (*i.e.* $0<L$, $L<t_b<2L$ or $t_b>2L$, equations (8.3)-(8.5)), equation (8.12) should ideally be solved for these

three time regimes. However, the upper limit for t_b which need be considered is clearly $t_b=2L$, *i.e.* a Raman collection fraction of 1. Furthermore, in the region $0<t<L$ (*i.e.* the leading edge of the Raman distribution) the Raman probability function rises more sharply than the fluorescence profile (Figure 8.1), so it is advantageous to collect all of the first half of the Raman distribution. This limits the optimum position for t_b to the range $L<t_b<2L$.

When equation (8.12) is evaluated over this range of values we obtain, after some simplifcation:

$$(2t_b-L-t_b^2/2L).D_1/D_2+2t_b/L = 4 \qquad (8.13)$$

where

$$D_1 = 1+2kL-kt_b-2e^{-k[t_b-L]}+e^{-kt_b} \qquad (8.14)$$

and

$$D_2 = t_b(1+2kL)-2L-kL^2-0.5(kt_b^2) + (2_e^{-[k(t_b-L)]}-e^{-kt_b}-1)/k \qquad (8.15)$$

Equation (8.13) was solved numerically to hield the optimum position t_b for any given k and L values, and the corresponding Raman fraction $Z(R)^*$ was then evaluated.

It was found that $Z(R)^*$ depends only upon the ratio of the IRF width to the fluorescence lifetime (L/τ_f). The variation of $Z(R)^*$ with (L/τ_f) is depicted in Figure 8.11. Clearly when $\tau_f<<L$, then $Z(R)^*\rightarrow 1$, as would be expected. Under more usual circumstances, $L<\tau_f$, and hence $0.67<Z(R)^*<0.75$. Therefore, the ideal collection fraction is not a constant 67%, as suggested by Harris *et al*[5]. However, it is important to consider the sensitivity of the R/N enhancement to variation of the collection fraction.

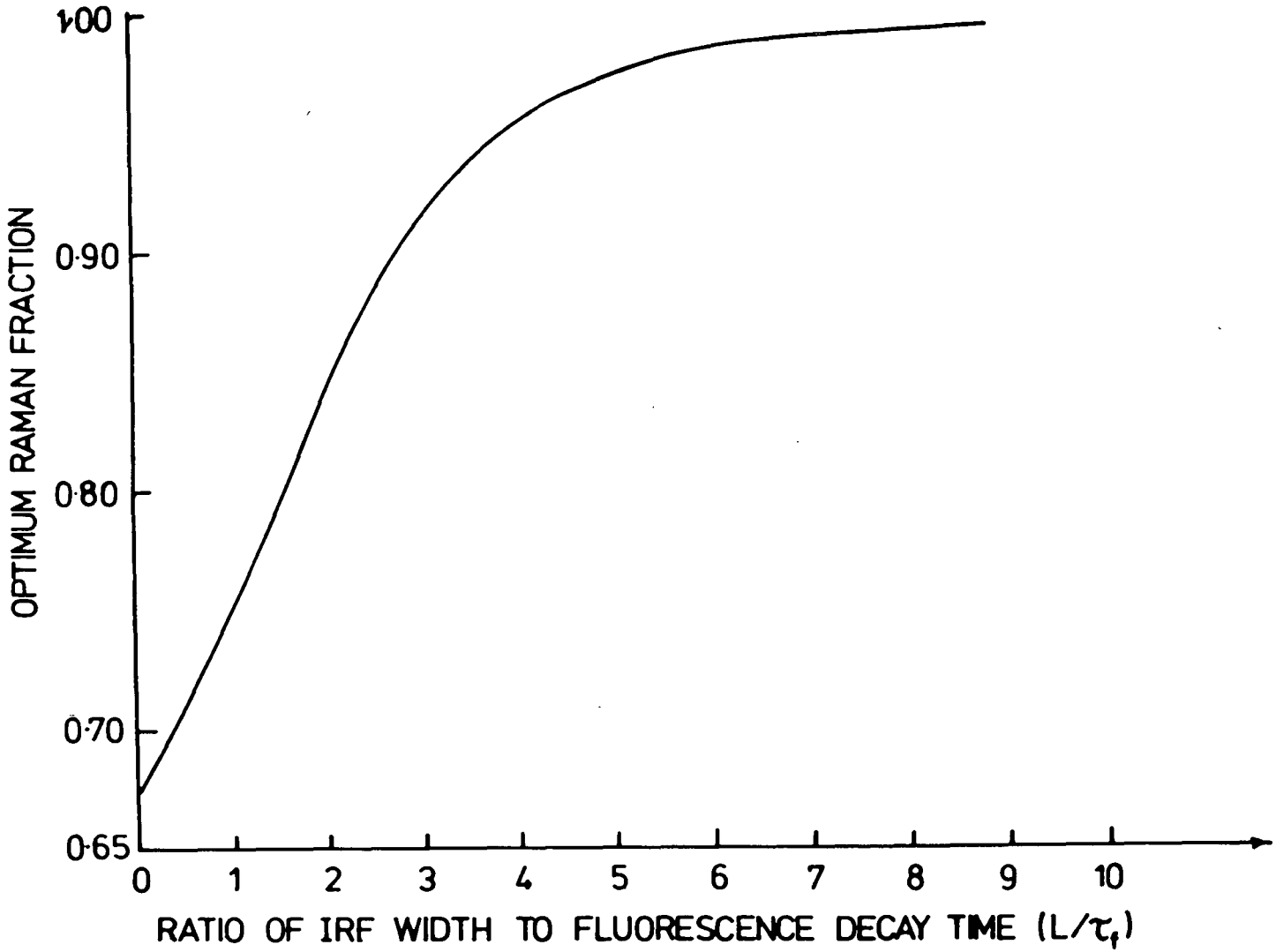

FIGURE 8.11 Variation of optimum Raman fraction as a function of L/τ_f. This fraction yields the best R/N improvement, assuming a perfect triangular IRF.

Table 8.6 illustrates the calculated effect on the signal/noise enhancement of (a) varying the lifetime of the fluorophore and keeping Z(R) constant at 0.67 and (b) varying Z(R) to maintain the optimum acceptance fraction. It appears that in practice there is very little benefit in carefully setting the gate to the ideal width, since the R/N enhancements are virtually identical with those obtained by selecting a constant acceptance fraction of 0.67. When τ_f<1 ns, slightly improved performance should be obtained by selecting the optimum gate-width.

TABLE 8.6 Calculated effect of setting the optimum gate width† upon E[R/N] as a function of fluorescence lifetime

τ_f(ns)	Z(R)*	E[R/N]	
		Z(R)=optimum	Z(R) = 0.67
25	0.68	4.457	4.457
15	0.68	3.477	3.477
10	0.69	2.863	2.863
5	0.70	2.077	2.076
3	0.72	1.664	1.661
2	0.74	1.415	1.410
1	0.82	1.215	1.208
0.5	0.94	0.978	0.930

† Calculations performed under the assumption that L = 1.75 ns.

Figure 8.12 summarises the calculated R/N improvements as a function of τ_f, while varying the gate width to maintain Z(R) at the optimum value for the τ_f value concerned. The enhancements were calculated *via* equation (8.13), and the Raman fractions were corrected in the usual way, *i.e.* $Z(R)_c$=0.9Z(R).

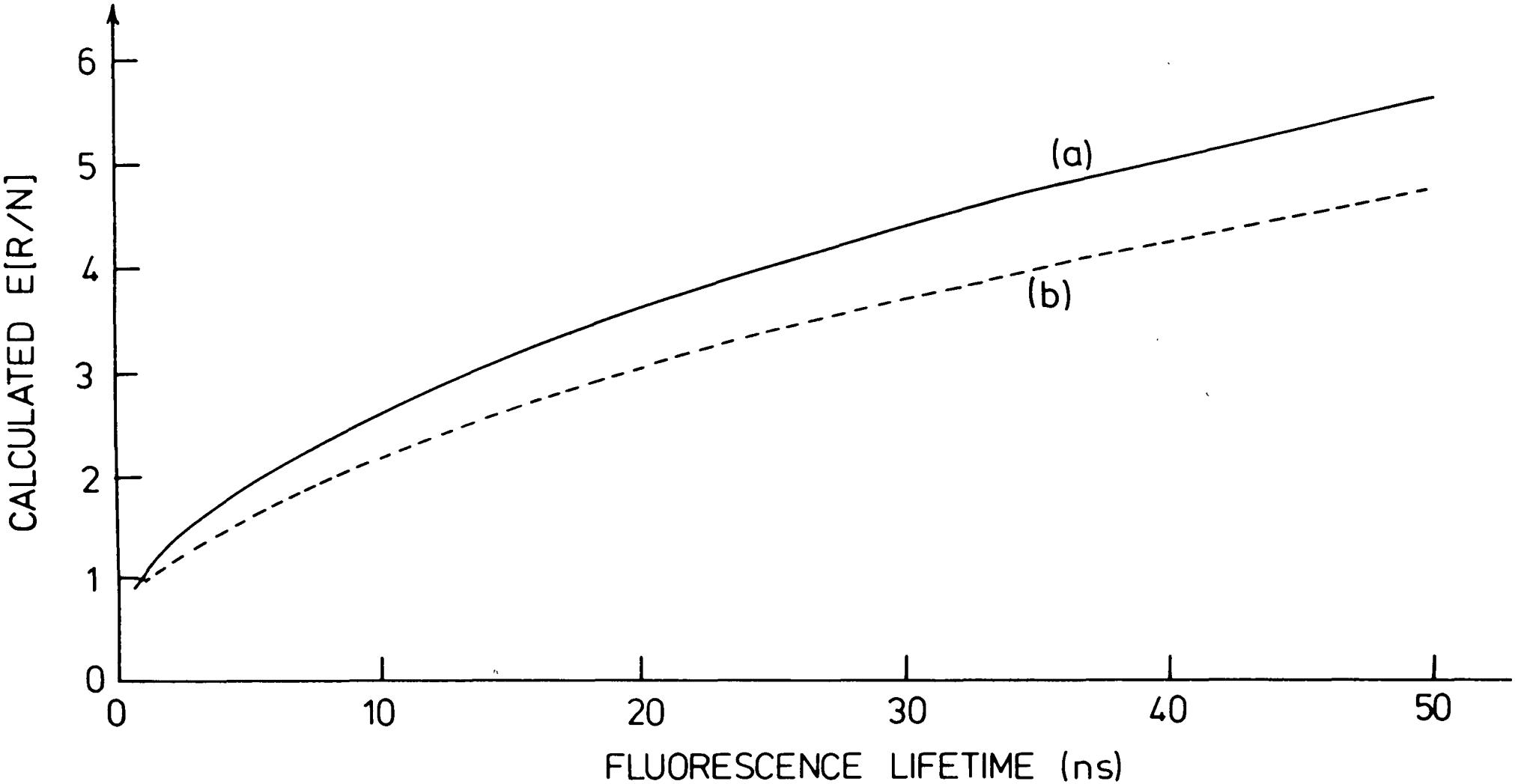

FIGURE 8.12 Calculated R/N improvements as a function of fluorescence lifetime, assuming $Z(R)_c = 0.9Z(R)$, $I_m/I_L = 100$. With a perfect system, $(Z)R)_c = Z(R)$, $I_m I_L = \infty$), a minimum E[R/N] of 1.0 would be obtained as $\tau_f \rightarrow 0$.

(a) Gate set to collect optimum fraction, (b) Gate set to span FWHM of IRF.

The ratio I_m/I_L was assumed to be 100:1 (I_m/I_T=1/1.19).

As expected, the calculated E[R/N] decreases as τ_f falls, such that when τ_f<1 ns, actual degradation in spectral quality occurs. In the ideal case, I_m/I_T=1 and $Z(R)_c$=Z(R), (*i.e.* a perfect triangular IRF is observed), and the enhancement values of Figure 8.12 would be multiplied by $(1.19)^{\frac{1}{2}}/0.9$, giving a minimum E[R/N] of 1 as $\tau_f \rightarrow 0$.

The maximum calculated enhancement in R/N was *ca.* 5.6, for a lifetime τ_f=50 ns. Slower decays were not considered, since substantial overlapping of fluorescence decays stimulated by adjacent laser pulses would begin to occur (at 4MHz repetition rate), resulting in more fluorescence photons falling within the gate. This necessitates a more complex treatment (Van Duyne *et al*[3]).

Also shown on Figure 8.12 is the effect of positioning the gate such as to capture the FWHM of the Raman photon distribution. It is clear that such a gate position is always inferior to one where the acceptance window opens at t=0 in order to capture the first Raman photons. This is interesting since previous authors (Van Duyne *et al*[3], Burgess and Shepherd[4]) only quote results obtained with the photon acceptance window set at the FWHM position.

8.3.8 Effect of varying IRF width (L)

In Chapter Four we considered the variation of E[R/F] and E[R/N] as a function of gate width for an ideal detector (L→0). It is interesting to perform an analogous calculation for a detector with finite IRF width. In this case, the parameter of interest is the ratio L/τ_f, whereas with an ideal system we considered t_g/τ_f.

Figure 8.13 illustrates the calculated variation in E[R/N] and E[R/F] as a function of L/τ_f, assuming that $I_m=I_T$ and $Z(R)_c = Z(R)$. The gate was assumed to be set at the optimum width for improving R/N. Also shown are the corresponding improvements for an ideal system ($L\rightarrow 0$) as a function of t_g/τ_f. It is interesting to note that a smaller gate is required in the ideal system to obtain the same improvement as in the non-ideal system. This is a consequence of the need to match the gate-width with the width of the IRF.

8.3.9 Comparison with a cw source

It is important to compare the results obtained with the gated detector and pulsed laser system with those expected for ungated detection and irradiation with a cw laser source operating at the same wavelength. The chief consideration here is the power reduction which is suffered on going from a cw laser to a mode-locked system. Here we choose the same cw dye laser power which was used for evaluation of the gated DAD (Chapter Seven), namely 100mW. The cavity-dumped output power was only 28 and 22 mW during the experiments described above, giving power reduction factors (α) of 0.28 and 0.22 respectively. The laser performance has since been substantially improved by the methods discussed in Chapter Five and output powers of *ca.* 50 mW are readily achievable (corresponding to α = 0.5) at 4 MHz pulse rate.

The R/N enhancement relative to ungated detection and cw excitation is given by equation (8.16)

$$E[R/N] = [\alpha(I_m/I_T)]^{\frac{1}{2}} Z(R)_c / [Z(F)_c]^{\frac{1}{2}} \qquad (8.16)$$

i.e. we must multiply all previously calculated R/N enhancements by $\alpha^{\frac{1}{2}}$, (including those illustrated in Figure 8.13), for com-

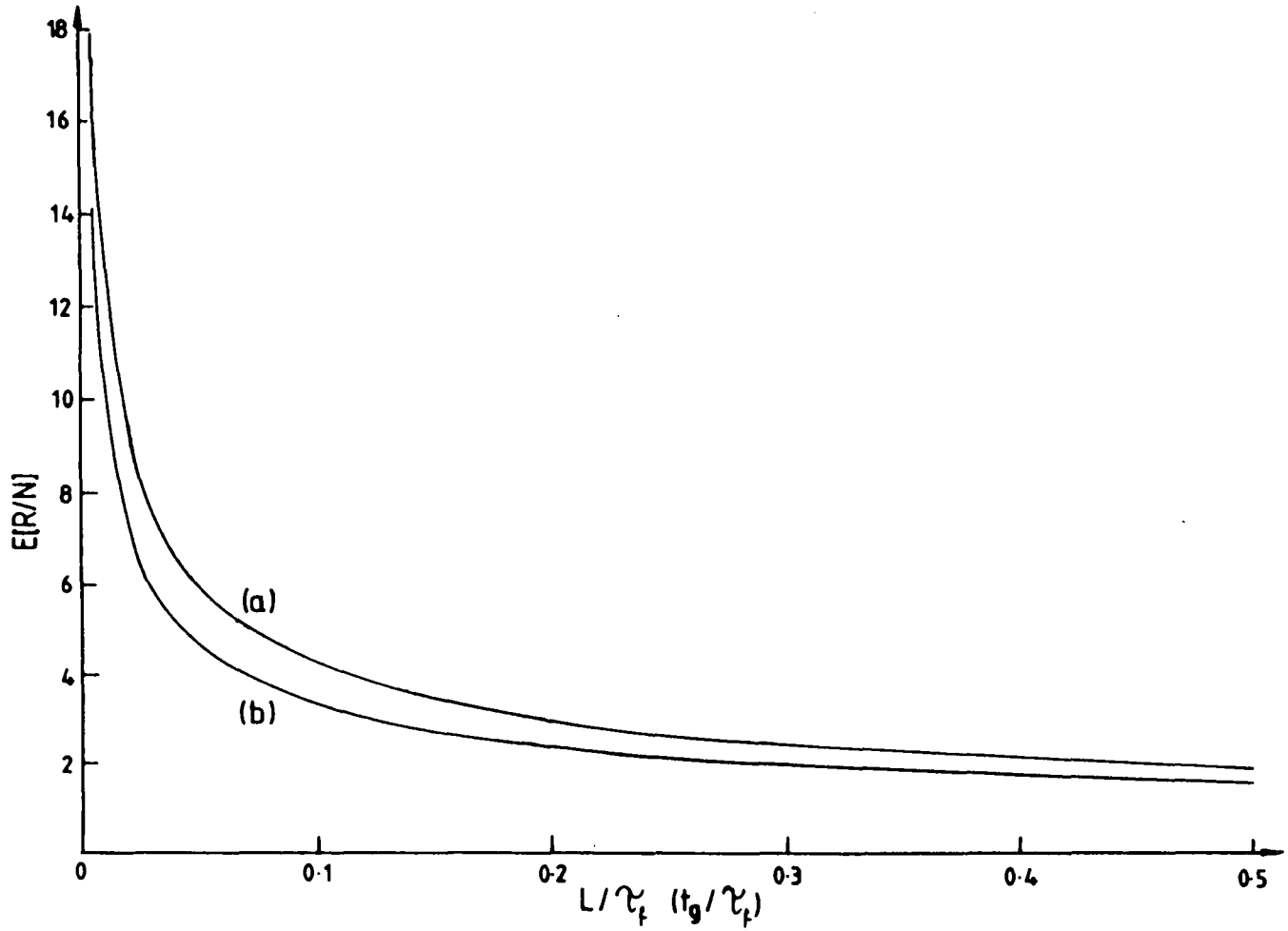

FIGURE 8.13 R/N enhancement for ideal (L→0) and non-ideal (L>0) IRFs,

(a) E[R/N] *versus* L/τ_f for a real detector (Gate set for optimum Raman fraction)

(b) E[R/N] *versus* t_g/τ_f (L=0, t_g = gate width).

Assumed that $I_m/I_T = 1$, $Z(R) = Z(R)_c$.

Enhancements should be multiplied by $\sqrt{\alpha}$ for comparison with cw excitation.

parison with cw excitation. We find that the calculated E[R/N] values now become 1.4 and 1.5 (α=0.28 and 0.22 respectively), or under the improved laser operating conditions (α=0.5) we would expect improvements of *ca.* 1.9 and 2.3 respectively, compared to ungated detection and cw excitation at 100mW. The fluorescence from the solution exhibiting non-Poisson fluctuations, however, would be expected to be affected considerably by this increased laser power, due to variations in the concentration of non-fluorescing species built up, the degree of solution heating and convection, *etc.* It is not a simple matter to calculate the effect of using cw excitation on such a sample. It should also be noted that it is not always possible to employ high power cw irradiation for reasons of sample decomposition.[13] In these situations, the pulsed laser-gated detection system is the most efficient method for obtaining spectra with good signal/noise levels at low incident laser intensity.

8.4 Comparison with previous work

Before going on to consider hardware modifications which we have made to improve the performance of our system, it is interesting to compare the relative effectiveness of the various experimental configurations which have been applied in previous published work. The work of Yaney[2,9] has already been discussed in some detail and will not be considered further.

Although all fluorescence rejection by time resolution methods rely upon the same physical phenomenon for their success, the instrumentation which has been used for achieving the resolution has varied widely.

Van Duyne *et al*[3] employed a mode locked Ar^+ laser with a TPHC/SCA gating system. The limiting factors were:

(a) A wide IRF was obtained (2.5 ns) which limited the rejection efficiency.

(b) The close proximity (*ca.* 9 ns) of the mode-locked laser pulses may result in considerable overlapping of fluorescence decays stimulated by adjacent laser pulses - this constrained the applicability of the technique to short-lived (τ_f<4.5 ns) fluorescent species.

As a result of these limitations, an improvement in R/N of 1.05 was observed for the spectrum of benzene doped with acridine orange (1.3×10^{-9} M, τ_f=4.4 ns). This was achieved with the acceptance window set for the FWHM of the Raman distribution (not the optimum position), and the improvement was over ungated detection using the mode-locked laser as the source - not in cw mode. The authors gave analytic equations appropriate for a δ function IRF, but did not give expressions relating to a triangular IRF.

Burgess and Shepherd[4] used essentially the same technique as Van Duyne, but reduced the IRF width to *ca.* 1.3 ns by using a PMT of low transit timespread (0.5 ns), a photodiode to provide the reference timing pulse, and a shorter laser pulse (*ca.* 0.5 ns). They observed enhancements in R/F of *ca.* 6 for an acridine orange doped system, and an R/N 'improvement' of 0.8 over ungated detection with the laser running in cw mode. The authors stated that the decrease in R/N may be rectified by increasing the time of measurement - this is of course true, but it defects the object of the experiment, since ungated detection with a cw laser would yield a better quality spectrum in a shorter time, if the spectra are shot-noise limited! However, the success in reducing non-Poisson fluctuations was noted and its importance recognised.

Harris *et al*[5] used a cavity-dumper to vary laser pulse repetition rate, and this allowed study of solutions containing longer-lived fluorescors. However, their sampling-oscilloscope gating system necessitated using a low laser repetition rate (42 kHz), and this resulted in a very low power reduction factor α, in the region of 2×10^{-3}. Therefore, although an enhancement of 115 in R/F was obtained for a solution of rubrene in benzene, the signal/noise ratio of the Raman band was actually decreased *ca.* 6.7 times relative to ungated detection and cw excitation. However, the use of a very noisy PMT (6000 cps dark count!) indicated the efficiency of the gating technique in discriminating against random noise more successfully than against the time correlated fluorescence signal, as would be expected. The authors attempted to calculate absolute Raman and fluorescence intensities from a knowledge of the relevant cross sections rather than simply the improvement upon gating. This was not very successful for the rubrene sample.

The most successful application of time-resolved rejection using a conventional dynode-chain PMT appears to have been made by Gustafson and Lytle[6], who employed a synchronously-pumped cavity-dumped dye laser, with gated photon detection as the time resolution method. They calculated R/N enhancements (with respect to cw excitation and detection) of 2.4 (α=0.25 and 9.7 (α=4) for benzene doped with rubrene (10^{-5} M), and an improvement of *ca.* 5.0 (α=1) was observed experimentally. No calculated value was stated for the α=1 case.

Unfortunately, no details of the method of calculation of the Raman and fluorescence acceptance fractions were given, and no example of a Raman photon distribution was included, although it appears that a 2.1 ns gate resulted in maximum rejection

efficiency. This would indicate that the IRF had a FWHM of *ca.* 1.75 ns if 67% of the Raman photon distribution was accepted. If the IRF was in fact 1.75 ns wide, then according to our calculations we would not expect an R/N enhancement of 2.4 over cw excitation for an α=0.25 system. This is nearer to the value calculated for gated over ungated detection under pulsed laser excitation in each case (Table 8.1). Without details of the calculations employed it is difficult to determine the source of this discrepancy. Furthermore, since the rubrene solution used had been degassed, we might expect some contribution from the non-Poisson intensity fluctuations which we observed in such solutions (Section 8.3.4), and which should make the observed improvements greater than the calculated values - so it is somewhat surprising that the authors obtained good agreement between theory and experiment under these conditions.

Watanabe *et al*[7] recently reported the use of an MCP-PMT in conjunction with a mode-locked dye laser and TAC, which resulted in a very narrow IRF,(67 ps FWHM),and hence effective fluorescence rejection,(E[R/N] = 4.2 for R6G contaminant with $\tau_f \simeq 4$ ns), compared to E[R/N] = *ca.* 2 in our case. However, this was achieved using a 31 ps gate, which is much shorter than the optimum calculated value of *ca.* 80 ps (68%,Figure 8.11). Therefore the full potential of the method was not demonstrated. No comparison with cw excitation was made. Calculations upon the effect of varying τ_f and gate position were presented, but the more important effect of gate width was not considered in detail. Such a system is obviously constrained to the study of short lived fluorophores, but the addition of a cavity-dumper would resolve this. It was clearly demonstrated that the MCP-PMT is superior to conventional tubes for this type of work.

The work of Watanabe *et al* is discussed in more detail in Section 8.6.4.

8.5 Modifications and improvements

8.5.1 Laser system

It should be apparent that there are essentially two ways in which the performance of our system might be improved, namely by improving the quality of the laser output, or by improving the timing resolution of the detection system. The comparison of the gated system with that employing cw excitation and detection illustrates that the power decrease suffered on going from a cw dye laser to a pulsed system seriously degrades the R/N ratio. For example, the maximum specified cw output from the dye laser (3W pump power) is *ca.* 600 mW, compared to the 50mW average power obtained at 4 MHz pulse rate. This reduces the ultimate R/N ratio of the gated spectrum by a factor of *ca.* 0.3 compared to that which would be obtained at an average pulsed power of 600 mW. This is an analogous problem to that encountered with the gated DAD, except that with the DAD the low (4kHz) gateable rate reduces α to *ca.* 0.0003.

It was described in Chapter Seven how one might succeed in increasing the power of the pulsed laser system at low repetition rates, in order to make the comparison with cw excitation more favourable. These techniques are not generally applicable to high repetition rates, and so would necessitate a decrease in the pulse rate to the order of kHz. It would be preferable to raise the value of α while maintaining high pulse rates.

Gustafson and Lytle[6] pointed out that the value of

α varies as the dye-laser wavelength is tuned, such that with their system they observed α=0.25 at 600 nm, but at 570 nm α was in fact 4, *i.e.* an increase in power was obtained with the sync pump system, compared to cw operation at 500 nm. However this is somewhat misleading, since the absolute power (pulsed mode) was reduced by *ca.* 0.4 at 570 nm, compared to that at 600 nm. Although the R/F and R/N enhancements may be calculated, the absolute R/N will vary greatly as the dye laser is tuned, because the Raman and fluorescence cross sections and the detector efficiency are wavelength dependent. This makes it difficult to calculate the effect of tuning the laser wavelength, and so this aspect will not be considered further.

It seems unlikely that significant ($\geq$x10) improvements in the pulsed laser output power will be made in the near future, and so we now consider improving the system performance by increasing the timing resolution of the apparatus.

8.5.2 Decreasing the width of the IRF

Figure 8.13 illustrated how the R/N enhancement is governed by the relative magnitudes of the IRF width and the fluorescence lifetime. It is clear that the IRF width must be significantly decreased in order to obtain worthwhile improvements. The finite IRF width arises as a result of timing jitter in the system, and has components arising from:

(a) the generation of the CDSO timing pulse (Chapter Six),

(b) triggering of the pulse generator,

(c) the transit-timespread of the PMT,

(d) triggering of the amplifier/discriminator,

(e) the finite timing resolution of the time-to amplitude converter,

(f) timing error due to variation in optical path length through the monochromator.

Factor (e) was discussed in Chapter Six and can be assumed to be insignificant compared to the observed timing error (1.75 ns). It was necessary to systematically investigate the remainder of the possible causes, since there was no way of knowing which gave the most significant contribution to the overall error.

8.5.3 Use of fast photodiode to provide STOP pulse

It was first suspected that the generation of the reference STOP pulse might be prone to significant timing jitter. An alternate timing reference was obtained by arranging a laser-pickoff and fast photodiode (Spectra Physics 403B) to sample a small (<1%) portion of the laser beam and so provide reference STOP timing pulses (Chapter Six). The photodiode output pulses were of the correct polarity (-) to trigger the TPHC direct, without prior conditioning by the pulse generator, and so the pulses were merely passed through a hard-wire delay unit (Ortec model 425A) in order to control their time of arrival. This ensured that there was no jitter between the laser pulses and the reference timing pulses.

When this was done, we found that the IRF width was not noticeably decreased. This strongly indicatesthat the PMT transit-time spread (TTS), or the amplifier/discriminator section, was introducing considerable timing jitter. The contribution of the timespread introduced by the monochromator may be shown to be negligible (Section 8.5.8).

8.5.4 Minimising the time spread due to the PMT

The TTS of the PMT, and the jitter in triggering the discriminator to produce a timing signal, is expected to make the largest contribution to the width of the IRF. The techniques which are available for reducing this time spread are well known,[14-16] and essentially involve increasing the voltage between the photocathode and first dynode (the TTS is proportional[15] to $1/v$), the use of special focussing electrodes, and focussing the input light beam to a point on the photocathode. This latter point is very important, since it has been shown,[14,16,17] that the transit time may vary considerably (several hundred ps) according to the portion of the photocathode which is illuminated. Thus the usual approach in Raman spectroscopy of uniformly illuminating the entire photocathode is unsatisfactory for timing purposes.

The PMT which is used in our system (RCA 31034-A05) is an excellent tube for general Raman spectroscopy, since it has a low dark count rate and good red sensitivity (300-850 nm). However, it was designed for photon counting rather than fast timing applications. Nonetheless, it has been demonstrated[1] that this tube type may be used in a timing system which gives rise to an IRF of *ca.* 800 ps FWHM, *i.e.* 1/2 that which we observed. It was therefore decided to modify the voltage divider of the tube in an attempt to reduce the TTS.

The tube was supplied as part of an Integrated Detector Assembly, (EG&G model 1191), which is essentially a photon counting package. Fast-timing applications demand a different voltage divider configuration,[14] and so the divider was rewired according to the manufacturer's instructions (C31034 data sheet) for a fast pulse response (Figure 8.14).

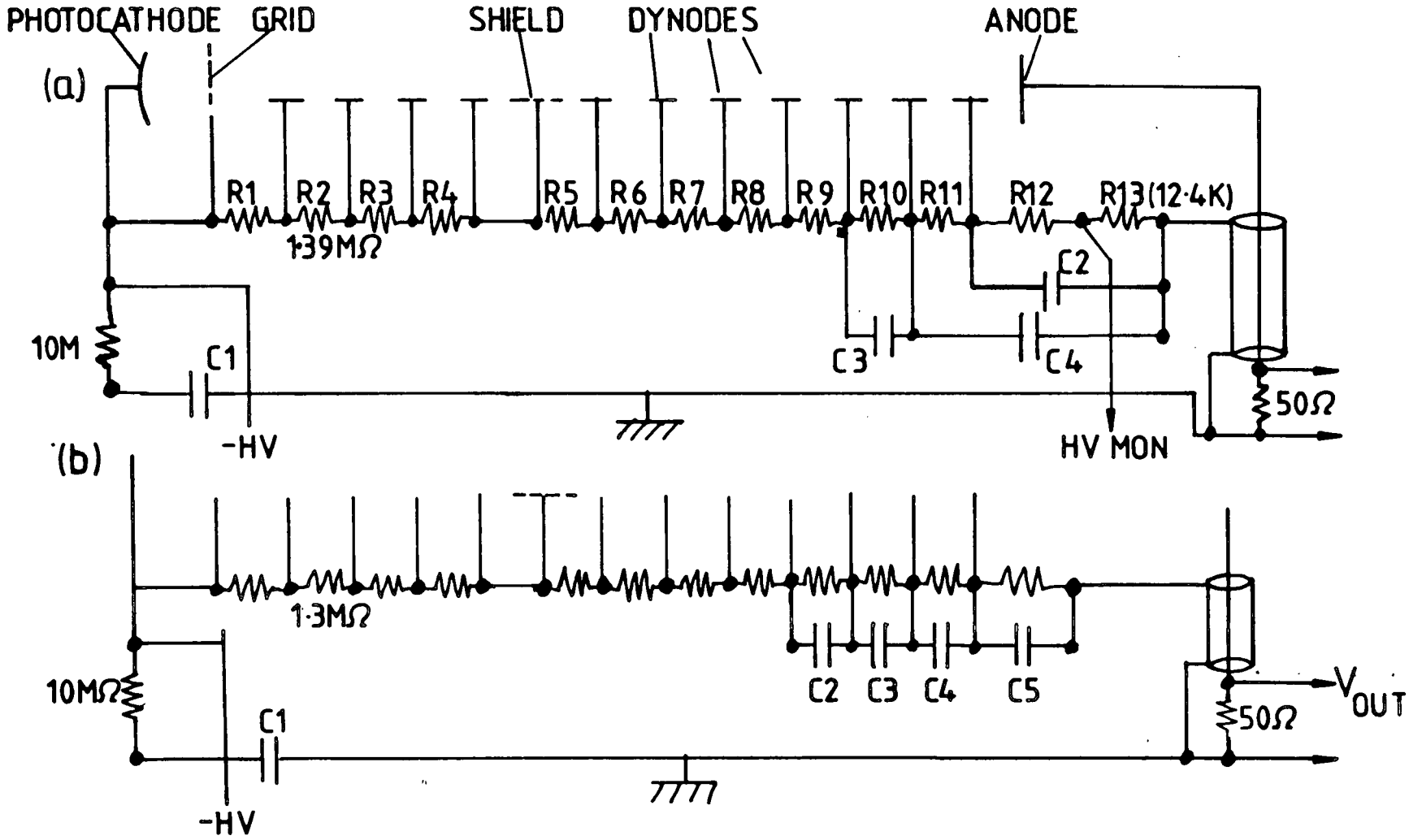

FIGURE 8.14 Voltage divider configurations: (a) Original and (b) Rewired system. All resistors 1MΩ unless otherwise noted. Configuration (a): all capacitors are 10nF. Configuration (b): C1=10nF, C2=5nF, C3=10nF, C4=20nF and C5=50nF.

The anode pulses from the rewired tube were then processed by the same preamplifier/discriminator/amplifier combination which was used previously. The IRF of the rewired IDA is illustrated in Figure 8.15. The distribution was recorded in the same way as the data in Figure 8.1, *i.e.* with the reference STOP pulse provided by the CDSO. Use of the fast photodiode to provide the reference pulse did not result in a narrower distribution. The voltage between the anode and cathode (V_{ac}) was adjusted to obtain the best IRF shape, found to occur when V_{ac}= -1700V.

It is clear from Figure 8.15 that rewiring the voltage divider has significantly reduced the TTS of the PMT, to yield an IRF of *ca.* 1.1 ns width, *ca.* 600 ps narrower than the previous value. Although this is encouraging, it is still higher than the 800 ps FWHM which should be achievable.[1] In order to further reduce the width, it was necessary to alter the method of generating the timing pulses from the PMT anode output pulse.

8.5.5 Constant fraction and leading edge discriminators for fast timing applications

The PMT anode pulses are unsuitable as timing inputs to the TPHC, (Figure 6.10), as they are of low voltage (order of mV) and are of variable amplitude. The TPHC requires a fast NIM pulse as input. Generation of this signal at a time that is precisely related to the anode pulse is a difficult problem which has been tackled in a variety of ways;[18] however, all attempts have been based upon processing the PMT pulses with a discriminator, which is triggered only when a certain property of the pulse satisfies a given criterion. Only two such techniques are discussed here, namely leading edge

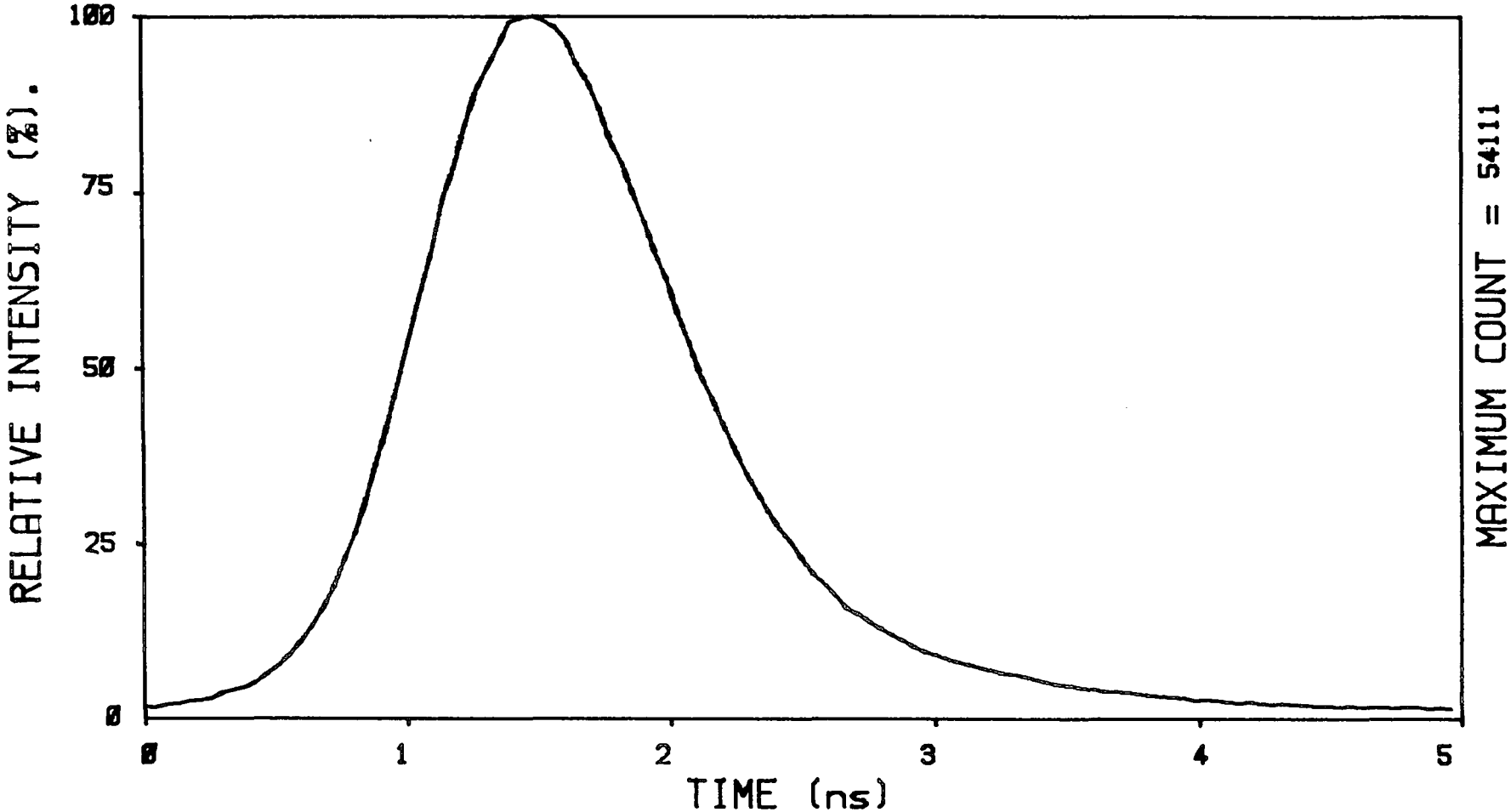

FIGURE 8.15 IRF of system with rewired PMT voltage divider. Anode pulses processed by amplifier/discriminator incorporated in IDA, *i.e.* a simple leading edge discriminator. FWHM = 1.1 ns.

discrimination (LED) and constant fraction discrimination (CFD). Paulus[18] has given an excellent introduction to the principles of fast timing techniques, and much of the explanation below is based upon his review.

8.5.5.1 Leading edge discrimination and time walk

LED is the simplest method of generating a time pickoff signal, where an output logic pulse is produced when the input signal exceeds a preselected threshold (V_{LE}). The primary disadvantage of this technique is that the time of production of the output pulse (t_{LE}) is a function of both the amplitude and the rise-time of the input signal (Figure 8.16). High time resolution can only be obtained when the input signal amplitudes span a narrow dynamic range and are of constant rise-time. Furthermore, noise on the input signal will introduce an uncertainty into the time of triggering of the discriminator. The effect of this noise is minimised when the input signals are of short rise-time, *i.e.* the voltage gradient is steep.

8.5.5.2 Constant fraction discrimination

It is clear from Figure 8.16 that for input signals of variable amplitude but constant rise-time, the time of production of the output pulse is constant if the discriminator is always triggered at a constant fraction of the input pulse amplitude. In order to achieve this type of discrimination, the input pulse is split into two signals (Figure 8.17), one of which is delayed (t_d) with respect to the other (which is attenuated and inverted). The attenuated, inverted signal is then added to the delayed pulse to produce a bipolar output signal, the zero crossing point of which always occurs at a constant time position, (corresponding to a constant fraction (f)

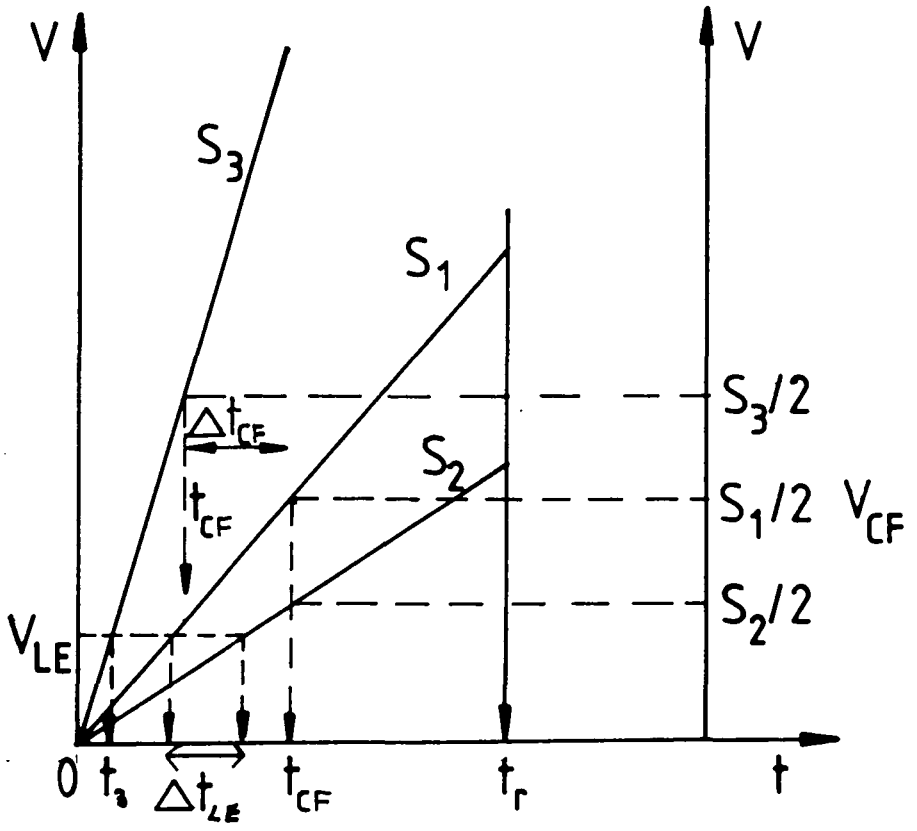

FIGURE 8.16 Origin of time walk.

A simple leading edge discriminator, set to trigger at a voltage V_{LE}, suffers a timing filter of Δt_{LE} when signals of varying amplitude, (S_1 and S_2), but constant risetime are processed. A discriminator which triggers at a constant fraction (V_{CF}) of the input pulse height (in this case ½) suffers no jitter provided that the signal risetime (t_r) is constant. If the risetime is not constant, neither constant fraction nor leading edge discrimination gives good results, as is illustrated by the timing jitters Δt_{LE} and Δt_{CF}.

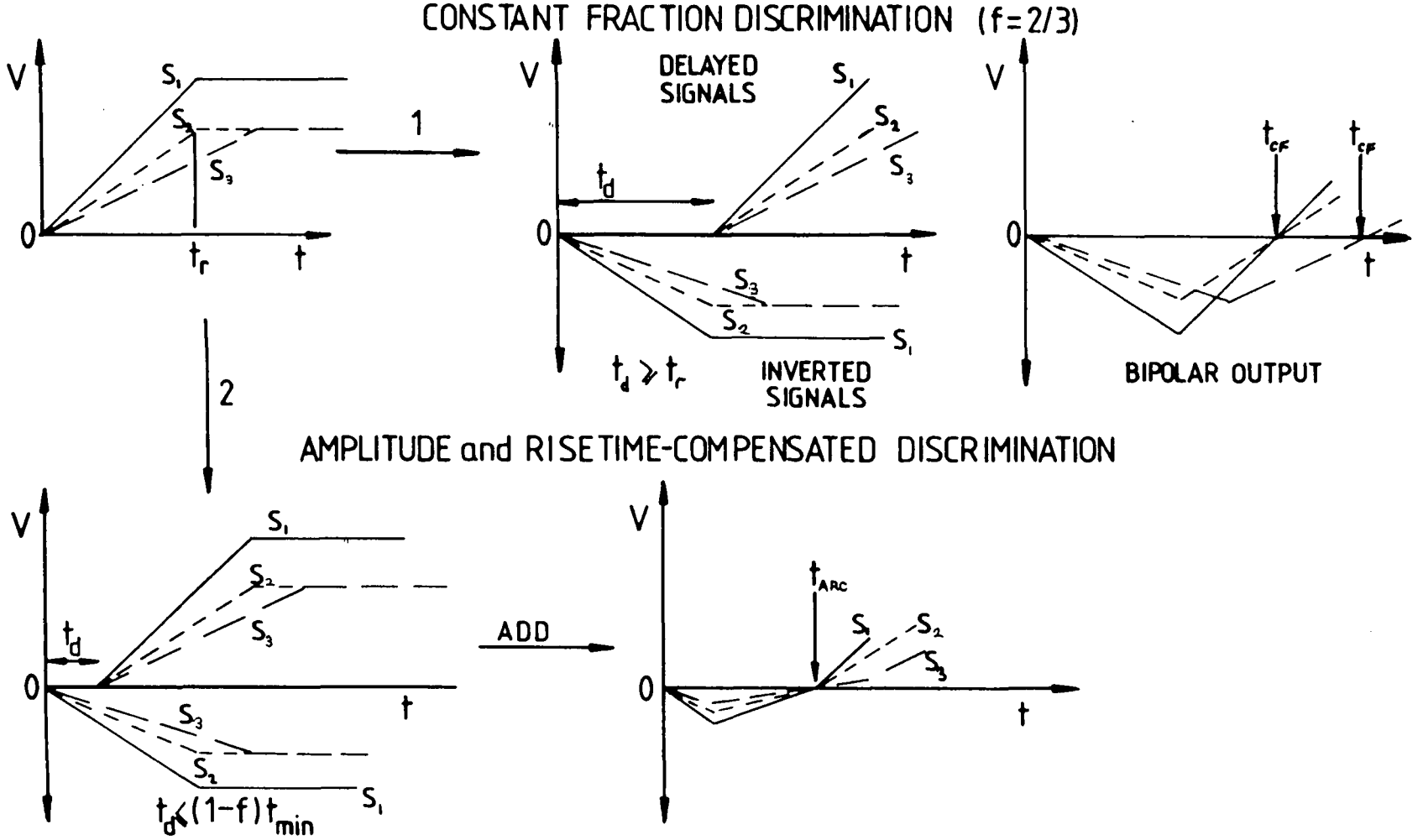

FIGURE 8.17 Principles of CF and ARC discrimination.

(1) Zero crossing point is independent of amplitude but varies with risetime when CFD is chosen ($t_d \geq t_r$).

(2) Zero crossing point is independent of both amplitude and risetime with ARC discrimination See text for details.

of the input pulse amplitude), irrespective of the amplitude of the input signal. In the example chosen in Figure 8.17, f=2/3. A zero crossing discriminator is then used to generate the output logic pulse. Again the effect of noise is minimised by having a steep bipolar output from the constant fraction unit.

In order to achieve CFD, the rise-time t_r must be constant, and the delay, t_d, must be selected so that $t_d > t_r(1-f)$, to ensure that the zero crossing point occurs after the attenuated signal reaches maximum amplitude. It must be emphasised that this mode of discrimination is not effective when the input signals have a wide variety of rise-times (Figure 8.17). Under these circumstances, amplitude and rise-time compensated (ARC)[18] discrimination is a superior method of generating the timing pulses.

8.5.5.3 Amplitude and rise-time compensated discrimination

ARC timing is obtained when $t_d < t_{min}(1-f)$, where t_{min} is the minimum rise-time expected for any input signal. This delay selection ensures that the zero crossing point occurs before the attenuated signal reaches maximum amplitude, and eliminates the rise-time dependence which limits the application of the CFD technique (Figure 8.17). Note, when the discriminator is operated with this delay, the timing point does not occur at a constant fraction of input amplitude, and so the term "constant fraction discriminator" is something of a misnomer.

It would appear that the ARC method should always be superior to CFD, since it is independent of both rise-time and amplitude of the input signal. However, the ARC

bipolar timing signal has a smaller gradient than the CFD signal, which makes the timing more susceptible to jitter from statistical noise on the input pulse. Commercial CFD units have a variable delay (t_d), and so the mode of discrimination (CFD or ARC) may be varied to produce the narrowest IRF for a given type of input signal.

8.5.6 Replacement of IDA discriminator with a constant-fraction discriminator

In order to carry out CFD or ARC discrimination, the PMT pulses must be processed before they reach the discriminator of the IDA. The anode pulses were first preamplified with the IDA preamplifier, and then fed through *ca.* 3 feet of coaxial cable to an ORTEC model 473A constant fraction discriminator. Observation of the PMT pulses on an oscilloscope (Tektronix 7904) showed that the pulse rise-times varied from *ca.* 2-3 ns, and so it was decided to use ARC timing. Since the fraction f is fixed at 30% with this CF unit, the selected delay t_d must satisfy $t_d<2(1-0.3)=1.4$ ns. A delay of 1.3 ns (coaxial cable) was chosen.

Figure 8.18 illustrates the IRF obtained with this new configuration. The IRF was resolved as two peaks, separated by *ca.* 1.2 ns. The first (main) pulse had a FWHM of *ca.* 775 os, while the following peak (*ca.* 1/4 of the main pulse intensity) was not entirely resolved, but appears to be of a similar width. This second feature was not reported by Spears *et al*[1] in their work on an identical PMT.

8.5.6.1 Origin of the IRF afterpulse

The occurrence of spurious peaks in the pulse distribution of a PMT is by no means a rare event. The features are usually referred to as afterpulses.[14] Afterpulses

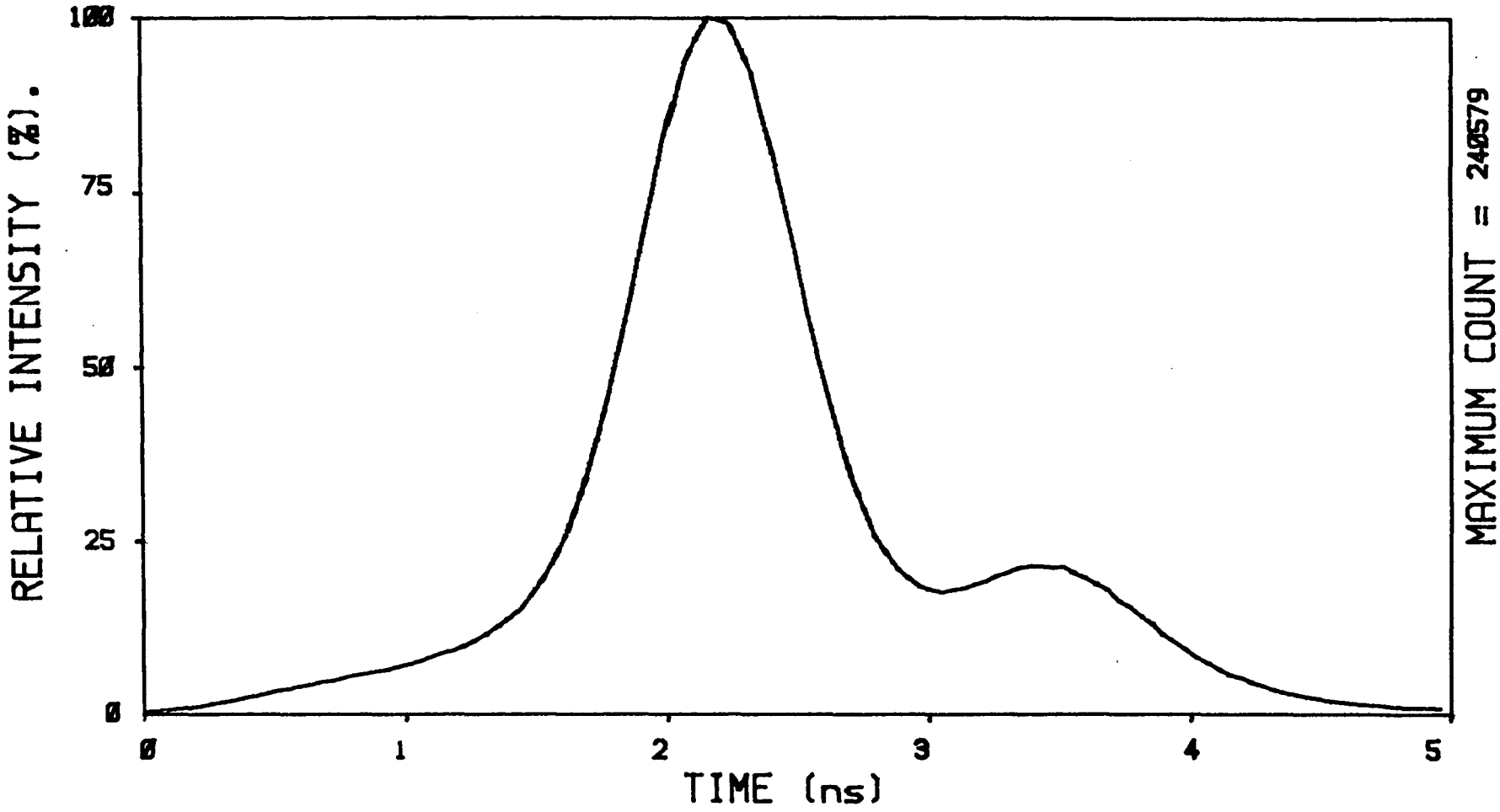

FIGURE 8.18 Effect of processing pre-amplified anode pulses with ARC discrimination. The IRF width is reduced to *ca.* 775 ps, revealing the presence of a previously unresolved afterpulse, *ca.* 1.2 ns after the main feature.

arise *via* two main mechanisms:

(a) Light feedback from the anode upon impact of the secondary electrons. When the light feedback reaches the photocathode, a further pulse of photoelectrons is generated. The time of generation of the afterpulse is given by the total transit-time of the tube plus the transit-time of the light that is fed back, and is typically of the order of 40-50 ns. Thus the pulse which we observe cannot be due to this cause.

(b) Ionization of gas in the region between the cathode and first dynode. Typical sources include N_2^+, H_2^+ and He^+, giving rise to afterpulses at characteristic time intervals in the region 200 ns to well over 1μs. Again, this time interval is far greater than that which we observed.

Therefore, the spurious feature cannot be assigned to one of the usual afterpulsing mechanisms. The pulse does not result from an impedance mismatch between the pre-amplifier output and the CFD, since reflections would be of a reduced amplitude compared to the main anode pulse. Raising the discrimination level of the CFD reduced both features in the distribution by the same fraction, indicating that the pulses which give rise to each feature are of the same amplitude but occur at a different time. At this stage the origin of the afterpulse was not clear.

8.5.7 Focussing of the image on the PMT photocathode.

Optimum timing resolution may only be obtained when light is focussed to a point on the photocathode, since electrons emitted from different regions of the surface experience different electric fields.[14] The system which was used for the previous experiments employed uniform illumination of the photo-

cathode, which could result in substantial (ns) transit-time differences for electrons emitted from different parts of the surface.[14] Although it is not clear how this could result in the behaviour which we observed, (we would expect one broad peak rather than two discrete ones), it was judged worthwhile to determine the effect of focussing the monochromator output.

Ideally, this would be done by incorporating a focussing assembly,and mounting the PMT upon a micropositioning stage,to allow the optimum region of the photocathode to be illuminated.[16,17] This procedure was not thought to be worthwhile at this stage, and so the configuration depicted in Figure 8.19 was used. An extended mount for the PMT housing was constructed, which incorporated a lens assembly whose position could be varied. Since the position of the photocathode was known, the lens assembly could be selected to focus radiation from the monochromator at the correct point. With the lens assembly fixed in position, the PMT was placed in the housing and the IRF measured in the usual manner (Figure 8.20).

Focussing the light onto the photocathode eliminated the second peak to yield a highly symmetrical IRF of *ca.* 775 ps FWHM. This strongly implies that the afterpulse arises in some way from the interaction of the light upon the photocathode, although the manner of this interaction is not clear. Furthermore, it was found that <u>incorrect</u> focussing of the <u>collection</u> optics of the monochromator could also generate the afterpulse, although correct focussing of these optics did not eliminate the afterpulse when the light was <u>not</u> focussed onto the photocathode! This presumably arises from variation of the focussed image position upon the photocathode as the image of the sample on the entrance slit of the monochromator is altered.

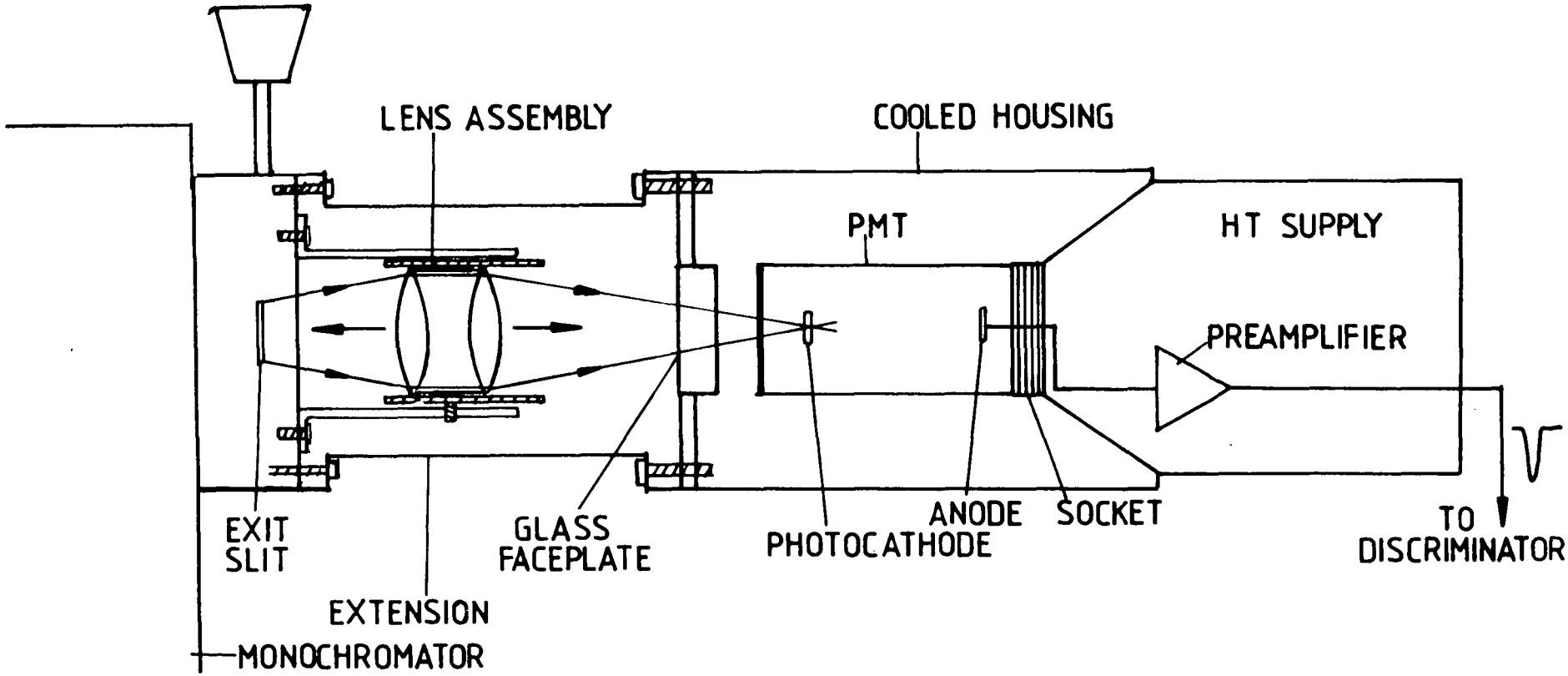

FIGURE 8.19 Focussing assembly for PMT (not to scale).
Lens assembly may be translated horizontally to focus image at desired point (achieved while holding card at position of photocathode and observing image). Position of assembly is then locked and PMT housing mounted on extension.

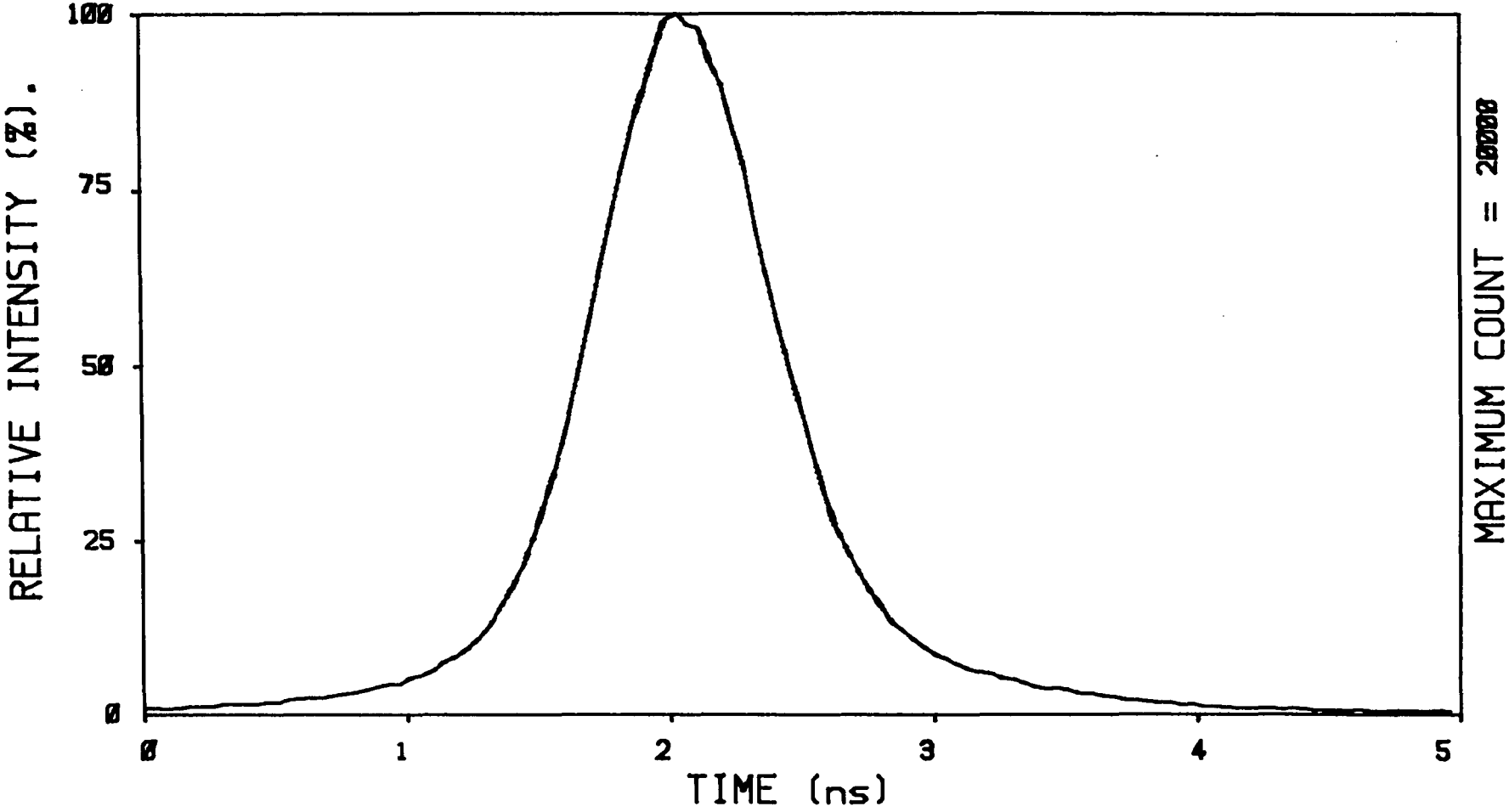

FIGURE 8.20 Effect of focussing image on photocathode. Afterpulse is removed by selectively illuminating only a small region of the photocathode.

8.5.8 Temporal broadening due to the monochromator

So far we have only considered broadening of the IRF due to jitter in the timing system. However, an important factor which is often ignored is the temporal broadening which occurs on the pasaage of an optical pulse through the monochromator.[19,20] This broadening arises from the different path-lengths which rays may traverse from the entrance to the exit slit, and can amount to hundreds of picoseconds.

Bebelaar[19] recently discussed, in simple terms, the origin of this time dispersion and methods for minimising its effect. For light of wavelength λ, diffracted into the first order from a diffraction grating, a path length difference of λ must exist between rays reflected from adjacent grooves (Figure 8.21). If N grooves are illuminated, the total path length difference between rays A and B is

$$\delta l = N\lambda \qquad (8.17)$$

For light travelling with velocity c, this length is equivalent to a time difference $\delta t = N\lambda/c$. Each of the gratings in our double monochromator is ruled with 1200 gr/mm, and has dimensions 100x100 mm, giving a total of 12×10^4 grooves per grating. If the entire grating were illuminated by light with λ=640 nm, (a typical wavelength of Raman scatter with our system), this would correspond to a timespread of *ca.* 256 ps. In a more rigorous analysis, Saari *et al*[20] showed that the broadened response has a Gaussian profile. Equation (8.17) actually provides a good estimate of the FWHM of the profile. With a double monochromator having gratings mounted for additive-dispersion, the timespreads due to each grating (Δt) add in quadrature,[20] *i.e.* the total timespread is

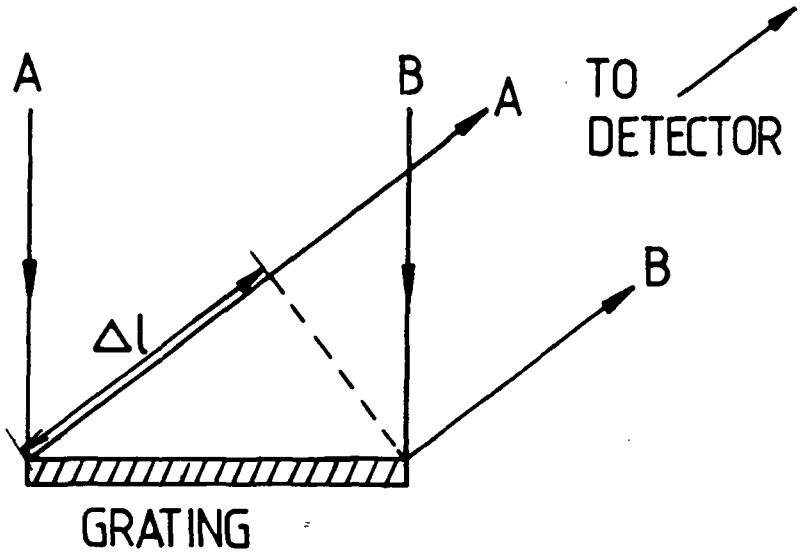

FIGURE 8.21 Origin of time dispersion in a monochromator. The ray A travels a distance Δl further than ray B in order to reach the detector. This introduces a time difference of $\Delta t = l/C$, where C is the velocity of light. See text for details.

$$T = (\Delta t^2 + \Delta t^2)^{1/2} = \sqrt{2}\Delta t \qquad (8.18)$$

Therefore, with both gratings fully illuminated in our system, the total timespread would be *ca.* 360 ps, *i.e.* a significant contribution to the IRF width. With our observed IRF width of *ca.* 775 ps, this would indicate that the contribution of the PMT/timing electronics is $(775^2-360^2)^{\frac{1}{2}}$=686 ps, *i.e.* the gratings would broaden the IRF by *ca.* 100 ps. However, in a real experiment, the whole area of the grating is not illuminated. When the image of diffusely scattered light was viewed on the surface of a grating, we observed that only *ca.* 1/2 of each grating was illuminated. This corresponds to a spread of 128 ps for each grating, or 180 ps for the pair, indicating that the broadening due to the PMT($(775^2-180^2)^{\frac{1}{2}}$=754 ps) dominates the width of the IRF.

In the present system, the monochromator makes little contribution to the width of the IRF. However, methods are considered below which should reduce the contribution of the detection system to *ca.* 50 ps, in which case the broadening due to the monochromator would dominate the IRF. Fortunately, methods exist to eliminate this effect. The most obvious route is to limit the number of grooves illuminated on each grating (since the time dispersion is proportional to N). However, this not only decreases the wavelength resolution of the system,[21] but also gives a poorer energy throughput and hence a smaller S/N. A far better solution is to use a compensator.[19] In a double monochromator, this entails mounting the gratings such that the dispersion due to the second grating is in the opposite direction to that of the first (subtractive dispersion). Thus while ray A lagged ray B after the first stage (Figure 8.21),

the phase lag is reversed in the second stage such that both rays have the same phase at the detector, *i.e.* they are coincident in time. Saari *et al*[20] demonstrated practically an exceptional narrowing in time response (800 ps→9 ps) on going from additive to subtractive dispersion in a double monochromator. This sort of technique will be essential in order to obtain the limiting time resolution of ultrafast microchannel plate PMTs (Section 8.6.4).

8.5.9 Conclusions upon modification of the present detection system

It has been shown that the IRF of the TCPC system described above can be reduced to less than 800 ps by three modifications.

(a) Rewiring the voltage divider for optimum fast-pulse output.

(b) Employing the ARC timing discrimination on the preamplified PMT anode pulses.

(c) Focussing the light emerging from the monochromator to a point on the photocathode.

These modifications have yielded an IRF width which is as narrow as any which has been reported with this PMT. However, even this improvement is not sufficient for our purposes. Figure 8.13 indicates that reducing the IRF by a factor of 0.44 (1.75 ns→0.775 ns) will only improve the E[R/N] value by *ca.* x1.6. To double the R/N enhancements which we have obtained would require a reduction of the IRF to *ca.* 500 ps FWHM.

It is actually more realistic to consider the enhancements which would be obtained compared to cw excitation, which entails multiplying the E[R/N] values on Figure 8.13 by $\sqrt{\alpha}$. We assume that the pulsed laser output is 50 mW average power,

with $I_m/I_T=1$, and also that a perfect triangular IRF is obtained ($Z(R)=Z(R)_c$). If a 3-fold improvement in R/N were acceptable (Chapter One), then for comparison with 100 mW cw excitation ($\alpha=0.5$) this demands that $L/\tau_f=ca.$ 0.8. The same improvement over excitation at 600 mW (max. output power of cw dye laser) would require $L/\tau_f=ca.$ 0.15. For a fluorescor with $\tau_f=10$ ns, this requires an IRF of *ca.* 800 or 150 ps FWHM respectively. However, 10 ns is actually quite a long fluorescence lifetime compared to that found for many samples.[22] For example, a random assortment of samples which we have studied in our laboratory (*e.g.* polymers, zeolites and oils) have had lifetimes in the region 2-5 ns. If we assume that 5 ns is a reasonable upper limit for fluorescing samples which are likely to be studied, this reduces the maximum acceptable IRF widths to *ca.* 400 ps and 75 ps respectively, depending upon whether comparison is made with 100 or 600 mW cw excitation. (We also note that an R/N improvement of x3 would be inadequate for many samples, in which case the IRF width would have to be reduced further).

It is unlikely that the present system can be modified to give the required decrease in IRF width, and so we now consider the availability of MPTs with superior timing resolution.

8.6 PMTs with ultrafast timing capability

The timing resolution of the detection system is essentially limited by the TTS of the PMT, which is in turn governed by the geometry, voltage-divider and electron optics design of any particular device.[14-17,23] A very wide range of PMTs exists for a variety of specific application.[24-26] For the purposes of our work, we require a tube with good timing resolution,

(<400 ps, ideally <100 ps), and with good sensitivity over the range 570-800 nm. Unfortunately, manufacturer's information upon the TTS of photomultipliers is relatively scarce, and so the largest source of relevant data is in the literature.

8.6.1 Timing resolution of classical dynode-chain PMTs

The lower limit of timing resolution achievable with classical, head-on type dynode-string PMTs appears to be in the region of *ca.* 300 ps.[15] This response was obtained with two of the most popular PMTs for fast timing applications, namely the RCA 8850 and 31024. These PMTs are only sensitive over the range 300-660 nm,[24] but a red-sensitive version (C31024A) is available which has good response (10% quantum efficiency) over the range 300-880 nm. Most of the published work involving fast timing applications has involved the use of these or similar tubes, although Bebelaar[23] recently obtained a 235 ps wide IRF with a modified Amperex XP2020 tube.

However, it has been demonstrated[7,17,27] that much better resolution can be achieved through the use of compact, side-on type PMTs, as opposed to the head-on types discussed above. For example, Kinoshita *et al*[27] utilised a Hamamatsu type R928 PMT to obtain an IRF of *ca.* 160 ps FWHM, while Canonica *et al*[17] observed an IRF of *ca.* 112 ps FWHM for both the above tube and an RCA R931A. The R928 has good spectral response over the range 185-930 ps,[28] and would be a suitable selection for our system. There is also the additional advantage that these tubes are cheap compared to the larger, more complex head-on types.

8.6.2 Timing resolution of microchannel plate PMTs

While the side-on type PMTs can provide good

timing resolution, the ultimate timing performance is obtained from PMTs which use a microchannel plate (Chapter Six) as the electron multiplier, rather than a string of discrete dynodes. The enhanced resolution arises because of the limited range of trajectories which the photoelectrons can adopt between the photocathode and the MCP, and on traversing the channel multipliers. Such tubes are becoming more widely used in TCPC,[23,28,29] and the performance of these, as well as conventional and crossed field types, has been recently investigated by Belelaar,[23] who reported a best timing resolution of *ca.* 50 ps for a Hamamatsu R1564U-01. (Good performance was also obtained (*ca.* 50 ps FWHM) with a Varian type VPM-154M cross-field PMT). Other authors[28,29] have obtained similar results with MCP-PMTs. The use of such a tube for TRFR is discussed in detail in Section 8.6.4.

8.6.3 Theoretical and practical limiting performance of the technique

The theoretical limiting improvement in R/N is, of course, infinite, and would be obtained when both the IRF and the gate width tend to zero. In practice this is not possible, and so it is important to consider what practical improvement should be attainable with state-of-the-art technology. At present, the width of the IRF is determined by the response of the detection system, since laser pulses of picosecond duration are obtainable from commercially available systems. From the discussion above it is apparent that the IRF should be reducible to *ca.* 100 ps with conventional, side-on PMTs, or to *ca.* 50 ps with an MCP-PMT. The improvements in R/N which would be expected with these PMTs may be calculated from Figure 8.13, by

setting L=50 ps or 100 ps. With the MCP-PMT, a 20-fold improvement in R/N (compared to ungated detection with the same average laser power) would be expected for the solution with τ_f=11.8 ns, which is in turn a seven fold improvement over the results which were obtained in our work. (The corresponding improvement with the side-on PMT would be *ca.* 14. It is therefore clear that obtaining a PMT of much lower TTS is crucial to the development of our system.

8.6.4 Performance of an actual MCP-PMT based system

We have already referred to the work of Watanabe *et al*[7] who utilised an MCP-PMT for fluorescence rejection studies. Since an extremely narrow IRF was obtained (67 ps), this was a good opportunity to demonstrate the full potential of TRFR in Raman spectroscopy, since the performance described in Section 8.6.3 above should have been achievable. Unfortunately, the experimental configuration which the authors chose resulted in a relatively poor performance compared to that which would have been obtained with a correctly optimised system.

The authors observed E[R/N]=4.2, for a solution of R6G in ethanol (τ_f=4 ns), with a 31 ps gate. From our calculations, an optimum gate width of 80 ps (Figure 8.11) should have given an R/N enhancement of *ca.* 10. For reasons which are not clear, the authors concentrated solely upon optimising the position of this 31 ps gate, rather than the more important consideration of the width. Their report stressed the success in achieving very narrow gate widths, while it is clear that choosing the narrowest gate is detrimental to the R/N ratio unless the IRF is also of a similar width.

It is interesting to note that Watanabe *et al* based their analysis upon a Gaussian approximation to the IRF. They stated that the calculated results were insensitive to the shape of the IRF, such that a numerical calculation using the exact IRF shape yielded very similar results. From their calculated curves of E[R/N] *versus* τ_f, they appear to calculate an improvement of *ca.* 9.5 when τ_f=4 ns, in good agreement with the result which we obtained with our simple model (10). This makes it all the more surprising that they did not select experimental conditions which demonstrated the validity of this calculation, and which should have more than doubled their observed improvements!

The authors[7] also included results which had been obtained with a side-on PMT, which gave an IRF of *ca.* 220 ps. They obtained E[R/N]=2.7 for solid R6G, (τ_f=600 ps), using a gate width of 220 ps, and doubling the accumulation time in gated detection mode. Under similar conditions with a triangular IRF, we calculate that an improvement of *ca.* 2.9 should be obtained, in good agreement with their observed results. Again, the authors did not select the optimum gate width, and it is not clear why they chose to study the more difficult (shorter τ_f) sample with the PMT with the poorer timing resolution! Nevertheless, this work was useful in that it confirmed the essential correctness of our calculations, as applied to the projected performance of a modified optimised system. It is to be regretted that Watanabe's work did not demonstrate the true potential of this system in rejecting short lived fluorescence.

8.7 Comparison of performance with that of the gated DAD

It is interesting to compare the performance of the TCPC apparatus with that of the gated DAD. We first consider the present systems, and then extend the comparison to the calculated performance of the modified, optimised systems. For simplicity, we assume that $I_m/I_T=1$, that the accumulation time is equal for both systems, and is also equal in both gated and ungated detection modes. We also assume that enhancements are calculated with respect to ungated detection and 100 mW cw excitation, and that τ_f= *ca.* 10 ns. In Chapter Seven (Section 7.6) it was shown that under these circumstances, use of the gated DAD would give E[R/N]=*ca.* 0.1, *i.e.* a tenfold degradation in R/N, assuming an output power of 0.2 mW at 4kHz. The PMT based system (775 ps IRF, 50 mW at 4MHz) should give an enhancement E[R/N] of *ca.* 3.0 (Figure 8.13), and so is clearly the superior rejection system at present.

The major change which is required for the DAD system is the substitution of a laser system which gives higher powers at kHz repetition rates. If 100 mW average power (4 kHz) were available, and the modifications to the IRF shape and the elimination of the ringing effect (discussed in detail in Chapter Seven) were carried out, an E[R/N] value of *ca.* 7 should be obtained.

The TCPC system performance rests mainly upon the width of the IRF, which can only be improved by the purchase of a PMT of much smaller TTS. A 50 ps FWHM IRF should be readily attainable through the use of an MCP-PMT, which would give E[R/N]=*ca.* 13 (assuming a pulsed intensity of 50 mW average power). Thus when both systems are optimised, the PMT based

apparatus should still give the best improvement in R/N. However, we should also consider the absolute R/N values of the spectra produced by each system. The DAD can accumulate *ca.* 700 spectral channels simultaneously, compared to the single PMT channel. Neglecting the effect of gating the detectors, the DAD has a S/N advantage of *ca.* $\sqrt{700}=26$ over the PMT, assuming equal quantum efficiencies for each detector. This indicates that when the modified gated DAD is mounted on a spectrograph with good stray-light rejection characteristics, (Chapter Nine) we might expect it to yield a spectrum of superior absolute R/N to the TCPC system, even though the R/N enhancement will probably be poorer. With the present system, the gated DAD produces inferior spectra to the PMT, as can be seen from the spectra in this and Chapter Seven.

8.8 Conclusions

A time-correlated photon-counting system has been demonstrated which yields a threefold improvement in the R/N ratio of the Raman spectrum of a sample contaminated by a fluorescor with τ_f=*ca.* 12 ns. The improvement when τ_f=4 ns was *ca.* 2. The phosphorescence (τ_f=*ca.* 3 ms) background of a sample of alumina containing Cr^{3+} impurities was shown to be almost totally suppressed with this apparatus, yielding an R/N improvement of >10. All improvements in R/N were related to ungated detection while utilising the same pulsed laser output.

What is really required is a system which provides worthwhile enhancements in R/N relative to ungated detection and cw laser excitation. This necessitates decreasing the width of the IRF of the detection system. The IRF width has been re-

duced by rewiring the PMT voltage divider, incorporating a constant-fraction discriminator on the PMT output, and focussing the light onto the photocathode. This reduced the observed FWHM from 1.75 ns to 775 ps, but even this only increases our R/N improvements by a factor of *ca.* 1.6. However, purchase of a microchannel plate PMT should reduce the IRF width to *ca.* 50 ps, and yield a seven-fold improvement in R/N compared to that observed with our present equipment. For example, for a fluorescor with τ_f=*ca.* 12 ns, we would expect to obtain an enhancement in R/N of *ca.* 19.6 (α=1). The corresponding improvement observed in our work was *ca.* 2.8. The improvements relative to ungated detection and cw excitation (100 and 600 mW) would be E[R/N]=13.9 and 5.7 respectively.

REFERENCES - CHAPTER EIGHT

1. K.G. Spears, L.E. Cramer and L.D. Holland, Rev.Sci.Instrum., 49(2), 255 (1978).

2. P.P. Yaney, J.Opt.Soc.Amer., 62(11), 1297 (1972).

3. R.P. Van Duyne, D.L. Jeanmaire and D.F. Shriver, Anal. Chem., 46(2), 213 (1974).

4. S. Burgess and I.W. Shepherd, J.Phys.E.:Sci.Instrum., 10, 617 (1977).

5. J.M. Harris, R.W. Chrisman, F.E. Lytle and R.S. Tobias, Anal.Chem., 48(13), 1937 (1976).

6. T.L. Gustafson and F.E. Lytle, Anal.Chem., 54(4), 634 (1982).

7. J. Watanabe, S. Kinoshita and T. Kushida, Rev.Sci.Instrum., 56(6), 1195, (1985).

8. A.J. Pearlstein, J.Phys.Chem., 89(6), 1054 (1985).

9. P.P. Yaney, J.Raman Spectrosc., 5, 219 (1976).

10. M.S. Mathur, C.A. Frenzel and E.B. Bradley, Spectrochim.Acta, 26A, 451 (1970).

11. "Laser Spectroscopy of Solids", W.M. Yen and P.M. Selzer (Eds.), Top.Appl.Phys.49, Springer-Verlag, Berlin, Heidelberg New York (1981).

12. B. Halperin, D. Nicollin and J.A. Koningstein, Chem.Phys., 42, 277 (1979).

13. T.R. Gilson and P.J. Hendra, "Laser Raman Spectroscopy", Wiley-Interscience, London, New York, Sydney, Toronto,(1970).

14. R.W. Engstrom, "Photomultiplier Handbook", RCA Corporation (1980).

15. B. Leskovar and C.C. Lo, Nucl.Instr.and Meth., 123, 145(1975)

16. B. Sipp and J.A. Miehe, Nucl.Instr.and Meth., 114, 249 (1974)

17. S. Canonica, J. Forrer and U.P. Wild, Rev.Sci.Instrum., 56 (9), 1754 (1985).

18. T.J. Paulus, IEEE Trans.Nucl.Sci., NS-32(3), 1242 (1985).

19. D. Bebelaar, Rev.Sci.Instrum., 57(8), 1686 (1986).

20. P. Saari, J. Aaviksoo, A. Frieberg and K. Timpmann, Opt.Commun., 39(1,2), 94 (1981).

21. F.J. Smith and J.H. Thomson, "Optics", J.Wiley and Sons, London, New York, Sydney, Toronto (1973).

22. R.A. Lampert, L.A. Chewter, D. Phillips, D.V. O'Connor, A.J. Roberts and S.R. Meech, Anal.Chem., 55(1), 68 (1983).

23. D. Bebelaar, Rev.Sci.Instrum., 57(6), 1116 (1986).

24. RCA Photomultiplier Catalogue,

25. Thorn-EMI Photomultiplier Catalogue.

26. Hamamatsu Photomultiplier Catalogue.

27. S. Kinoshita and T. Kushida, Rev.Sci.Instrum., 53(4), 469 (1982).

28. T. Murao, I. Yamazaki and K. Yoshihara, Appl.Opt., 21(13). 2297 (1982).

29. I. Yamazaki, N. Tamai, H. Kume, H. Tsuchiya and K. Oba, Rev.Sci.Instrumn. 56(6), 1187 (1985).

CHAPTER NINE

CONCLUSIONS AND FUTURE WORK

9.1 General conclusions

At present, no entirely satisfactory fluorescence rejection technique has been demonstrated which is generally applicable irrespective of sample nature, although time-resolved rejection methods are now rapidly approaching this performance. Many specialised techniques have been reported which are more or less successful for a limited range of sample types, but these are by no means generally applicable. Here some general conclusions are drawn upon the work performed in this laboratory and that reported in the literature.

(a) The ideal fluorescence suppression method is to avoid electronic excitation of the fluorescor, *i.e.* by removing it if it is an impurity, or by using a laser frequency which does not fall within an absorbtion band of the sample. If these methods cannot be employed, then one must discriminate between fluorescence and Raman photons on the basis of their physical or temporal properties.

(b) A wide range of techniques has been demonstrated which improve the R/F ratio of a spectrum, but it is the R/N ratio which determines the quality of the spectrum. When the fluorescence flux follows Poisson statistics ($N=\sqrt{F}$), the noise only decreases as the square root of the fractional reduction in F, and so R/N improvements are always correspondingly worse than R/F improvements, regardless of the suppression technique which is used. The situation is worsened by the fact that most methods inevitably reduce the Raman signal also, and so unless the fractional reduction in the Raman signal is less than the square root of that of the fluorescence, the R/N will actually be degraded.

When non-Poisson fluctuations (*e.g.* laser power drift, sample degradation/movement/turbulence) dominate the background noise, then the corresponding R/N improvements are usually much greater, and are often of the same magnitude as the R/F improvements.

(c) One of the most widely studied methods of suppressing fluorescence has been to time-resolve the Raman and fluorescence photons, using pulsed laser excitation and gated photon detection. The method is generally applicable irrespective of sample state, and rejection efficiency is governed only by the lifetime of the fluorescor and the timing resolution of the detector.

The success of TRFR methods has, until recently, been overestimated in the literature, mainly because results demonstrating large improvements in the R/F ratio have been stressed, rather than the more important changes in the R/N ratio. In fact, it is only comparitively recently (*i.e.* the last few years) that instruments with sufficient temporal resolution to significantly improve the R/N ratio (and hence spectral quality) have become available.

The truth of this assertion is demonstrated by the fact that since the earliest evaluation of TRFR 14 years ago, only two reports[1,2] of the application of this technique to problems of chemical interest have appeared! These applications were successful because the samples were carefully chosen such that the luminescence lifetimes were of the order of ms rather than ns. The overwhelming majority of samples of interest do not satisfy this criterion, and so demand the much higher timing resolution which has become available with synchronously-pumped

dye lasers and modern gated detection systems. It is expected that more practical applications of the TRFR technique will be reported in the future.

(d) The absolute R/N of the time-resolved spectrum depends critically upon the power of the pulsed laser system. This is important for any comparison of a gated spectrum with one accumulated under normal conditions (cw excitation and detection), since the absolute R/N of the spectrum should increase linearly with the square root of the average output power of the laser. Thus even though efficient fluorescence rejection may be obtained using a pulsed laser and gated detection, the absolute R/N is often decreased compared to a spectrum obtained with cw excitation, simply because of the low power of the pulsed laser. This is exemplified in our work on the gated DAD (Chapter Seven), and in the report of Harris *et al*,[3] who obtained a 100-fold improvement in R/F, but a *ca*. sevenfold decrease in R/N, compared to cw excitation and ungated detection with a fluorophore of *ca*. 16 ns lifetime.

Therefore, good time resolution is not sufficient by itself in a TRFR system; it must operate under conditions where the average laser power is as high as possible, subject to constraints imposed by sample decomposition. This necessity can sometimes outweigh considerations of the rejection efficiency.

9.2 Conclusions upon the DAD and PMT-based rejection systems

Detailed results and conclusions for the performance of the two rejection systems have been given in the preceding chapters, but it is convenient to summarise the net results of our work here.

(a) Both systems yield improvements in R/N compared with spectra obtained with ungated detection and excitation by the same (pulsed) laser output, provided that the leakage-light contribution is not significant. This latter factor is crucial for the gated DAD performance.

(b) Under normal circumstances, spectra would be obtained by ungated detection using high (≥100 mW) power cw laser excitation. If such spectrum is taken as the reference by which the gated spectra are judged, only the PMT-based system presently yields improvements in R/N on gating; gating the DAD degrades the R/N ratio such that better spectra would be obtained by operating the DAD continuously, and employing cw excitation.

(c) The performance of the PMT system is sufficient to give some (*ca.* threefold) improvement in the R/N ratio when long lived fluorescors ($\tau_f \geq 10$ ns) are present. This is reduced to a *ca.* twofold improvement when $\tau_f < 5$ ns. Therefore, unless non-Poisson intensity fluctuations dominate the background noise, even the TCPC system will not enable good quality spectra to be recorded when strongly fluorescing, short lived species are present.

(d) At present, the DAD performance is limited mainly by the low gateable repetition rate and hence low laser power. Modifications which will result in a pulsed laser power of *ca.* 100mW (average) at 4kHz should be achievable, which, coupled with alterations to the DAD IRF, (elimination of ringing and sharpening of the gate fall time), should yield a useful system (E[R/N] = *ca.* 7 when τ_f = 10 ns).

(e) Improvement of the TCPC performance can be most easily achieved by increasing the timing resolution of the system.

Use of an MCP-PMT should reduce the IRF width to *ca.* 50 ps or less, giving an E[R/N] of *ca.* 13 (assuming 50mW pulsed excitation at 4MHz, τ_f = 10 ns). This is comparable with the dramatic improvement observed on studying phosphorescent alumina (τ_f = *ca.* 3 ms) with the present apparatus.

9.3 Comparison of gated DAD and TCPC techniques

A direct comparison of the DAD and TCPC systems must include consideration of several factors. If both techniques are optimised, the R/N enhancements expected with the PMT are about twice those expected for the DAD. However, the DAD might well be superior in terms of the absolute R/N of the recorded spectra, simply because it records *ca.* 700 spectral channels simultaneously, as opposed to the single PMT channel. Neglecting gating of the detectors, and assuming equal quantum efficiencies in each case, the DAD has an S/N advantage of *ca.* 26.5 over the PMT, assuming equal accumulation times for a spectrum spanning 700 channels. This easily cancels out the PMT's twofold advantage in R/N enhancement on gating, when both systems are optimised. Furthermore, the rapid accumulation and storage of spectra by the DAD enhances its utility compared to the PMT, particularly in terms of kinetic studies. Therefore it is highly likely that the gated DAD would be the preferred technique, provided that high power laser pulses can be supplied at *ca.* 5 kHz repetition rates.

9.4 Future work

9.4.1 Optimisation of laser/detection systems

The future work which needs to be undertaken in order to produce viable TRFR systems has already been discussed

in detail in Chapters Seven and Eight, but the order in which such work should be performed in order to obtain the maximum immediate benefit has not been considered. The discussion above suggests that when both techniques are optimised, the gated DAD will probably be superior, because it brings all of the advantages of multichannel spectroscopy to the TRFR system. However, in the immediate future, modification of the TCPC system would be the simplest course, since it does not involve any complex and expensive alterations to the laser system. Therefore, the most important modification to be made in the near future must be the acquisition of an MCP-PMT. There is little point in attempting to modify the DAD operating characteristics until a suitable laser system has been obtained, which would be a more long-term process than the purchase of an MCP-PMT.

9.4.2 Modification of the monochromator

It is unlikely that additive-dispersion double monochromators will be suitable for either optimised detection system. This is because they will contribute significant (>100 ps) temporal broadening to the IRF of the TCPC apparatus, once the transit-timespread of the PMT has been reduced to <100 ps. Therefore a subtractive-dispersion spectrometer is likely to be required, since the timespread introduced by the first grating is then reversed by the second in this configuration.

This temporal broadening is not important for a gated DAD, since the switching time of the gate is a few ns rather than ps. However, an additive-dispersion monochromator is not satisfactory for use with a multichannel detector, because there is a significant stray light problem when the intermediate and exit slits are fully opened in order to obtain the required

wavelength dispersion at the detector. For example, with our present monochromator and DAD, reflective solid samples cannot be studied at Raman shifts much below 800-1000 cm^{-1}, which is clearly an intolerable situation.

In order to overcome this problem, a subtractive-dispersion double monochromator should be used, in conjunction with a single-stage spectrograph, which disperses the radiation from the double monochromator onto the detector.[4] This system has inherently greater stray light rejection, since it allows a narrow entrance slit to be used on the spectrograph which receives the radiation from the double monochromator.

It is apparent that a subtractive-dispersion monochromator will be required irrespective of which detection system is chosen, and in fact the same monochromator should be satisfactory for both methods.

9.5 Final conclusions

At present, neither the TCPC or gated DAD systems yield significant R/N enhancements for materials contaminated by short lived (τ_f<5 ns) fluorescing species. Even with longer lived fluorescors, (≥10 ns), the R/N improvements are not large enough to yield good quality spectra of scatterers with strong fluorescence backgrounds. Therefore the applications of the present system are strictly limited.

However, modifications have been identified for each system which would yield apparatus capable of studying the majority of "real-world" samples, as opposed to the carefully selected model compounds which have previously been investigated by this

technique. This will enable the full potential of time-resolved fluorescence-rejection techniques to be realised for the first time since their initial conception over 14 years ago.

REFERENCES - CHAPTER NINE

1. P.P. Yaney, J.Raman Spectrosc., 5, 219 (1976).

2. P.P. Yaney, J.Opt.Soc.Am., 62(11), 1297 (1972).

3. J.M. Harris, R.W. Chrisman, F.E. Lytle and R.S. Tobias, Anal.Chem., 48(13), 1937 (1976).

4. R.K. Chang and M.B. Long in "Light Scattering in Solids 2", (Top.Appl.Phys., 50), Springer-Verlag, Berlin, Heidelberg, New York (1982).

APPENDIX ONE

List of abbreviations and acronyms which are commonly used in this thesis

ARC - Amplitude and Risetime Compensated (discrimination).

AM - Amplitude Modulated.

CARS - Coherent Antistokes Raman Spectroscopy

CDSO - Cavity-Dumper Synchronised Output.

CFD/CFTD - Constant Fraction (Timing) Discriminator.

DAD - Diode Array Detector.

DSR - Digital Shift Register (*cf.* DAD).

FET - Field Effect Transistor (*cf.* DAD).

FT - Fourier Transform.

FM - Frequency Modulated.

IDA - Integrated Detector Assembly.

IR - Infrared.

IRF - Impulse/Instrument Response Function.

LED - Leading-Edge Discriminator/Discrimination.

LIA - Lock-In Amplifier.

MCA - Multichannel Analyser.

OMD - Optical Multichannel Detector/Detection.

PHA - Pulse-Height Analysis.

PMT - Photomultiplier Tube.

PSD - Phase-Sensitive Detection.

RR - Resonance Raman.

SCA - Single Channel Analyser.

SERS - Surface Enhanced Raman Spectroscopy.

SPD - Silicon Photodiode.

TAC - Time-to Amplitude Conversion.

TCPC - Time-Correlated Photon Counting.

TPHC - Time-to-Pulse-Height Converter (Analagous to TAC).

TRFR - Time-Resolved Fluorescence Rejection.

TTS - Transit-timespread.

APPENDIX TWO

Principal components of the apparatus used in this work

1. Laser system

Spectra-Physics model 171 argon ion laser
Model 342 mode-locker and 452A mode-locker driver
Model 375 dye laser
Model 573 birefringent tuning filter (2 plate)
Model 570 tuning wedge
Model 344S cavity-dumper and 454 driver
Model 403B fast photodiode
Tektronix model 7904 oscilloscope (500MHz), with 7S11 sampling head.

2. Diode array detection system

Spectroscopy Instruments (SI) model IRY700 intensified diode array.
Model ST-110 controller
Model MD 100 Fast Pulser
DEC LS1-11 minicomputer

3. Photomultiplier-based detection system

RCA model 1191 Integrated Detector Assembly (C31034-A-05 PMT)
EG&G ORTEC model 473A Constant Fraction Timing Discriminator
Model 467 Time-to-Pulse-Height Converter/Single Channel Analyser
Model 535 Quad Fast-Amplifier
Model 425A Delay unit
Model 441 Ratemeter
Norland-Inotech 5300 Multichannel Analyser
Sirius Microcomputer (ACT computers Ltd.)
Phillips model PM 5712 pulse generator.

4. Monochromators

Spex Ramalog 4 Raman spectrometer (model 1401 double monochromator)
Cary 82 Raman spectrometer (triple monochromator)

Ancillary apparatus is described in the text.

APPENDIX THREE

RESEARCH COLLOQUIA, SEMINARS, LECTURES AND CONFERENCES

The Board of Studies in Chemistry requires that each postgraduate research thesis contains an appendix, listing:

(A) all research colloquia, research seminars and lectures arranged by the Department of Chemistry during the period of the author's residence as a postgraduate student;

(B) Lectures organised by Durham University Chemical Society;

(C) all research conferences attended and papers presented by the author during the period when research for the thesis was carried out;

(D) details of the postgraduate induction course.

(A) LECTURES ORGANISED BY DURHAM UNIVERSITY - 1983-1986.

5.10.83 Prof. J.P. Maier (Basel, Switzerland) "Recent approaches to spectroscopic characterization of cations".

12.10.83 Dr. C.W. McLeland (Port Elizabeth, Australia), "Cyclization of aryl alcohols through the intermediacy of alkoxy radicals and aryl radical cations".

19.10.83 Dr. N.W. Alcock (Warwick), "Aryl tellurium (IV) compounds, patterns of primary and secondary bonding".

26.10.83 Dr. R.H. Friend (Cavendish, Cambridge), "Electronic properties of conjugated polymers".

30.11.83 Prof. I.M.G. Cowie (Stirling), "Molecular interpretation of non-relaxation processes in polymer glasses".

2.12.83 Dr. G.M. Brooke (Durham), "The fate of the ortho-fluorine in 3,3-sigmatropic reactions involving polyfluoro-aryl and -hetero-aryl systems".

14.12.83 Prof. R.J. Donovan (Edinburgh), "Chemical and physical processes involving the ion-pair states of the halogen molecules".

10. 1.84 Prof. R. Hester (York)
"Nanosecond Laser Spectroscopy of Reaction Intermediates"

18. 1.84 Prof. R.K. Harris (UEA)
"Multi-nuclear solid state magnetic resonance"

8. 2.84 Dr. B.T. Heaton (Kent)
"Multi-nuclear NMR studies"

15. 2.84 Dr. R.M. Paton (Edinburgh)
"Heterocyclic Syntheses using Nitrile Sulphides"

7. 3.84 Dr. R.T. Walker (Birmingham),
"Synthesis and Biological Properties of some 5-substituted Uracic Derivatives; yet another example of serendipity in Anti-viral Chemotherapy"

21. 3.84 Dr. P. Sherwood (Newcastle)
"X-ray photoelectron spectroscopic studies of electrode and other surfaces"

21. 3.84 Dr. G. Beamson (Durham/Kratos)
"EXAFS: General Principles and Applications"

23. 3.84 Dr. A. Ceulemans (Leuven)
"The Development of Field-Type models of the Bonding in Molecular Clusters"

2. 4.84 Prof. K. O'Driscoll (Waterloo)
"Chain Ending reactions in Free Radical Polymerisation"

3. 4.84 Prof. C.H. Rochester (Dundee)
"Infrared Studies of adsorption at the Solid-Liquid Interface"

25. 4.84 Dr. R.M. Acheson (Biochemistry, Oxford)
"Some Heterocyclic Detective Stories"

27. 4.84 Dr. T. Albright (Houston, U.S.A.)
"Sigmatropic Rearrangements in Organometallic Chemistry"

14. 5.84 Prof. W.R. Dolbier (Florida, USA)
"Cycloaddition Reactions of Fluorinated Allenes"

16. 5.84 Dr. P.J. Garratt (UCL)
"Synthesis with Dilithiated Vicinal Diesters and Carboximides"

22. 5.84 Prof. F.C. de Schryver (Leuven)
"The use of Luminescence in the study of micellar aggregates" and
"Configurational and Conformational control in excited state complex formation"

23. 5.84 Prof. M. Tada (Waseda, Japan)
"Photochemistry of Dicyanopyrazine Derivatives"

31. 5.84 Dr. A. Haaland (Oslo)
"Electron Diffraction Studies of some organometallic compounds"

11. 6.84 Dr. J.B. Street (IBM, California)
"Conducting Polymers derived from Pyrroles"

19. 9.84 Dr. C. Brown (IBM, California)
"New Superbase reactions with organic compounds"

21. 9.84 Dr. H.W. Gibson (Signal UOP, Illinois)
"Isomerization of Polyacetylene"

19.10.84 Dr. A. Germain (Languedoc, Montpellier)
"Anodic Oxidation of Perfluoro Organic Compounds in Perfluoroalkane Sulphonic Acids"

24.10.84 Prof. R.K. Harris (Durham)
"N.M.R. of Solid Polymers"

28.10.84 Dr. R. Snaith (Strathclyde)
"Exploring Lithium Chemistry: Novel Structures, Bonding and Reagents"

7.11.84 Prof. W.W. Porterfield (Hampden-Sydney College, USA)
"There is no Borane Chemistry (only Geometry)"

7.11.84 Dr. H.S. Munro (Durham)
"New Information from ESCA Data"

21.11.84 Mr. N. Everall (Durham)
"Picosecond Pulsed Laser Raman Spectroscopy"

27.11.84 Dr. W.J. Feast (Durham)
"A Plain Man's Guide to Polymeric Organic Metals"

28.11.84 Dr. T.A. Stephenson (Edinburgh)
"Some recent studies in Platinum Metal Chemistry"

12.12.84 Dr. K.B. Dillon (Durham)
"^{31}P N.M.R. Studies of some Anionic Phosphorus Complexes"

11. 1.85 Emeritus Prof. H. Suschitzky (Salford)
"Fruitful Fissons of Benzofuroxanes and Isobenzimic azoles (umpolung of o-phenylenediamine)"

13. 2.85 Dr. G.W.J. Fleet (Oxford)
"Synthesis of some Alkaloids from Carbohydrates"

19. 2.85 Dr. D.J. Mincher (Durham)
"Stereoselective Synthesis of some novel Anthracyclinones related to the anti-cancer drug Adriamy and to the Steffimycin Antibiotics"

27. 2.85 Dr. R. Mulvey (Durham)
"Some unusual Lithium Complexes"

6. 3.85 Dr. P.J. Kocienski (Leeds)
"Some Synthetic Applications of Silicon-Mediated Annulation Reactions"

7. 3.85 Dr. P.J. Rodgers (I.C.I. plc. Agricultural Division, Billingham)
"Industrial Polymers from Bacteria"

12. 3.85 Prof. K.J. Packer (B.P. Ltd./East Anglia)
"N.M.R. Investigations of the Structure of Solid Polymers"

14. 3.85 Prof. A.R. Katritzky F.R.S. (Florida)
"Some Adventures in Heterocyclic Chemistry"

20. 3.85 Dr. M. Poliakoff (Nottingham)
"New Methods for detecting Organometallic Intermediates in Solution"

28. 3.85 Prof. H. Ringsdorf (Mainz)
"Polymeric Liposomes as Models for Biomembranes and Cells?"

24. 4.85 Dr. M.C. Grossel (Bedford College, London)
"Hydroxypyridone dyes - Bleachable one-dimensional Metals?"

25. 4.85 Major S.A. Shackelford (U.S. Air Force)
"In Situ Mechanistic Studies on Cendensed Phase Thermochemical Reaction Processes: Deuterium Isotope Effects in HMX Decomposition, Explosives and Combustion"

1. 5.85 Dr. D. Parker (I.C.I. plc. Petrochemical and Plastics Division, Wilton)
"Applications of Radioisotopes in Industrial Research"

7. 5.85 Prof. G.E. Coates (formerly of University of Wymoning, U.S.A.)
"Chemical Education in England and America: Successes and Deficiencies"

8. 5.85 Prof. D. Tuck (Windsor, Ontario)
"Lower Oxidation State Chemistry of Indium"

8. 5.85 Prof. G. Williams (U.C.W. Aberystwyth)
"Liquid Crystalline Polymers"

9. 5.85 Prof. R.K. Harris (Durham)
"Chemistry in a Spin: Nuclear Magnetic Resonance"

14. 5.85 Prof. J. Passmore (New Brunswick, U.S.A.)
"The Synthesis and Characterisation of some Novel Selenium-Iodine Cations, aided by ^{77}Se N.M.R. Spectroscopy"

15. 5.85 Dr. J.E. Packer (Auckland, New Zealand)
Studies of Free Radical Reactions in aqueous solution using Ionising Radiation"

17. 5.85 Prof. I.D. Brown (McMaster University, Canada)
"Bond Valence as a Model for Inorganic Chemistry"

21. 5.85 Dr. D.L.H. Williams (Durham)
"Chemistry in Colour"

22. 5.85 Dr. M. Hudlicky (Blacksburg, U.S.A.)
"Preferential Elimination of Hydrogen Fluoride from Vicinal Bromofluorocompounds"

22. 5.85 Dr. R. Grimmett (Otago, New Zealand)
"Some Aspects of Nucleophilic Substitution in Imidazoles"

4. 6.85 Dr. P.S. Belton (Food Research Institute, Norwich)
"Analytical Photoacoustic Spectroscopy"

13. 6.85 Dr. D. Woolins (Imperial College, London)
"Metal - Sulphur - Nitrogen Complexes"

14. 6.85 Prof. Z. Rappoport (Hebrew University, Jerusalem)
"The Rich Mechanistic World of Nucleophilic Cinylic Substitution"

19. 6.85 Dr. R.N. Mitchell (Dortmund)
"Some Synthetic and NMR - Spectroscopic Studies of Organotin Compounds"

26. 6.85 Prof. G. Shaw (Bradford)
"Synthetic Studies on Imidazole Nucleosides and the Antibiotic Coformycin"

12. 7.85 Dr. K. Laali (Hydrocarbon Research Institute, University of Southern California)
"Recent Developments in Superacid Chemistry and Mechanistic Considerations in Electrophilic Aromatic Substitutions: A Progress Report"

13. 9.85 Dr. V.S. Parmar (University of Delhi),
"Enzyme Assisted ERC Synthesis"

30.10.85 Dr. S.N. Whittleton (University of Durham),
"An Investigation of a Reaction Window"

5.11.85 Prof. M.J. O'Donnell (Indiana-Purdue University),
"New Methodology for the Synthesis of Amino acids"

20.11.85 Dr. J.A.H. MacBride (Sunderland Polytechnic).
"A Heterocyclic Tour on a Distorted Tricycle-Biphenylene"

28.11.85 Prof. D.J. Waddington (University of York),
"Resources for the Chemistry Teacher"

15. 1.86 Prof. N. Sheppard (University of East Anglia),
"Vibrational and Spectroscopic Determinations of the Structures of Molecules Chemisorbed on Metal Surfaces"

29. 1.86 Dr. J.H. Clark (University of York),
"Novel Fluoride Ion Reagents"

12. 2.86 Prof. O.S. Tee (Concordia University, Montreal),
"Bromination of Phenols"

12. 2.86 Dr. J. Yarwood (University of Durham),
"The Structure of Water in Liquid Crystals"

19. 2.86 Prof. G. Procter (University of Salford), "Approaches to the Synthesis of some Natural Products"

26. 2.86 Miss C. Till (University of Durham), "ESCA and Optical Emission Studies of the Plasma Polymerisation of Perfluoroaromatics"

5. 3.86 Dr. D. Hathway (University of Durham), "Herbicide Selectivity"

5. 3.86 Dr. M. Schroder (University of Edinburgh), "Studies on Macrocycle Complexes"

12. 3.86 Dr. J.M. Brown (University of Oxford), "Chelate Control in Homogeneous Catalysis"

14. 5.86 Dr. P.R.R. Langridge-Smith (University of Edinburgh), "Naked Metal Clusters - Synthesis, Characterisation and Chemistry"

9. 6.86 Prof. R. Schmutzler (University of Braunschweig), "Mixed Valence Diphosphorous Compounds"

23. 6.86 Prof. R.E. Wilde (Texas Technical University), "Molecular Dynamic Processes from Vibrational Bandshapes"

B. Lectures Organised by Durham University Chemical Society during the period 1983-1986

20.10.83 Prof. R.B. Cundall (Salford) "Explosives

3.11.83 Dr. G. Richards (Oxford) "Quantum Pharmacology"

10.11.83 Prof. J.H. Ridd (U.C.L.). "Ipso-Attack in Electrophilic Aromatic Substitution"

17.11.83 Dr. J. Harrison (Sterling Organic), "Applied Chemistry and the Pharmaceutical Industry" "Joint Lecture with the Society of Chemical Industry)

24.11.83 Prof. D.A. King (Liverpool), "Chemistry in 2-Dimensions"

1.12.83 Dr. J.D. Coyle (The Open University), "The Problem with Sunshine"

26. 1.84 Prof. T.L. Blundell (Birkbeck College, London) "Biological Recognition: Interactions of Macromolecular Surfaces"

2. 2.84 Prof. N.B.H. Jonathan (Southampton), "Photoelectron Spectroscopy - A Radical Approach"

16. 2.84 Prof. D. Phillips (The Royal Institution), "Luminescence and Photochemistry - a Light Entertainment"

23. 2.84 Prof. F.G.A. Stone F.R.S. (Bristol), "The Use of Carbene and Carbyne Groups to Synthesise Metal Clusters" (The Waddington Memorial Lecture)

1. 3.84 Prof. A.J. Leadbetter (Rutherford Appleton Labs.), "Liquid Crystals"

8. 3.84 Prof. D. Chapman (Royal Free Hospital School of Medicine, London) "Phospholipids and Biomembranes: Basic Science and Future Techniques"

28. 3.84 Prof. H. Schmidbaur (Munich, F.R.G.), "Ylides in Coordination Sphere of Metal: Synthetic, Structural and Theoretical Aspects" (R.S.C. Centenary Lecture)

18.10.84 Dr. N. Logan (Nottingham), "N_2O_4 and Rocket Fuels"

23.10.84 Dr. W.J. Feast (Durham), "Syntheses of Conjugated Polymers. How and Why?"

8.11.84 Prof. B.J. Aylett (Queen Mary College, London), "Silicon - Dead Common or Refined?"

15.11.84 Prof. B.T. Golding (Newcastle-upon-Tyne), "The Vitamin B_{12} Mystery"

22.11.84 Prof. D.T. Clark (I.C.I. New Science Group), "Structure, Bonding, Reactivity and Synthesis as revealed by ESCA" (R.S.C. Tilden Lecture)

29.11.84 Prof. C.J.M. Stirling (University College of North Wales "Molecules taking the Strain"

6.12.84 Prof. R.D. Chambers (Durham), "The Unusual World of Fluorine"

24. 1.85 Dr. A.K. Covington (Newcastle-upon-Tyne), "Chemistry with Chips"

31. 1.85 Dr. M.L.H. Green (Oxford), "Naked Atoms and Negligee Ligands"

7. 2.85 Prof. A. Ledwith (Pilkington Bros.), "Glass as a High Technology Material" (Joint Lecture with the Society of Chemical Industry)

14. 2.85 Dr. J.A. Salthouse (Manchester), "Son et Lumiere"

21. 2.85 Prof. P.M. Maitlis, F.R.S. (Sheffield),
"What Use is Rhodium?"

7. 3.85 Dr. P.W. Atkins (Oxford),
"Magnetic Reactions"

17.10.85 Dr. C.J. Ludman (University of Durham)
"Some Thermochemical aspects of Explosions"
"A Demonstration Lecture)

24.10.85 Dr. J. Dewing,(U.M.I.S.T.),
"Zeolites - Small Holes, Big Opportunities"

31.10.85 Dr. P. Timms,(University of Bristol),
"Some Chemistry of Fireworks"
(A Demonstration Lecture)

7.11.85 Prof. G. Ertl, (University of Munich),
"Heterogeneous Catalysis",
(R.S.C. Centenary Lecture)

14.11.85 Dr. S.G. Davies (University of Oxford),
"Chirality Control and Molecular Recognition"

21.11.85 Prof. K.H. Jack, F.R.S. (University of Newcastle/Tyne),
"Chemistry of Si-Al-O-N Engineering Ceramics"
(Joint Lecture with the Society of Chemical Industry)

28.11.85 Dr. B.A.J. Clark (Research Division, Kodak Ltd.)
"Chemistry and Principles of Colour Photography"

23. 1.86 Prof. Sir Jack Lewis, F.R.S. (University of Cambridge),
"Some More Recent Aspects in the Cluster Chemistry
of Ruthenium and Osmium Carbonyls"
(The Waddington Memorial Lecture)

30. 1.86 Dr. N.J. Phillips,(University of Technology, Loughborough)
"Laser Holography"

13. 2.86 Prof. R. Grigg (Queen's University, Belfast),
"Thermal Generation of 1,3-Dipoles"
(R.S.C. Tilden Lecture)

20. 2.86 Dr. C.J.F. Barnard,(Johnson Matthey Group Research),
"Platinum Anti-Cancer Drug Development - From
Serendipity to Science"

27. 2.86 Prof. R.K. Harris, (University of Durham),
"The Magic of Solid State NMR"

6. 3.86 Dr. B. Iddon (University of Salford),
"The Magic of Chemistry"
(A Demonstration Lecture)

(C) Research Conferences attended (* indicates Paper presented)

11 4.84 Graduate Symposium, Durham.

20. 3.85 Spectroscopic Investigation of Chemisorbed Layers, Daresbury Laboratory.

*29. 3.85 Graduate Symposium, Durham.

7-11. 4.86 Applying Microprocessors to Experiments - A Practical Introduction, University of Manchester (residential course).

8. 7.86 Infrared and Raman Discussion Group Meeting, University of Durham Industrial Research Laboratories (UDIRL).

9. 7.86 Industrial Applications of Raman Spectroscopy, UDIRL.

(D) First Year Induction Course, October 1983

This course consists of a series of one hour lectures on the services available in the department.

1. Departmental organisation
2. Safety matters
3. Electrical appliances and infrared spectroscopy
4. Chromatography and Microanalysis
5. Atomic absorptiometry and inorganic analysis
6. Library facilities
7. Mass spectrometry
8. Nuclear magnetic resonance spectroscopy
9. Glassblowing technique.